

Magnetic and Velocity Field of Sunspots in the Photosphere and Upper Chromosphere

Von der Fakultät für Elektrotechnik, Informationstechnik, Physik
der Technischen Universität Carolo-Wilhelmina
zu Braunschweig
zur Erlangung des Grades eines
Doktors der Naturwissenschaften
(Dr.rer.nat.)
genehmigte
Dissertation

von Jayant Joshi
aus Damri-Dungarpur, India

Bibliografische Information der Deutschen Nationalbibliothek

Die Deutsche Nationalbibliothek verzeichnet diese Publikation in der Deutschen Nationalbibliografie; detaillierte bibliografische Daten sind im Internet über <http://dnb.d-nb.de> abrufbar.

1. Referentin oder Referent: Prof. Dr. Sami K. Solanki
 2. Referentin oder Referent: Prof. Dr. Karl-Heinz Glaßmeier
- eingereicht am: 9. Dezember 2013
mündliche Prüfung (Disputation) am: 6. März 2014

ISBN 978-3-944072-01-2

uni-edition GmbH 2014

<http://www.uni-edition.de>

© Jayant Joshi



This work is distributed under a
Creative Commons Attribution 3.0 License

Printed in Germany

Vorveröffentlichungen der Dissertation

Teilergebnisse aus dieser Arbeit wurden mit Genehmigung der Fakultät für Elektrotechnik, Informationstechnik, Physik, vertreten durch die Mentorin oder den Mentor/die Betreuerin oder den Betreuer der Arbeit, in folgenden Beiträgen vorab veröffentlicht:

Publikationen

- **Joshi, J.**, Pietarila, A., Hirzberger, J., Solanki, S. K., Aznar Cuadrado, R., Merenda, L., Convective Nature of Sunspot Penumbra Filaments: Discovery of Downflows in the Deep Photosphere, *Astrophysical Journal Letters*, 734, L18 (2011).

Tagungsbeiträge

- **Joshi, J.**, Lagg, A., Hirzberger, J., Solanki, S. K., 3D Structure of a Sunspot: From Photosphere to Upper Chromosphere (Oral), *The Solar System within Geo- and Astrophysics (Rocks 'n' Stars)*, Veranstaltungszentrum am Wilhelmsplatz, Göttingen, Germany, 8.-11. Oktober (2012)
- **Joshi, J.**, Lagg, A., Hirzberger, J., Solanki, S. K., Kim, H., 3D Structure of a Sunspot: From Photosphere to Upper Chromosphere (Poster), *Hinode-6 meeting*, St Andrews, Scotland, UK, 14.-17. August (2012)
- **Joshi, J.**, Danilovic, S., Hirzberger, J., Rubio da Costa, F., Solanki, S. K., Spectroscopy of a Sunspot Penumbra in the Deep Photospheric C 15380 Å Spectral Line (Poster), *Hinode-5 meeting*, Cambridge, Massachusetts, USA, 10.-15. Oktober (2011)

— *To my parents* —

Contents

Abstract	11
1 Sunspots: Introduction	13
1.1 Sunspots: Global structure	14
1.1.1 Magnetic field	14
1.1.2 Evershed flow	16
1.2 Sunspots: Fine structures	18
1.2.1 Umbral dots	18
1.2.2 Light-bridges	19
1.2.3 Penumbra	20
1.2.3.1 Intensity structure	20
1.2.3.2 Magnetic field	21
1.2.3.3 Fine structures of the Evershed flow	23
1.2.3.4 Net circular polarization	23
1.3 Umbra: Theoretical models	24
1.4 Penumbra: Models and simulations	26
1.4.1 The uncombed model	26
1.4.2 Siphon flows	27
1.4.3 Moving magnetic flux tubes	29
1.4.4 Convective roll	32
1.4.5 Gappy penumbra	32
1.4.6 3D MHD simulations of sunspot	34
2 Spectro-polarimetry	37
2.1 Stokes parameters	37
2.2 Zeeman effect	38
2.2.1 Polarization and strength of the Zeeman components	40
2.3 Paschen-Back effect	41
2.4 Radiative Transfer Equation	41
2.5 Solution to the RTE	44
2.5.1 Milne-Eddington approximation	45
2.6 Inversion of the Stokes profiles	46
2.6.1 HeLix ⁺	46
2.6.2 SPINOR	47
2.7 Instrumentation	48
2.7.1 SST and CRISP	48

2.7.2	VTT and TIP-2	48
2.7.3	Hinode SOT/SP	49
3	Penumbrae: Convective Structure in the Deep Photosphere	51
3.1	Introduction	51
3.2	SST/CRISP observations and data reduction	52
3.2.1	Image reconstruction	52
3.2.2	Doppler velocity	53
3.2.3	Straylight Correction	55
3.3	Results	58
3.4	Discussion	60
4	Vertical Magnetic Field Gradient in the Photospheric Layers of Sunspot	63
4.1	Introduction	63
4.2	VTT/TIP-2 observations and analysis	64
4.2.1	Observations	64
4.2.2	SPINOR inversion of the Si I and Ca I lines	67
4.2.2.1	Influence of straylight	69
4.2.3	Inversion results	73
4.3	Hinode SOT/SP observations	77
4.4	Comparison with 3D MHD simulations	82
4.5	Opposite polarity patches in penumbrae	91
4.6	Discussion	91
5	3D Structure of a Sunspot: From the Photosphere to the Upper Chromosphere	97
5.1	Introduction	97
5.2	VTT/TIP-2 Observations	100
5.2.1	HeLIX ⁺ inversions of the He I 10830 Å triplet	102
5.3	Analysis and results	104
5.3.1	Parameter maps	104
5.3.2	Radial cuts through the sunspots	109
5.3.3	Scatter plots	110
5.3.4	Azimuthal averages	110
5.3.5	Vertical gradient of B	113
5.3.6	Magnetic field twist	113
5.4	Discussion and conclusion	115
5.4.1	Magnetic field strength	115
5.4.2	Vertical gradient of B	118
5.4.3	Inclination	119
5.4.4	Twist of sunspot's magnetic field	120
6	Summary and Outlook	121
	Bibliography	125
	Publications and Presentations	149

Acknowledgements	151
Curriculum Vitae	153

Abstract

Sunspots, the dark blemishes on the solar surface have been widely studied for the past 400 years. Sunspots are the most readily identifiable manifestation of magnetic field concentrations on the solar surface. Interaction of the sunspot magnetic field with the plasma makes them one of the most interesting objects for research in solar physics.

This thesis presents a study of the photospheric and upper chromospheric velocity and magnetic field structure of sunspots by analyzing spectro-polarimetric observations. These observations comprise different spectral lines obtained with two ground based telescopes and a space borne telescope.

The lower brightness of sunspots on the solar surface is due to the presence of strong magnetic fields (up to 4 kG in the umbra), which makes the overturning convection inefficient. Convection is the main heat transport mechanism in the quiet Sun. The Penumbra, the annular part around the umbra has a brightness of about 75% of that in the quiet Sun. At the same time it has an average magnetic field strength of around 1.5 kG. The brightness of penumbrae has been an enigma for solar physicists for a long time. Theoretical models like the gappy penumbra model and the convective roll model as well as magneto-hydrodynamic (MHD) simulations suggest that the heat transport in penumbrae is based on the presence of overturning convection. Direct observational evidence for the presence of convective flows in penumbral filaments was missing so far. In Chapter 3 we present observations of a penumbra in the C I 5380 Å spectral line formed in the deep photosphere. These high spatial resolution observations (0.14") are obtained with the Swedish 1-m Solar Telescope (SST). Doppler map clearly shows the presence of several dark downflow lanes at the edges of the penumbral filaments which surround the bright upflows at the center of the filaments, supporting overturning convection as a mechanism of heat transport in penumbrae.

Chapter 4 analyses the vertical gradient of the magnetic field strength in sunspots in the photosphere. This study includes two different sets of observations: (1) Observations with the Solar Optical Telescope (SOT) onboard the Hinode satellite. (2) Observations with the Tenerife Infrared Polarimeter-2 (TIP-2) mounted at the German Vacuum Tower Telescope (VTT). The spatially coupled inversions (using the SPINOR code) of the Zeeman sensitive Fe I 6301.5 Å and Fe I 6302.5 Å spectral lines observed with the SOT show local patches in the penumbra where the magnetic field decreases with optical depth. Such detection of local magnetic "canopies" have not been reported earlier in the literature. These patches coincide with the bright inner parts of penumbral filaments and indicates that the stronger fields from the dark spines expand and cover i.e. overlie the weaker and more horizontal fields. The radial profile of the vertical gradient obtained with azimuthal averages shows that in the inner penumbra the magnetic field decreases with depth in the lower photosphere whereas in the outer penumbra it has the opposite trend. This result

is consistent with low spatial resolution ($1''0$) spectro-polarimetric observations obtained with VTT/TIP-2. These particular observations include the photospheric Si I 10827.1 Å and Ca I 10833.4 Å spectral lines. These observational results are compared with MHD simulations of a sunspot. These comparisons show that the decreasing magnetic field strength with optical depth can be attributed to highly corrugated iso-optical depth surfaces.

The 3D structure of a sunspot's magnetic field is studied in Chapter 5 by comparing the measurements of photospheric and the upper chromospheric magnetic field. Here the photospheric magnetic field is obtained by inversion (using the SPINOR code) of the Si I 10827.1 Å and Ca I 10833.4 Å spectral lines together, whereas inversion of the He I triplet at 10830 Å using the HeLIx⁺ code provided the upper chromospheric magnetic field. These observations were recorded with VTT/TIP-2. The umbral magnetic field strength in the upper chromosphere is found to be lower by a factor 1.4-1.6 compared to the photosphere. The vertical gradient of the magnetic field strength between the photosphere and the upper chromosphere is in a range between 0.5 G km^{-1} and 1.0 G km^{-1} in the umbra. The difference of the magnetic field strength between both atmospheric layers steadily decreases from the sunspot center to the outer boundary of the sunspot. The magnetic canopy at the upper chromospheric heights is found just outside the visible boundary of the sunspot. The most striking result found is that the magnetic field vector is less inclined in the upper chromosphere compared to the photosphere. A higher magnetic field strength is observed in a light-bridge in the upper chromosphere compared to that in the photosphere.

1 Sunspots: Introduction

The Sun is a magnetic star. The solar magnetic field is thought to be generated through a dynamo process, an interaction between differential rotation and turbulence just below the convection zone of the Sun (see, e.g., review by [Charbonneau 2005](#)). Toroidal magnetic flux generated by the dynamo action rises from the base of the convection zone to the surface of the Sun through buoyancy.

The magnetic field appears in a wide range of spatial scales with different magnitudes in the photosphere, the visible surface of the Sun. Regions of enhanced surface magnetic fields are called active regions, usually display a bipolar configuration. The largest features, both in terms of size and the magnetic field strength, are sunspots. Magnetic field structures on the solar surface also appear on the scale as small as the diffraction limit of the present generation's telescopes. The smallest magnetic field structures are also known as the magnetic elements. Outside active regions, i.e. in the quiet Sun, magnetic elements appear with enhanced density in network which are basically the boundaries of large scale convective cells. These large scale convective cells of size 20-40 Mm are known as supergranules. The magnetic field which appears in between the magnetic network is known as the internetwork magnetic field. For reviews on small-scale solar magnetic fields see, [Solanki \(1993\)](#) and [de Wijn et al. \(2009\)](#).

The magnetic field of the Sun varies with time in a cyclic manner with a periodicity approximately of 11 years. This is clearly evident in the temporal variation of daily numbers of the sunspots visible on the solar surface (see Fig. 1.1). The magnetic polarity reverses after ≈ 11 years so that the full magnetic cycle of the Sun has a mean period of 22 years. The dynamo is not only widely accepted as the root cause for the generation of the magnetic field but also for the solar cycle.

Active regions are relevant for all energetic phenomena on the Sun, like flares or coro-

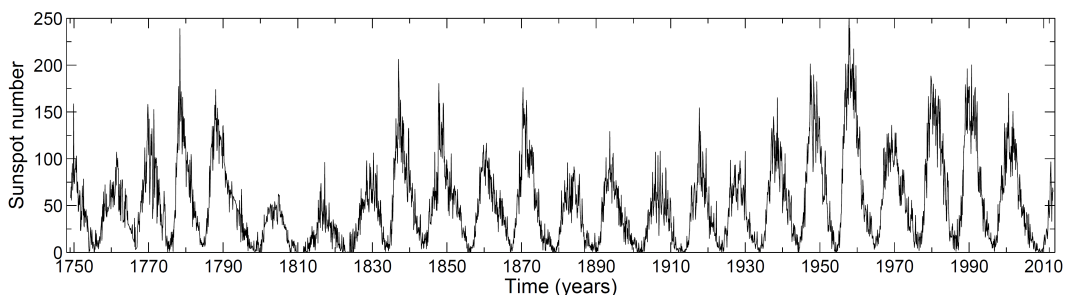


Figure 1.1: Solar cycle: monthly averaged sunspot number between 1750 to 2012 (Credit: <http://www.ngdc.noaa.gov>).

nal mass ejections (CMEs). Being a major constituent of active regions, sunspots plays an important role for the understanding all these activities and the underlying physical processes of magneto-convection.

The present chapter introduces observational facts about sunspots on a global as well as on spatially small scales. The large scale structure of sunspots is summarized in Section 1.1, Section 1.2 deals with the fine structure of sunspots. Remaining parts of this chapter (Sections 1.3 and 1.4) summarize the current theoretical understating of a sunspot's structures.

1.1 Sunspots: Global structure

Sunspots are generally identified as dark features on the Solar surface, i.e. in the photosphere. Sunspots have a central dark part called umbra which is surrounded by a relatively brighter part, the penumbra (see Fig. 1.2). When a dark spot (naked umbra) appears without penumbra then it is called pore. Sunspots appear in a wide range of sizes and can have a maximum size of ~ 60000 km (diameter), the smallest sunspots have a diameter of around 3500 km (Bray and Loughhead 1964). Sunspots appear darker than the surrounding quiet photosphere because they harbor strong magnetic fields which suppress convection, the main energy transport mechanism below the solar surface.

1.1.1 Magnetic field

Hale (1908a,b) discovered that sunspots are magnetic foot-prints on the solar surface. Like the temperature the magnetic field is also not uniformly distributed across the body of sunspot. Generally, the strongest magnetic field belongs to the geometric center of a sunspot (see Fig. 1.3). The maximum strength of the magnetic field of sunspots varies in a range between 2000 and 4000 G, depending on the size of the sunspot (e.g., Ringnes and Jensen 1960, Brants and Zwaan 1982, Kopp and Rabin 1992, Collados et al. 1994, Solanki 1997). The azimuthally averaged field strength in a sunspot decreases steadily from the sunspot's center to its periphery. The intensity, and therefore also the temperature, shows a clear jump at the umbra-penumbra boundary, when their azimuthally averaged radial profiles are produced. The relation between the continuum intensity (also temperature) and the magnetic field strength has been amply studied. It shows a relatively smooth variation of the magnetic field compared to the temperature (Kopp and Rabin 1992, Martinez Pillet and Vazquez 1993, Solanki et al. 1993, Balthasar and Schmidt 1994, Stanchfield et al. 1997, Leka 1997, Mathew et al. 2003, 2004).

The radial dependency of the magnetic field strength (see Fig. 1.4) has been studied extensively, most recently by Lites et al. (1990), Solanki et al. (1992), McPherson et al. (1992), Kopp and Rabin (1992), Hewagama et al. (1993), Balthasar and Schmidt (1993), Skumanich et al. (1994), Keppens and Martinez Pillet (1996), Westendorp Plaza et al. (2001b), Mathew et al. (2003) and Borrero and Ichimoto (2011). These studies show that at the sunspot's visible boundary in the photosphere the magnetic field strength amounts to 700-1000 G on average. Near the umbra-penumbra boundary the magnetic field strength is found to be 1400-2000 G (Lites et al. 1990, 1991, Schmidt et al. 1992, Balthasar and Schmidt 1993, Skumanich et al. 1994, Keppens and Martinez Pillet 1996, Mathew et al.

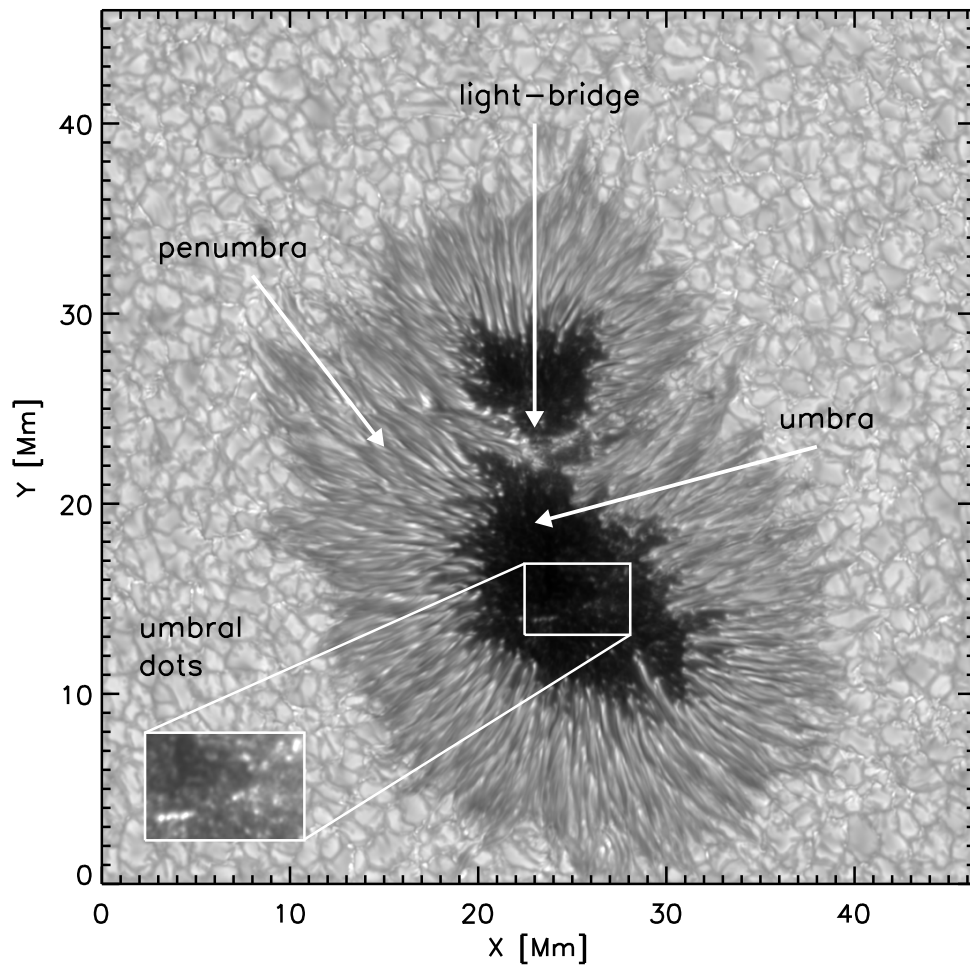


Figure 1.2: Sunspot's morphology: This image of a sunspot was taken with the Swedish 1-m Solar Telescope (SST). Different parts like umbra, penumbra, light-bridge and umbral dots can be identified. For better visibility of the umbral dots a part of the umbra is shown in *lower left* of the image (image courtesy of M. van Noort).

2003, Westendorp Plaza et al. 2001b).

The magnetic field at the center of a sunspot is mostly vertical (normal to the solar surface) where the magnetic field strength is also strongest. The magnetic field becomes steadily more inclined towards the sunspot's boundary and it is close to horizontal at the sunspot's outer boundary, i.e. making an angle of $70\text{-}80^\circ$ to the surface normal (see Figs. 1.3 and 1.4). The magnetic field strength and the inclination angle are well correlated in sunspots.

Our current knowledge of the vertical structure and gradient of the sunspot's magnetic field is less studied when compared to its spatial structure. Chapter 4 contains a study of vertical gradients of the magnetic field in the photospheric layer. A comparison of the sunspot's magnetic field between its photospheric and upper chromospheric layers is done in Chapter 5.

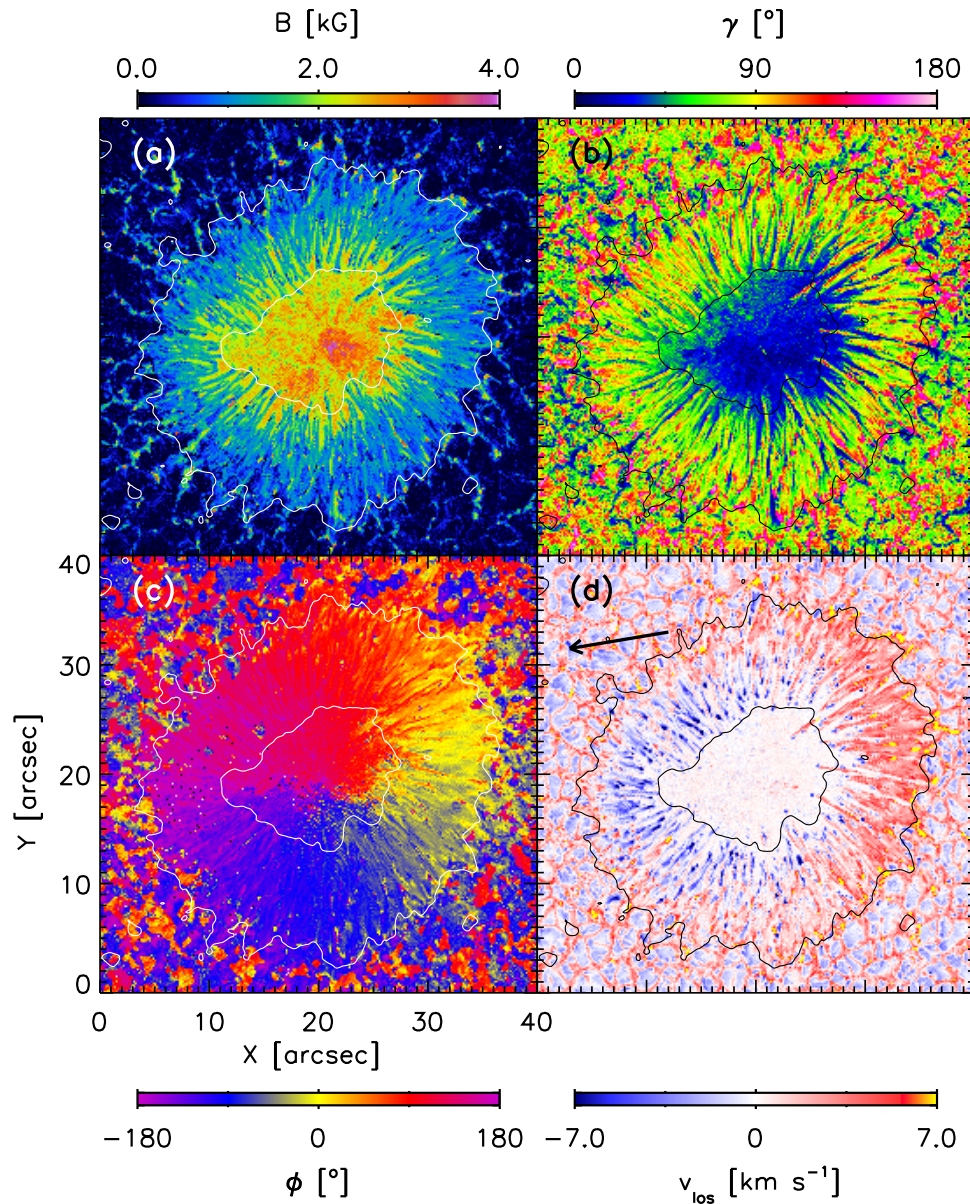


Figure 1.3: Maps of a sunspot’s vector magnetic field and line-of-sight (LOS) velocity: (a) Magnetic field strength, B , (b) inclination of the magnetic field vector, γ , (c) azimuth angle of the magnetic field vector, ϕ and (d) LOS velocity, v_{los} of a sunspot observed with the Solar Optical Telescope (Tsuneta et al. 2008) on board the Hinode satellite (Kosugi et al. 2007). All the physical parameters are shown at optical depth $\tau=1$ at 630 nm. The parameters are retrieved through a coupled inversion technique using the SPINOR code (see Chapter 2). Inner and outer contours in all the panels represent the umbra-penumbra boundary and the outer boundary of the sunspot. The arrow in panel (d) indicates the disk center direction (inversion results courtesy of G. Narayan).

1.1.2 Evershed flow

Evershed in 1909 found a systematic wavelength shift in many photospheric absorption lines in penumbrae. He found that limb-side penumbrae show redshifts of spectral lines

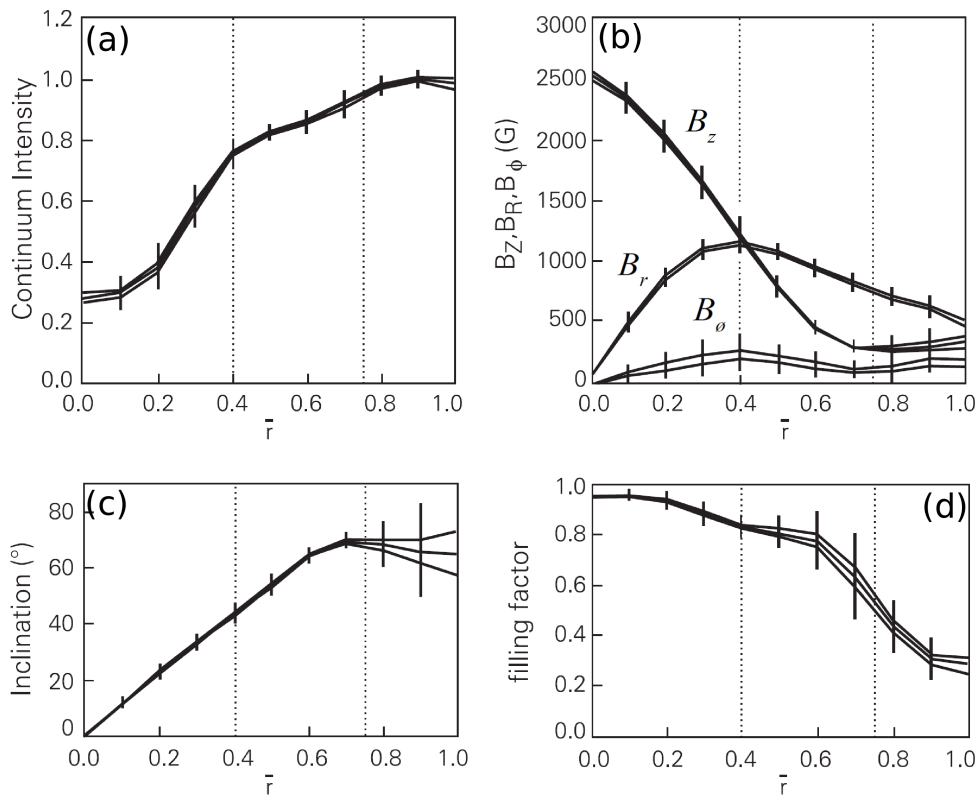


Figure 1.4: Averaged radial properties of 19 sunspots as a function of normalized radial distance, r from the sunspot center. (a) Continuum intensity, (b) three components of magnetic field strength, vertical (B_z), radial (B_r) and azimuthal (B_ϕ), (c) inclination of the magnetic field vector and (d) the magnetic filling factor (adapted from [Keppens and Martinez Pillet 1996](#)).

while disk center side penumbrae show blueshifts. Evershed interpreted this shifts of spectral line as outward mass flow in sunspot penumbrae. He also investigated sunspots at different locations on the solar disk (center-to-limb variation) and found that the shift is maximum when sunspots are observed close to solar limb. He concluded that these flows are parallel to the solar surface. The blue- and redshifts in penumbrae are known since then as Evershed effect. The Evershed effect in a sunspot observed with the Solar Optical Telescope (SOT) on board the Hinode satellite (for details about Hinode, see Chapter 2 Section 2.7.3) is shown in Fig. 1.3(d).

The Evershed flow has a higher magnitude in the outer penumbra compared to that in the inner penumbra. Already before the 1970s it was known that spectral lines in penumbrae are not only shifted but also asymmetric ([St. John 1913](#), [Servajean 1961](#), [Holmes 1961, 1963](#), [Maltby 1964](#), [Schröter 1965](#)). These line asymmetries can be caused by unresolved fine structures as well as due to a height dependence of the Evershed flow. The Evershed flow is height dependent and stronger in deeper layers of the photosphere ([St. John 1913](#), [Maltby 1964](#), [Roupe van der Voort 2002](#), [Schlichenmaier et al. 2004](#)).

Some authors reported a sharp decrease of the Evershed flow exactly at the outer boundary of sunspots ([Brekke and Maltby 1963](#), [Wiehr et al. 1986](#), [Wiehr and Stellmacher 1989](#), [Wiehr and Degenhardt 1992](#), [Title et al. 1992, 1993](#), [Wiehr 1996](#), [Hirzberger and](#)

Kneer 2001), whereas there is convincing evidence in favor of the existence of the Evershed flow beyond the visible boundary of sunspots (Sheeley 1972, Küveler and Wiehr 1985, Dialetis et al. 1985, Alissandrakis et al. 1988, Dere et al. 1990, Börner and Kneer 1992, Rimmele 1994, 1995a). Solanki et al. (1994) showed that very small mass flux compared to the Evershed flow continues to flow radially outward beyond the penumbra boundary above the magnetic canopy (a detailed discussion about the magnetic canopy is presented in Chapters 4 and 5) and later supported by the observations of Rezaei et al. (2006).

Strong downflows in the outer and middle penumbra together with strong upflows in the inner penumbra have established that most of the Evershed flow which is initiated in the inner penumbra flows back to below the solar surface in the middle and outer penumbra (Schlichenmaier and Schmidt 2000, Westendorp Plaza et al. 2001b, Tritschler et al. 2004, Sánchez Almeida et al. 2007, Ichimoto et al. 2007a, Franz and Schlichenmaier 2009, Tiwari et al. 2013a, van Noort et al. 2013). Westendorp Plaza et al. (1997) and Tiwari et al. (2013a) found higher mass flux associated with downflows as compared to that associated with upflows. Tiwari et al. (2013a) attributed this observed asymmetry to the highly corrugated optical surfaces in the penumbra.

1.2 Sunspots: Fine structures

Modern day high spatial resolution observations of sunspots reveal a high level of fine structure, both in umbrae and penumbrae (see Figs. 1.2 and 1.3). Knowledge of fine spatial details of magnetic and velocity field structure arose new insight and make us to gather this observational facts which can help to improve our understanding about building blocks, formation and the stability of sunspots. This section recounts mostly static observational facts about umbral and penumbral fine structures. Progress about theoretical interpretation of these structures is accounted in Sections 1.3 and 1.4.

1.2.1 Umbral dots

Before 1970s bright granular structures in umbrae of size $1''.0$ - $3''.0$ were observed (e.g., by Chevalier 1914a,b, 1916, Bray and Loughhead 1959, Loughhead and Bray 1960). However, Thiessen (1950) had observed much finer bright structure of size $0''.3$ in the umbra. Danielson (1964) named these observed small-scale bright structures in the umbra, umbral dots.

High resolution observations with the Swedish 1-meter Solar Telescope (SST) revealed that the average diameter of umbral dots ranges between 175 and 230 km (Sobotka et al. 1997a,b, Sobotka and Hanslmeier 2005, Riethmüller et al. 2008, Hamedivafa 2008). Detailed studies by Sobotka et al. (1997a,b) and Riethmüller et al. (2008) showed that the lifetimes of umbral dots follows an exponential distribution.

Already from the early 1970s to the 1990s many observations reported that umbral dots exhibit weaker magnetic field compared to surrounding umbra (Kneer 1973, Buurman 1973, Adjabshirzadeh and Koutchmy 1983, Pahlke and Wiehr 1990, Schmidt et al. 1994, Tritschler and Schmidt 1997). However, a few observations reported that there is

no difference in field strength of umbral dots and surrounding umbra. (Zwaan et al. 1985, Lites et al. 1989, 1991).

Kneer (1973) and Pahlke and Wiehr (1990) detected upflows in umbral dots in the range of $1\text{-}3\text{ km s}^{-1}$, while other authors found only very weak upflows ($50\text{-}300\text{ m s}^{-1}$) (Rimmele 1997, Hartkorn and Rimmele 2003, Socas-Navarro et al. 2004) or no flow at all (Zwaan et al. 1985, Schmidt et al. 1994, Wiehr 1994).

3D magnetohydrodynamic (MHD) simulations of umbral dots by Schüssler and Vögler (2006) showed that umbral dots are vertical columns of magneto-convection in the umbra where hot plasma rises up to the surface by pushing magnetic field to the sides and then radiate surplus energy before flowing down at the edges of the umbral-dot. Dark lanes in umbral dots are the intrinsic property of the simulated umbral dots (Schüssler and Vögler 2006) which has also been found in observations by Bharti et al. (2007) and Rimmele (2008).

Studies by Socas-Navarro et al. (2004) and Riethmüller et al. (2008, 2013) show a weakening of the field strength and an enhancement of temperature and upflows in umbral dots. Riethmüller et al. (2013) systematically found downflow lanes which surround upflows at the center of umbral dots, supporting the MHD simulation of Schüssler and Vögler (2006).

It is important to mention here that umbral dots are classified as peripheral (close to the umbral boundary) and central umbral dots. They exhibit difference in dynamics and physical properties. Details can be found in the review on umbral dots in the Ph.D. thesis of Riethmüller (2013).

1.2.2 Light-bridges

Light-bridges are bright elongated structures which divide the umbra into two or more parts (see Fig. 1.2). Light-bridges appear with different width and fine structure. Light-bridges with granular-like sub-structure are known as 'photospheric' light-bridges, whereas some light-bridges look-like intrusions of penumbral filaments into the umbrae and are classified as 'penumbral' light-bridges. Narrow light-bridges exhibit similarities with umbral dots in many aspects. Beckers and Schröter (1969), Abdussamatov (1971b), Lites et al. (1990, 1991), Rüedi et al. (1995) and Leka (1997) reported reduced magnetic field strengths in light-bridges at the photospheric level. An investigation of 15 light-bridges by Leka (1997) showed that the magnetic field strength is reduced in range of $200\text{-}1500\text{ G}$. A field free intrusion in a light-bridge was observed by Lites et al. (1991) and Leka (1997). The magnetic field is found to be more inclined in light-bridges compared to the surrounding umbra (Beckers and Schröter 1969, Lites et al. 1991, Wiehr and Degenhardt 1993, Rüedi et al. 1995, Leka 1997, Katsukawa et al. 2007, Jurčák et al. 2006).

Similar to umbral dots, a central dark lane is also found in the 'penumbral' light-bridges (Berger and Berdyugina 2003, Lites et al. 2004, Bharti et al. 2007, Giordano et al. 2008, Sobotka and Puschmann 2009, Rouppe van der Voort et al. 2010), suggesting that magneto-convection takes place in light-bridges.

Rimmele (1997) found the first direct evidence of the magneto-convection in a light-bridge by detecting downflows at its edges. A study of horizontal motions of fine structure in a light-bridge by Hirzberger et al. (2002) supports the presence of convective cells. More recently cooler downflows in light bridges have been observed by many researchers

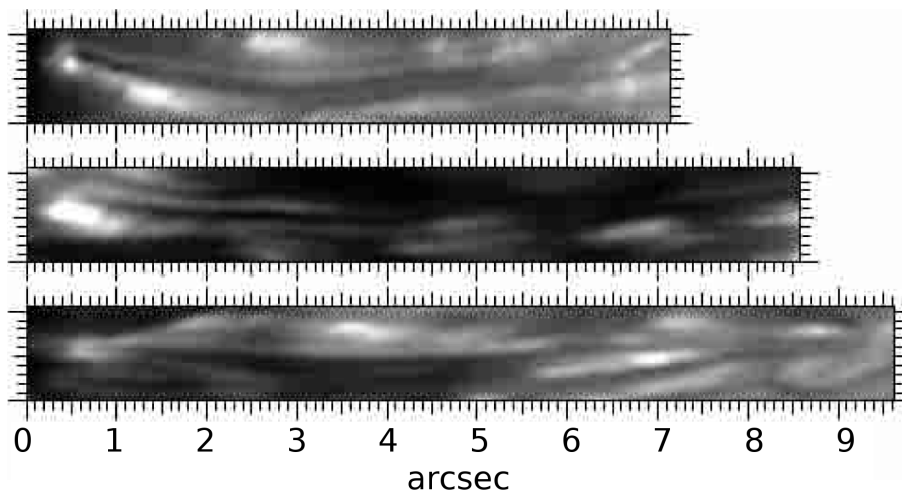


Figure 1.5: Bright penumbral filaments with central dark cores observed at a spatial resolution of $0''.1$ with the SST (adapted from [Roupe van der Voort et al. 2004](#)).

([Giordano et al. 2008](#), [Roupe van der Voort et al. 2010](#)).

[Jurčák and Sobotka \(2007\)](#) found that the magnetic field is more inclined and exhibits an enhanced strength in the upper photosphere above the light-bridge, forming a canopy-like structure. Their observations also suggest that a light-bridge is a nearly field free intrusion into the umbra and the surrounding umbral field expands and fills the area above the light-bridge.

A connection between light-bridges and chromospheric activity has been pointed out by many authors ([Asai et al. 2001](#), [Bharti et al. 2007](#), [Louis et al. 2008](#), [Shimizu 2011](#)). [Berger and Berdyugina \(2003\)](#), [Katsukawa \(2007\)](#) found coronal brightenings above a light-bridge and [Liu \(2012\)](#) observed coronal jets associated with light-bridges.

[Rüedi et al. \(1995\)](#) compared the vertical magnetic field strength of the photospheric and the upper chromospheric layers of a light-bridge and found that the light-bridge in photosphere has a reduced LOS magnetic field strength compared to the umbra, whereas in the upper chromosphere it is similar in the light-bridge and in the umbra. In extension to the study of [Rüedi et al. \(1995\)](#), in Chapter 5 we analyze full Stokes vectors to compare magnetic structures of a light-bridge in its photospheric and upper chromospheric layers.

1.2.3 Penumbra

Sunspot penumbrae are also structured in all physical aspects like intensity, plasma flow and magnetic field. The current section summarizes the properties of penumbral fine structure.

1.2.3.1 Intensity structure

At high spatial resolution observations better than $1''$, a filamentary structure in penumbrae can be seen very clearly. Dark and bright filaments are orientated in the radial direction (see Fig. 1.2). The width of bright filaments has been studied previously by many

researchers and it was found to be in range of $0''.3-0''.7$ (Danielson 1961a, Muller 1973, Toenjes and Woehl 1982, Denker 1998, Sobotka et al. 1999). At the same time many authors found that spatial intensity power spectra shows peak at the spatial frequency of the resolution limit (Harvey and Breckinridge 1973, Stachnik et al. 1983, Denker et al. 1995, Sanchez Almeida 1998). Sütterlin (2001) performed a power spectrum study with data recorded at the Dutch Open Telescope (DOT, Rutten et al. 1997), and showed that the filaments are well resolved and have a preferred width of $0''.35$. Scharmer et al. (2002) found that the width is even narrower, and lies in the range of $0''.20-0''.25$ (150-180 km). Contrary to Sütterlin (2001) and in support of Scharmer et al. (2002), Rouppe van der Voort et al. (2004) did not find peaks in power spectra in observation of spatial resolution $0''.12$ (80 km). This allows for presence of structure even finer than the highest spatial resolution currently available.

At high spatial resolution one can see that every bright filament is sub-structured. With the SST Scharmer et al. (2002) discovered dark cores within bright penumbral filaments (also see Fig. 1.5). These dark cores are predominantly visible in filaments which are close to the umbra-penumbra boundary. Bellot Rubio et al. (2005) and Langhans et al. (2007) found a typical width of dark cores of $0''.2$.

Almost all bright filaments consist of a brighter coma-like structure. These structure move radially inward and are known as penumbral grains (Muller 1973, 1976, Toenjes and Woehl 1982, Shine et al. 1987, Wang and Zirin 1992, Sobotka et al. 1995, Denker 1998, Sobotka et al. 1999, Sobotka and Sütterlin 2001). Inward moving coma-like structures of filament's are also called filament's heads, while the end part towards periphery of the sunspot is known as the tail of the filament. Since the plasma flow in penumbrae (the Evershed flow) is always in outward direction the question arises, what an inward motion of penumbral grains represents. This problem is still not satisfactory solved.

Recent study by Tiwari et al. (2013a) see also (see also Bharti et al. 2010) showed that penumbral filaments have a brighter head, and intensity steadily decreases towards the tail. Tiwari et al. (2013a) also showed an enhancement in intensity at the tail of filaments.

1.2.3.2 Magnetic field

To understand the origin and the physics behind the intensity patterns in penumbrae it is important to understand the structure of the magnetic field. A first effort in this direction was made by Beckers and Schröter (1969). They found that the magnetic field is more inclined and stronger in darker filaments compared to that in bright filaments. Evidence of fluctuations in the magnetic field inclination is strengthened in the early 1990s (Lites et al. 1990, Kalman 1991, Degenhardt and Wiehr 1991, Schmidt et al. 1992, Title et al. 1992, 1993). These authors found fluctuation of $10-40^\circ$ on arcsec and sub-arcsec scale. This fluctuation of the magnetic field inclination in penumbrae is known as fluted magnetic field (for reviews see, Keller et al. 1992, Skumanich et al. 1994, Solanki 2003). Studies of the correlation between inclination and brightness show controversial results. The results of Schmidt et al. (1992), Hofmann et al. (1994), Rimmele (1995b), Wiehr (2000) and Westendorp Plaza et al. (2001b) suggest that darker filaments are more horizontal. Lites et al. (1993), Title et al. (1993) and Stanchfield et al. (1997) did not find a significant correlation in the outer penumbra. Lites et al. (1993) observed that intense field which is more vertical than surrounding and they named these fields as spines.

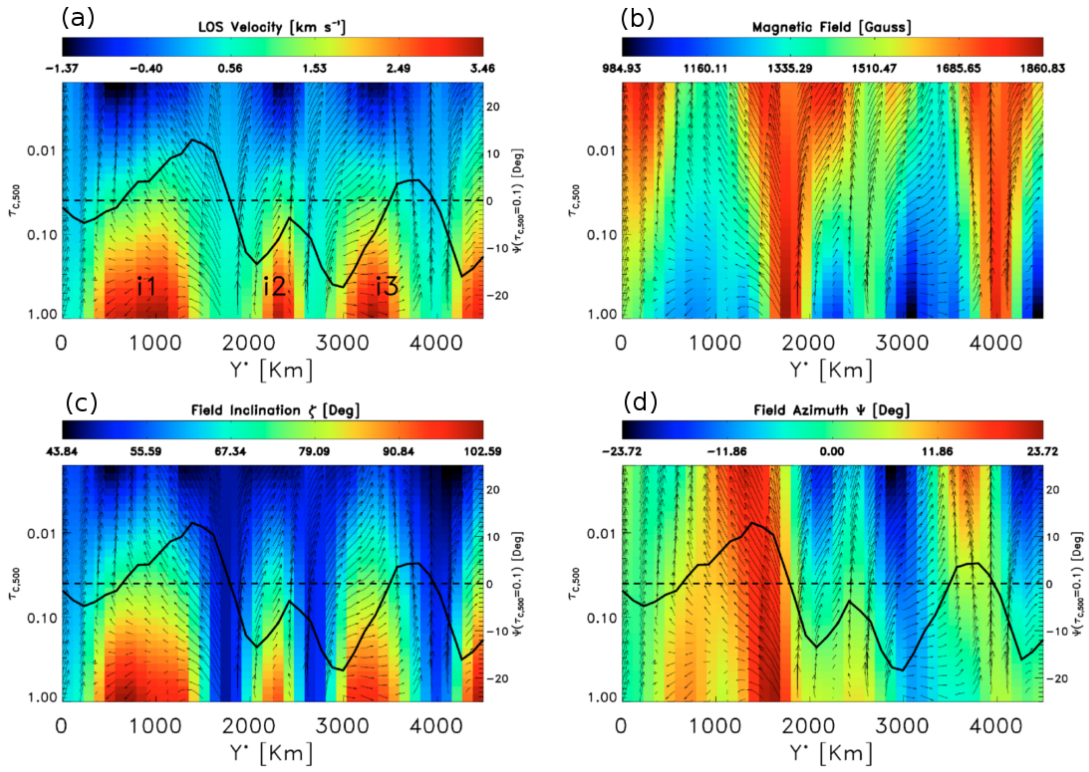


Figure 1.6: Wrapping of the background magnetic field around penumbral filaments: Height stratification of the LOS velocity (a), magnetic field strength (b), inclination angle (c) and azimuth angle (d). The Optical height (τ) stratification is shown along a slit perpendicular to the radial direction in the penumbra. The inclination and the azimuth angles are shown in a local frame of reference. 0° inclination corresponds to vertical direction. Arrows in all the panels show the direction of the magnetic field vectors (adapted from Borrero et al. 2008).

The magnetic field strength also fluctuates in azimuthal direction. It has been established through many authors. Beckers and Schröter (1969), Harvey and Hall (1971), Abdussamatov (1976) and Wiehr (2000) found that darker filaments have a strong magnetic field, whereas Wiehr and Stellmacher (1989) and Westendorp Plaza et al. (2001a) propose stronger fields in brighter filaments. Hofmann et al. (1994) also obtained similar results, but only in the inner penumbra while in the outer penumbra they found the opposite. On the other hand there are also studies which show no fluctuation in the magnetic field strength (Mattig and Mehlretter 1968, Stellmacher and Wiehr 1981, Lites et al. 1990, Schmidt et al. 1992, Title et al. 1993, Rimmele 1995a). Title et al. (1993) see fluctuations in the LOS magnetograms but they interpret them as fluctuations only in inclination. Results from most of these studies are affected by low spatial resolution, incomplete information of the full Stokes vector and the method of retrieving magnetic parameters.

The results of Tiwari et al. (2013a) seem to settle the controversies regarding correlation between the magnetic field and the brightness. They showed that the magnetic field structure in the bright filaments significantly changes from the head to tail. They found that at the bright head of the filaments magnetic field vectors are close to vertical, similar

to that in the dark background, hence ruling out any kind of correlation there. In the middle part of the penumbral filaments the magnetic field becomes horizontal compared to background where the field is relatively vertical and stronger but the filament brightness is comparable with the background. At the tail of filaments the magnetic field submerges to the solar surface.

The vertical extension of penumbral fine structure has also been studied by a few authors. [Borrero et al. \(2008\)](#) and [Tiwari et al. \(2013a\)](#) found that background magnetic field forms spines that expands in the upper photosphere above the bright penumbral filaments. Such a geometry was first proposed by [Solanki and Montavon \(1993\)](#). An example of the vertical extension of penumbral fine structure from the study by [Borrero et al. \(2008\)](#) is shown in Fig. 1.6.

1.2.3.3 Fine structures of the Evershed flow

Like the brightness and the magnetic field, the Evershed flow is also structured on fine scales. To understand the origin and the driving force of the Evershed flow it is important to know its fine structure and its relation to the brightness and the magnetic field structure.

Early studies indicated that the Evershed flow is located in dark filaments ([Beckers and Schröter 1969](#), [Title et al. 1993](#), [Shine et al. 1994](#), [Hofmann et al. 1994](#), [Rimmele 1995b](#), [Stanchfield et al. 1997](#), [Roupe van der Voort 2002](#), [Tritschler et al. 2004](#), [Langhans et al. 2005](#)). In contrast, other authors found that there is no relation between the Evershed flow channels and brightness variations ([Wiehr and Stellmacher 1989](#), [Lites et al. 1990](#), [Schlichenmaier and Schmidt 2000](#), [Hirzberger and Kneer 2001](#)). Recent high resolution observations seem to be converging towards a picture which shows that the Evershed flow is concentrated to bright filaments in the inner penumbra and to dark filaments in the outer penumbra ([Schlichenmaier et al. 2005](#), [Hirzberger et al. 2005](#), [Bellot Rubio et al. 2006](#), [Ichimoto et al. 2007a](#), [Jurcák et al. 2007](#)).

The Evershed flow is found to be concentrated in regions of weaker magnetic field ([Degenhardt and Wiehr 1991](#), [Schmidt et al. 1992](#), [Title et al. 1993](#), [Rimmele 1995b](#), [Westendorp Plaza et al. 2001a](#), [Borrero et al. 2005](#), [Ichimoto et al. 2007a](#)). [Bellot Rubio et al. \(2004\)](#) and [Borrero et al. \(2005\)](#) concluded from their observations that the velocity vector is parallel to the local magnetic field vector.

1.2.3.4 Net circular polarization

The net circular polarization (NCP) is another tool which gives insight to understanding sunspot penumbrae and their vertical structure. The NCP in a spectral line is defined as the integral of the Stokes V profile over the entire line, $NCP = \int V(\lambda) d\lambda$, i.e. it is a measure of the asymmetry of the areas of the blue and red lobes of Stokes V profiles. It is found that on the limb-side of penumbrae the sign of NCP is the same as the sign of the blue lobe of the Stokes V profile in the umbra. The sign of NCP in the disk center-side of the penumbrae is found to be opposite to that on the limb-side. The penumbra of a sunspot at disk center has the same sign of NCP as that of the limb-side penumbra. These properties of the NCP are already known from low spatial resolution observations by [Illing et al. \(1974a,b\)](#), [Henson and Kemp \(1984\)](#) and [Makita and Ohki \(1986\)](#).

The NCP in the infrared Fe I 1.56 μm line shows a different spatial distribution than in

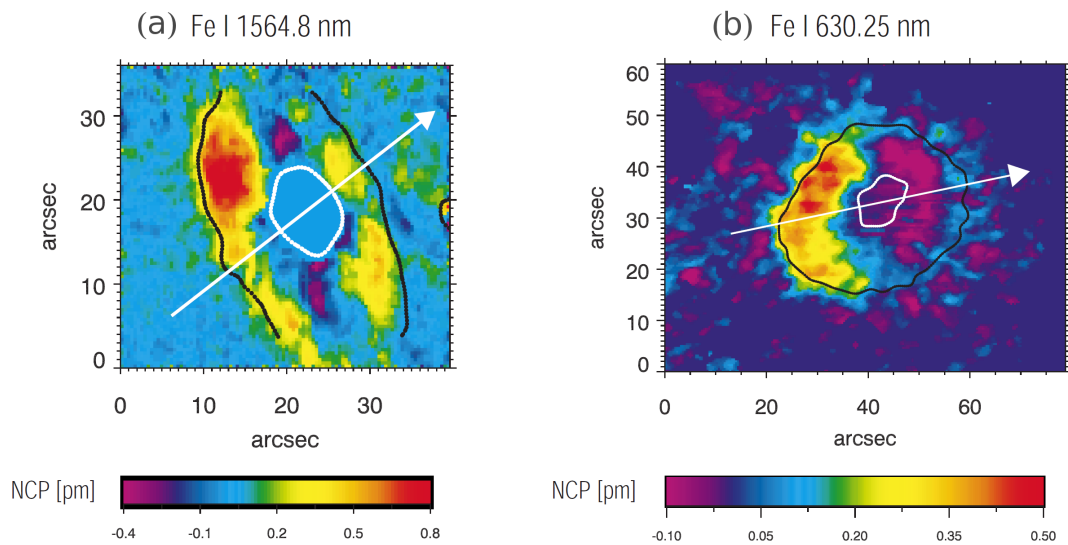


Figure 1.7: Maps of net circular polarization (NCP) of sunspot: (a) NCP map in Fe I $1.56\mu\text{m}$ line and (b) NCP map in Fe I 6301.5Å line. In both panels arrows mark the line of symmetry (adapted from Müller et al. 2002).

spectral lines in the visible range, e.g. Fe I 6301.5Å . The spatial distribution of the NCP in the Fe I $1.56\mu\text{m}$ and Fe I 6301.5Å lines are shown in panels (a) and (b) of Fig. 1.7. Maps of the NCP in Fe I 6301.5Å show a symmetric distribution along the line of symmetry (the line joining the sunspot center and the solar disk center), whereas it is asymmetric in the Fe I $1.56\mu\text{m}$ line.

High resolution observations revealed that the maps of NCP also show a filamentary structure (Tritschler et al. 2007), although Tritschler et al. (2007) did not find any correlation between the filamentary structure of the NCP and the Evershed flow channels. Ichimoto et al. (2008b) studied the NCP from the Hinode SOT/SP observations. They found that the NCP in filamentary structure at the limb-side penumbra has the same sign as the blue-lobe of Stokes V in the umbra. These filamentary structures in maps of NCP coincide with the Evershed flow channels. Observations of Ichimoto et al. (2008b) revealed the same sign of the NCP in the disk-ward Evershed channels as in the limb-ward penumbra, but opposite sign of NCP between the Evershed flow channels.

1.3 Umbra: Theoretical models

The relative darkness and the rich fine structure of sunspots constitute a challenging and enigmatic problem for theoretical models. In addition, the dynamical time-scale (the time of magneto-acoustic wave to propagation across a sunspot) is only about one hour, while the sunspot's lifetime is up to several weeks. Therefore this long-term stability of sunspots is an open question. In contrast to that, the fine structures, i.e., umbral dots, penumbral filaments, penumbral grains, etc., have significantly faster dynamics compared to life time of sunspots, in the range of minutes to a few hours. The strong magnetic field of sunspots suppresses overturning convection which is the main mechanism of heat transport to the

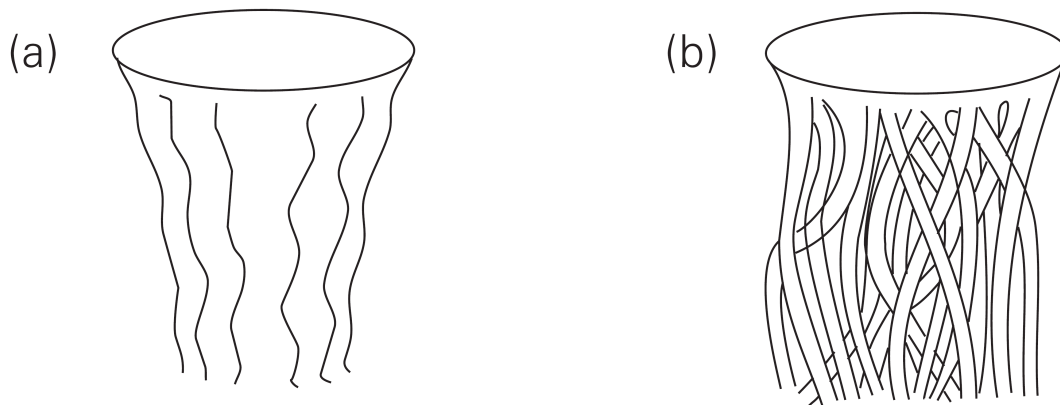


Figure 1.8: Panel (a) depicts a sketch of subsurface structure of monolithic model and panel (b) that of cluster model of sunspot (adapted from [Thomas and Weiss 1992](#)).

solar surface. Therefore sunspots are cooler compared to the surrounding photosphere and appear darker ([Biermann 1941](#)). [Jahn \(1992\)](#) presented an alternative scenario, based on a monolithic flux tube (e.g. [Cowling 1957](#), sketch is shown in Fig. 1.8a) which expands from the deeper layers towards the surface of the Sun to balance the stratified gas pressure of field free surrounding. In this scenario the magnetic field forms a funnel-like shape where the diameter of the monolithic flux tube is smaller (stronger B) in sub-surface layers compared to the surface. In a situation where this flux system is thermally isolated from its surrounding, any form of possible energy transport from the deeper layers to the surface will cause a reduced heat flux at the surface and thus it becomes cooler, because of the increased cross section of the flux tube.

Sunspot umbrae have temperatures around 4000 K and [Deinzer \(1965\)](#) showed that the heat transport through conduction and radiation is not sufficient to maintain this temperature. Thus, convection is not completely inhibited in the sunspot umbrae. [Deinzer \(1965\)](#) and [Jahn \(1989\)](#) used the concept of mixing length theory with a depth dependent mixing length to show the convective heat transport in sunspots. These models were based on a model of [Hoyle \(1949\)](#), where umbra, penumbra and the quiet Sun are assumed to be thermally isolated against each other. The boundary between penumbra and the quiet Sun is known as magnetopause.

[Parker \(1975\)](#) and [Piddington \(1975\)](#) showed that the monolithic structure of the sunspot is unstable to the fluting or interchange instability. Fluting instability arises at curved interface (due to expansion with height of the sunspot's magnetic field in stratified gas pressure) between the sunspot and field free surrounding. This curved interface should be unstable to small displacement. [Parker \(1979a,b,c\)](#) suggested that the fragmentation of a single, large flux tube into many thin flux tubes beneath the surface can act as a process of stabilizing the flux tube through minimizing the energy. Basically, the magnetic curvature force (responsible for the fluting instability) weakens through fragmentation into thinner flux tubes. [Meyer et al. \(1977\)](#) proposed that the buoyancy stabilizes the sunspot's monolithic structure (when the total flux of a sunspot is larger than 10^{20} Mx) to the fluting instability close to the surface because the magnetopause has a large inclination angle with respect to the vertical. A similar picture was presented by [Schüssler \(1984\)](#) and

[Buente et al. \(1993\)](#). A fragmented large flux tube is known also under different names like jelly fish model, cluster model and spaghetti model in the literature ([Parker 1979c](#), [Spruit 1981](#), [Choudhuri 1992](#)). A sketch of the cluster model is shown in Fig. 1.8(b).

The cluster model naturally explains the observation of umbral dots through the presence of convection in field free areas between the thin flux tubes. Umbral dots are, however, also explained by magneto-convective processes in the monolithic model ([Jahn 1992](#), [Schüssler and Vögler 2006](#)). [Rempel and Schlichenmaier \(2011\)](#) pointed out some questions in the cluster model, which still remain to be answered: what process keeps the magnetic and the non-magnetic part of the cluster model together? How does the cluster model explain the monotonic decrease of the magnetic field strength from the sunspot's center to the periphery?

As the direct observation of the sub-photospheric structure is not possible, it is difficult to settle the debate about the exact structure of sunspots in their deeper layers. Local helioseismology is a promising candidate to improve our understanding of the sub-photospheric structure of sunspots. So far, helioseismic inversion techniques are not able to derive this structure with sufficient confidence ([Gizon et al. 2009](#), [Moradi et al. 2010](#)).

1.4 Penumbra: Models and simulations

The heat flux in sunspot penumbrae amounts to approximately 75% of the heat flux in the quiet Sun, while the average magnetic field strength is still high, being ~ 1500 G. Many heat transport mechanisms have been proposed, e.g., hot flows along flux tubes, convective rolls in radially aligned horizontal flux tubes, convection in field free gaps, or interchanging convection of thin flux tubes. Along with the heat transport in penumbrae, there are other observational facts like the Evershed flow, the filamentary structure of the brightness, the magnetic field and the plasma flow, and the relation of these physical parameters to each other, which all pose challenges for the explanation using theoretical models. The spatial distribution of the NCP is one of those challenges for theoretical models. This section summarizes different theoretical models and MHD simulations.

1.4.1 The uncombed model

[Auer and Heasley \(1978\)](#), [Sanchez Almeida and Lites \(1992\)](#) and [Landolfi and Landi Degl'Innocenti \(1996\)](#) indicated that the gradient of v_{los} with respect to the optical depth τ alone cannot produce the amount of NCP observed and they proposed that only a gradient of \mathbf{B} along with the gradient of v_{los} can explain the observed NCP.

[Sanchez Almeida and Lites \(1992\)](#) pointed out that the NCP requires a steep vertical gradient of the inclination of the magnetic field vector (around $45^\circ \tau^{-1}$) and also of v_{los} (around 1.5 km s^{-1}). [Solanki and Schmidt \(1993\)](#) showed that a steep gradient of inclination leads to a mechanical instability in the sunspot.

[Solanki and Montavon \(1993\)](#) proposed an uncombed model of the sunspot magnetic field which successfully explains the observed NCP and also naturally exhibits the presence of azimuthal variations of the magnetic field strength, the inclination and the Evershed flows. In the uncombed model horizontal flux tubes, carrying the Evershed flows, are embedded in a more vertical background field. A sketch of the uncombed model

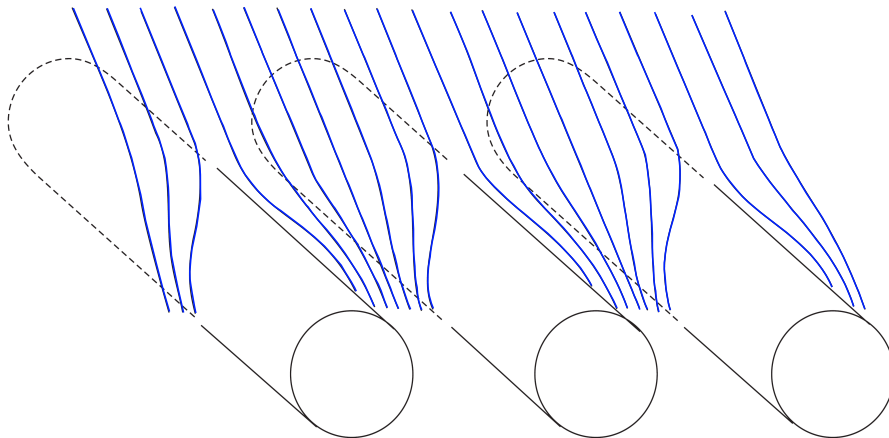


Figure 1.9: Uncombed penumbra: A sketch of the horizontal magnetic flux tube embedded in a relatively less inclined background magnetic field (adapted from Solanki 2003).

is presented in Fig. 1.9. According to this model the LOS of an observer penetrates a three-fold layered atmosphere where the background magnetic field is wrapped around the horizontal flux tube (see Fig. 1.9). Two sudden changes of the inclination of the magnetic field, first from the more vertical to the horizontal and second from the horizontal to the more vertical, are responsible for the observed NCP. The uncombed model also successfully explains the center-to-limb variation of the NCP, i.e. when the sunspot is observed at different heliocentric angles (Solanki and Montavon 1993, Martínez Pillet 2000, Borrero 2007). A three-dimensional model developed by Schlichenmaier and Schmidt (2000), Müller et al. (2002) and Müller et al. (2006) showed that a variation in the azimuth direction of the field vector, $\Delta\phi$, has a significant influence on the NCP. They explained the asymmetry of the NCP with respect to line-of-symmetry of the sunspot when observed in the Fe I $1.56\mu\text{m}$ lines by a variation of the azimuthal angle $\Delta\phi$. Borrero and Solanki (2010) included the effect of the overturning convection (i.e. a lateral flow, see Section 1.4.5) and concluded that this flow does not result in a significant effect on the NCP.

The main features of the uncombed model, namely more vertical field spreading to cover the interlaced horizontal field bundles, has been supported by many observational studies (Martínez Pillet 2000, 2001, Schlichenmaier and Collados 2002, Müller et al. 2002, Mathew et al. 2003, Bellot Rubio et al. 2003, 2004, Borrero et al. 2004, 2005, 2006, Jurčák and Sobotka 2007, Borrero et al. 2008, Beck 2011). One feature of the model, however, namely that the horizontal field is in the form of flux tubes is being debated with increasing evidences suggesting that it is in need of revision.

1.4.2 Siphon flows

Meyer and Schmidt (1968a,b) explained the Evershed flow by the siphon flow mechanism. Sophisticated theoretical studies concerning the siphon flow were done by many authors (Thomas 1988, Degenhardt 1991, Thomas and Montesinos 1991). The siphon flow model assumes an Ω -shaped magnetic loop which has one foot point in the penumbra and an

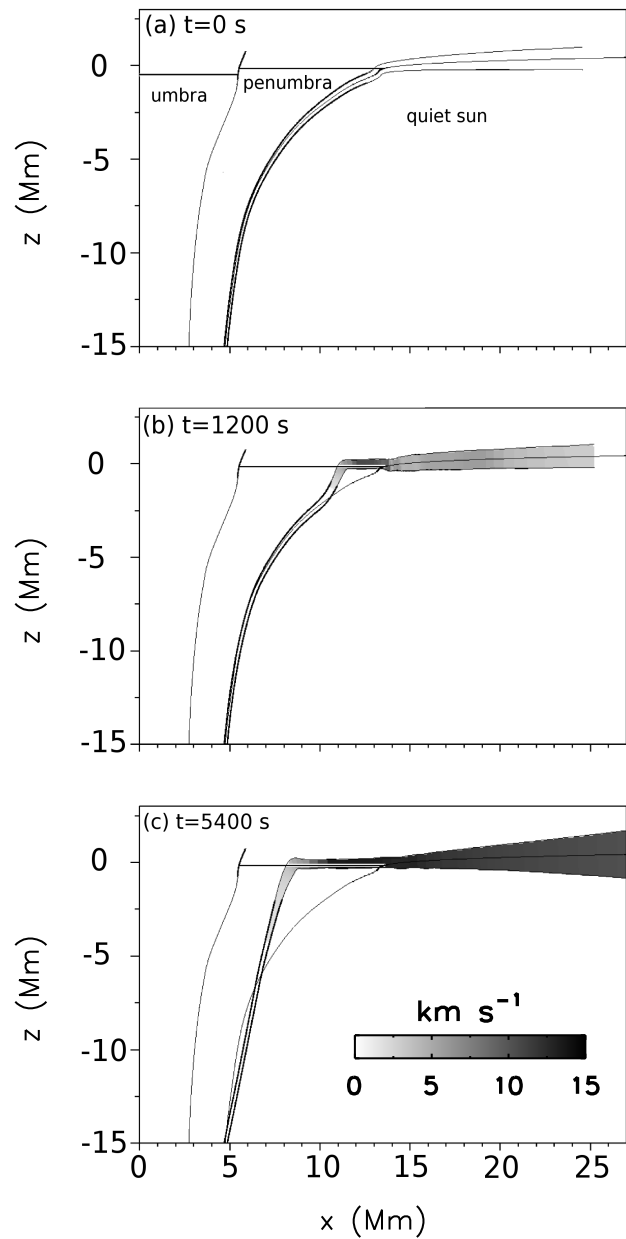


Figure 1.10: Temporal evolution of a moving magnetic flux tube in a MHD simulation by [Schlichenmaier et al. \(1998a,b\)](#): Panel (a) shows a thin flux tube lying at time $t=0$ s. Panel (b) shows the rising buoyant flux tube at $t=1200$ s, which is radiatively heated from the quiet Sun through the magnetopause. Panel (c) represents the horizontal flux tube at $t=5400$ s. The abscissa represents the radial direction in sunspot. The ordinate denotes the geometrical height. $z=0$ corresponds to the solar surface (adapted from [Schlichenmaier et al. 1998a](#)).

other one outside of the sunspot. If the outer foot point has a stronger field strength compared to the inner foot point then due to the requirement of pressure equilibrium to the ambient gas a higher gas pressure results in the inner foot point. This will lead to an outward flow in the penumbra. Magnetic elements with higher magnetic field strength in the quiet Sun compared to penumbral field strengths are possible through the process of the convective collapse (Parker 1978, Spruit 1979).

Thomas and Montesinos (1990) showed that such a loop in equilibrium should have a much smaller length compared to the width of the penumbra, causing the Evershed flow to take place in smaller loops with their inner foot point located at different radial distances in the penumbra (del Toro Iniesta et al. 2001). It is well established that magnetic field strength decreases with radial distance from the sunspot center. In this situation the siphon flow should be directed inwards. Schlichenmaier (2002, 2003) proposed a serpentine flux tube which has its one foot point outside sunspot. This serpentine flux tube repeatedly dives below the penumbral surface and appears back above it again. This model also suggests downflow channels within the penumbra which has been supported by observations (Westendorp Plaza et al. 1997, Schlichenmaier and Schmidt 2000, Bellot Rubio et al. 2003, Franz and Schlichenmaier 2009).

1.4.3 Moving magnetic flux tubes

Jahn and Schmidt (1994) proposed that the heat transport in penumbrae is driven by the interchanging convection of flux tubes. Their sunspot model consists of three differently stratified atmospheres for umbra, penumbra and the quiet Sun. The umbra and penumbra as well as the penumbra and the quiet Sun are separated by current sheets. The latter is known as the magnetopause. As described earlier in Section 1.3, the umbra is thermally isolated from the penumbra in this model, whereas the heat transport between the quiet Sun and the penumbra, through the inclined magnetopause is allowed. Jahn and Schmidt (1994) suggested that flux tubes lying at the magnetopause are heated and rise to the penumbra, before returning back to sub-surface after radiating their energy. Interchanging convection transport energy that leaked through the magnetopause to the solar surface within the penumbra.

Schlichenmaier et al. (1998a,b) carried out MHD simulations of a single, 1D flux tube (thin flux tube) in the stratified penumbral background atmosphere borrowed from the model of Jahn and Schmidt (1994). The flux tube is radiatively heated at the magnetopause, expanding and rising due to buoyancy. Since the radiative heating is more efficient at the surface and just below the surface, the flux tube rises first at the outer edge of the penumbra (see Fig. 1.10(b)). In the sub-photospheric layers the super-adiabatically stratified atmosphere leads to a convectively unstable atmosphere. Therefore, the rise of the flux tube is accelerated and at the end flux tube reaches to the convectively stable penumbral surface. At the surface the flux tube gains a new equilibrium where the buoyancy force (acting downwards) balances the magnetic pressure gradient (acting upward) of the surrounding. To maintain the pressure equilibrium, a gradient in the gas pressure develops within the flux tube with a higher pressure at the foot point (innermost part of the flux tube at the surface) compared to that in the outer part (penumbral outer boundary) of the flux tube. This gradient of the gas pressure drives a horizontal outflow within the flux tube. An upflow at the foot point of the flux tube is maintained by the super-adiabatically

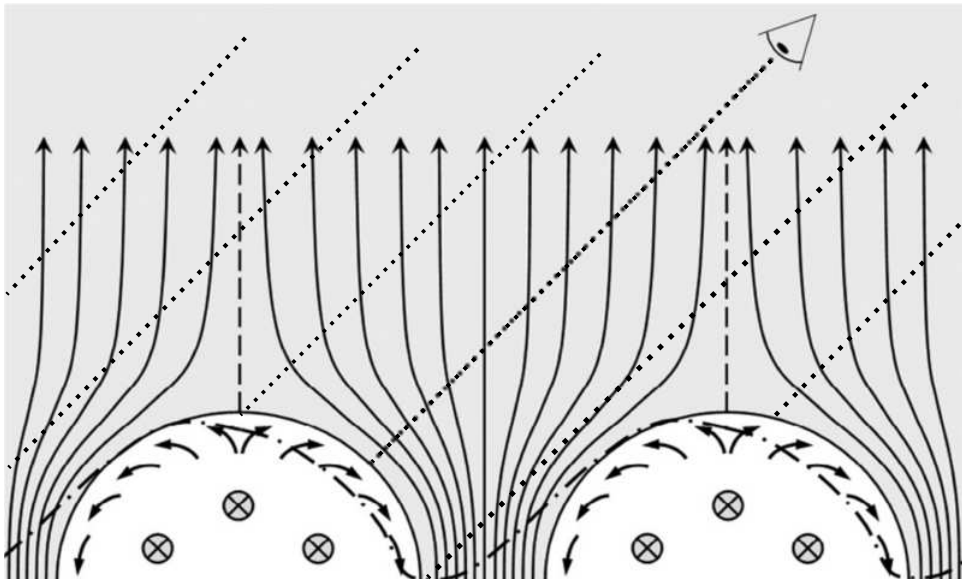


Figure 1.11: Sketch of the convective roll model. The magnetic field geometry and flow structure is shown in the vertical cut perpendicular to penumbral filaments. Penumbral filaments are shown by *white* semi circular areas, where circular *crosses* show field direction which is pointing through the *paper*. Arrows in penumbral filament show the direction of the convective flow. Vertical arrows in *gray* areas represent the direction of the background magnetic field in the penumbra (adapted from [Zakharov et al. 2008](#)).

stratified background atmosphere and the pressure gradient in the horizontal part of the tube is maintained by the radiative cooling.

The inward migration of the foot point of the flux tube is an intrinsic property of this simulation, which is controlled by three forces: the curvature force due to the bending of the tube at the foot point, the centrifugal force due to the flow in the curved tube and the buoyancy force. All these forces act perpendicular to the tube. When the sub-photospheric part of the tube becomes vertical, the buoyancy force becomes negligible and when the flow speed in the tube reaches the Alfvén velocity then the centrifugal force equals to the curvature force and the inward migration of the foot point stops.

The moving magnetic flux tube model is consistent with many observational facts of penumbrae. Bright heads of the filaments followed by dark tails are explained by the hot upflow at the foot point of the tube which radiatively cools down. The outflow in the horizontal part of the flux tube due to the gradient in the gas pressure can explain the Evershed flow. As mentioned above the inward migration of the flux tube is in agreement with inward moving penumbral grains. This model naturally encompasses the uncombed model, and hence, also explains the observed NCP.

Instead of the interchange convection of flux tubes, a continuation of the hot upflow in the flux tube is proposed to explain the heat transport in the penumbra. [Schlichenmaier and Solanki \(2003\)](#) showed that the hot upflow cannot provide sufficient heat flux for the entire length of the penumbra. They proposed that these flow channels should bend back to the surface within the body of the penumbra, which can provide enough space for more upflow channels.

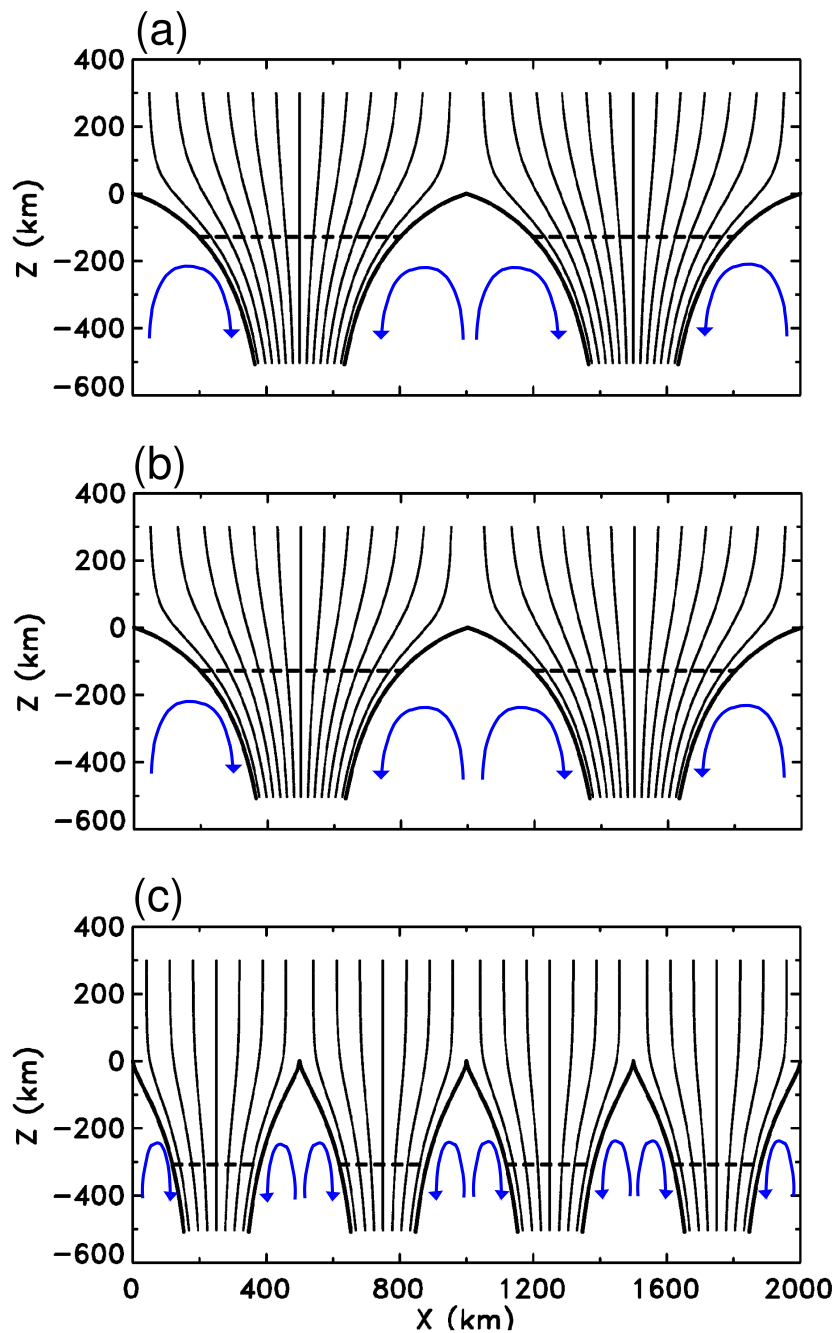


Figure 1.12: Geometry of the gappy penumbra model. x -axes represent cuts perpendicular to the penumbral filaments and z -axes represent the geometrical height. Panels (a), (b) and (c) depict outer, middle and inner penumbra, respectively. nearly vertical lines in all the panels show the direction of the penumbral magnetic field which is separated by the field-free gaps in deeper geometrical layers. *Blue* arrows represents the plasma flow due to the overturning convection in the field free gaps (adapted from [Scharmer and Spruit 2006](#)).

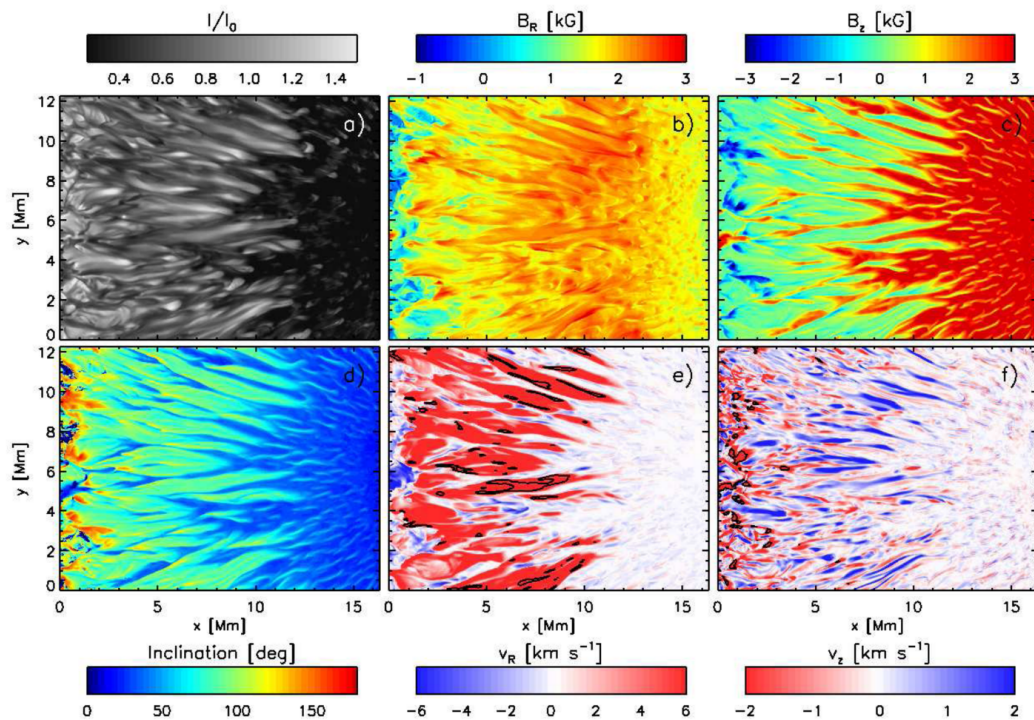


Figure 1.13: Penumbral fine structure from the 3D MHD simulation by [Rempel et al. \(2009b\)](#): (a) The intensity, (b) the radial magnetic field strength, (c) the vertical magnetic field strength, (d) the inclination of the magnetic vector, (e) the radial velocity and (f) the vertical velocity. All parameters are shown at $\tau=1$. *Red* color in panel (e) corresponds to radial outflow and *black* contours encircle the areas where the outflow speed is higher than 10 km s^{-1} . In panel (f) *red* and *blue* color indicates upflow and downflow, respectively and the areas where the downflow speed exceeds to 5 km s^{-1} are shown by *black* contours (adopted from [Rempel 2011](#)).

1.4.4 Convective roll

[Danielson \(1961b\)](#) proposed a convective roll mechanism to explain the brightness of penumbrae. In his model a bright penumbral filament is formed by two convective rolls with opposite direction of rotation. These rolls have a direction perpendicular to the penumbral filaments. [Danielson \(1961b\)](#) only considered the horizontal magnetic field in penumbra when he proposed the convective roll model.

To explain observations [Zakharov et al. \(2008\)](#) suggested a magnetic field configuration (Fig. 1.11) which is basically the uncombed model with the convective rolls in the radially aligned weak horizontal magnetic flux tubes. At the center of the bright filaments two convective rolls bring up hot plasma (upflow) which then radiatively cools down and flows back to the surface (downflow) at the edges of the filaments.

1.4.5 Gappy penumbra

[Spruit and Scharmer \(2006\)](#) and [Scharmer and Spruit \(2006\)](#) proposed a model in which the bright penumbral filaments are radially elongated field free gaps. In these gaps over-

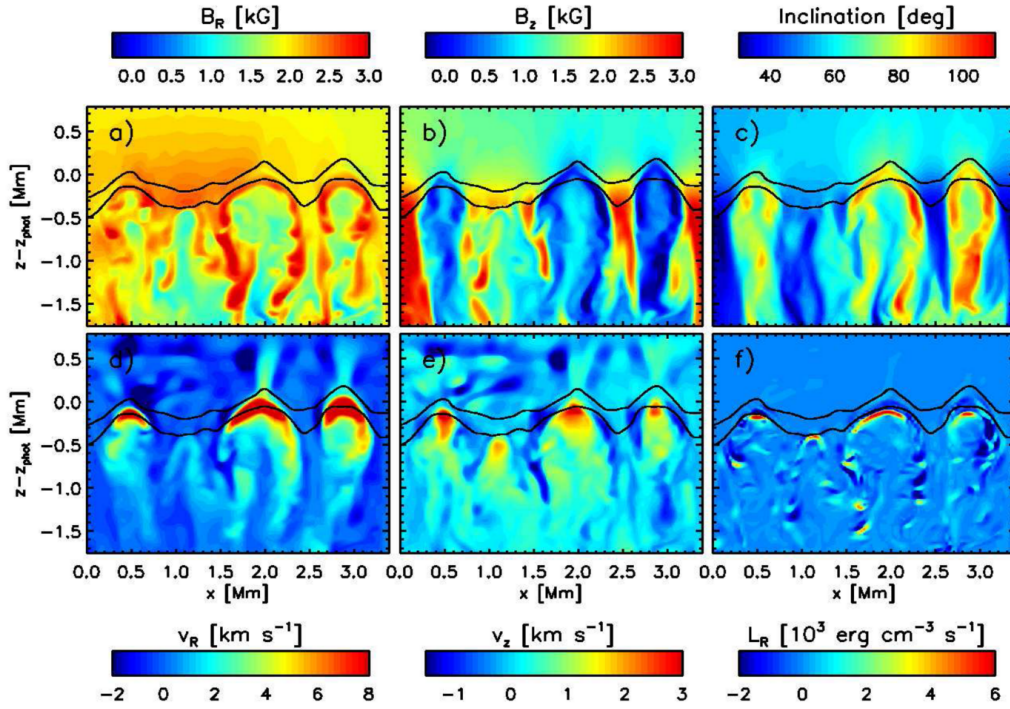


Figure 1.14: Height stratification of penumbral fine structure from the 3D MHD simulations by [Rempel et al. \(2009b\)](#): x -axes correspond to the direction perpendicular to the penumbral filaments and z -axes correspond to the geometrical height. *Lower* and *upper* curves in all panels show $\tau=1$ and $\tau=0.01$ levels respectively. Panels represent various physical parameters as follows: (a) the radial magnetic field strength, (b) the vertical magnetic field strength, (c) the inclination of the magnetic field vector (0° corresponds to vertical direction with same polarity as the umbral magnetic field), (d) the radial velocity, (e) the vertical velocity and (f) energy conversion by the horizontal Lorentz force along filaments. Positive values in the panel (d) show radial outflows and positive values in the panel (e) indicate upflows (adopted from [Rempel 2011](#)).

turning convection takes place and brings a sufficient amount of the heat to the penumbral surface. These elongated convective cells are separated by a potential magnetic field. A sketch of the gappy penumbra model is shown in Fig. 1.12. The gappy penumbra model predicts upflows along the axis of the bright penumbral filaments and lanes of dark downflows at the edges of the penumbral filaments. The field free gaps in the inner penumbra are narrower compared to the outer penumbra due to the magnetostatic equilibrium and the flux conservation. The stronger and more vertical magnetic component of the inner penumbra squeezes the field free gaps, so that the magnetic field forms a cusp-like shape where the magnetic field lines are lying horizontal above the field free gaps. In the outer penumbra the field free gaps have flat tops because the magnetic field strength is weaker compared to the inner penumbra. In the gappy penumbra model the magnetic component in the inner penumbra produces a Wilson depression on the order of 200-300 km, so the field free gaps appear as elevated structures. This explains the observed dark cored bright filaments ([Spruit and Scharmer 2006](#), [Scharmer and Spruit 2006](#)). [Scharmer et al. \(2008b\)](#)

interpreted the Evershed flow as the horizontal component (i.e. in radial direction) of the overturning convection in the field free gaps, this interpretation is based on 3D MHD simulation of a penumbra by [Heinemann et al. \(2007\)](#). Although, these simulation do not show 'real' field free gaps.

First direct observational evidence of cool downflows next to hot upflows and hence of convective motions in penumbral filaments is presented in Chapter 3 of this thesis and by [Joshi et al. \(2011\)](#). Similar results were also found by [Scharmer et al. \(2011\)](#), [Scharmer and Henriques \(2012\)](#), [Scharmer et al. \(2012\)](#) and [Tiwari et al. \(2013a\)](#). These observations are consistent with both the convective roll and the gappy penumbra model, because both models predict similar velocity structure at the surface. Note that downflows in the penumbra have been seen earlier by [Franz and Schlichenmaier \(2009\)](#), but these downflows are concentrated at the outer boundary of the penumbra.

1.4.6 3D MHD simulations of sunspot

[Heinemann et al. \(2007\)](#) performed the first realistic radiative MHD simulations of a sunspot¹ in a slab geometry, i.e in a rectangular part of a sunspot. In the simulation of [Heinemann et al. \(2007\)](#) the penumbral filaments and also the overall extent of the penumbra are very short compared to observations. Penumbral filaments in this simulation show some agreement with observational facts, like dark cores, inclined magnetic field in the filaments compared to dark background and inward (towards umbra) propagation of penumbral grains.

[Rempel et al. \(2009b\)](#) simulated a bigger sunspot (diameter of 20 Mm) in slab geometry. Compared to [Heinemann et al. \(2007\)](#) (diameter of 4 Mm) the filamentary structure is more prominent.

[Rempel et al. \(2009a\)](#) simulated a full (round) sunspot (see Fig. 4.20 in Chapter 4) and a more detailed analysis is presented in [Rempel \(2011\)](#). Similar to [Rempel et al. \(2009b\)](#), this simulation produced a filamentary penumbra as well as umbral dots, both as magneto-convective phenomenon.

The horizontal structure of physical properties of a small part of the penumbra from the simulation of [Rempel et al. \(2009a\)](#) is shown in Fig. 1.13. A vertical cross section of a penumbral filament formed in this simulation is shown in Fig. 1.14. In this simulation the bright filaments have radially aligned horizontal magnetic fields which show an enhancement around $\tau=1$. At the central axes of the bright filament an upflow occurs which is surrounded by lanes of downflows showing the overturning convection in the lateral direction. The simulations also show a strong radial outflow reaching up to 14 km s^{-1} in the bright filaments. In these simulations many penumbral properties are consistent with the observations: the penumbral brightness, the Evershed flow, the azimuthal fluctuation in the magnetic field strength and in the inclination. The Evershed flow in this simulation is magnetized (in agreements with observations, e.g., [Solanki et al. 1994](#), [Borrero et al. 2005](#), [Ichimoto et al. 2008b](#), [Borrero and Solanki 2010](#)) which is more in line with flux-tube models, while, the brightness of penumbra filaments, caused by the overturning convection, shows similarities with the gappy penumbra model. The simulations suggest a picture in which penumbral filaments are strongly elongated convective cells, in agree-

¹[Schüssler and Vögler \(2006\)](#) presented the first realistic radiative MHD simulations of a umbra.

ment with the flow geometry proposed by [Tiwari et al. \(2013a\)](#).

2 Spectro-polarimetry

In this chapter we introduce important methods and techniques used to extract parameters of physical significance of the solar atmosphere from the observational data which are presented in the following chapters. This chapter describes physical processes like the Zeeman effect and the Paschen-Back effect. These processes play an important role in polarizing the electromagnetic radiation emitted from the solar atmosphere in the presence of a magnetic field. The second part of the chapter deals with the Radiative Transfer Equation (RTE) and its formal solution. We follow the approach of [del Toro Iniesta \(2003\)](#) and [Landi Degl'Innocenti and Landolfi \(2004\)](#). To retrieve atmospheric parameters, state-of-the-art inversion techniques are used in the following chapters, which are briefly explained in this chapter. Telescopes and instruments used to obtain spectro-polarimetric observations which are analyzed in the thesis are mentioned in the last part of the present chapter.

2.1 Stokes parameters

The Stokes parameters are a quantitative representation of a polarized quasi-monochromatic electromagnetic plane wave. The electric field components, perpendicular to the direction of propagation, of such a wave can be written as follows:

$$E_x(t) = \left[a_x(t) e^{i\varphi_x(t)} \right] e^{-2\pi\nu t - 2\pi z/\lambda}, \quad (2.1)$$

$$E_y(t) = \left[a_y(t) e^{i\varphi_y(t)} \right] e^{-2\pi\nu t - 2\pi z/\lambda}, \quad (2.2)$$

where E_x and E_y represent electric field components orthogonal to each other. φ_x and φ_y denote phases of the respective components. a_x and a_y denote the amplitudes. z is the direction of the wave propagation and ν is the mean frequency of the wave.

The Stokes parameters are defined as follows:

$$I = \langle a_x^2 \rangle + \langle a_y^2 \rangle, \quad (2.3)$$

$$Q = \langle a_x^2 \rangle - \langle a_y^2 \rangle, \quad (2.4)$$

$$U = 2\langle a_x a_y \cos \delta(t) \rangle, \quad (2.5)$$

$$V = 2\langle a_x a_y \sin \delta(t) \rangle, \quad (2.6)$$

where δ is the phase difference between the two orthogonal electric field components, i.e. $\varphi_x - \varphi_y$ and $\langle \rangle$ denotes a time average. Stokes I corresponds to the total intensity. Stokes

Q and U quantify the linearly polarized fraction of an electromagnetic wave and Stokes V stands for circular polarization.

The Stokes parameters exhibit the following relation.

$$I^2 \geq Q^2 + U^2 + V^2. \quad (2.7)$$

When the light is fully polarized then equality holds and when it is partially polarized then the square of the Stokes I is always greater than the sum of squares of the remaining Stokes parameters.

2.2 Zeeman effect

The Zeeman effect is the most widely used diagnostic tool to measure magnetic fields on the solar surface. This section describes the Zeeman effect.

The Hamiltonian of an electron, \mathcal{H}_0 in an atom consists of two parts, one is the electrostatic interaction, \mathcal{H}_C , which includes the Coulomb force of the nucleus and the repulsive force of the electron cloud. Another interaction which has to be considered is the coupling of the spin angular momentum, S , of the electron with the orbital angular momentum, L , to constitute the total angular momentum, J . The Hamiltonian of the spin-orbit coupling is denoted here by \mathcal{H}_{LS} . So, the Hamiltonian of an electron can be written as follows:

$$\mathcal{H}_0 = \mathcal{H}_C + \mathcal{H}_{LS}, \quad (2.8)$$

In the presence of an external magnetic field another term adds to the Hamiltonian of the electron, which represents the interaction between the external magnetic field and the magnetic moment of the electron. Now the Hamiltonian can be written as,

$$\mathcal{H} = \mathcal{H}_C + \mathcal{H}_{LS} + \mathcal{H}_B, \quad (2.9)$$

where, \mathcal{H}_B denotes the interaction between the magnetic moment of the electron and the external magnetic field which, formulates as below:

$$\mathcal{H}_B = \mu B, \quad (2.10)$$

$$\mu = \mu_0(L + S), \quad (2.11)$$

$$\mu_0 = \frac{eh}{4\pi m_e c}. \quad (2.12)$$

Here, e and m_e denote the electron charge and the mass of the electron. h denotes the Planck constant and c the speed of electromagnetic waves. μ_0 is the Bohr-magneton. New energy levels can be derived by perturbation analysis. There are three different scenarios: when $\mathcal{H}_{LS} \gg \mathcal{H}_B$, i.e. the external magnetic field is weak and energy associated with the LS coupling is dominates. This regime is known as the Zeeman regime. When the external magnetic field is strong and hence, $\mathcal{H}_{LS} \ll \mathcal{H}_B$, electron encounters the Paschen-Back regime. There is also an intermediate regime where $\mathcal{H}_{LS} \approx \mathcal{H}_B$.

As mentioned above, in the presence of a weak magnetic field the effect of \mathcal{H}_B on the unperturbed Hamiltonian, \mathcal{H}_0 , can be analyzed by applying perturbation theory. If

$\mathcal{H}_{LS} \gg \mathcal{H}_B$, the correction to the degenerated energy, E_j (which basically are the eigenvalues of \mathcal{H}_0), of an energy level with the total angular momentum, J , can be derived by diagonalizing \mathcal{H}_B on the basis of the degenerate eigenvector of \mathcal{H}_0 . The eigenvectors of \mathcal{H}_0 can be written in the form $|JM\rangle$. The diagonal terms of \mathcal{H}_B turn out to be,

$$\langle JM | \mathcal{H}_B | JM \rangle = Mg \frac{ehB}{4\pi m_e c}, \quad (2.13)$$

where M is a projection of the total angular momentum, J , to the direction of the external magnetic field, B , and g is the Landé factor in the Russel-Saunders or LS coupling which can be written as:

$$g = \begin{cases} \frac{3}{2} + \frac{S(S+1)L(L+1)}{2J(J+1)} & \text{if } J \neq 0 \\ 0 & \text{otherwise.} \end{cases} \quad (2.14)$$

The external magnetic field removes the degeneracy of any atomic level corresponding to a given value of the total angular momentum, J , and splits the energy states into $2J+1$ equally spaced energy levels with possible values of $M = -J, \dots, 0, \dots, +J$. The splitting of the energy levels is proportional to B and g .

The formation of spectral lines are consequences of atomic transitions between two levels, say, between lower level, l , and upper level, u , with energies E_l and E_u , respectively. A transition from the lower to the upper level leads to an absorption line and the emission lines are formed due to transition from the upper level to the lower level. Conservation of angular momentum allows transition only when $\Delta J = J_l - J_u = 0, \pm 1$. As described above, in presence of an external magnetic field the energy of any atomic level also depends on M and the atomic levels are split into sub-levels. Atomic transition is also possible between two energy levels with broken degeneracy. The selection rule for electric-dipole transitions allows transitions only when $\Delta M = M_l - M_u = 0, \pm 1$. Transitions with $\Delta M = \pm 1$ are called σ -components and those with $\Delta M = 0$ are called π -components. The wavelength of the π -components is similar to that which is originated from the transition between the degenerate energy levels, while the σ -components are shifted toward the red (σ_r) and the blue side (σ_b) of spectrum with respect to the π -component. The shift of the σ -components with respect to wavelength of the π -component, λ_0 , can be estimated as follows:

$$\Delta\lambda = \frac{e\lambda_0^2 B}{4\pi m_e c} (M_l g_l - M_u g_u). \quad (2.15)$$

When a transition occurs between $J_l=0 \rightarrow J_u=1$ or vice versa or when both energy levels have the same Landé factor g , then the simplest case occurs and the spectral line splits only into three components (σ_b, π, σ_r). This simplest case is known as normal Zeeman effect. Transitions other than described above lead to the anomalous Zeeman effect and have multiple π - and σ -components (see Fig. 2.1). In the case of anomalous Zeeman splitting, an effective Landé factor, g_{eff} , is defined in analogy of g for a Zeeman triplet. g_{eff} has the form:

$$g_{\text{eff}} = \frac{1}{2}(g_l + g_u) + \frac{1}{4}(g_l - g_u)[J_l(J_l + 1) - J_u(J_u + 1)]. \quad (2.16)$$

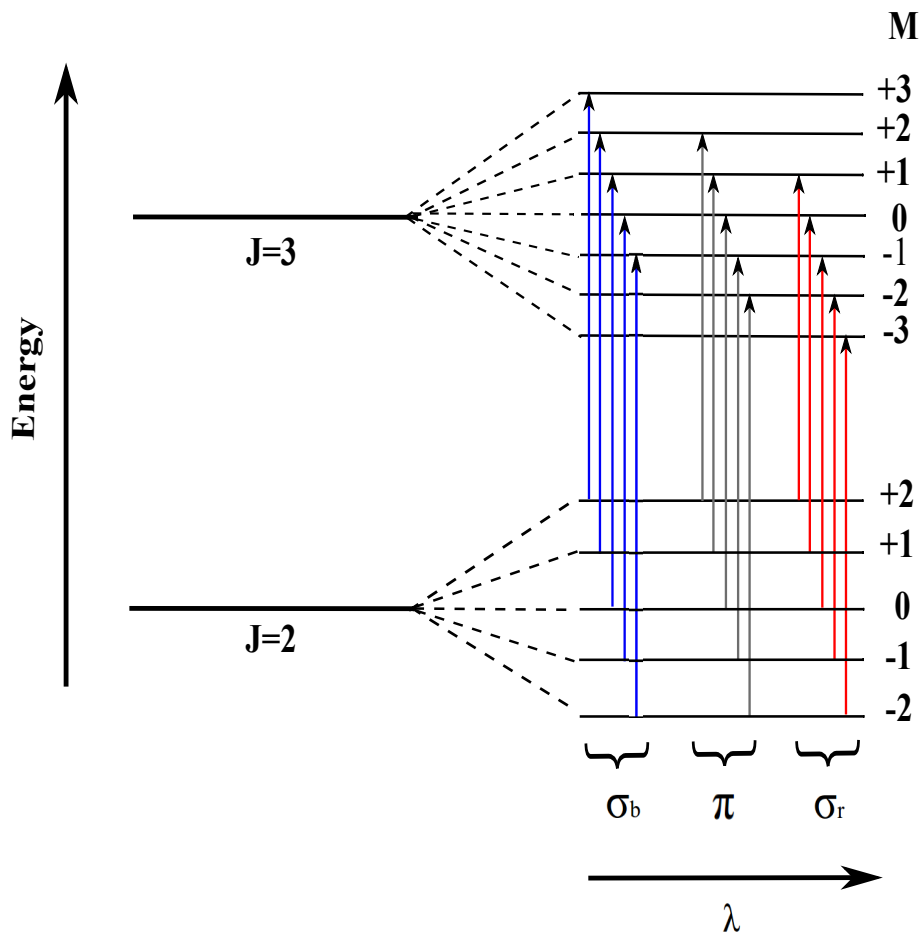


Figure 2.1: Possible transitions between the Zeeman split levels of two energy levels with $J_l=2$ and $J_u=3$. J denotes the total angular momentum. The lower and upper energy levels are denoted by subscript l and u , respectively.

2.2.1 Polarization and strength of the Zeeman components

The polarization of the Zeeman components depending on the angle between line-of-sight and the magnetic field vector is summarized below.

- *Transverse Zeeman effect:* When the angle between the observer's line-of-sight and the magnetic field vector, γ , is equal to 90° then the π -components ($\Delta M = 0$) are linearly polarized in the direction of the magnetic field vector and the σ -components ($\Delta M = \pm 1$) are linearly polarized perpendicular to the direction of the magnetic field vector.
- *Longitudinal Zeeman effect:* When the observer's line-of-sight is parallel to the magnetic field vector ($\gamma=0^\circ$ or $\gamma=180^\circ$) then both σ -components are circularly polarized and the π -components are not visible. When $\gamma=0^\circ$ for an emission line then the σ -components, corresponding to $\Delta M = -1$, are left circularly polarized and the σ -components, corresponding to $\Delta M = +1$, are right circularly polarized. For an

Table 2.1: Unnormalized strength, $S_{ij}(M, 90^\circ)$, of the Zeeman components.

	$M \rightarrow M - 1$ ($\Delta M = -1$)	$M \rightarrow M$ ($\Delta M = 0$)	$M \rightarrow M + 1$ ($\Delta M = +1$)
$J \rightarrow J + 1$	$(J - M + 1)(J - M + 2)$	$4 + (J + 1)^2 - M^2$	$(J + M + 1)(J + M + 2)$
$J \rightarrow J$	$(J + M)(J - M + 1)$	$4M^2$	$(J - M)(J + M + 1)$
$J \rightarrow J - 1$	$(J + M)(J + M - 1)$	$4(J^2 - M^2)$	$(J - M)(J - M - 1)$

emission line when $\gamma=180^\circ$, or $\gamma=0^\circ$ for an absorption line¹ the polarization of the σ -components is reversed.

Let the $S_{ij}(M, \gamma)$ be unnormalized strength of the Zeeman components, when viewed at an angle, γ , with respect to the magnetic field vector and under the assumption that all Zeeman sub-levels are equally populated. Here $j = p, b, r$, corresponding to the Zeeman components, π , σ_b and σ_r . And $i_j = 1, \dots, N_j$, where N_j is the total number of corresponding σ - and π -components. Unnormalized strength, $S_{ij}(M, 90^\circ)$ is shown in Table 2.1.

Normalized strengths, $s_{ij}(M, \gamma)$, of the Zeeman components, can be written as follow:

$$s_{ij} = S_{ij} \left(\sum_{i_j=1}^{N_j} S_{i_j} \right)^{-1}. \quad (2.17)$$

2.3 Paschen-Back effect

The Paschen-Back effect takes place when the external magnetic field is strong enough that the splitting of the energy levels is comparable to the separation between two degenerate energy state, i.e., the strong external magnetic field dominates over the LS coupling and both L and S are independently precessing around the external field direction. In case of the Zeeman effect the correction to the energy levels can be analyzed by perturbation theory, but in case of the Paschen-Back effect perturbation theory cannot be applied. The correction to the energy levels can be estimated by diagonalizing the total Hamiltonian, H , on the basis of the eigenvector of \mathcal{H}_0 . The elements of such a matrix have the form:

$$\langle JM | \mathcal{H}_B | J'M' \rangle = \mu_0 \langle JM | (L + 2S)B | J'M' \rangle. \quad (2.18)$$

The eigenvector and eigenvalues of H can only be found through numerical methods. Detailed calculations are shown by [Landi Degl'Innocenti and Landolfi \(2004\)](#).

2.4 Radiative Transfer Equation

The Radiative Transfer Equation (RTE) in its general (vector) form describes how a beam of light is transferred through a medium in the presence of a magnetic field which in-

¹The Zeeman effect for an absorption line is known as the reverse Zeeman effect.

fluences the state of polarization of the radiation. This general RTE was first derived by Unno (1956) using classical electrodynamics and later Rachkovsky (1962) included magneto-optical effects. If it is assumed that the radiation is propagating in z - direction, normal to the solar surface, then the RTE can be expressed as,

$$\frac{d\mathbf{I}(z)}{dz} = \hat{\mathbf{k}} [\mathbf{I}(z) - \mathbf{S}(z)], \quad (2.19)$$

where, \mathbf{I} is the Stokes vector, $\mathbf{I}=[I,Q,U,V]$, emerging from the solar atmosphere. \mathbf{S} is the source function which, in Local Thermodynamical Equilibrium (LTE), has the form of a Planck function, $\mathcal{B}(T(z))$, at the local temperature, T , at height z . If the radiation field is unpolarized then the source function has the form $\mathbf{S}=[\mathcal{B}(T(z)), 0, 0, 0]$. Here $\hat{\mathbf{k}}$ is the propagation matrix, also known as the absorption matrix. The propagation matrix can be decomposed into two parts, where one part takes care of the continuum and the other one for the spectral line. Now, $\hat{\mathbf{k}}$ can be written as

$$\hat{\mathbf{k}} = \mathbf{k}_c(\mathbf{1} + \eta_0\hat{\Phi}), \quad (2.20)$$

$$\eta_0 = \frac{\mathbf{k}_{\text{lin}}}{\mathbf{k}_c}, \quad (2.21)$$

where \mathbf{k}_c represents the continuum absorption coefficient and \mathbf{k}_{lin} is the line absorption coefficient. The ratio of these two is defined as line to continuum absorption coefficient, η_0 . $\hat{\Phi}$ includes the normalized absorption and the dispersion profiles. $\mathbf{1}$ is the 4×4 identity matrix.

After redefining the propagation matrix, $\hat{\mathbf{k}} = \mathbf{1} + \eta_0\hat{\Phi}$, the RTE can be written in continuum optical depth scale, $d\tau_c = -\hat{\mathbf{k}} dz$, as following:

$$\frac{d\mathbf{I}(\tau_c)}{d\tau_c} = \hat{\mathbf{k}} [\mathbf{I}(\tau_c) - \mathbf{S}(\tau_c)]. \quad (2.22)$$

In vectorial form the RTE would be

$$\frac{d}{d\tau_c} \begin{pmatrix} I \\ Q \\ U \\ V \end{pmatrix} = \begin{pmatrix} \eta_I & \eta_Q & \eta_U & \eta_V \\ \eta_Q & \eta_I & \rho_V & -\rho_U \\ \eta_U & -\rho_V & \eta_I & -\rho_Q \\ \eta_V & \rho_U & \rho_Q & \eta_I \end{pmatrix} \begin{pmatrix} I - S \\ Q \\ U \\ V \end{pmatrix}. \quad (2.23)$$

The elements of the propagation matrix can be written as

$$\eta_I = 1 + \frac{\eta_0}{2} \left(\varphi_p \sin^2 \gamma + \frac{1}{2} [\varphi_b + \varphi_r] (1 + \cos^2 \gamma) \right), \quad (2.24)$$

$$\eta_Q = \frac{\eta_0}{2} \left(\varphi_p - \frac{1}{2} [\varphi_b + \varphi_r] \right) \sin^2 \gamma \cos 2\phi, \quad (2.25)$$

$$\eta_U = \frac{\eta_0}{2} \left(\varphi_p - \frac{1}{2} [\varphi_b + \varphi_r] \right) \sin^2 \gamma \sin 2\phi, \quad (2.26)$$

$$\eta_V = \frac{\eta_0}{2} [\varphi_r - \varphi_b] \cos \gamma, \quad (2.27)$$

$$\rho_Q = \eta_0 \left(\psi_p - \frac{1}{2} [\psi_b + \psi_r] \right) \sin^2 \gamma \cos 2\phi, \quad (2.28)$$

$$\rho_U = \eta_0 \left(\psi_p - \frac{1}{2} [\psi_b + \psi_r] \right) \sin^2 \gamma \sin 2\phi, \quad (2.29)$$

$$\rho_V = \frac{\eta_0}{2} [\psi_b + \psi_r] \cos \gamma, \quad (2.30)$$

where γ represents the inclination of the magnetic field vector with respect to observer's line-of-sight and ϕ is the azimuth angle. The absorption and anomalous dispersion profiles under the classical Lorentz electron theory and considering thermal motions (including Doppler broadening and collisions) of the medium, can be written as:

$$\varphi_j = \sum_{i_j=1}^{N_j} s_{i_j} H(a, \nu + \nu_D + \nu_{i_j}), \quad (2.31)$$

$$\psi_j = 2 \sum_{i_j=1}^{N_j} s_{i_j} F(a, \nu + \nu_D + \nu_{i_j}), \quad (2.32)$$

in Eqn. 2.24-2.30 with $j = p, b, r$, corresponding to the Zeeman components, π, σ_b and σ_r . The Voigt function, H , and the Faraday function, F , at a given damping, a (in units of Doppler width), are shown below

$$H(a, \nu') = \frac{a}{\pi} \int_{-\infty}^{\infty} \frac{e^{-y^2}}{(\nu' - y)^2 + a^2} dy, \quad (2.33)$$

$$F(a, \nu') = \frac{1}{2\pi} \int_{-\infty}^{\infty} \frac{(\nu' - y) e^{-y^2}}{(\nu' - y)^2 + a^2} dy. \quad (2.34)$$

The shift in each component of the Zeeman pattern is caused by two effects: (1) The Zeeman splitting causes a shift in the absorption and the dispersion profiles of each component by, $\nu_{i_j} = \frac{\Delta\lambda_{i_j}}{\Delta\lambda_D}$. $\Delta\lambda_{i_j}$ is given in Eqns. 2.15-2.16. (2) The Doppler effect which produce equal shifts of all components of the Zeeman pattern due to a net macroscopic velocity along the vertical axis, ν_D :

$$\nu_D = \frac{v_z \lambda_0}{c \Delta\lambda_D}. \quad (2.35)$$

The Doppler width, λ_D , and the Damping, a , can be written as

$$\lambda_D = \frac{\lambda_0}{c} \left(\frac{2KT}{M} + v_{\text{mic}}^2 \right)^{1/2}, \quad (2.36)$$

$$a = \frac{\lambda_0^2}{4\pi c \Delta \lambda_D} \Gamma, \quad (2.37)$$

where, Γ can be decomposed into broadening due to the radiative lifetime of the energy level and the collisional line broadening. The Doppler width is calculated from temperature, T , and microturbulence, v_{mic} . K is the Boltzmann constant and M is the rest mass of the atom.

2.5 Solution to the RTE

Let us consider the transformation of the Stokes vector from one optical depth, τ_c , to another optical depth, τ'_c , in a situation that no emission process takes place between the two points. This transformation of the Stokes vector can be dealt with the evolution operator, $\hat{O}(\tau_c, \tau'_c)$, as follow:

$$\mathbf{I}^*(\tau_c) = \hat{O}(\tau_c, \tau'_c) \mathbf{I}^*(\tau'_c), \quad (2.38)$$

where the index * indicates the solution of the homogeneous equation associated with the non-homogeneous differential equation Eqn. 2.22. The Evolution operator obeys the following conditions.

$$\hat{O}(\tau_c, \tau_c) = \mathbf{1}, \quad (2.39)$$

$$\hat{O}(\tau_c, \tau'_c) = \hat{O}(\tau_c, \tau'_c) \hat{O}(\tau'_c, \tau''_c), \quad (2.40)$$

Integration of Eqn. 2.22 over two optical depth points, τ_0 and τ_1 , which are the bottom and top of the atmosphere under consideration, gives

$$\mathbf{I}(\tau_1) = \hat{O}(\tau_1, \tau_0) \mathbf{I}(\tau_0) - \int_{\tau_0}^{\tau_1} \hat{O}(\tau_1, \tau_c) \hat{\mathbf{k}}(\tau_c) \mathbf{S}(\tau_c) d\tau. \quad (2.41)$$

Any photon emitted at τ_0 does not reach to τ_1 in an optically thick atmosphere, i.e. when the observer is located at $\tau_1=0$ and the bottom of the atmosphere is deep enough ($\tau_0 \rightarrow \infty$), then

$$\lim_{\tau_0 \rightarrow \infty} \hat{O}(0, \tau_0) \mathbf{I}(\tau_0) = 0. \quad (2.42)$$

A formal solution of the RTE can be obtained using Eqn. 2.40 and 2.41:

$$\mathbf{I}(0) = \int_0^{\infty} \hat{O}(0, \tau_c) \hat{\mathbf{k}}(\tau_c) \mathbf{S}(\tau_c) d\tau. \quad (2.43)$$

The evolution operator cannot be obtained analytically for a general atmosphere and has to be determined by numerical methods.

Using the properties of the evolution operator, a differential equation can be derived as follow:

$$\frac{d\hat{O}(\tau_c, \tau'_c)}{d\tau_c} = \hat{\mathbf{k}}(\tau_c)\hat{O}(\tau'_c, \tau_c). \quad (2.44)$$

Here the evolution operator is an exponential of a matrix,

$$\hat{O}(0, \tau_c) = e^{-\int_0^{\tau_c} \hat{\mathbf{k}}(\tau) d\tau}, \quad (2.45)$$

this exponential is only a formal way of expressing an infinite series, because of an important property of the matrix algebra: matrices do not commute in general.

2.5.1 Milne-Eddington approximation

In the Milne-Eddington approximation the propagation matrix is constant with respect to the atmospheric height, $\hat{\mathbf{k}}(\tau_c) = \hat{\mathbf{k}}_0$, and the source function varies linearly with optical depth, $\mathbf{S}(\tau_c) = [S_0 + S_1\tau_c, 0, 0, 0]$. Here S_0 and S_1 are constant. In the Milne-Eddington approximation, we can integrate Eqn. 2.44:

$$\hat{O}(0, \tau_c) = e^{-\int_0^{\tau_c} \hat{\mathbf{k}}_0 d\tau}. \quad (2.46)$$

Using Eqn. 2.46 and the assumption that the source function varies linearly with optical depth, Eqn. 2.43 can be rewritten:

$$\mathbf{I}(0) = \int_0^{\infty} e^{-\hat{\mathbf{k}}_0\tau_c} \hat{\mathbf{k}}_0(S_0 + S_1\tau_c) d\tau. \quad (2.47)$$

The explicit form of the Stokes vector can be obtained by analytically solving this equation:

$$I(0) = S_0 + \frac{S_1\eta_I}{\Delta}[\eta_I^2 + \rho_Q^2 + \rho_U^2 + \rho_V^2], \quad (2.48)$$

$$Q(0) = -\frac{S_1}{\Delta}[\eta_I^2\eta_Q + \eta_I(\eta_V\rho_U - \eta_U\rho_V) + \rho_Q R], \quad (2.49)$$

$$U(0) = -\frac{S_1}{\Delta}[\eta_I^2\eta_U + \eta_I(\eta_Q\rho_V - \eta_V\rho_Q) + \rho_U R], \quad (2.50)$$

$$V(0) = -\frac{S_1}{\Delta}[\eta_I^2\eta_V + \eta_I(\eta_U\rho_Q - \eta_Q\rho_U) + \rho_V R], \quad (2.51)$$

where,

$$\Delta = \eta_I^2(\eta_I^2 - \eta_Q^2 - \eta_U^2 - \eta_V^2 + \rho_Q^2 + \rho_U^2 + \rho_V^2) - R^2, \quad (2.52)$$

$$R = \eta_Q\rho_Q + \eta_U\rho_U + \eta_V\rho_V. \quad (2.53)$$

This solution is known as the Unno-Rachkowsky solution of the RTE (Unno 1956, Rachkovsky 1962, 1967).

2.6 Inversion of the Stokes profiles

The study of the magnetic and velocity field structure of a sunspot in the photosphere and the upper chromosphere in a later part of the thesis is carried out by analyzing different spectral lines such as Si I 10827.1 Å, Ca I 10832.4 Å and the He I triplet at 10830 Å. To obtain physical parameters of the solar atmosphere we carried out inversions of spectro-polarimetric observations of these spectral lines. The basic idea of the inversion is the synthesis of Stokes profiles by solving the RTE with an initial guess of relevant physical parameters of the atmosphere under consideration. These atmospheric parameters are free parameters in the inversion. The resulting synthetic Stokes profiles are then compared with the observed Stokes profiles. The initial guess parameters are iteratively changed by means of a χ^2 minimization algorithm, until the the best fit of the synthetic Stokes profiles to the observed Stokes profiles is obtained. We used two different inversion codes in the thesis: HeLIx⁺ and SPINOR.

2.6.1 HeLIx⁺

The study presented in Chapter 5 about the upper chromospheric magnetic field of a sunspot is carried out by analyzing the He I triplet at 10830 Å (for details of the He I triplet see Chapter 5). HeLIx⁺ (Helium Line Information Extractor) developed by [Lagg et al. \(2004, 2009\)](#). HeLIx⁺ solves the RTE analytically under the Milne-Eddington approximation. Because the He I triplet forms only in the upper chromosphere and there is no contribution from the photosphere and because it is mostly optically thin, the Milne-Eddington approximation is a justifiable approach as long as we are only interested in the magnetic and velocity fields and not in the temperature structure of the atmosphere, or exact height of formation. The components of the He I triplet are sensitive to both the Zeeman effect and the Paschen-Back effect. The HeLIx⁺ inversion code considers the Zeeman splitting in the incomplete Paschen-Back regime. Shifts and relative strengths of the Zeeman components of the He I triplet in the incomplete Paschen-Back regime are estimated using an approximation by means of polynomials as proposed by [Socas-Navarro et al. \(2005\)](#).

In the HeLIx⁺ inversion code it is assumed that the Zeeman components of the spectral line have the form of Voigt functions. Initially, an arbitrary model atmosphere is assumed which consists of 8 free parameters. These parameters are the magnetic field strength, B , the inclination of the magnetic field vector, γ , the azimuth angle of the magnetic field vector, ϕ , the LOS velocity, v_{los} , the Doppler width, $\Delta\lambda_D$, the damping constant, a , the gradient of the source function, S_1 , and the opacity ratio between line-center and continuum, η_0 . The source function at $\tau=0$ is excluded from free parameters because the intensity of the unpolarized signal, I , outside the line must be equal to the observed continuum intensity I_c : $S_0 + \mu S_1 = I_c$.

The evaluation of the fitness of the synthetic Stokes profiles to the observed Stokes profiles is based on a minimization of the goodness function δ :

$$\begin{aligned}
\delta = & \sum_{\lambda_i=0}^N \frac{\omega_I}{I_c \sigma_I} (I_{\text{obs}} - I_{\text{syn}})^2 \\
& + \sum_{\lambda_i=0}^N \frac{\omega_Q}{\sigma_Q} (Q_{\text{obs}} - Q_{\text{syn}})^2 \\
& + \sum_{\lambda_i=0}^N \frac{\omega_U}{\sigma_U} (U_{\text{obs}} - U_{\text{syn}})^2 \\
& + \sum_{\lambda_i=0}^N \frac{\omega_V}{\sigma_V} (V_{\text{obs}} - V_{\text{syn}})^2,
\end{aligned} \tag{2.54}$$

where N denotes the number of wavelength positions in the observations. The subscript 'obs' and 'syn' represents observed and synthesized Stokes profiles and ω is a wavelength dependent weighting function which can be set differently for each of the Stokes parameters. The σ represent strengths of the signals:

$$\begin{aligned}
\sigma_I = & \frac{1}{N} \sum_{\lambda_i=0}^N |I_{\text{obs}}/I_c - 1|, \\
\sigma_{Q,U,V} = & \frac{1}{N} \sum_{\lambda_i=0}^N |(Q, U, V)_{\text{obs}}|.
\end{aligned} \tag{2.55}$$

To find the global minimum of the δ , the HeLIx⁺ inversion code uses the genetic algorithm PIKAIA (Charbonneau 1995). To ensure a realistic value of the free parameters every parameter is bounded by a range and the PIKAIA algorithm finds the global minimum within the set range, independently of the initial values set for the parameters.

2.6.2 SPINOR

The Stokes-Profiles-INversion-O-Routines (SPINOR, Frutiger et al. 1999, 2000) inversion code is capable of obtaining the stratified atmosphere with respect to the optical depth, τ , by fitting the observed Stokes profiles. The SPINOR code is based on STROPRO routines developed by Solanki (1987) which synthesizes the Stokes profiles under LTE assumption. To obtain the continuum absorption coefficients, the SPINOR code uses the MULTI 2.2 opacity package (Carlsson 1986) which considers the contribution from, H, He, H⁻, He⁻, H₂⁺, H₂⁻ and other minor donor species. The Rayleigh and the Thompson scattering are considered in the code.

Broadening of the spectral lines due to collision with neutral Hydrogen is included by using the ABO theory (Anstee and O'Mara 1995, Barklem and O'Mara 1997, Barklem et al. 1998). To fit the synthetic stokes profiles to the observed one, the SPINOR code uses the Levenberg-Marquandt algorithm (Press et al. 1986) with a χ^2 merit function. The Levenberg-Marquardt algorithm is much faster than genetic algorithms. The disadvantage of this minimization algorithm is that it only finds local minima and so the results depend

on the initial guess values provided for the free parameters of the model atmosphere. To overcome this an iterative approach has been applied to the inversion code: results from the first run of the code are smoothed over a certain spatial domain which is then considered as the new guess atmosphere, assuming that the atmosphere is smooth in nature. This is repeated until the global goodness of the fit is achieved. This procedure avoids outliers at individual spatial pixels where the code might have reached a local minimum.

2.7 Instrumentation

In this Section we briefly describe telescopes and instruments used for spectro-polarimetric observations presented in the following chapters.

2.7.1 SST and CRISP

The Swedish 1-m Solar Telescope (SST, [Scharmer et al. 2003](#)) is located on the island of La Palma (Spain) at an altitude of about 2400 m above the sea level. The primary turret system has a single high quality lens which at the same time serves as vacuum window. The secondary optical system is a so-called Schupmann system including a field mirror and a 24 cm corrector comprising a lens and a mirror. This system is to compensate for the chromatic aberrations of the 1-m singlet lens ([Scharmer and Blomberg 1999](#)). To correct wavefront distortions caused by atmospheric seeing an adaptive optics (AO) system is used at the SST. The AO system senses the shape and distortion of the wavefront using a Shack-Hartmann type sensor and the distortions are corrected through a deformable mirror and a tip-tilt mirror.

To study the small scale velocity structure in a sunspot penumbra (presented in Chapter 3) we used the Crisp Imaging Spectro-Polarimeter (CRISP, [Scharmer et al. 2008a](#)) mounted at the SST. CRISP is a combination of an imaging system, a polarimeter and detectors. The imaging system is based on a dual Fabry-Perot tunable filter system in a telecentric mount which operates in the range between 510 and 860 nm. It has a high-resolution high-reflectivity etalon which is followed by a low-resolution low-reflectivity etalon. The polarimeter is built of two Liquid Crystal Variable Retarders (LCVRs). The retardance of the LCVRs can be varied by applying different voltages, thus modulating the incoming light beam by using an appropriate modulation scheme. Using a polarizing beam splitter as an analyzer, two perpendicularly polarized light beams which are linear combinations of Stokes parameters are recorded on two 1k×1k-pixel Sarnoff Charge Coupled Devices (CCD). A third CCD is used to record broad-band images through the order-sorting pre-filter. All the CCDs are synchronized by using an external chopper in order to allow post-facto image restoration.

2.7.2 VTT and TIP-2

The German Vacuum Tower Telescope (VTT) is situated at the island of Tenerife. It consists of a coelostat system which directs the sunlight into the telescope. The coelostat mirrors provide non-rotating solar images. The primary mirror has a diameter of 70 cm and a focal length of 46 m. The VTT is also equipped with an AO system. The wavefront

sensor of the AO is also a Shack-Hartmann type with 36 subapertures. The deformable mirror has 35 actuators. In addition to the deformable mirror a tip-tilt mirror corrects the image-jitter.

The data presented in Chapters 4 and 5 have been obtained with the Echelle spectrograph combined with the Tenerife Infrared Polarimeter-2 (TIP-2, Collados et al. 2007).

TIP-2 consists of a pair of Ferroelectric Liquid Crystals (FLCs) which are followed by a polarizing beam splitter. TIP-2 is operational in the spectral range between 1.0 and 2.3 μm and it has a typical spectral sampling of 11.6 mÅ per pixel at 10800 Å. The slit length of the spectrograph is 80". To record the spectrum a 1k×1k-pixel HgCdTe hybrid detector is used.

2.7.3 Hinode SOT/SP

The study presented in Chapter 4 is also based on observations from the Solar Optical Telescope (SOT, Tsuneta et al. 2008, Suematsu et al. 2008, Ichimoto et al. 2008a, Shimizu et al. 2008) on board the Hinode satellite (Kosugi et al. 2007) which was launched in September 2006. SOT consists of a narrow-band filtergraph (NFI), and a broad-band filtergraph (BFI), and a Spectro-Polarimeter (SP). The SP (comprising a Littrow-Echelle spectrograph) records the full Stokes vector of the Fe I 6301.5 and 6302.5 spectral line pair at 112 wavelength positions. The SOT/SP has a spectral resolution of 30 m Å with a noise level of $10^{-3} I_c$ for all four Stokes parameters at an exposure time of 4.8 s per slit position. The length of the slit of the spectrograph is 162" on the solar disk.

3 Penumbrae: Convective Structure in the Deep Photosphere[★]

We study the velocity structure of penumbral filaments in the deep photosphere to obtain direct evidence for the convective nature of sunspot penumbrae. A sunspot was observed at high spatial resolution with the Swedish 1-meter Solar Telescope in the deep photospheric C λ 5380 Å absorption line. The Multi-Object Multi-Frame Blind Deconvolution (MOMFBD) method is used for image restoration and straylight is filtered out. We report here the observations of clear redshifts in the C λ 5380 Å line at multiple locations in sunspot penumbral filaments. For example, the bright head of filaments show large concentrated blueshift and are surrounded by darker, redshifted regions, suggestive of overturning convection. Elongated downflow lanes are also located beside bright penumbral fibrils. Our results provide the strongest evidence yet for the presence of overturning convection in penumbral filaments and highlight the need to observe the deepest layers of the penumbra in order to uncover the energy transport processes taking place there.

3.1 Introduction

In recent years, indirect evidence for the presence of convection in sunspot penumbral filaments has been growing (e.g., [Scharmer 2009](#)). E.g., the twisting motion of penumbral filaments is taken as a signature of overturning convection ([Ichimoto et al. 2007b](#), [Zakharov et al. 2008](#), [Spruit et al. 2010](#), [Bharti et al. 2010](#)). Using high resolution spectropolarimetric observations, [Zakharov et al. \(2008\)](#) estimated that such motions can provide sufficient heat to the surface layers of the penumbra to explain its relatively high brightness. The correlation of the apparent velocity of the twisting motion with the local brightness of the filaments obtained by [Bharti et al. \(2010\)](#), supports convection as a major source of heat transport in sunspot penumbral filaments. Overturning convection in penumbral filaments is a natural and important feature in 3D MHD simulations of sunspots ([Rempel et al. 2009a,b](#), [Rempel 2011](#)). In particular, [Rempel et al. \(2009b\)](#) found upflows along the central axes and downflows at the edges of the filaments (see Figs. 1.13 and 1.14 of Chapter 1). Direct observational evidence for this scenario is, however, so far missing, although the twisting filaments provide indirect support. The simulations indicate that the convective structures and motions are restricted to the subsurface and surface layers. Since most spectral lines used for diagnostic purposes sample mid-photospheric heights, this may explain why it has not been possible to obtain direct evidence of over-

[★] This chapter is published in *Astrophysical Journal Letters*, 734, L18 (2011).

turning convection in penumbral filaments (see, e.g., [Franz and Schlichenmaier 2009](#), [Bellot Rubio et al. 2010](#)).

In this study we probe the deep layers of the photosphere in search of such downflows by analyzing high resolution observations in the C I 5380.3 Å line obtained at the Swedish 1-meter Solar Telescope. In the quiet Sun, the C I 5380.3 Å line has a mean formation height of around 40 km above the continuum optical depth $\tau_c = 1$ at 500 nm ([Stuerenburg and Holweger 1990](#)) making it ideal for this purpose.

3.2 SST/CRISP observations and data reduction

We observed a decaying sunspot with a one-sided penumbra in active region NOAA 11019 (cf. [Fig. 3.2](#)) with the Swedish 1-meter Solar Telescope (SST) on 2 June, 2009. The center of the field of view (FOV) was located at $\mu = 0.84$ (heliocentric angle = 32.7°). During the observations the seeing conditions were good to excellent, with only few interruptions by poorer seeing.

Using the CRISP imaging spectro-polarimeter we carried out consecutive spectral scans of the photospheric C I 5380.3 Å, Fe I 5250.2 Å and the chromospheric Ca II 8542 Å spectral lines. Here we analyze only the C I 5380.3 Å line¹. We recorded the C I 5380 Å line at 8 wavelength positions, $\lambda - \lambda_0 = [-300, -120, -80, -40, 0, 40, 80, 120]$ mÅ (see [Fig. 3.1](#)). Scanning the line in all four Stokes parameters required 14 s for the C I 5380.3 Å line. The cadence of these observations, including the Fe I 5250.2 Å and Ca II 8542 Å scans (not considered in the present study) is 29 s.

3.2.1 Image reconstruction

To achieve near diffraction limited spatial resolution ($0''.14$), images were reconstructed using the Multi-Object Multi-Frame Blind Deconvolution (MOMFBD) method ([van Noort et al. 2005](#), [Löfdahl 2002](#)). MOMFBD restores images affected by seeing induced image blurring and distortions. These are the residual distortions after the adaptive optics system. MOMFBD combines multiple realization (short exposure images) of multiple objects which have a known wavefront relation with each other. In the case of CRISP, images from each camera is considered as an individual object, which are restored jointly.

To reduced false signals in the estimation of derived quantity (the Doppler velocity) near-perfect alignment is achieved between different objects by using a pinholes calibration process. The pinholes serve as an object which is the same for all the wavelength positions and all the polarization states and, thus, can be used to ensure alignment of different objects in sub-pixel accuracy.

Images observed in the C I 5380 Å and Fe I 5250 Å lines were aligned with sub-pixel accuracy by cross-correlating the corresponding continuum images.

¹The Fe I 5250.2 Å line is used only to identify "quiet Sun" locations, where the polarization signal in this line is below a given threshold.

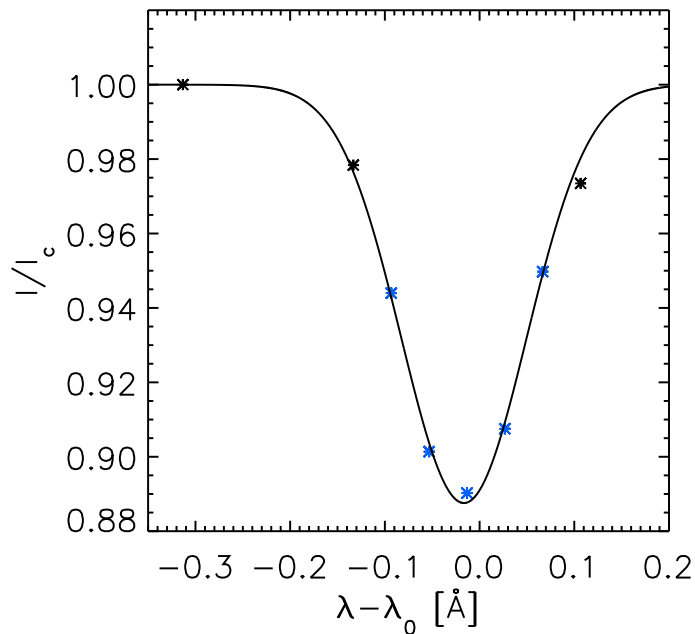


Figure 3.1: Normalized intensity profile, I/I_c , of a penumbral pixel, here I_c denotes continuum intensity. Asterisks show the eight wavelength positions, $\lambda - \lambda_0 = [-300, -120, -80, -40, 0, 40, 80, 120]$ mÅ, sampling the C I 5380 Å line. Asterisks colored in blue show wavelength positions used to estimate the Doppler velocities by fitting a Gaussian function. The solid line shows fitted Gaussian.

3.2.2 Doppler velocity

We determined Doppler velocities by fitting a Gaussian function to the C I line (see Fig. 3.1). Due to the low Landé factor ($g_{\text{eff}} = 1$, Solanki and Brigljevic 1992) and large thermal width of the line, this is an acceptable approach even in a sunspot. The good quality of the Gaussian fit throughout the penumbra suggests that the line is unblended there, unlike in the umbra. Another reason for expecting that the line is unblended (or at the most rather weakly blended) in the penumbra is that the line strength increases strongly with temperature, a nearly unique property of C I lines among photospheric spectral lines.

The resulting velocity maps show variations of the mean quiet Sun velocities across the FOV caused by the absolute wavelength positions varying across the FOV due to cavity errors of the etalons of CRISP. These wavelength shifts are smeared out in a continuously changing manner due to varying seeing conditions. The applied calibration data (flat fields), which are well defined in pixel space, are no longer connected to pixel space of the science data after restoration (Schnerr et al. 2010). Therefore, the cavity errors cannot be fully removed with the flat fields. The absolute wavelength shifts caused by the cavity errors are wavelength dependent and the residuals after correction for flat-field cavity shifts are much higher in the 5380 Å band than in the 6300 Å and 6560 Å bands, used in previous studies carried out with CRISP (see, e.g., Scharmer et al. 2008a, Rouppe van der Voort et al. 2010, Ortiz et al. 2010). Since the residual wavelength shifts across the FOV are expected to be large-scale, however, they do not rule out a study of penumbral fine structure. In order to determine a confidence level of the resulting absolute velocity reference point of the Doppler velocities we selected 19 quiet Sun subfields of $6'' \times 6''$ size

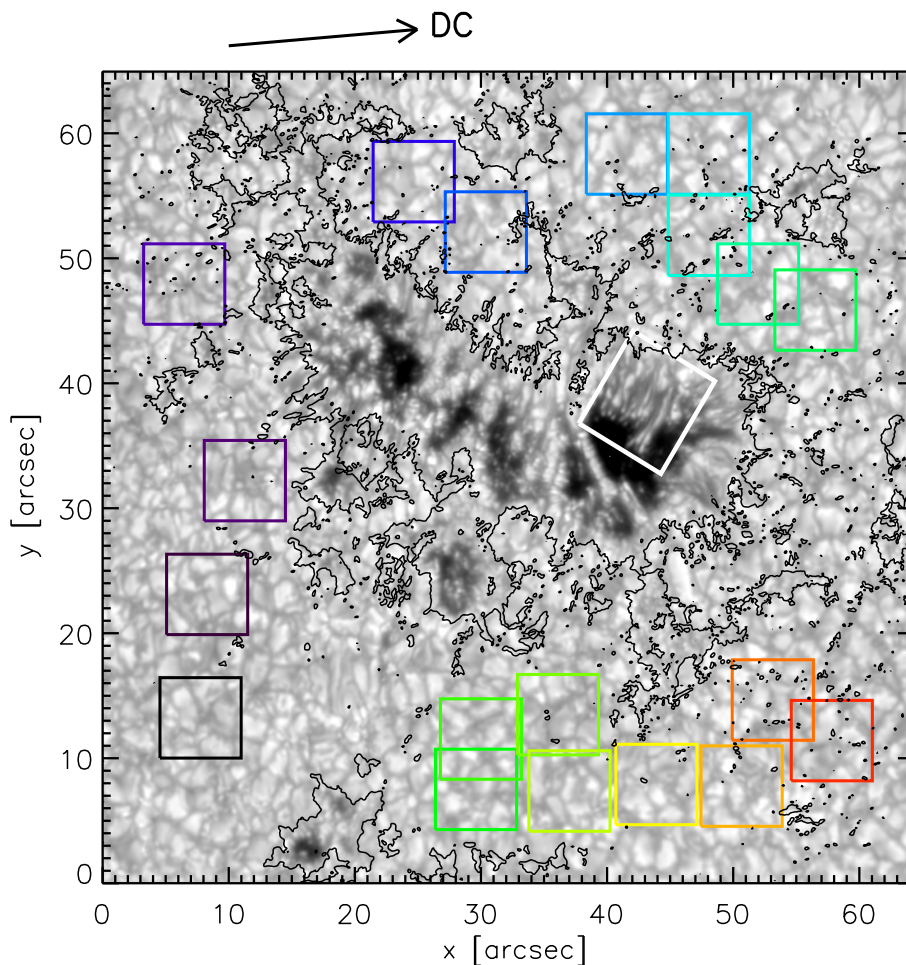


Figure 3.2: Continuum image at 5380 \AA of the decaying sunspot with a penumbra mainly on one side. Black contours outline regions where the absolute circular polarization averaged over the two line wings ($\pm 40 \text{ m\AA}$ from average line center) of the Fe I 5250 \AA line is greater than 4 %. Colored boxes ($6'' \times 6''$) show the different quiet Sun fields used to calculate the velocity reference value. The thick white rectangle marks the portion of the image shown in Fig. 3.6 in detail. The arrow points to disk-center.

throughout the FOV, indicated by the colored squares in Fig. 3.2. The relative quietness of the selected subfields was assured by a threshold value (4 %) of spectrally averaged absolute circular polarization² in the line wings ($\pm 40 \text{ m\AA}$ from average line center) of the Fe I 5250.2 \AA line. We calculated mean Doppler velocities of the C I 5380 \AA line by spatially averaging the line profiles in each subfield and repeated this procedure for all the observed sequences, i.e., over 20 min. The results from this procedure are shown in Fig. 3.3. The velocity in each subfield fluctuates randomly, but does not exhibit a systematic variation with time. In order to get a mean quiet Sun velocity reference, we fitted a Gaussian to the velocity distribution and obtained a mean value of -480 m s^{-1} and a full

²A full polarimetric model of the SST in the observed spectral range was not available at the time of publication of this study by Joshi et al. (2011). Therefore, a complete correction for instrumental cross-talk was not performed. Displayed polarimetric information can be considered only as a rough estimate of the magnetic field structure in the FOV.

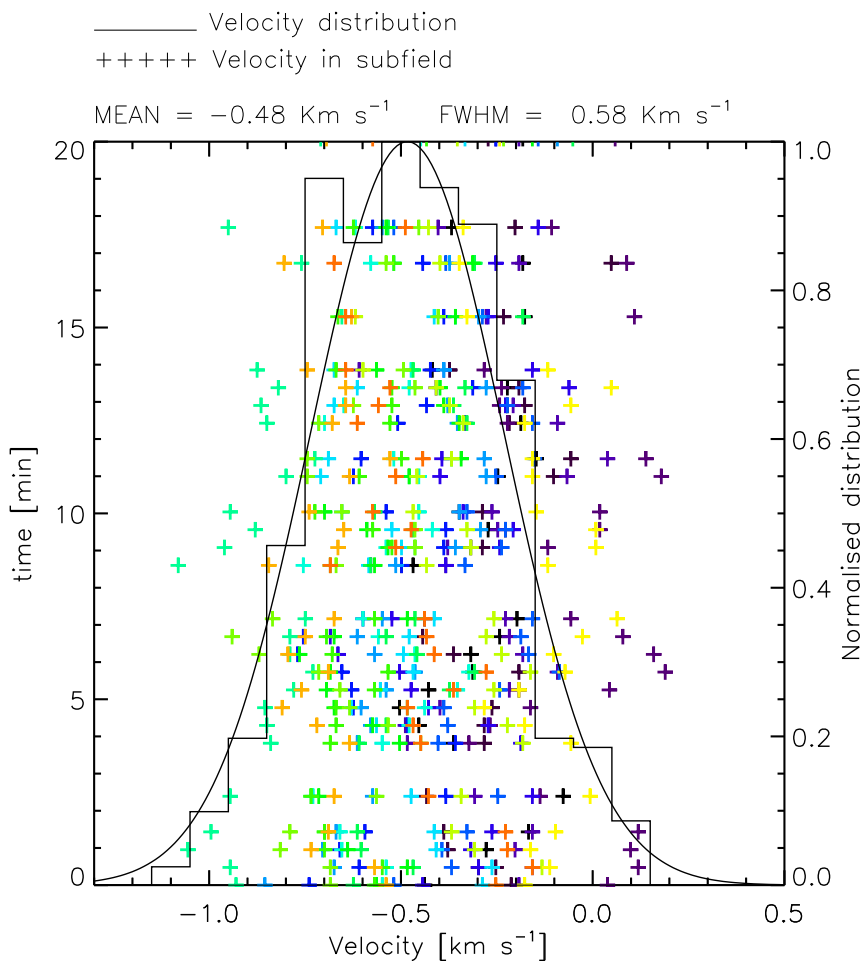


Figure 3.3: Mean velocities obtained from average line profiles of the subfields shown in Fig. 3.2 (abscissa) vs. time of observation relative to the time of the first recording (ordinate). Colors correspond to the subfields bounded by squares of with the same colors in Fig. 3.2. The velocity distribution and a Gaussian fit are represented by solid lines.

width at half maximum (FWHM) of 580 m s^{-1} for the C I 5380 Å line, i.e., the residual uncertainty (1σ) in the absolute Doppler velocities is $\pm 248 \text{ m s}^{-1}$. After applying this procedure, the mean values of the obtained velocity maps are calibrated for a convective blueshift of -922 m s^{-1} for the C I 5380.3 Å line (de La Cruz Rodríguez et al. 2011). For the further analysis we selected the scan of the C I 5380.3 Å line made under the best seeing conditions.

3.2.3 Straylight Correction

Ground-based observations are strongly affected by straylight³, so that, e.g., contrasts are significantly lower than in data recorded above the Earth’s atmosphere (see, e.g., Danilovic et al. 2008, Hirzberger et al. 2010). We also expect the velocity to be re-

³Instead of the misleading term “straylight” one should use “false light” or “parasitic light” since this effect is rather produced by high-order aberrations of the optical system (atmosphere and telescope). The actual straylight contribution is mostly negligible

duced through straylight. The amount of straylight and the shape of the corresponding straylight point spread function is strongly dependent on the seeing conditions and on the instrument design. The straylight point spread functions can be approximated from fitting observations of the solar limb (aureolas, see, e.g., [Sobotka et al. 1993](#)) or from fitting the profiles of planetary limbs during transits (see, e.g., [Bonet et al. 1995](#), [Mathew et al. 2009](#), [Wedemeyer-Böhm and Rouppe van der Voort 2009](#)). Since we do not have these auxiliary data, we applied a rough estimation, assuming that the biggest amount of the straylight stems from regions within $1.6''$ around the respective positions (approximately the tenfold of the spatial resolution of the data), i.e., we approximated the straylight point spread function with a Gaussian of $1.6''$ width. For deconvolving the images we used the Wiener filter given in [Sobotka et al. \(1993\)](#) and applied a slight modification, so that it has the shape

$$F(k) = \frac{1}{c} \frac{MTF(k) + 1}{MTF(k)^2 + 1/c}, \quad (3.1)$$

where MTF is the modulation transfer function (the modulus of the Fourier transform of the point spread function), k is the spatial wavenumber and c is a free parameter which defines the straylight contribution that has to be deconvolved. $F(k)$ for different choices of c are plotted in Fig. 3.4. The advantage of the present form of the filter compared to the one used in [Sobotka et al. \(1993\)](#) is that it converges to unity for large k , i.e., it does not affect the small-scale structures of the images.

In the present study the value of parameter c has been chosen equal to 2.0, so that the resulting quiet Sun rms image contrast for the continuum point (at $\lambda = \lambda_0 - 300 \text{ m\AA}$)

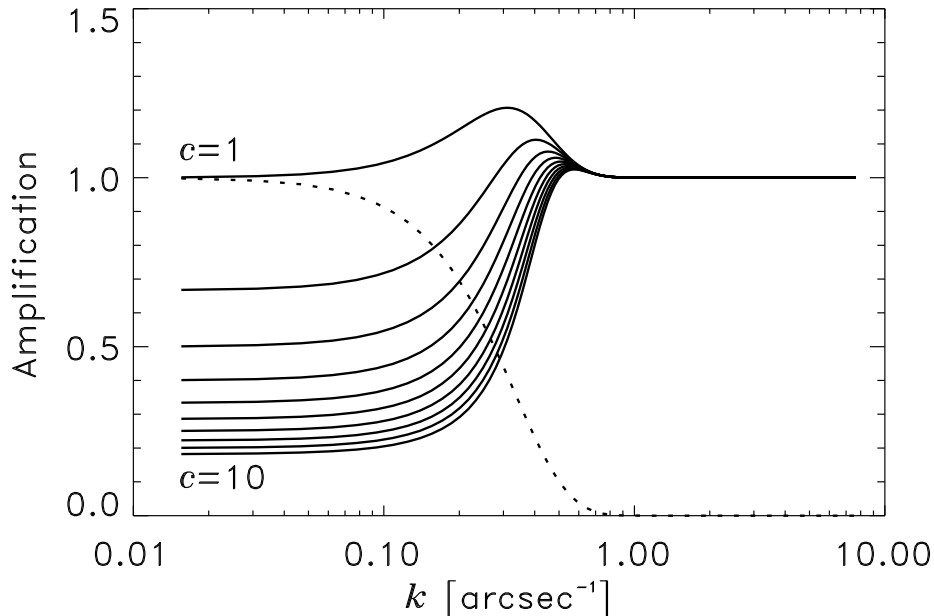


Figure 3.4: Applied filter to deconvolve straylight. The solid curves denote filter shapes for $c = 1 \dots 10$ (see Eq. (1)). The dotted curve represents the MTF , i.e., the Fourier transform of a Gaussian of $1.6''$ width.

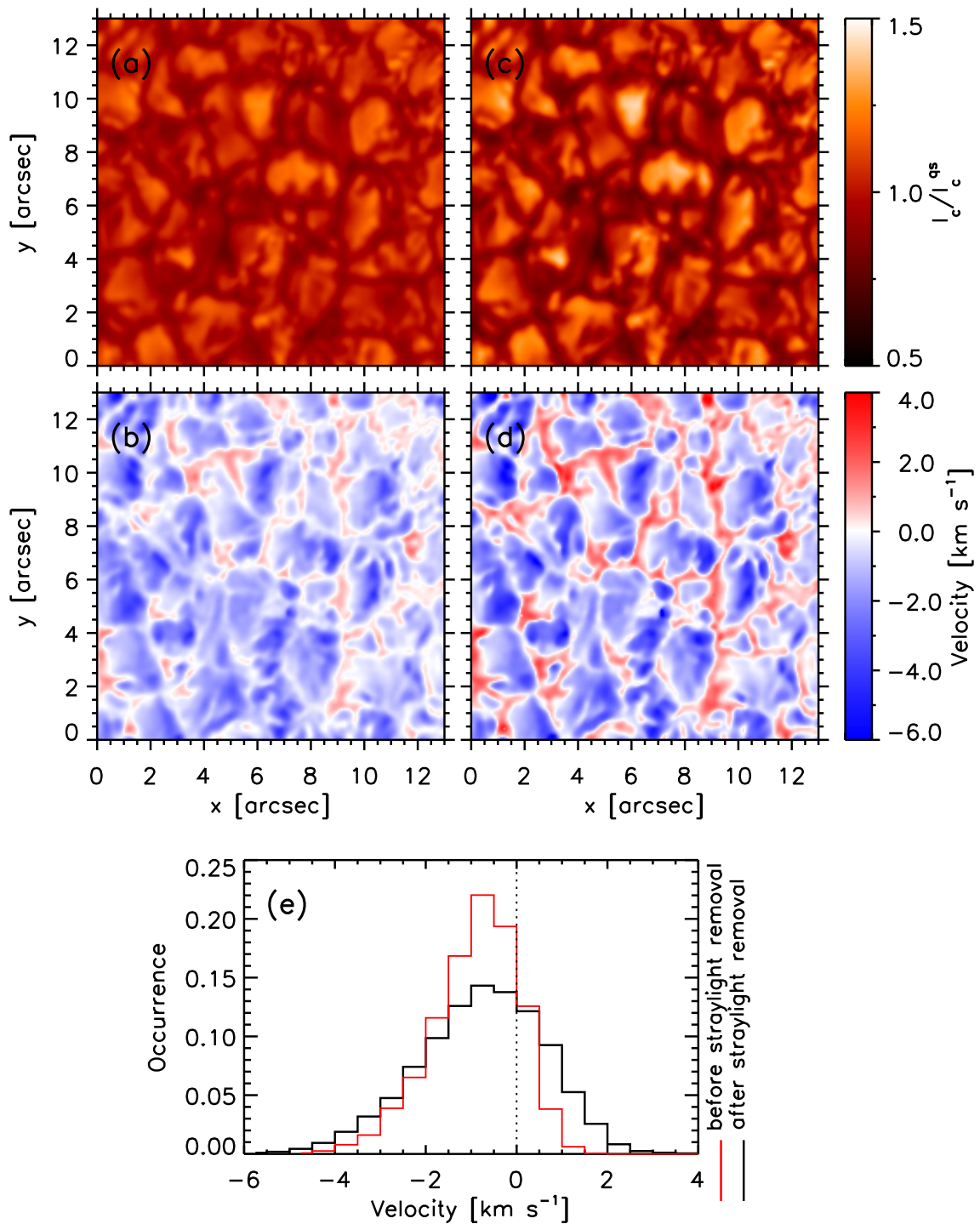


Figure 3.5: Panels (a) and (b) display a quiet Sun continuum map near the C I 5380.0 Å line and the corresponding Doppler map before straylight removal, respectively. Panel (c) and (d) are continuum map and Doppler map after straylight removal while histograms of Doppler velocity before (red) and after (black) straylight removal are plotted in panel (e).

of the best scan increases from 8.5% in the original image to 13.0% in the deconvolved image, which is closer to, but still somewhat smaller than the contrast obtained from data at a similar wavelength that are much less contaminated by straylight (continuum at 5250.4 Å in IMAx/Sunrise observations, see [Martínez Pillet et al. 2011](#)). We finally used this conservative choice, although we also tested other straylight functions, including broad Gaussians with widths up to 16". The results of using stronger straylight removal (larger c) or broader Gaussians, remained similar, but provided stronger downflows and, for larger c , also higher contrast. Stronger straylight removal also led to bigger scatter in the velocities and somewhat more distorted line profiles, which was another reason to keep to the conservative value of straylight.

We selected a 13" × 13" field in the quiet Sun to compare velocities before and after straylight removal. Results are shown in Fig. 3.5. The redshift in inter-granular lanes increases disproportionately through straylight removal (see panels (b), (c) and (d) of Fig. 3.5). Downflows are particularly affected by straylight because they are narrower and are present in darker features. The fact that the downflows remain weaker than upflows also after our standard straylight removal confirms that we have been conservative in the removed amount of straylight.

3.3 Results

Panels (a) and (c) of Fig. 3.6 show a portion of the observed penumbra as seen in the continuum intensity (at $\lambda = \lambda_0 - 300 \text{ mÅ}$), before and after straylight removal, respectively. The corresponding maps of Doppler velocity are plotted in panels (b) and (d). Obviously both blue- and redshifts are present in the penumbra, in particular after straylight removal. A striking feature in Fig. 3.6(b) is the localized patches of strong blueshift, up to 3.3 km s^{-1} , coinciding with the bright heads of penumbral filaments. These bright heads are surrounded by lanes of gas nearly at rest or slightly redshifted. In panel (b) significant redshifts are visible only at two locations, once at the side of a filament reaching into the umbra (at $x = 6''$ and $y = 1''$) and once, rather weakly around the bright and strongly blueshifted head of a filament (at $x = 6.5''$ and $y = 4.5''$).

A number of new redshifted patches are found in the Doppler map after straylight removal (panel d), appearing dominantly at locations previously seemingly at rest in panel (b). We have grayed out areas where intensity is below $0.6I_c^{\text{qs}}$ (here I_c^{qs} denotes averaged quiet Sun continuum intensity), because χ^2 values of the Gaussian fits to the line profiles are high in these areas since the line is very weak there and possibly blended (as suggested by the fact that we obtain mainly strong blueshifts in the umbra contrary to all previous studies based on other spectral lines). Redshifts (largest value 2.0 km s^{-1}) show a tendency to be located in dark regions, as can be judged by considering the white contours in panel (c). These contours outline the redshift of panel (d). Redshifts are now found clearly around the head of multiple filaments (e.g., at $x = 2''$ and $y = 3''$ and around the filaments protruding into the umbra). Narrow redshifted areas are also found in the middle and outer penumbra beside and between bright filaments.

Clearly, in the lower photosphere redshifts are present at many different locations in the penumbra. We expect that only a part of redshifted features actually present in the penumbra has been detected.

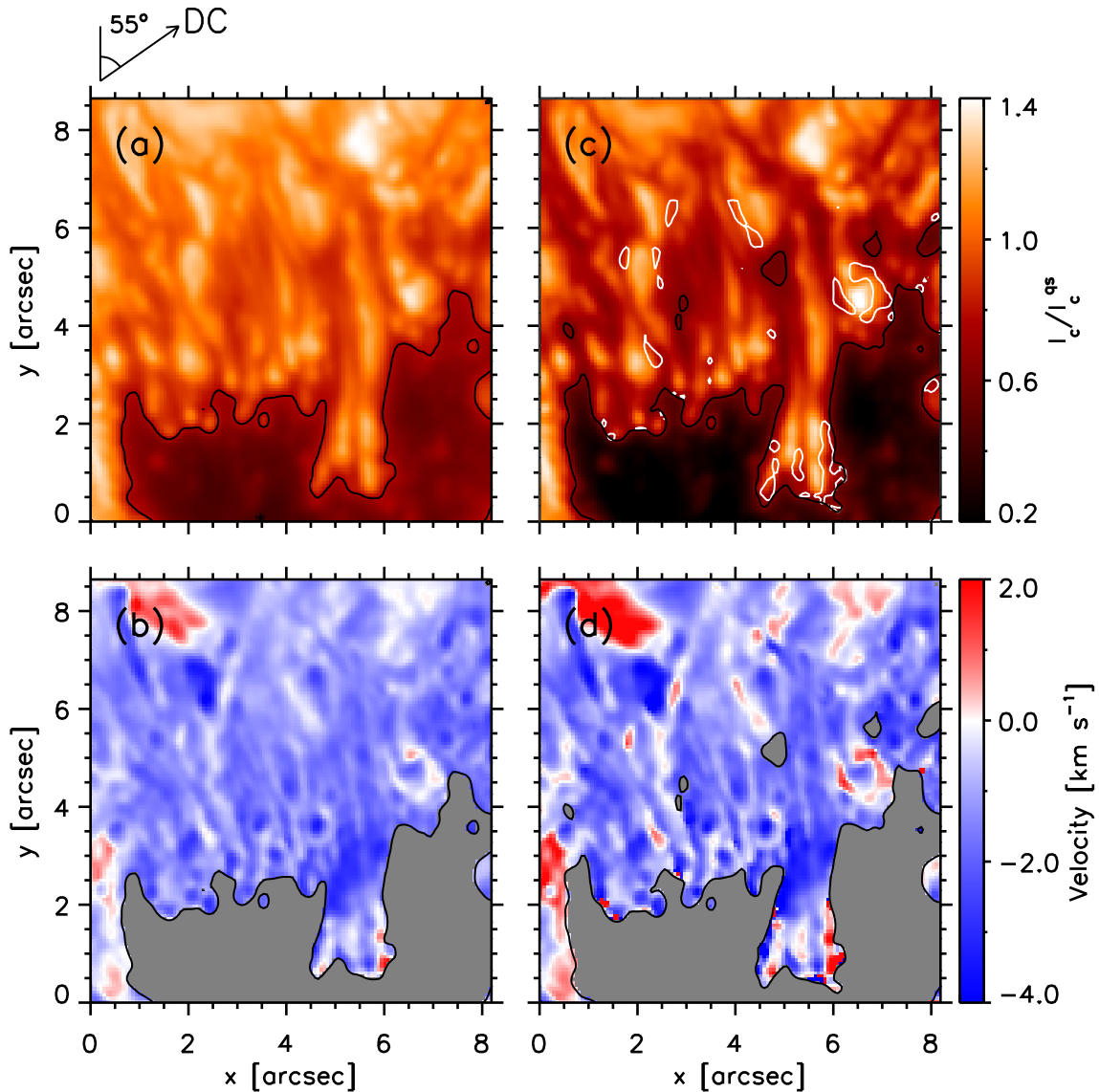


Figure 3.6: (a) Continuum intensity map in the penumbral region of the observed sunspot obtained from the C 15380 Å line. The displayed region is marked by the thick white rectangle in Fig. 3.2. (b) the corresponding Doppler velocity, (c) continuum intensity map after straylight removal, (d) Doppler velocity after straylight removal. Gray color encircled by black contours in panels (b) and (d) represent areas where continuum intensity is less than $0.6 I_c^{\text{qs}}$. White contours in panel (c) outline penumbral downflows and show that these are located in darker parts of the penumbra. The arrow above panel (a) indicates the direction toward solar disk center.

3.4 Discussion

We have provided the first direct measurements of downflows reaching 2.0 km s^{-1} in the body of a penumbra. The studied sunspot, located at $\mu = 0.84$, had only a partial penumbra, on the disk-center side of the spot, so that all well-defined filaments partially point to disk center. Hence the Evershed flow contributes a blueshift, so that redshifts in Fig. 3.6(d) must be caused by downflows (or inflow, which appears rather unlikely, however).

The $\text{C I } 5380 \text{ \AA}$ line reveals a highly structured velocity pattern, with large variations in velocity around the head of filaments. Typical blueshift of 3 km s^{-1} found in the bright head of the filaments, surrounded by gas displaying redshift (after straylight removal) or no shift. We interpret them as strong localized upflows of hot gas in the head of the filaments following [Rimmele and Marino \(2006\)](#), but cannot rule out that they are due to Evershed flow. A fraction of this gas starts moving along the axis of the filaments and forming the Evershed flow ([Scharmer et al. 2008a](#)). The rest of the gas moves to the sides of the filaments and flows downward. Further downflows are found alongside bright filaments in the middle and outer part of this penumbra. Such downflows have been predicted by models of penumbral convection (e.g., [Rempel et al. 2009a,b](#), [Scharmer and Spruit 2006](#)). Earlier observational studies have provided only indirect evidence for such downflows ([Ichimoto et al. 2007b](#), [Zakharov et al. 2008](#), [Bharti et al. 2010](#), [Spruit et al. 2010](#)).

The velocity at the heads of the filaments reaches values up to 3.3 km s^{-1} , interpreted here as upflows, agrees with earlier observational results ([Rimmele 1995b](#), [Rimmele and Marino 2006](#), [Hirzberger and Kneer 2001](#), [Hirzberger et al. 2005](#)). Such upflows are also consistent with the moving flux tube model presented by [Schlichenmaier et al. \(1998a\)](#), which predicts an upflow of 4 km s^{-1} at the footpoints of the penumbral filaments, but equally with the interpretation of [Scharmer et al. \(2008a\)](#) that the Evershed flow is a horizontal flow component of overturning convection. In recent years, convection has become an important candidate to explain the heat transport in penumbrae. Based on the observed 1 km s^{-1} upflow at the axis of the filament in the upper layers of the photosphere, [Zakharov et al. \(2008\)](#) estimated the heat transport by convection in the penumbra to be sufficient for maintaining the brightness of the penumbra. The upflows up to 3.3 km s^{-1} in the bright heads of penumbral filaments with downflows at the filament sides, found in the present study, and the coincidence of the strongest upflows with bright filaments and downflows with dark filaments strongly support that the heat transport in the penumbra is accomplished by convection.

In the outer sections of penumbral filaments (i.e. further from the umbra) we found maximum blueshifts of up to 3.0 km s^{-1} . If we assume that this blueshift is due to the Evershed effect, its projection in the direction of disk center and parallel to the solar surface gives 8.5 km s^{-1} of radial outflow. This upper limit agrees well with results from the simulation by [Rempel \(2011\)](#) which shows Evershed flow speeds above 8 km s^{-1} near $\tau = 1$.

The true strength of the penumbral downflows are expected to be larger than found here for the following reasons. For the same reasons we expect a number of the locations still seemingly at rest, in reality be filled with downflowing gas:

1. Incomplete removal of straylight. We have been rather conservative when removing

straylight, since the assumed granular contrast of 13% is smaller than values found by [Mathew et al. \(2009\)](#) at 5550 Å from Hinode and [Martínez Pillet et al. \(2011\)](#) at 5250 Å from SUNRISE.

2. A blueshift imposed by the LOS-component of the Evershed flow. The major axis of most of the filaments makes an angle of $\sim 55^\circ$ with the line joining the sunspot and the disk center. Thus, we expect radial outflow due to Evershed effect to contribute as $v_{\text{LOS}} = v_E \sin \theta \cos 55^\circ = 0.35v_E$ (where v_E represents the Evershed velocity) to the LOS velocity. The Evershed flow probably hides a significant amount of the redshift due to downflowing gas (cf. [Bharti et al. 2011](#)).
3. The geometry of the filaments. As proposed by [Zakharov et al. \(2008\)](#) the penumbral $\tau = 1$ surface is strongly corrugated (see Fig. 1.11 of Chapter 1), so that we see the disk center side of the filaments more clearly than the other side (see their Fig. 4). Hence, in our sunspot we might expect the downflows to be better visible on the diskward side of a filament where they may be partly covered by the filament lying in front of them. This interpretation is supported by the fact that the strongest downflows are found on the diskward side of a filament extending into the umbra, where no other filament can block the view of its edge.

In summary, we report the observations of downflows at the edges of bright penumbral filaments in the deep photospheric layers. Such downflows are expected for overturning convection in the penumbra.

Comments on “Stray-light correction in 2D spectroscopy”, by Schlichenmaier and Franz

Recently [Schlichenmaier and Franz \(2013\)](#), hereinafter SM) studied the effect of stray-light correction on downflows in a sunspot penumbrae using the Hinode SOT/SP data. Based on this study SM claim that downflows detected by [Joshi et al. \(2011\)](#), and so in the present chapter, from SST/CRISP observations are results of overcompensation of straylight. The straylight correction by [Joshi et al. \(2011\)](#) was very conservative in that regard and actually considerably undercompensated the straylight. Below we give some arguments in favor of this statement.

1. Even after straylight compensation the average LOS velocity in the quiet sun in our data set is negative, being 780 m s^{-1} (compared with 910 m s^{-1} before we started making the correction). The velocity estimated from averaged quiet Sun profiles is almost the same with and without the straylight correction applied. In the case of complete straylight removal, one would expect an average velocity of roughly around zero (mass conservation would require zero, if density and heights of formation were the same in both up- and downflows). A residual blueshift of 780 m s^{-1} is much larger than the blueshifts in Hinode SOT/SP data (SM). Also, the difference between the average quiet Sun blueshift before and after straylight removal of 130 m s^{-1} corresponds to a rather mild change (see Tables 2 and 3 of SM). These numbers speak strongly for the fact that we have not overestimated the straylight.

2. Another fact is that Hinode has a factor of ~ 2 lower maximum spatial resolution than the SST, so that even if straylight is compensated properly, it is unlikely to see downflows in SOT/SP observations of the same strength, if these are concentrated in narrow channels.
3. The Hinode straylight is not as low as claimed by SM. The Point Spread Function (PSF, including primary aperture, obscuration, spider and SP defocus) calculated by [Danilovic et al. \(2008\)](#) results in $\sim 80\%$ contamination of signal in each pixel from neighboring pixels (FWHM of the central peak of the PSF is $\sim 0''.32$). They also need an additional 4.7% straylight to bring down the rms contrast of quiet Sun MHD simulations (14.4%) to the quiet Sun rms contrast observed with Hinode (7.0%).
4. The work of [Tiwari et al. \(2013a\)](#), confirms the above points. They corrected self-consistently for the PSF of Hinode (no free parameters were allowed there, the PSF follows strictly the one introduced by [Danilovic et al. 2008](#)). For details on the inversion please check [van Noort \(2012\)](#); and [van Noort et al. \(2013\)](#). [Tiwari et al. \(2013a\)](#) found clear downflows at the sides of many penumbral filaments, although they used a totally different approach and a different data set than those used by [Joshi et al. \(2011\)](#). As pointed out above (point 2), these downflows are expected not to be as strong as those obtained from the SST with appropriate straylight removal.
5. We find one of the statements by SM to be misleading to readers (In Section 5, 3rd paragraph, they say: “[Joshi et al. \(2011\)](#) compare the granular contrast of their observation with IMaX measurements ([Martínez Pillet et al. 2011](#)) to estimate the amount of stray light ($\alpha \approx 0.34$, cf. Fig. 2) in their data”. This is correct, but incomplete and hence misleading.

Basically, the rms contrast in our study, after straylight correction, is 13.0% which is lower than the IMaX contrast ($14\%-15\%$) and also lower than the rms contrast in MHD simulations (which agrees well with the IMaX data). Therefore, in our study the IMaX rms contrast was only used as an upper limit to stay on the conservative side, thus avoiding overcompensation (as pointed out in [Joshi et al. \(2011\)](#), Section 2.1, 2nd paragraph).

Given the above, it is clear that the conclusions of SM do not hold and that they lead the reader astray into thinking that the results of [Joshi et al. \(2011\)](#) are based on faulty straylight removal.

4 Vertical Magnetic Field Gradient in the Photospheric Layers of Sunspot

Spectro-polarimetric observations of sunspots are analyzed. Independently observations were obtained with the Hinode SOT/SP and with the Tenerife Infrared Polarimeter-2 (TIP-2) mounted at the German Vacuum Tower Telescope (VTT). We apply state-of-the-art inversions techniques to both data sets to retrieve the magnetic field and the corresponding vertical gradient along with other atmospheric parameters in the solar photosphere. In the sunspot penumbra we detected patches of negative vertical gradients of the magnetic field strength, i.e. the magnetic field strength decreases with depth in the photosphere. The negative gradient patches are arranged in a ring-like structure in the inner and partly in the middle penumbra in both data sets. From the SOT/SP observations we found that the negative gradient patches are restricted mainly to the deep photospheric layers and are concentrated near the edges of the penumbral filaments. The appearance of the negative gradient does not depend on the location of the sunspot on the solar disk (for $\mu=0.84$). MHD simulations also show negative gradients in the inner penumbra in azimuthal averages. We interpret the negative vertical gradient of the magnetic field strength in VTT/TIP-2 and SOT/SP data as being partly caused by the highly corrugated iso- τ surfaces. Another reason is likely the cancellation of polarized signal due to the presence of unresolved opposite polarity patches in the deeper layers of the penumbra.

4.1 Introduction

The vertical gradient of the magnetic field vector in sunspot photospheres has been studied extensively (for reviews see, e.g. [Solanki 2003](#), [Borrero and Ichimoto 2011](#)). Depending on the diagnostic tools, a wide range of values from 1.0 to 4.0 G km⁻¹ for the vertical gradient of the magnetic field strength in sunspot umbrae have been found ([Borrero and Ichimoto 2011](#), [Balthasar and Gömöry 2008](#), [Sánchez Cuberes et al. 2005](#), [Orozco Suarez et al. 2005](#), [Mathew et al. 2003](#), [Westendorp Plaza et al. 2001c](#)). Positive values indicate an increase of the magnetic field strength with geometrical depth. Studies which display the vertical field gradient as a function of the normalized radius of the sunspot also differ significantly. [Westendorp Plaza et al. \(2001c\)](#), [Borrero and Ichimoto \(2011\)](#) and [Orozco Suarez et al. \(2005\)](#) interpret the observations to say that the sunspot magnetic field forms canopy-like structures in the middle and outer penumbrae. In contrast, [Mathew et al. \(2003\)](#), [Sánchez Cuberes et al. \(2005\)](#), [Balthasar and Gömöry \(2008\)](#) merely conclude that the magnetic field increases with depth everywhere in the sunspot. [Tiwari et al. \(2013a\)](#) also do not find evidence for such a canopy-like structure in the outer penumbra.

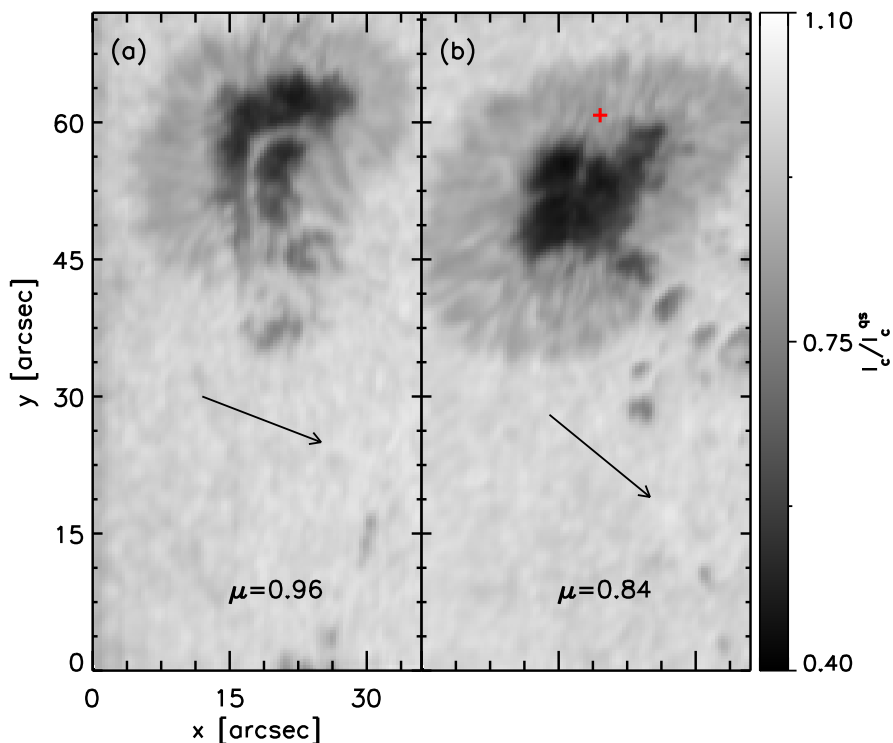


Figure 4.1: (a) Normalized continuum intensity I_c/I_c^{qs} map of the observed sunspot in AR NOAA 11124 observed on 14 November, 2010, recorded with VTT/TIP-2. I_c denotes continuum intensity and I_c^{qs} denotes averaged quiet Sun continuum intensity. (b) I_c/I_c^{qs} map of the same sunspot observed on 16 November, 2010. Arrows in both maps indicate the direction to disk center.

In the present chapter we study the radial dependence of the vertical gradient of the magnetic field strength of a sunspot observed on two different days by VTT/TIP-2 and of another sunspot observed by Hinode SOT/SP. To retrieve atmospheric parameters from VTT/TIP-2 data we carry out inversions of Stokes profiles of the Si λ 10827.1 Å and Ca λ 10833.4 Å spectral lines together. We also use prior spatially coupled inversions of the Hinode SOT/SP observations (i.e., the Fe λ 16301.5 Å and Fe λ 16302.5 Å lines) to determine the vertical field gradients. We compare the results from the different data sets with each other and with 3D MHD simulations of a sunspot by [Rempel et al. \(2009a\)](#) to understand the origin of the negative gradient of the magnetic field in the penumbra.

4.2 VTT/TIP-2 observations and analysis

4.2.1 Observations

We observed a leading sunspot in the active region NOAA 11124 on 14 and 16 November, 2010. Spectro-polarimetric observations were carried out at the German Vacuum Tower Telescope (VTT) with the Tenerife Infrared Polarimeter-2 (TIP-2, [Collados et al. 2007](#)). The spectral domain of the observations ranges from 10825 Å to 10835 Å and the spectral sampling corresponds to 10 mÅ per pixel. The diffraction limit of VTT at 10830 Å is

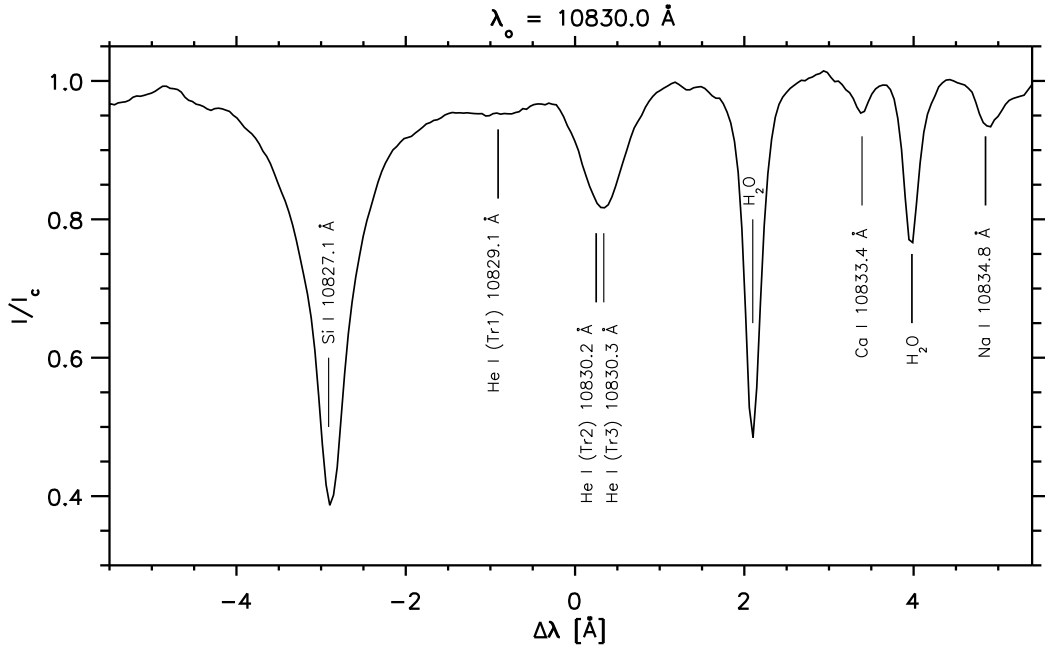


Figure 4.2: Averaged quiet Sun spectrum obtained with VTT/TIP-2 on 14 November, 2010. $\Delta\lambda = \lambda - \lambda_0$, where $\lambda_0 = 10830.0$.

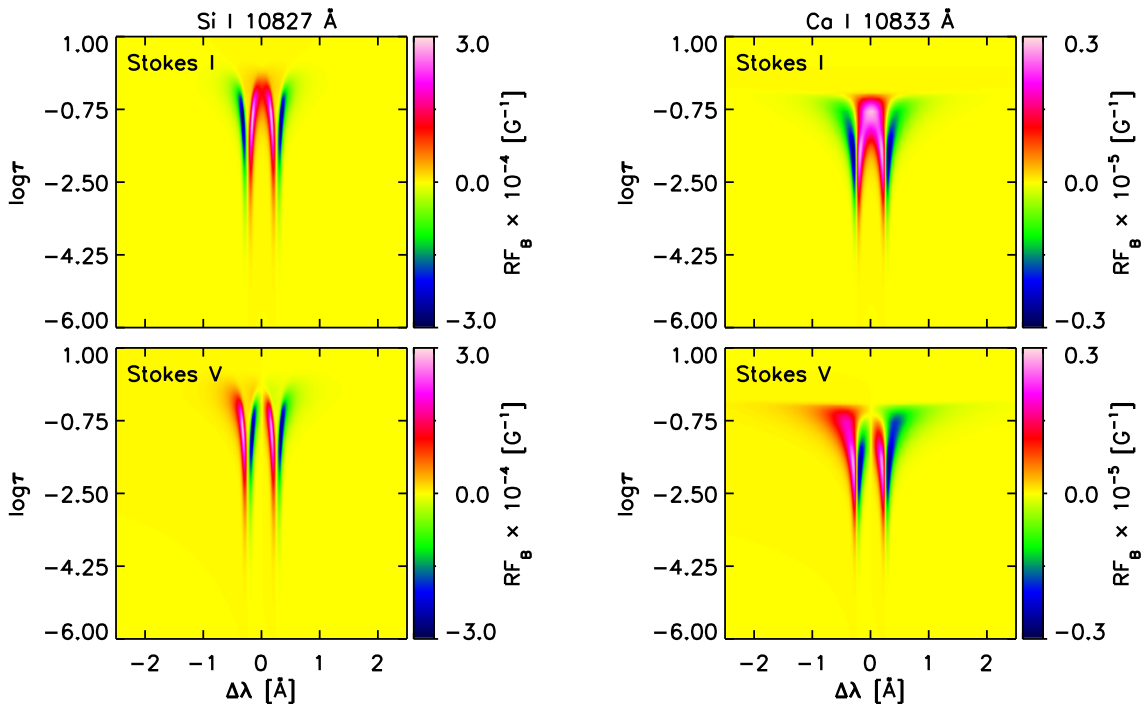


Figure 4.3: Magnetic field response functions (RFs) of the Si I 10827.1 Å (left) and Ca I 10833.4 Å (right) lines respectively, for Stokes *I* and *V* profiles (identified inside the panel). The shown RFs are estimated for an umbral atmosphere from a MHD simulations by [Rempel et al. \(2009a\)](#).

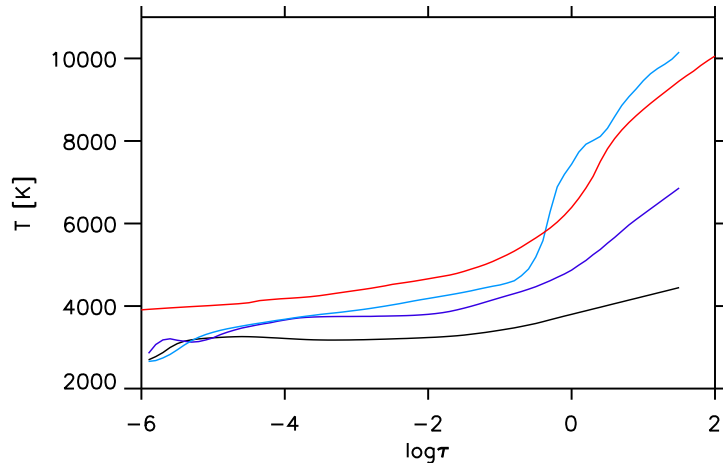


Figure 4.4: Temperature stratification of four atmospheres used to estimate response functions to magnetic field of the Si I 10827.1 Å and Ca I 10833.4 Å lines. *Black, dark blue* and *light blue* curves correspond to temperature profiles of an umbral, bright penumbral and dark penumbral pixel from the MHD simulations by Rempel et al. (2009a). The *red* curve corresponds to the HSRASP atmosphere (Chapman 1979).

Table 4.1: Line parameters.

Line	wavelength [Å]	$\log(gf)$	Abundance	g_{eff}
Si I	10827.1	0.210 [†]	7.549 [‡]	1.5
Ca I	10833.4	0.058 [§]	6.360 ^{§§}	1.5

[†] Shi et al. (2008)

[‡] Shchukina et al. (2012)

[§] We estimated this value of $\log(gf)$ for Ca I 10833.4 Å line by fitting the quiet Sun profile observed with a Fourier Transform Spectrometer (FTS) (Livingston and Wallace 1991, Wallace et al. 1993) using the HSRASP atmosphere (Chapman 1979).

^{§§} Grevesse and Sauval (1998)

approximately 0".40, but due to moderate seeing conditions spatial resolution of our data is estimated to be $\sim 1".0$. Scans of the field-of-view (FOV) for full Stokes vector measurements require ~ 20 minutes. The step-size for scanning was set to 0".36 and the pixel size in the slit direction was 0".16. In order to improve the signal-to-noise ratio we binned four pixels in the direction of dispersion and two pixels in slit direction. The heliocentric coordinates of the centers of the observed FOVs were (12°N, 10°W) on 14 November, 2010 and (14°N, 32°W) 16 November, 2010.

Panels (a) and (b) of Fig. 4.1 show the sunspot on 14 and 16 November, 2010, respectively, as observed in the continuum intensity at 10833 Å. The sunspot shows a light-bridge on 14 November, which disappeared after two days. In general, the sunspot has grown and matured in these two days, being more symmetric and simpler on 16 November, 2010. Fig. 4.2 displays the spectrum recorded on 14 November, 2010 after averaging

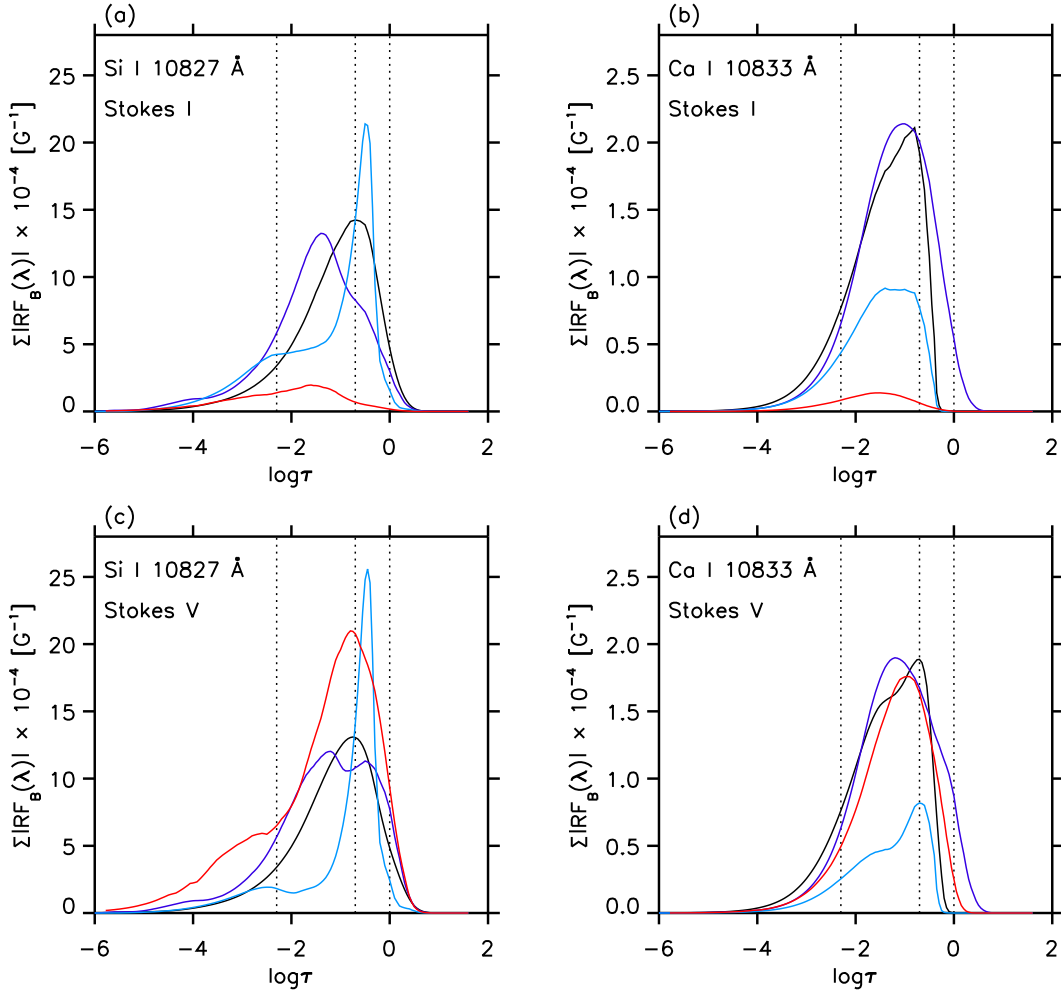


Figure 4.5: Wavelength integrated magnetic field response functions (RFs) of the Si I 10827.1 Å and Ca I 10833.4 Å lines. Panels (a) and (c) show RFs of Stokes I and V for Si I line. RFs of Stokes I and V for the Ca I line are displayed in Panels (b) and (d). The presented RFs are estimated for an umbral (*black*), dark penumbral (*dark blue*), bright penumbral (*light blue*) pixel and for the HSRASP atmosphere (*Red*). The three *dotted* vertical lines indicate positions of $\log \tau$ nodes used in SPINOR inversions (see Section 4.2.2).

over 225 quiet Sun pixels.

The collected data have been treated by applying the standard data reduction steps. The continuum level was corrected using an FTS spectrum (Livingston and Wallace 1991, Wallace et al. 1993).

4.2.2 SPINOR inversion of the Si I and Ca I lines

To analyze the photospheric properties of the sunspot's magnetic field we apply inversion of Stokes profiles of Si I 10827.1 Å and Ca I 10833.4 Å lines to solve the radiative transfer equations (RTEs) under the assumption of local thermodynamic equilibrium (LTE).

Although the Ca I line is rather weak (see Fig. 4.2), including it puts more constraints on the free parameters in the inversions process and gives more reliable atmospheres as

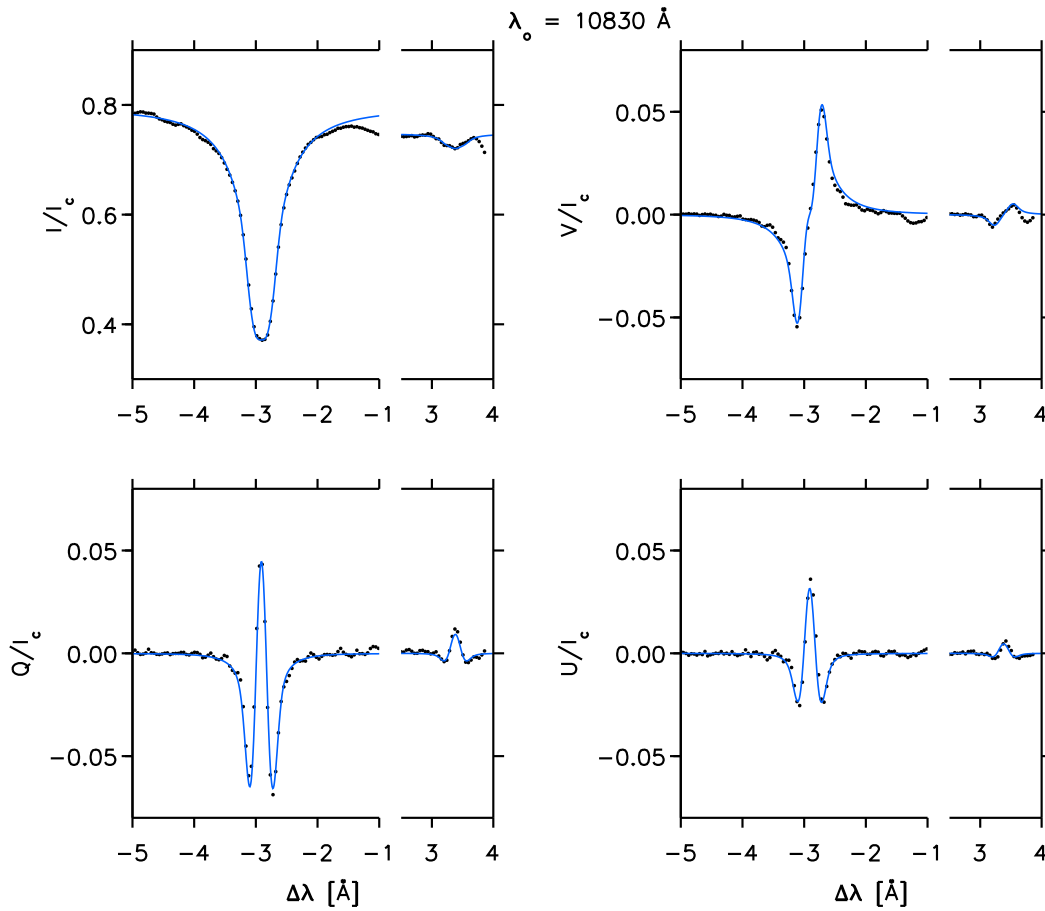


Figure 4.6: Best fit SPINOR inversions of sample Stokes profiles observed by VTT/TIP-2: *Dotted black* curves represent observed Stokes profiles and *solid blue* curves represent best fits. The position of Stokes profiles shown here is marked by a *red plus* sign in Fig. 4.1(b).

compared to inversions of the Si ι line alone. The line parameters of both lines are given in Table 4.1. Magnetic field response functions (RFs) of Stokes I and V profiles for both lines, estimated for an umbral atmosphere from a snapshot of the 3D MHD simulations of Rempel et al. (2009a), are shown in Fig. 4.3. We also estimated the magnetic field RFs for a bright and a dark penumbral atmosphere, also taken from the MHD simulations of Rempel et al. (2009a) along with the HSRASP atmosphere (Chapman 1979). Temperature stratifications of all four atmospheres used to estimate RFs are shown in Fig. 4.4. RFs integrated over the entire line profiles ($\Delta\lambda = \pm 2.0 \text{ \AA}$, but without neighboring lines) of Stokes I and V are presented in Fig. 4.5. It is evident from the RFs that the Ca ι line exhibits weaker response to the magnetic field compared to the Si ι line, mainly because it is weaker line, and covers a slightly smaller range in $\log \tau$. The RF of the Si ι line extends beyond $\log(\tau_{630}) = -3.0$, where τ_{630} corresponds to the optical depth at 630 nm¹. Note that such a λ -integrated RF is only a very rough guide for the heights at which the magnetic field is sampled.

¹ Reference wavelength for optical depth τ is chosen to be 630 nm throughout this chapter, to facilitate comparison with Hinode SOT/SP observations.

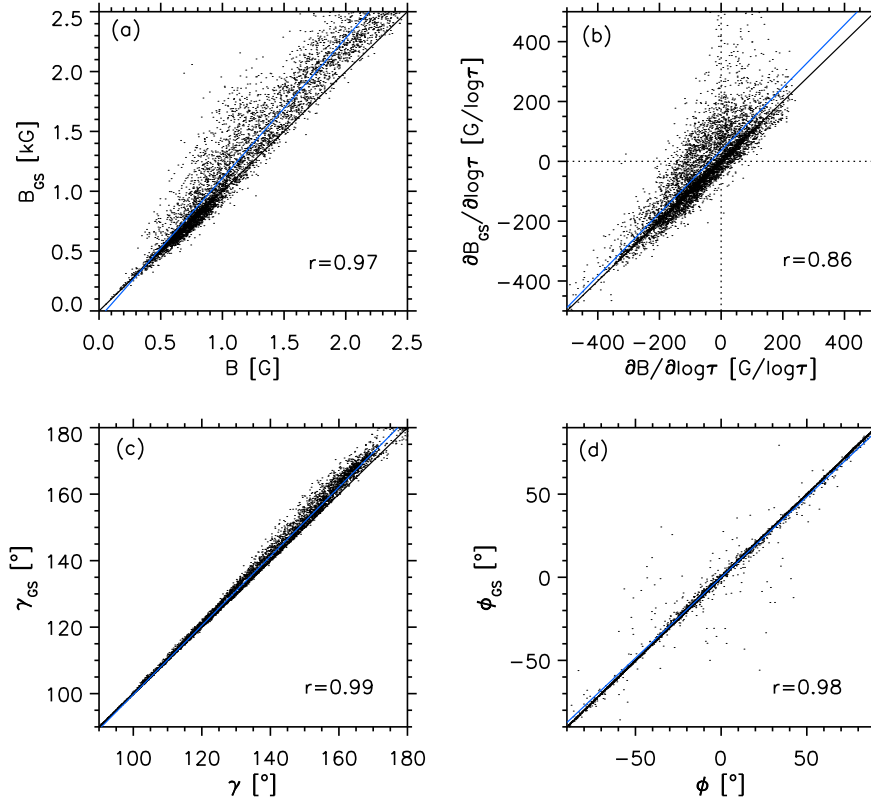


Figure 4.7: Scatter plots of the magnetic field components obtained from SPINOR inversions without considering straylight vs. those with considering straylight. The plotted data were obtained on 14 November, 2010 with VTT/TIP-2. Panels (a), (b), (c) and (d) show B , $\partial B/\partial \log \tau$, γ and ϕ , respectively. The *Blue* line in all panels represents the linear regression. The correlation coefficient, r , is shown at the *lower right* corner of each panel.

To retrieve atmospheric parameters in the photosphere, the SPINOR inversion code (Frutiger et al. 1999, 2000) has been used. The initial model atmosphere consists of a magnetic field strength, B , which varies linearly with $\log \tau$. Three nodes for the line-of-sight (LOS) velocity, v_{los} , and the temperature, T , have been used. The other atmospheric parameters such as inclination of the magnetic field relative to LOS, γ , azimuth direction, ϕ , micro-turbulent velocity, v_{mic} , have been forced to be constant with height. The three nodes used are at $\log \tau=0.0$, -0.7 and -2.3 . An example of observed Stokes profiles and best fitted Stokes profiles through SPINOR inversions is presented in Fig. 4.6. We have not considered any straylight correction when computing these profiles.

4.2.2.1 Influence of straylight

To examine the effect of straylight on the retrieved magnetic field vector and on the vertical gradient of B , we fitted the same atmospheric model with a second atmosphere component, representing the contribution of global straylight. By global straylight we mean that the straylight function does not vary spatially in the observed FOV. It is assumed to originate from the quiet Sun. The straylight contribution is denoted by a filling factor, α in following equation,

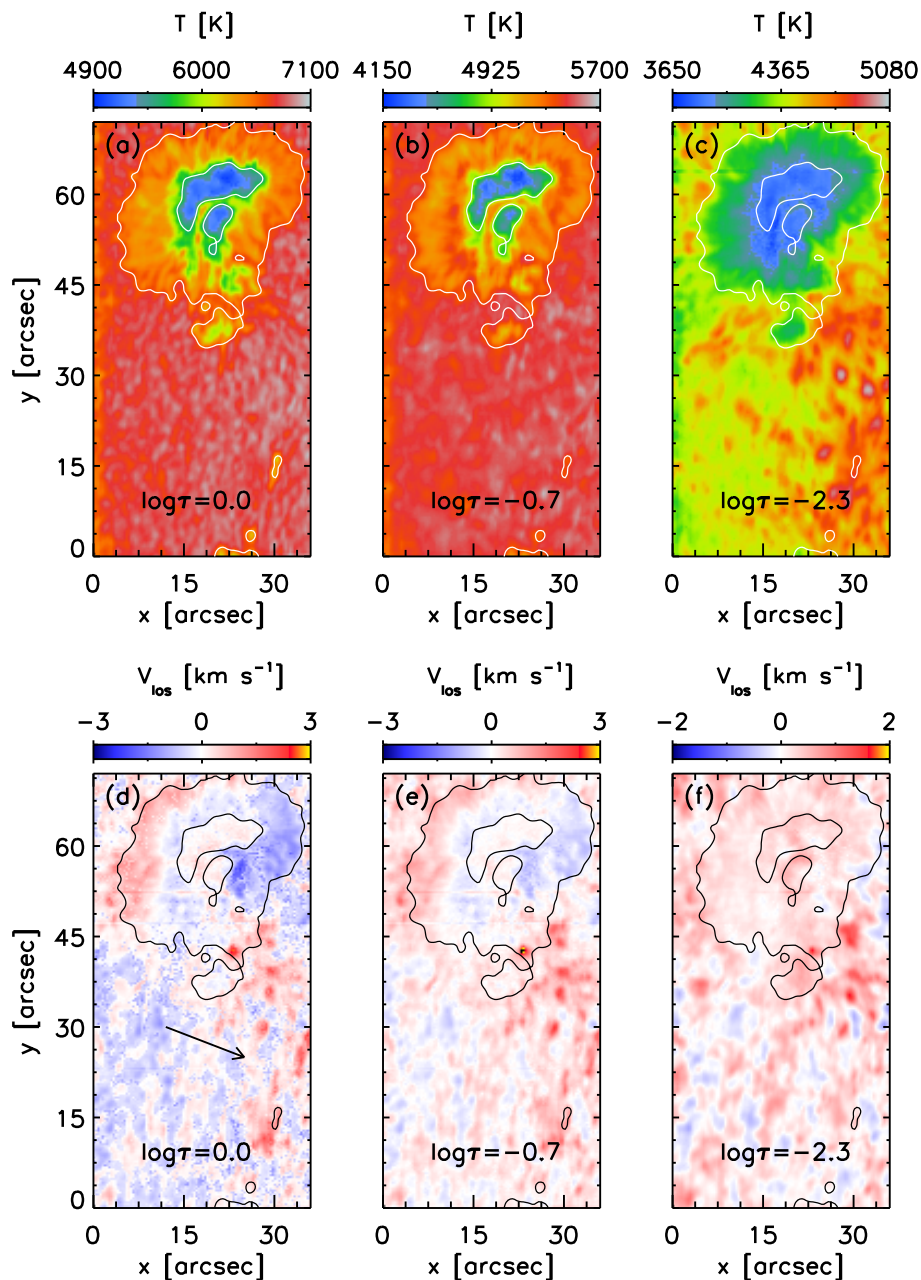


Figure 4.8: Panels (a), (b) and (c) represent maps of the temperature T at $\log \tau=0.0$, $\log \tau=-0.7$ and $\log \tau=-2.3$, respectively, as obtained by SPINOR inversions of the sunspot observed on 14 November, 2010. Panels (d), (e) and (f) show maps of line-of-sight (LOS) velocity v_{los} at the same $\log \tau$ values. Inner and outer contours represent the umbra-penumbra boundary and the outer boundary of the sunspot, respectively. *Arrow* in the panel (d) indicates the direction to disk-center.

$$I_O = (1 - \alpha)I_M + \alpha I_{GS}, \quad (4.1)$$

where I_O is the observed Stokes I parameter, I_M represents Stokes I of the magnetic component and I_{GS} is the Stokes I parameter of the straylight component. α is an additional free

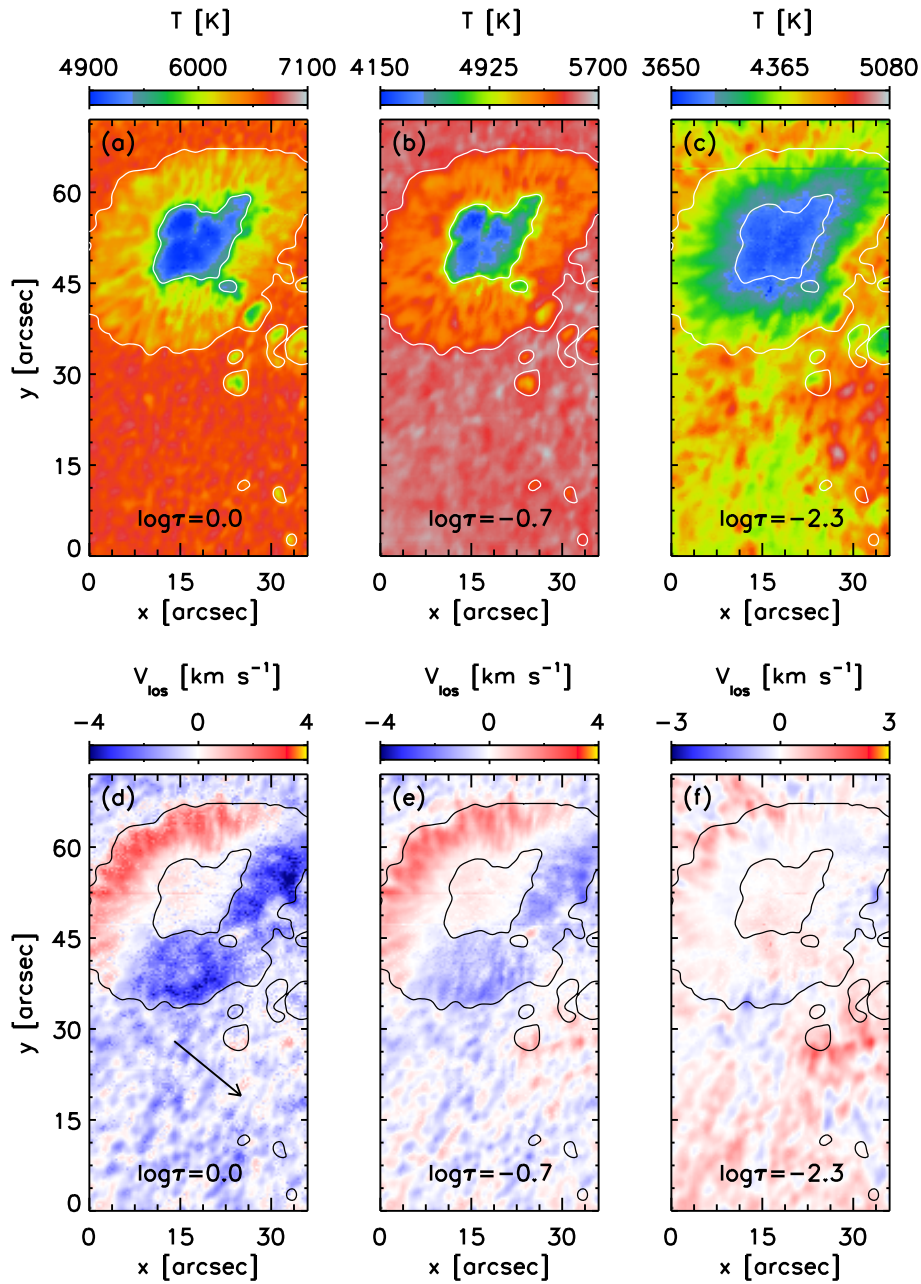


Figure 4.9: Same as Fig. 4.8, but for observations recorded on 16 November, 2010.

parameter in the inversions. We are aware that this is a simplified approach that neglects that the straylight decreases with distance from the quiet Sun and that in the penumbra, polarized straylight, probably, is important as well. This approach is taken purely for test purposes since the fits of synthesized Stokes profiles to the observed Stokes profiles are very good even without any consideration of straylight.

A comparison of the obtained magnetic field vectors inferred with and without straylight is presented in Fig. 4.7, showing very good correlation. Among all parameters the vertical gradient displays the least correlation (86%). Although B is somewhat underestimated (by 6% in the umbra) when straylight is not considered, we see negative and

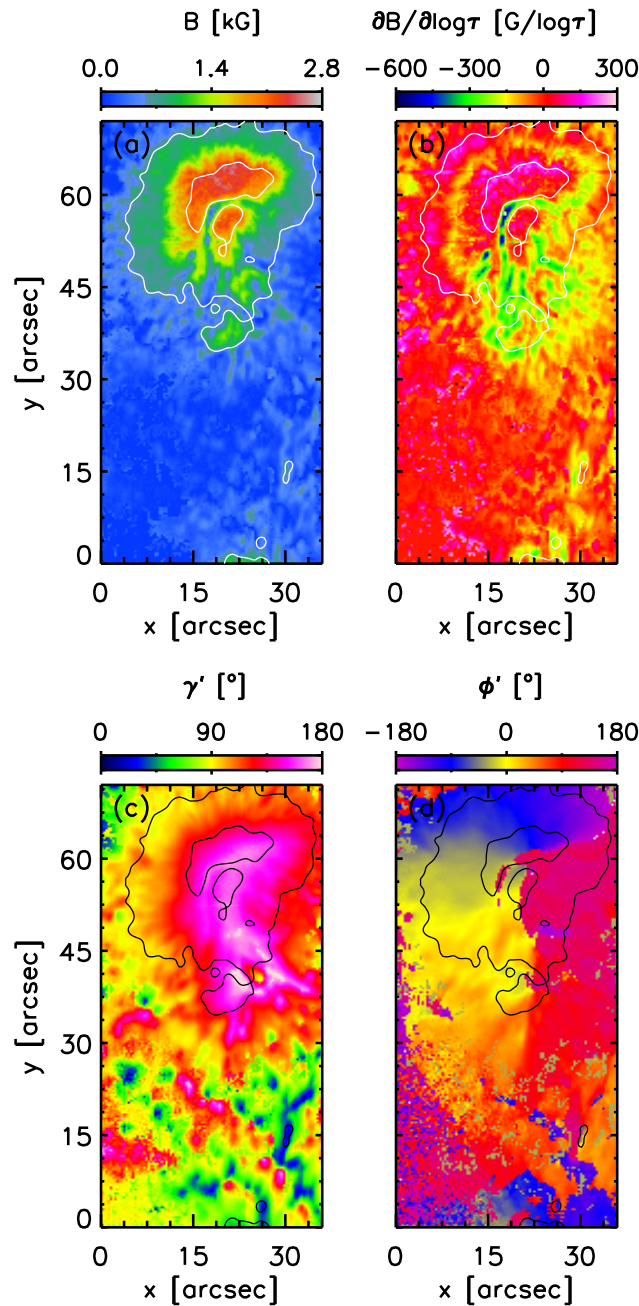


Figure 4.10: Magnetic field vector obtained from the observations recorded on 14 November, 2010 with VTT/TIP-2. (a) Magnetic field strength B , (b) gradient of the magnetic field strength with respect to $\log \tau$, $\partial B / \partial \log \tau$, (c) inclination angle, γ' , of the magnetic field vector and (d) azimuth direction, ϕ' , of the magnetic field vector.

positive vertical gradients of B in both approaches of inversion. This test suggests that neglecting straylight does not effect the qualitative structure of the vertical gradient of the magnetic field in the sunspot, although there are some quantitative differences. For the analysis presented in this chapter we therefore use the parameters retrieved from inversions neglecting the straylight contribution. For the Hinode/SOT data the influence of spatially inhomogeneous straylight is taken into account. For details see [van Noort \(2012\)](#).

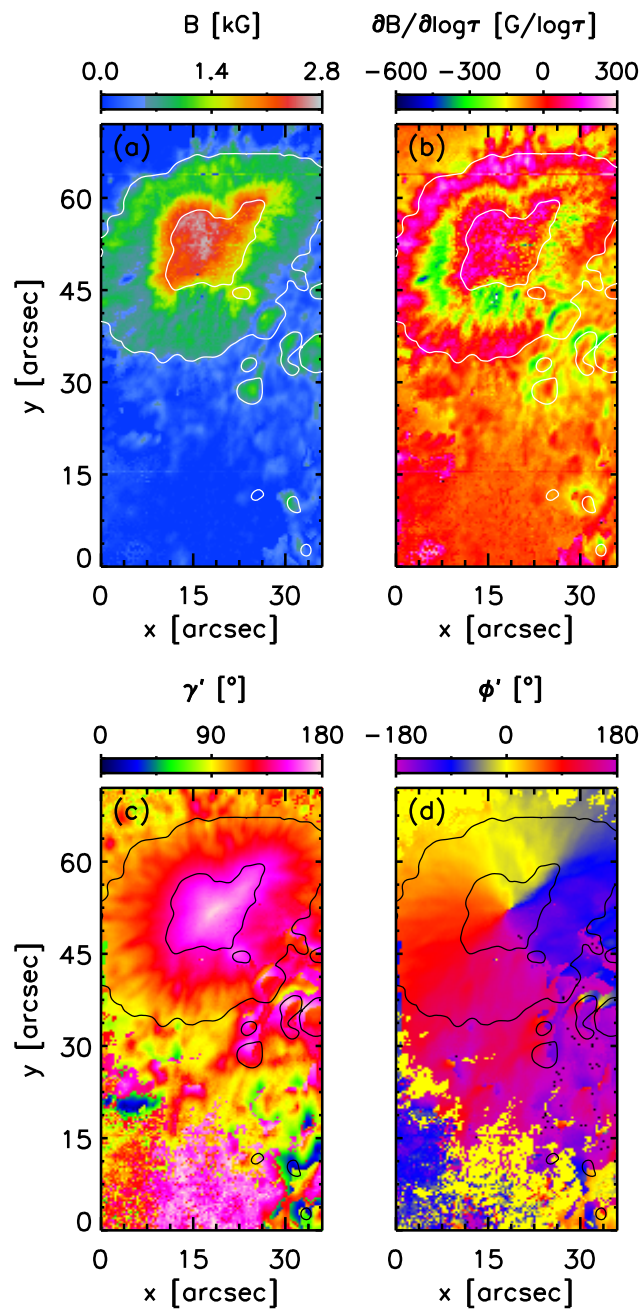


Figure 4.11: Same as Fig. 4.10, but for observations recorded on 16 November, 2010.

4.2.3 Inversion results

Fig. 4.8 depicts temperature and v_{los} maps retrieved from inversions of the observation recorded on 14 November, 2010. Inner and outer contours in all panels of Fig. 4.8 represent the umbra-penumbra boundary and the outer boundary of the sunspot.

Bard and Carlsson (2008) have shown that the line core of Si I 10827.1 Å is affected by non-local thermodynamic equilibrium (NLTE) conditions. They demonstrated that

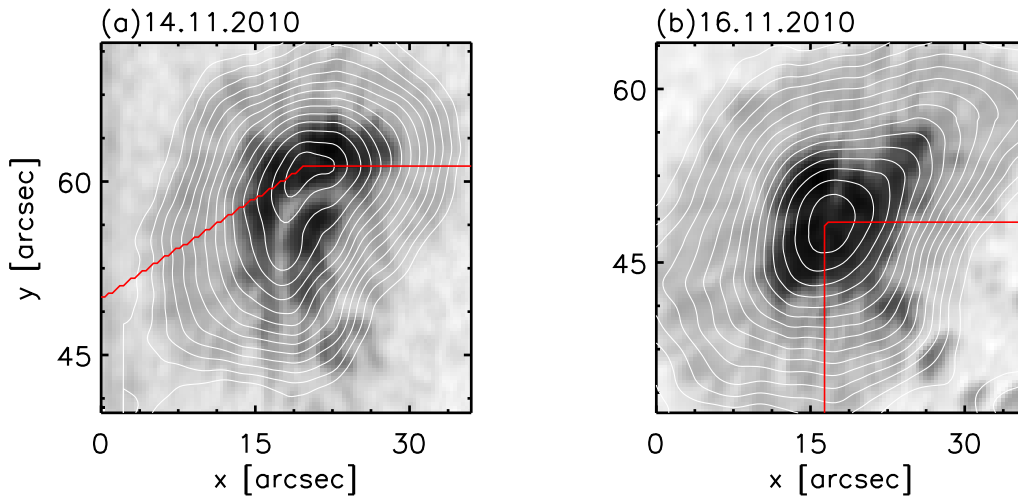


Figure 4.12: Continuum intensity maps from 14 November, 2010 (panel (a)) and 16 November, 2010 (panel (b)), with contours which are used to calculate azimuthal averages. The areas below the *red* lines were neglected because of the complex structure of the sunspot there.

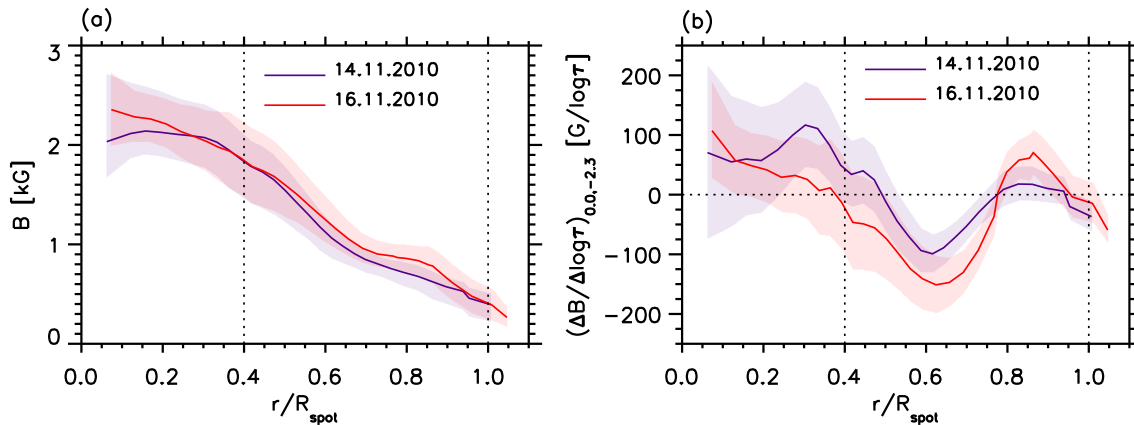


Figure 4.13: Azimuthally averaged parameters: Panel (a) shows radial dependence of B of the sunspot observed on 14 November, 2010 (*violet* curve) and 16 November, 2010 (*red* curve) with VTT/TIP-2. Panel (b) represents the vertical gradient of the magnetic field strength $(\Delta B/\Delta \log \tau)_{0.0,-2.3}$ as a function of r/R_{spot} . The colors of the curves in this panel are the same as in panel (a). *Shaded* areas represent standard deviations. *Dotted* vertical lines in both panels indicate the umbra-penumbra boundary and the outer boundary of the sunspot.

the line core intensity of Si I 10827.1 Å in NLTE conditions is lower than the line core intensity in LTE conditions. [Kuckein et al. \(2012a\)](#) studied the effect on atmospheric parameters inferred from neglecting NLTE conditions in inversions. They found that the most affected parameter is the temperature while the influence on the magnetic field vectors and velocities are negligible.

The zero level of v_{los} is calibrated by setting the average value of v_{los} at $\log \tau=0$ in the umbra to zero. The convective blueshift is estimated by fitting the line core of the averaged

quiet Sun profile of the Si I line. The obtained values of convective blueshift on 14 November, and 16 November, 2010 are $\sim 110 \text{ m s}^{-1}$ ($\mu = 0.96$) and $\sim 180 \text{ m s}^{-1}$ ($\mu = 0.84$), respectively. The larger blueshift at $\mu = 0.84$ is in line with the behavior of photospheric spectral lines (e.g. Balthasar 1984). The obtained values for the convective blueshift are also in agreement with findings of Kuckein et al. (2012b) who stated that the convective blue shift is very small for the Si I line, although they do not provide any number.

The temperature map at $\log \tau = -0.7$ for the 14 November, 2010 (see Fig. 4.8(b)) shows higher values in the inner penumbra compared to the outer penumbra. At $\log \tau = -2.3$ (see Fig. 4.8(c)) no signature of the light-bridge is visible in the temperature map. The v_{los} maps (Fig. 4.8(d)-(f)) show the Evershed flow pattern only at $\log \tau = 0.0$ and $\log \tau = -0.7$. The maximum values of the Evershed flow are 1.5 km s^{-1} and 1.0 km s^{-1} at $\log \tau = 0.0$ and $\log \tau = -0.7$, respectively.

Fig. 4.9 depicts the temperature and v_{los} maps of the same sunspot observed on 16 November, 2010. On this date the Evershed flow reached values up to 3.0 km s^{-1} and 2.5 km s^{-1} at $\log \tau = 0.0$ and $\log \tau = -0.7$, respectively.

Fig. 4.10 shows the magnetic field parameters retrieved from inversions of the observations from 14 November, 2010. Panels (a) and (b) display maps of B and $\partial B / \partial \log \tau$, i.e. $\partial B / \partial \log \tau$ at $\log \tau = 0.0$ of the observed FOV, respectively. Inclination and azimuth angles of magnetic field vectors are presented in panels (c) and (d). The magnetic field vectors presented here are projected to disk center coordinates using the transformation matrix given by Wilkinson et al. (1989). The 180° ambiguity in azimuth direction is resolved by the "acute angle" method (Sakurai et al. 1985, Cuperman et al. 1992). Inclination and azimuth angle of \mathbf{B} after projection to the solar disk center coordinates are denoted by γ' and ϕ' , respectively. Magnetic field parameters obtained from the observations recorded on 16 November, 2010 are shown in Fig. 4.11. Whereas on 14 November the maximum B amounts to $\sim 2500 \text{ G}$ and appears in the darkest part of the umbra, it increases up to $\sim 2800 \text{ G}$ two days later. Maps of $\partial B / \partial \log \tau$ show consistent results on both days. In the umbra $\partial B / \partial \log \tau$ is positive, i.e. B increases with optical depth. In the undisturbed part of the inner and middle penumbra the gradient maps show a ring-like structure where $\partial B / \partial \log \tau < 0$, i.e. B decreases with optical depth. In the outer penumbra $\partial B / \partial \log \tau > 0$ and just outside the visible boundary of the sunspot, again $\partial B / \partial \log \tau < 0$.

To study the radial dependence of the properties of the sunspot atmosphere, we use azimuthal averages of all parameters. The azimuthal averages are computed along 25 isothermal contours obtained from a smoothed temperature map at $\log \tau = -2.3$ (see panels (a) and (b) of Fig. 4.12). We do not consider the parts of the penumbra below the *red* lines shown in Fig. 4.12(a) and (b), since the field structure there is strongly disturbed.

The radial dependences of B and $(\Delta B / \Delta \log \tau)_{0.0, -2.3}$ are displayed in Fig. 4.13. Formula of $(\Delta B / \Delta \log \tau)$ is shown below.

$$\left(\frac{\Delta B}{\Delta \log \tau} \right)_{a,b} = \frac{(\Delta B)_{a,b}}{(\Delta \log \tau)_{a,b}} = \frac{B(b) - B(a)}{b - a}, \quad (4.2)$$

where a and b denote lower and upper $\log \tau$ surfaces, respectively.

On 14 (16) November, $(\Delta B / \Delta \log \tau)_{0.0, -2.3}$ has a value of 120 (100) $\text{G} / \log \tau$ on average in the darkest part of umbra with a maximum amplitude of 185 (175) $\text{G} / \log \tau$. In the inner penumbra, i.e. from $r = 0.4 R_{\text{spot}}$ to $r \approx 0.75 R_{\text{spot}}$, $(\Delta B / \Delta \log \tau)_{0.0, -2.3} < 0$ with an average rate of -90 (-150) $\text{G} / \log \tau$. Between $r \approx 0.75 R_{\text{spot}}$ and $r = R_{\text{spot}}$ the $(\Delta B / \Delta \log \tau)_{0.0, -2.3} > 0$.

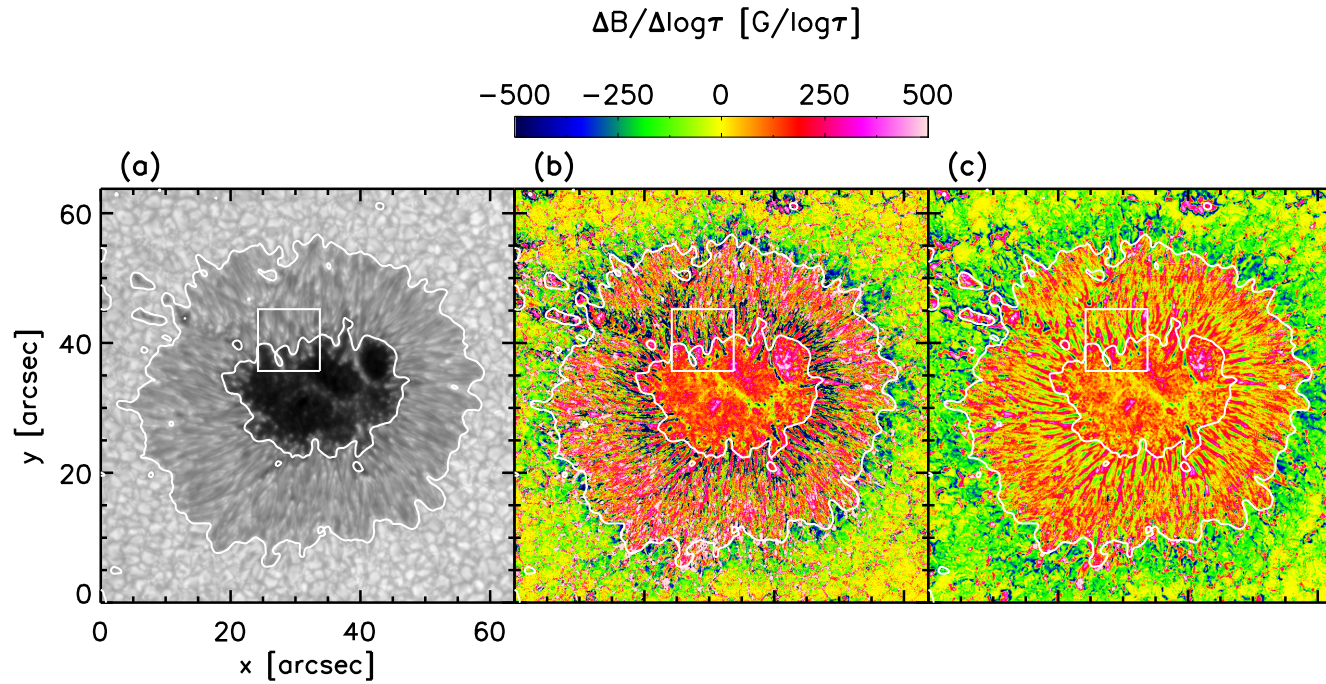


Figure 4.14: Continuum intensity (panel (a)) and $(\Delta B / \Delta \log \tau)$ maps of a sunspot in active region NOAA 10933, observed with Hinode SOT/SP. Panels (b) and (c) represents $(\Delta B / \Delta \log \tau)_{0.0, -0.9}$ and $(\Delta B / \Delta \log \tau)_{-0.9, -2.5}$, respectively. Both $(\Delta B / \Delta \log \tau)$ maps are displayed in the same scale shown by the color-bar at the top of panel (b). Inner and outer contours in all panels represents the umbra-penumbra boundary and the outer boundary of the sunspot, respectively.

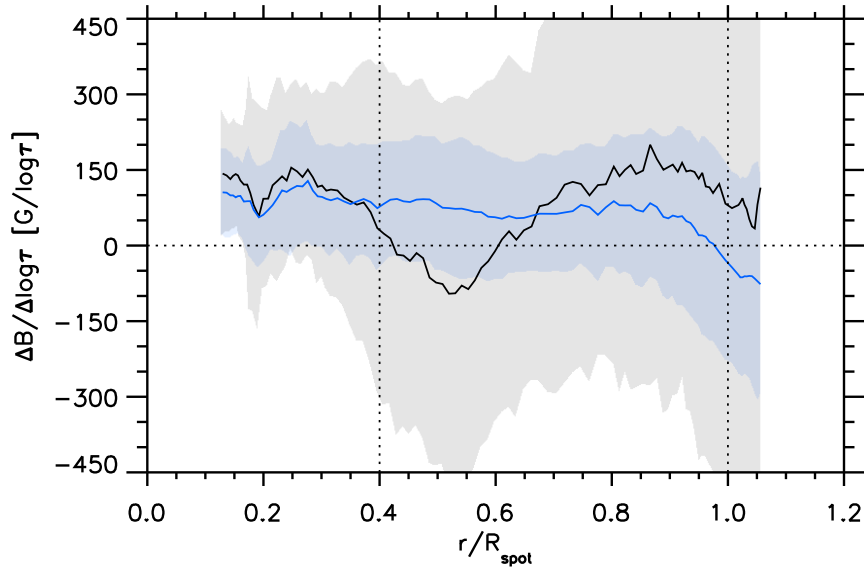


Figure 4.15: Azimuthally averaged $(\Delta B/\Delta \log \tau)$ as a function of normalized radial distance r/R_{spot} , from the center of the sunspot observed with SOT/SP. *Black* and *blue* curves depict $(\Delta B/\Delta \log \tau)_{0.0,-0.9}$ and $(\Delta B/\Delta \log \tau)_{-0.9,-2.5}$, respectively. *Shaded* areas represent the standard deviations. *Dotted* vertical lines indicate the umbra-penumbra boundary and the outer boundary of the sunspot.

4.3 Hinode SOT/SP observations

Low spatial resolution observations of a sunspot can lead to under- or overestimation of B and $(\Delta B/\Delta \log \tau)$ due to unresolved multiple magnetic components with different orientation of the magnetic vector within the resolution elements. The unexpected result that B decreases with optical depth in the inner penumbra leads to the question if this outcome is a spurious result of the low spatial resolution of the VTT/TIP-2 data.

To answer this question we analyze high spatial resolution Hinode SOT/SP observations. SOT/SP records full Stokes profiles of the Fe I 6301.5 Å and Fe I 6302.5 Å spectral lines. The SOT/SP observations analyzed here belong to active region NOAA 10933, which were taken on January 5, 2007 close to disk center (5°N, 2°W). This data set has been inverted by [Tiwari et al. \(2013a\)](#) and [van Noort et al. \(2013\)](#) and we employ atmospheric parameters retrieved from them. These authors used the spatially coupled inversion technique of [van Noort \(2012\)](#) to infer atmospheric parameters. The particular inversion considered here has been performed with an enhanced spatial sampling of 0".08, compared to 0".16 of the original Hinode SOT/SP (see, [van Noort et al. 2013](#)).

The initial atmospheric model used by [Tiwari et al. \(2013a\)](#) consists of three nodes each for T , v_{los} , B , γ , ϕ and v_{mic} . The three nodes are at $\log \tau = 0.0$, -0.9 and -2.5 .

Fig. 4.14 shows the map of continuum intensity and $(\Delta B/\Delta \log \tau)$ maps. The map of $(\Delta B/\Delta \log \tau)_{0.0,-0.9}$ (panel (b)) shows patches of negative values in the inner penumbra, i.e. at these locations B decreases with optical depth. Patches of negative values also exist in the map of $(\Delta B/\Delta \log \tau)_{-0.9,-2.5}$, the upper² layer (see panels (c) of Fig. 4.14), but they

²We call the atmosphere between $\log \tau = 0$ and -0.9 as lower and between $\log \tau = -0.9$ and -2.5 as upper layer of photosphere.

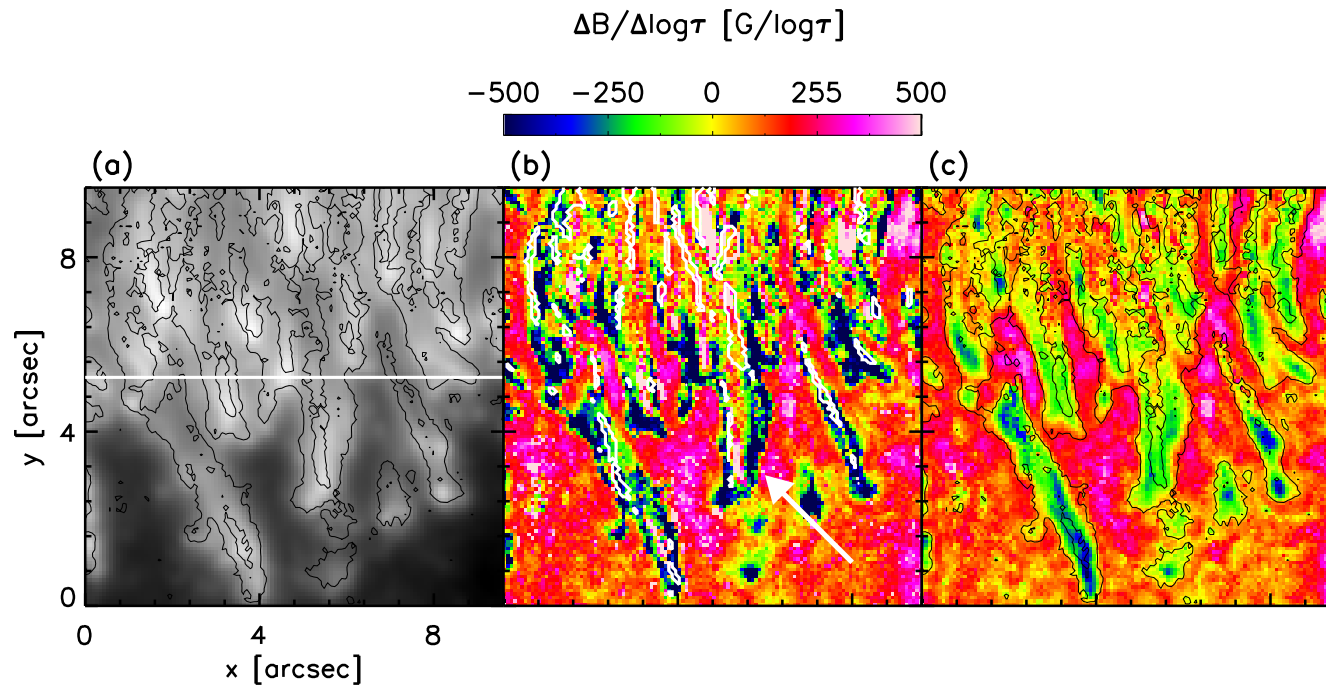


Figure 4.16: Same as figure 4.14, but only showing the area within the *white* box in panel (a) of Fig. 4.14. *Black* contours in the panels (a) and (c) encircle negative $(\Delta B/\Delta \log \tau)_{0.0,-0.9}$ and *white* contours in the panel (b) indicate areas of polarity opposite to that in the umbra.

are smaller in number and with lower amplitude. Just outside the visible boundary of the sunspot there are patches of $(\Delta B/\Delta \log \tau) < 0$ which makes a ring-like structure and expands outward with height.

To derive the dependence of $(\Delta B/\Delta \log \tau)$ on the radial distance from the sunspot center we use the same method as applied to the VTT/TIP-2 data (see Section 4.2.3). The radial dependence of $(\Delta B/\Delta \log \tau)_{0.0,-0.9}$ shows a qualitative similarity with that of $(\Delta B/\Delta \log \tau)_{0.0,-2.3}$ found from the VTT/TIP-2 observations. Quantitatively, the values retrieved from the SOT/SP observations are higher: in the umbra the average value of $(\Delta B/\Delta \log \tau)_{0.0,-0.9}$ is found to be $150 \text{ G}/\log \tau$ (see Fig. 4.15). In the inner penumbra, between $r \simeq 0.4R_{\text{spot}}$ and $r \simeq 0.6R_{\text{spot}}$, $(\Delta B/\Delta \log \tau)_{0.0,-0.9}$ is negative, with the maximum negative value of $80 \text{ G}/\log \tau$ at $r=0.5R_{\text{spot}}$. $(\Delta B/\Delta \log \tau)_{0.0,-0.9}$ is positive beyond $r \simeq 0.6R_{\text{spot}}$. $(\Delta B/\Delta \log \tau)_{-0.9,-2.5}$ amounts to $120 \text{ G}/\log \tau$ on average in the umbra and remains positive also in the penumbra. Outside the boundary of the sunspot on average $(\Delta B/\Delta \log \tau)_{-0.9,-2.5}$ is negative.

The maps of $(\Delta B/\Delta \log \tau)$ are highly structured which can be seen in Fig. 4.16, showing a zoomed-in version of Fig. 4.14. Contours in panels (a) and (c) of Fig. 4.16 separate patches with negative and positive values of $(\Delta B/\Delta \log \tau)_{0.0,-0.9}$. It is evident that the patches where $(\Delta B/\Delta \log \tau) < 0$ mostly coincides with bright filaments. $(\Delta B/\Delta \log \tau)$ has higher values in the lower layer (panel (b)) compared to the upper layer (panel (c)). The largest negative $(\Delta B/\Delta \log \tau)$ values present near the edges of the filaments. $(\Delta B/\Delta \log \tau)$ shows also fine structure within the body of individual filaments. Most parts of the filaments display $(\Delta B/\Delta \log \tau)_{0.0,-0.9} < 0$ while at the centers of filaments $(\Delta B/\Delta \log \tau)_{0.0,-0.9}$ is positive (indicated by an arrow in panel (b) of Fig. 4.16). This substructure of the gradient only exists in the lower layer whereas in the upper layer the filaments have mostly negative $(\Delta B/\Delta \log \tau)_{-0.9,-2.5}$. Contours colored in *white* in panel (b) of Fig. 4.16 show locations where the polarity of B is opposite to that of the umbra. Narrow patches of opposite polarity are co-located with the patches of $(\Delta B/\Delta \log \tau) < 0$. The opposite polarity patches are narrower than the patches where $(\Delta B/\Delta \log \tau)_{0.0,-0.9} < 0$.

Is this a generic property of filaments? To answer this question we analyzed the properties of the averaged filament constructed by Tiwari et al. (2013a). They averaged 60 penumbral filaments, 20 each from the inner, middle and outer penumbra. Prior to averaging they straighten all filaments and then normalized their lengths. The inner, middle and outer filaments exhibit strong similarities in all physical properties, such as the plasma flow and the magnetic field (Tiwari et al. 2013a). The temperature structure is also similar, but does show some changes with the radial distance from the sunspot center.

Averaged physical properties of filaments are displayed in Fig. 4.17. The structure of $(\Delta B/\Delta \log \tau)$ of the averaged filament is similar to that noticed in individual filaments (see Fig. 4.16), although much smoother. The inner (i.e. near umbra) half ($x < 0.5$ in Fig. 4.17) of the filament has $(\Delta B/\Delta \log \tau)_{-0.9,-2.5} < 0$. At the center, along the axes of the filament $(\Delta B/\Delta \log \tau)_{-0.0,-0.9} > 0$. The outer half ($x > 0.5$) has $(\Delta B/\Delta \log \tau)_{-0.9,-2.5} > 0$.

Fig. 4.18 displays $(\Delta B/\Delta \log \tau)_{0.0,-0.9}$ and I_c/I_c^{qs} , along a slit (see Fig. 4.16) in the penumbra cutting across penumbral filaments. I_c and I_c^{qs} represents continuum intensity and averaged continuum intensity in the quiet Sun, respectively. Along the slit positive and negative patches of $(\Delta B/\Delta \log \tau)_{0.0,-0.9}$ are present equally. $(\Delta B/\Delta \log \tau)_{0.0,-0.9}$ at the location of penumbral filaments has negative values with larger magnitudes than the positive $(\Delta B/\Delta \log \tau)_{0.0,-0.9}$ of the dark background. Hence, azimuthal average of

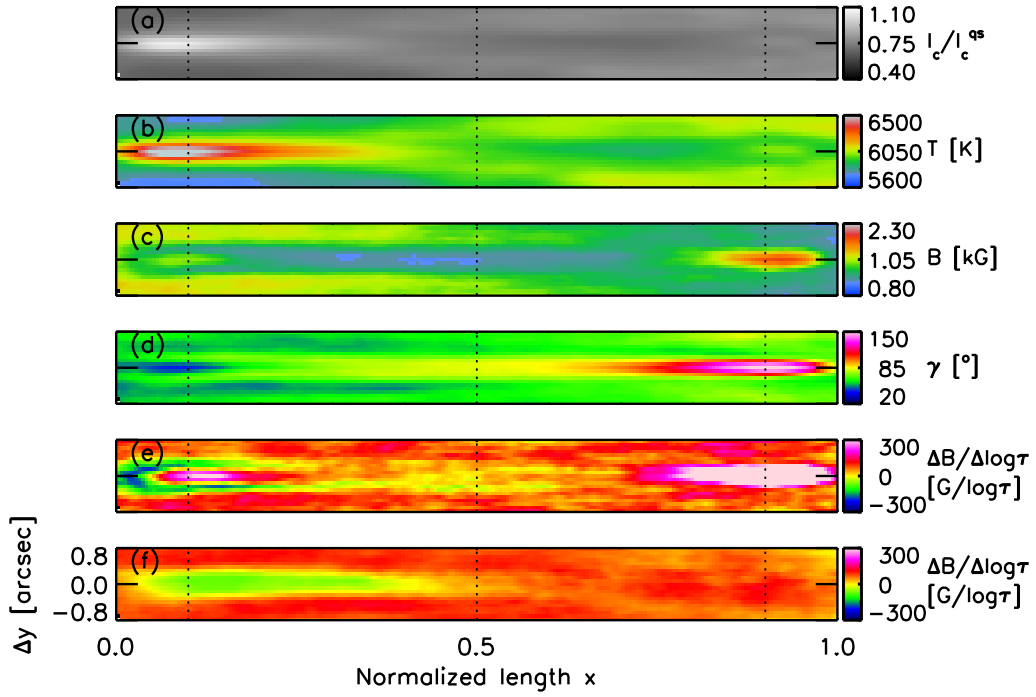


Figure 4.17: Physical properties of the standard filament from [Tiwari et al. \(2013a\)](#). (a) Continuum intensity normalized to the quiet Sun continuum; (b) T at $\log \tau=0.0$; (c) B at $\log \tau=0.0$; (d) γ at $\log \tau=0.0$; (e) $(\Delta B/\Delta \log \tau)_{0.0,-0.9}$ and (f) $(\Delta B/\Delta \log \tau)_{-0.9,-2.5}$. Left- and rightmost parts of the panels corresponds to the inner and outer part of the filament, respectively.

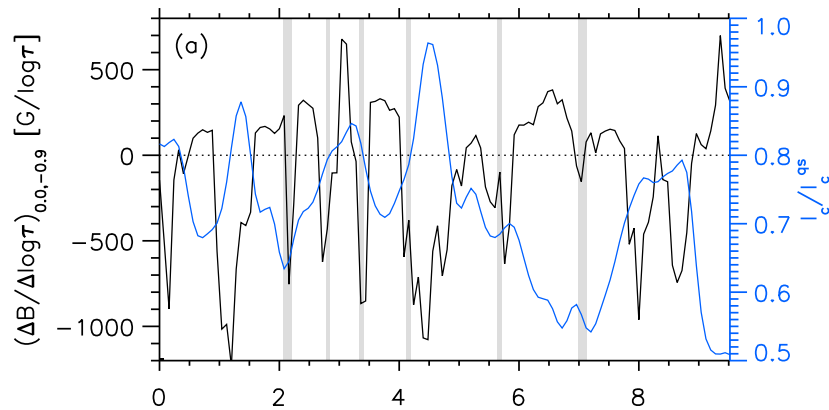


Figure 4.18: Fluctuations of I_c/I_c^{qs} (blue curve), $(\Delta B/\Delta \log \tau)_{0.0,-0.9}$ (black curve) along a slit shown in Fig 4.16(a). Gray shaded areas corresponds to position of polarity opposite to that in the umbra.

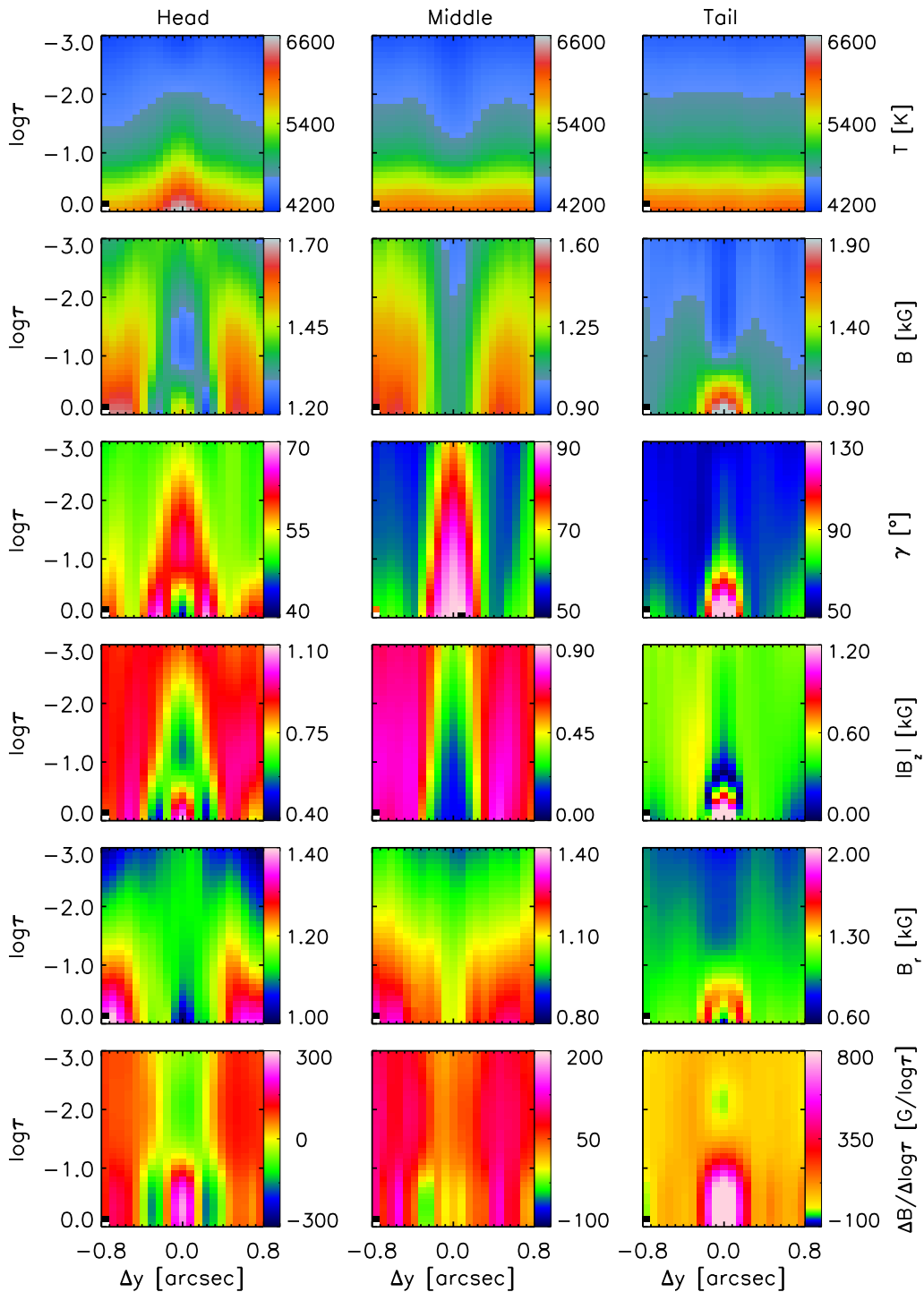


Figure 4.19: Optical depth stratification of various physical parameters of the standard filament displayed in Fig. 4.17 perpendicular to its axis. Panels in the first, second and third column represent the head, middle and tail of the filament respectively. From top to bottom (for each column): T , B , γ , the vertical component of magnetic field B_z , the radial component of magnetic field B_r and $(\Delta B / \Delta \log \tau)$. The head, middle and tail positions are marked by *dashed* vertical lines in Fig. 4.17.

$(\Delta B/\Delta \log \tau)_{0.0,-0.9}$ turns out to be negative in the inner penumbra.

To figure out the penumbral magnetic field structure which can produce such a magnetic field gradient, it is important to see how the magnetic field is stratified with optical depth. The optical depth stratification of various physical parameters is shown in Fig. 4.19. The positions of the stratified atmosphere displayed in Fig. 4.19 are indicated by *dashed* vertical lines in Fig. 4.17. If one looks at the head of the filament (panels in the first column of Fig. 4.19), it is clear that at the center of the filament ($\Delta y=0''$) B becomes weaker and more horizontal between $\log \tau=-0.9$ and $\log \tau=-2.5$ compared to the atmospheric layer below $\log \tau=-0.9$ and those above $\log \tau=-2.5$. Between $\log \tau=-0.9$ and $\log \tau=-2.5$ the vertical component of the magnetic field, B_z , also becomes weaker, whereas the radial component of the magnetic field, B_r , becomes stronger. Thus, between $\log \tau=-0.9$ and $\log \tau=-2.5$ the magnetic field is weaker and more horizontal and is surrounded by stronger and more vertical magnetic field. At the edge ($\Delta y \simeq \pm 0.4''$) of the filament head, B is horizontal and weaker in the deeper atmosphere and becomes more vertical and stronger in upper atmosphere. The more vertical and stronger field in the upper part of the atmosphere is thought to be field from the surrounding spines, expanding and closing above the filament. This might explain why we see $(\Delta B/\Delta \log \tau) < 0$ at the location of the filament.

At the middle and tail part of the filament (second and third columns of panels in Fig. 4.19) the horizontal field at the filament center is stronger compared to the relatively more vertical field overlying the horizontal field of the filament. Hence at the middle and tail part of the bright filament $(\Delta B/\Delta \log \tau) > 0$.

4.4 Comparison with 3D MHD simulations

To better understand the origin of the $(\Delta B/\Delta \log \tau)_{0.0,-0.9} < 0$ in sunspot penumbrae detected in the VTT/TIP-2 and SOT/SP observations, we analyzed a snapshot from 3D MHD simulations of a sunspot by Rempel et al. (2009a); cf. Rempel (2011). The advantage of studying the MHD simulations is that we can determine the gradient on a geometrical depth scales (which is more natural for magnetic field), rather than optical depth. Fig. 4.20 shows a continuum intensity map and maps of $(\Delta B/\Delta d)$ calculated for the depth intervals, $d - d_{\text{photo}}=288$ km to 144 km, $d - d_{\text{photo}}=144$ km to 0 km, and $d - d_{\text{photo}}=0$ km to -144 km. Here d denotes the geometrical depth (i. e. d increases into the Sun) and d_{photo} denotes the average geometrical depth of the quiet Sun photosphere at $\log \tau=0$. The $\log \tau=0$ surface in the penumbra in the MHD simulations is on average ~ 300 km deeper than in the quiet Sun, so we do not look at gradients of B below $d - d_{\text{photo}}=300$ km. There are patches where $(\Delta B/\Delta d) < 0$ in the middle and outer penumbra between $d - d_{\text{photo}}=288$ km and 144 km. This is due to the fact that the penumbra is rather shallow in the MHD simulations and $d - d_{\text{photo}}=288$ km is still below the vertical extension of the middle and outer penumbra. We see very few patches where $(\Delta B/\Delta d) < 0$ in the upper two layers compared to the Hinode SOT/SP and VTT/TIP-2 observations. This is also visible in the azimuthal averages of $(\Delta B/\Delta d)$, see Fig. 4.21 which shows an absence of $(\Delta B/\Delta d) < 0$ in the upper layers ($d - d_{\text{photo}}=144$ km to 0 km and $d - d_{\text{photo}}=0$ km to -144 km) within the sunspot while the lower layer ($d - d_{\text{photo}}=288$ km to 144 km) exhibit negative values of $(\Delta B/\Delta d)$ in the middle and outer penumbra. The uppermost layer shows $(\Delta B/\Delta d) < 0$ outside the bound-

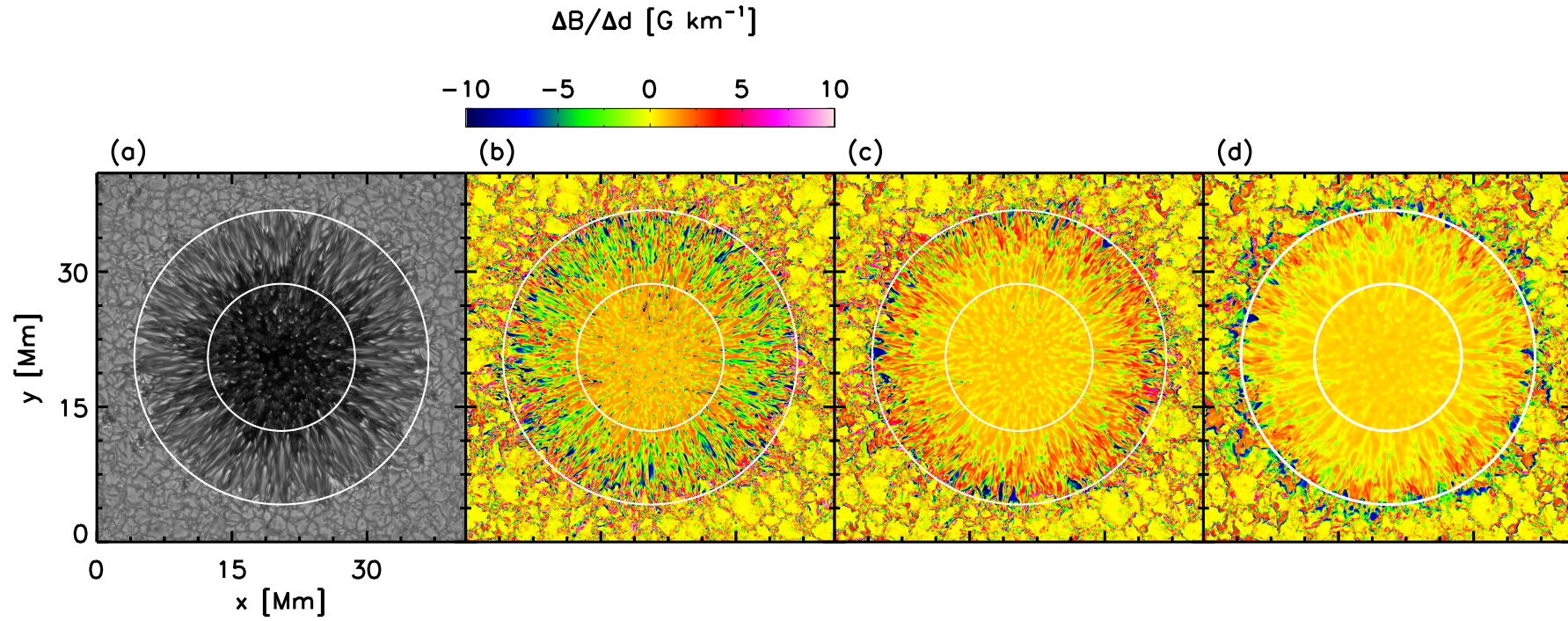


Figure 4.20: Continuum intensity (panel (a)) and $(\Delta B/\Delta d)$ maps from a 3D MHD simulations of a sunspot by [Rempel et al. \(2009a\)](#). Panels (b), (c) and (d) show $(\Delta B/\Delta d)$ estimated between $d - d_{\text{photo}} = 288$ km and 144 km, $d - d_{\text{photo}} = 144$ km and 0 km and $d - d_{\text{photo}} = 0$ km and -144 km, respectively. All $(\Delta B/\Delta d)$ maps are displayed in the same scale shown by the color-bar at the top of panel (b). *White* circles in all panels represent the umbra-penumbra boundary and the outer boundary of the sunspot.

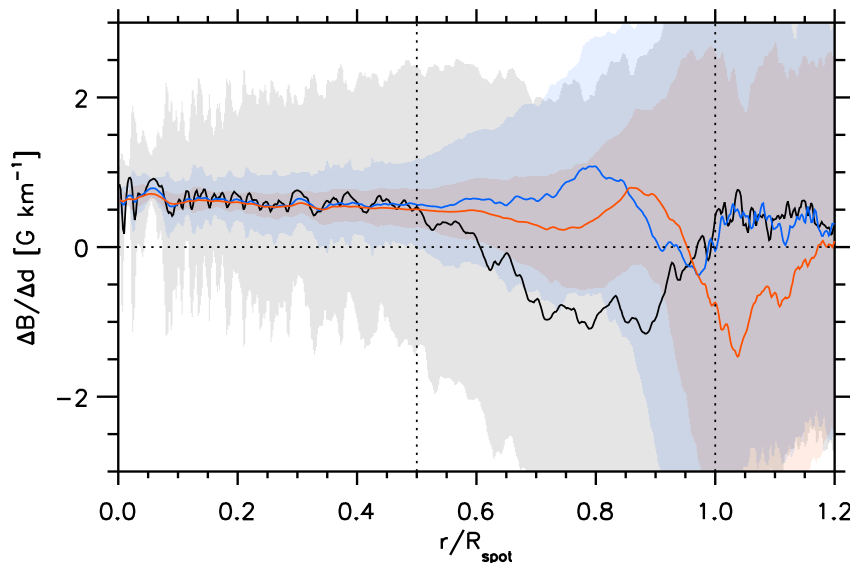


Figure 4.21: Azimuthally averaged $(\Delta B/\Delta d)$ as a function of normalized radial distance r/R_{spot} , from the 3D MHD simulations. *Black, blue and red* curves depict $(\Delta B/\Delta d)$ estimated between $d - d_{\text{photo}}=288$ km and 144 km, $d - d_{\text{photo}}=144$ km and 0 km and $d - d_{\text{photo}}=0$ km and -144 km. *Shaded* areas represent standard deviations. *Dotted* vertical lines indicate the umbra-penumbra boundary and the outer boundary of the sunspot.

ary of the sunspot. The shaded areas in Fig. 4.21 show standard deviations of $(\Delta B/\Delta d)$ along the circles which are used to estimate azimuthal averages.

As mentioned above, the uppermost layers in the MHD simulations do not show negative gradient (in geometrical depth scales) in the inner penumbra. Whereas the SOT/SP and VTT/TIP-2 observations show that the vertical gradient (in optical depth scales) of the inner penumbra is negative in the azimuthal averages. There are multiple possible reasons for such a discrepancy between the MHD simulations and the observations:

1. The gradients of B related to geometrical depth may not be directly comparable to gradients at a given optical depth (since iso-optical depth surfaces are strongly corrugated).
2. There are shortcomings in the simulations, which lead to departure from realism in the synthetic sunspot's magnetic structure.
3. The inversions of the observed Stokes profiles may be imperfect regarding the magnetic structure, although the inversions of the two rather different data sets (different spectral lines, different spatial resolution, ground-based vs. space-borne, etc.) followed different approaches (straylight and PSF removed vs. non consideration of straylight), result in qualitatively similar magnetic field gradients.

For a closer comparison of the MHD atmosphere with the VTT/TIP-2 and SOT/SP observations, we consider point (1): we computed $(\Delta B/\Delta \log \tau)$ between two iso- τ surfaces everywhere in the sunspot following Eqn. 4.2. To this end we synthesized iso- τ surfaces in the MHD simulations using the SPINOR code.

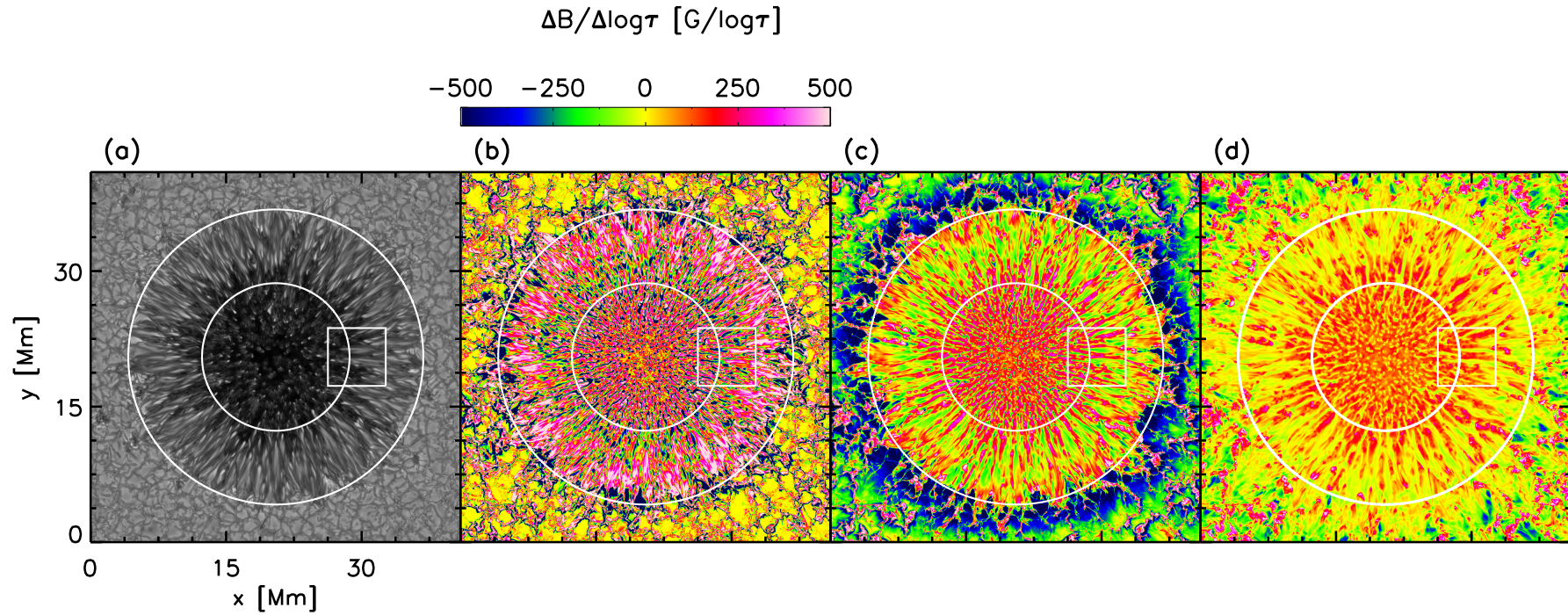


Figure 4.22: Continuum intensity (panel (a)) and $(\Delta B / \Delta \log \tau)$ maps from the MHD simulations of a sunspot. Panels (b), (c) and (d) display $(\Delta B / \Delta \log \tau)_{0.0, -0.9}$, $(\Delta B / \Delta \log \tau)_{-0.9, -2.5}$ and $(\Delta B / \Delta \log \tau)_{-2.5, -3.5}$, respectively. All $(\Delta B / \Delta \log \tau)$ maps are presented in the same scale shown by the color-bar at the top of panel (b). The circles in all panels represent the umbra-penumbra boundary and the outer boundary of the sunspot, respectively.

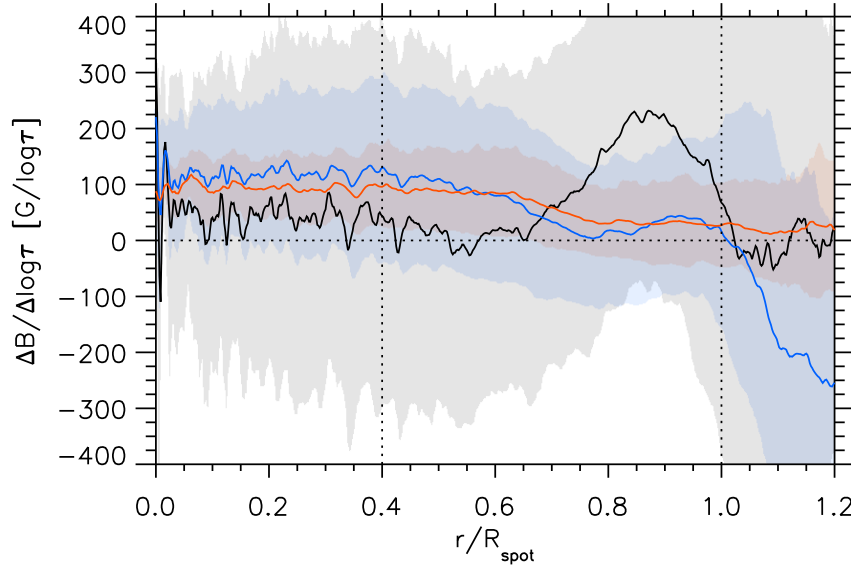


Figure 4.23: Azimuthally averaged $(\Delta B/\Delta \log \tau)$ as a function of normalized radial distance r/R_{spot} , from the MHD simulations of a sunspot. *Black, blue and red* curves depict $(\Delta B/\Delta \log \tau)_{0.0,-0.9}$, $(\Delta B/\Delta \log \tau)_{-0.9,-2.5}$ and $(\Delta B/\Delta \log \tau)_{-2.5,-3.5}$, respectively. *Shaded* areas represent standard deviations. *Dotted* vertical lines indicate the umbra-penumbra boundary and the outer boundary of the sunspot.

Fig. 4.22 depicts maps of $(\Delta B/\Delta \log \tau)$ from the MHD simulations between different $\log \tau$ surfaces. The $(\Delta B/\Delta \log \tau)_{0.0,-0.9}$ map show patches with negative values in the inner penumbra, similar to what is seen in the SOT/SP observations. Patches with negative values in the $(\Delta B/\Delta \log \tau)_{-0.9,-2.5}$ and $(\Delta B/\Delta \log \tau)_{-2.5,-3.5}$ maps are, however, shifted to the middle and outer penumbra, respectively. This behavior is not visible in the SOT/SP data. There the patches of $(\Delta B/\Delta \log \tau) < 0$ are mostly found in the inner penumbra. This is valid also for the upper layers (see Fig. 4.14).

At the boundary of the sunspot we see a ring where the $(\Delta B/\Delta \log \tau)_{0.0,-0.9} < 0$, which located further out in the $(\Delta B/\Delta \log \tau)_{-0.9,-2.5}$ map.

Fig. 4.23 shows the azimuthally averaged $(\Delta B/\Delta \log \tau)$ as derived from the MHD simulations, again as a function of the normalized sunspot radius. The shaded areas represent standard deviations. The radial dependence of $(\Delta B/\Delta \log \tau)_{0.0,-0.9}$ is qualitatively similar to that of the SOT/SP observations, which show negative values ($-25 \text{ G/log } \tau$) in the inner penumbra. Although these negative gradients are very weak compared with observational data. In the middle and outer penumbra $(\Delta B/\Delta \log \tau)_{0.0,-0.9} > 0$. Significant quantitative differences between the MHD simulations and the SOT/SP observations are present in $(\Delta B/\Delta \log \tau)_{0.0,-0.9}$ values. The radial dependence of $(\Delta B/\Delta \log \tau)_{-0.9,-2.5}$ in the MHD simulations is very similar to that of the SOT/SP observations: $(\Delta B/\Delta \log \tau)_{-0.9,-2.5} > 0$ at all radial distance in the sunspot. Outside of the sunspot $(\Delta B/\Delta \log \tau)_{-0.9,-2.5} < 0$. The radial dependence of $(\Delta B/\Delta \log \tau)_{-2.5,-3.5}$ is very similar to $(\Delta B/\Delta \log \tau)_{-0.9,-2.5}$ inside the sunspot's boundary, just outside the boundary $(\Delta B/\Delta \log \tau)_{-2.5,-3.5} > 0$. The standard deviations of the fluctuations of B in the azimuthal averages have higher values in the MHD simulations compared to the SOT/SP observations. We attribute this to the higher spatial resolution of the MHD data.

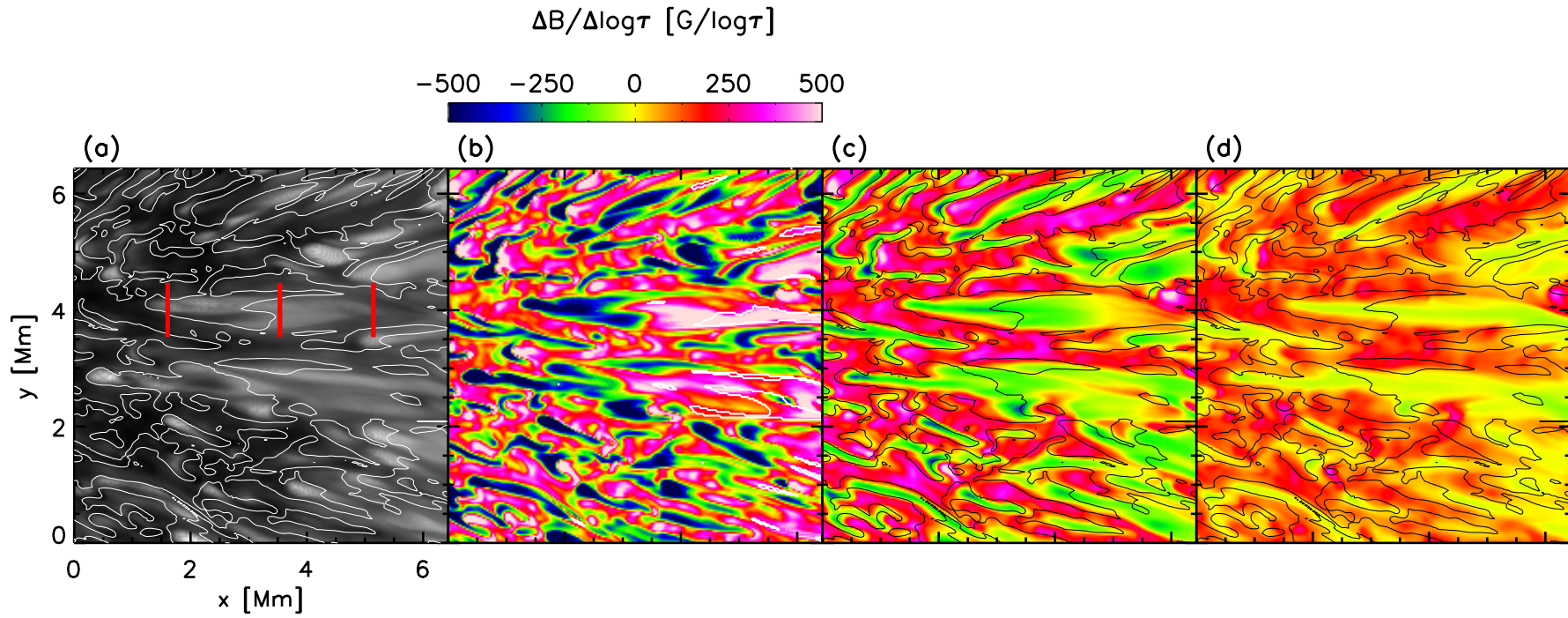


Figure 4.24: Blowups of the areas within the *white* box as in Fig. 4.22. Contours in the panels (a), (c) and (d) encircle negative $(\Delta B/\Delta \log \tau)_{0,0,-0.9}$ and *white* contours in the panel (b) indicates areas with polarity opposite to that in the umbra. Three vertical bars in panel (a) mark the vertical cuts displayed in Fig. 4.25.

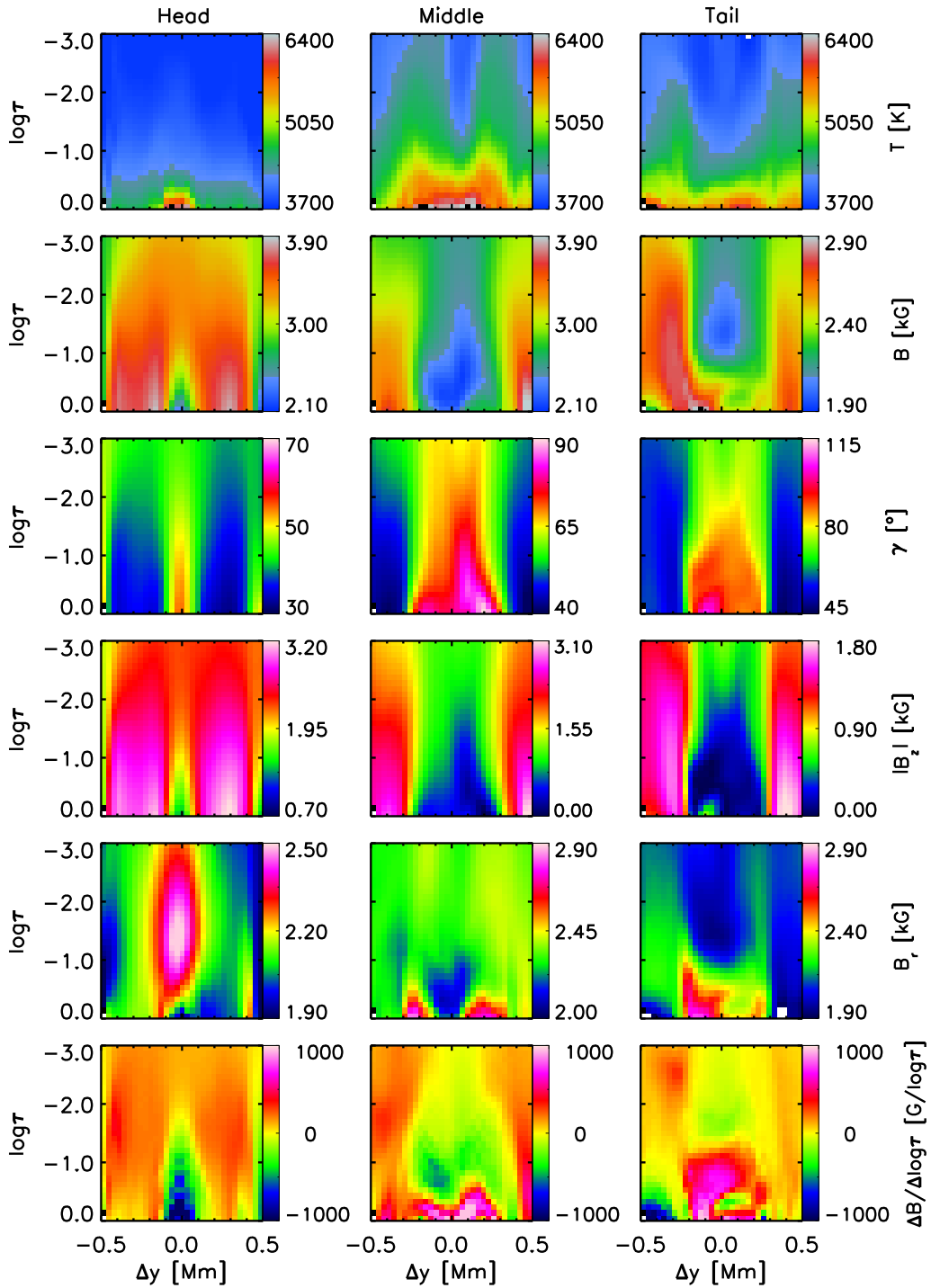


Figure 4.25: Optical depth stratification of various physical parameters perpendicular to the axis of a filament in the MHD simulation. The location of the plotted cuts are indicated by *red bars* in Fig. 4.24(a). Panels in the first, second and third column represent the head, middle and tail of the filament, respectively. From top to bottom (for each column): T , B , γ , B_z , B_r and $(\Delta B / \Delta \log \tau)$.

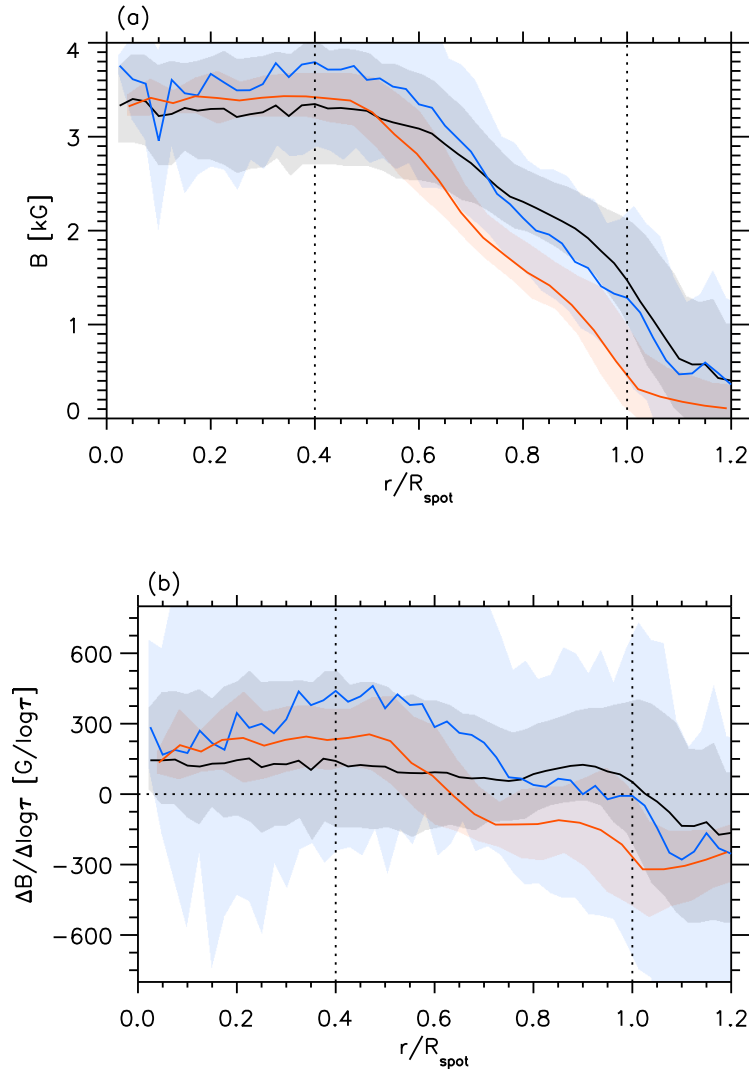


Figure 4.26: Radial dependence of B at $\log \tau=0$ (panel (a)) and $(\Delta B / \Delta \log \tau)_{0.0-2.3}$ (panel(b)) from the MHD simulation. *Black* curves are estimated directly from the MHD simulations, *blue* curves are results of inversions of synthesized Stokes profiles from the MHD simulations at native resolution. *Red* curves are from inversions of synthesized Stokes profiles from the MHD simulations degraded to a spatial resolution of $\sim 1''$. *Shaded* areas represent standard deviation. The *dotted* vertical lines in both panels indicate the umbra-penumbra boundary and the outer boundary of the sunspot.

Blowups of the region inside the white squares of Fig. 4.22 are displayed in Fig. 4.24. In the MHD simulations too patches where $(\Delta B / \Delta \log \tau) < 0$ coincide with bright filaments. In the lower layers patches with negative $(\Delta B / \Delta \log \tau)$ exist only in the parts around the heads of the filaments. In the upper layers the largest parts of the filament's body shows a weak negative $(\Delta B / \Delta \log \tau)$.

The height stratifications of the physical properties of a penumbral filament at the head, middle and tail are shown in Fig. 4.25. In the lower layers (below $\log \tau = -1.5$) the head of the filament shows weaker and more horizontal B which is surrounded by stronger and more vertical B . Thus, below $\log \tau = -1.5$ the filament has $(\Delta B / \Delta \log \tau) < 0$. At the

head of the filament the radial magnetic field, B_r , increases from $\log \tau=0$ up to $\log \tau=-0.9$. At the middle part and the tail of the filament, B_r is strongest around $\log \tau=0$. This layer is covered by strong B_z at the top. Thus in the lower layers the decreasing B_r causes a positive $(\Delta B/\Delta \log \tau)$ whereas in the upper atmosphere $(\Delta B/\Delta \log \tau)$ becomes negative because the stronger B_z lies above the weaker B_r . We note that Fig. 4.25 should be compared with Fig. 4.19 only after taking into account that, whereas Fig. 4.19 corresponds to the average of 60 filaments, Fig. 4.25 represents just an individual simulated filament. We thus cannot rule out that some of the differences between both figures are due to the choice of this filament.

Effect of spatial resolution on $(\Delta B/\Delta \log \tau)$

To understand the effect of the simplified model atmosphere used to fit the Stokes profiles observed with VTT/TIP-2, we inverted Stokes profiles of the Si I 10827 Å and Ca I 10833 Å spectral lines synthesized along vertical rays passing through every (x, y) grid point of the MHD simulations. The inversions start from the same set of initial parameters as used to fit the VTT/TIP-2 data. One set of inversions is carried out at the native resolution of the MHD simulations, another are after degrading the synthesized Stokes images by a point spread function (PSF) which has a Gaussian shape with FWHM of 1"0, close to the spatial resolution of the VTT/TIP-2 data presented in Section 4.2.

In Fig. 4.26, the radial dependence of B (at $\log \tau=0$) and $(\Delta B/\Delta \log \tau)$, deduced from the inversions of the synthetic data are compared with the original B and $(\Delta B/\Delta \log \tau)$ values obtained from the MHD simulations. From the sunspot center to half of the sunspot radius, B is reproduced quite successfully by the inversions of synthesized Stokes profiles both at native and degraded spatial resolution of the MHD simulations. In the outer half part of the sunspot B is underestimated by $\sim 200 G$ when we perform inversions of Stokes profiles synthesized in native spatial resolution. The inversion of spatially degraded Stokes profiles results in a further underestimate of B by up to $\sim 1000 G$. The vertical gradient $(\Delta B/\Delta \log \tau)_{0.0,-2.3}$ obtained by inversions at the native spatial resolution produces a quantitatively different radial profile compared to $(\Delta B/\Delta \log \tau)_{0.0,-2.3}$ calculated directly from the MHD simulations, although qualitatively the two curves are similar. Between $r \simeq 0.20R_{\text{spot}}$ and $r \simeq 0.75R_{\text{spot}}$ the inversions with the simplified model overestimate $(\Delta B/\Delta \log \tau)_{0.0,-2.3}$, while between $r \simeq 0.75R_{\text{spot}}$ and $r = R_{\text{spot}}$ they underestimate $(\Delta B/\Delta \log \tau)_{0.0,-2.3}$. The inversion results of the spatially degraded Stokes profiles show a qualitative difference to the true gradient in the model leading to $(\Delta B/\Delta \log \tau)_{0.0,-2.3} < 0$ in the outer penumbra. The main result, from the VTT/TIP-2 data, namely the dominant presence of $(\Delta B/\Delta \log \tau)_{0.0,-2.3} < 0$ in parts of the penumbra is reproduced, although there are qualitative differences (e.g. these negative value of $(\Delta B/\Delta \log \tau)_{0.0,-2.3}$ occur in different parts of the penumbra in the observations and the MHD simulations).

This experiment demonstrates that the lower spatial resolution can lead to negative $(\Delta B/\Delta \log \tau)$. But, what could be a potential mechanism which can lead to the negative $(\Delta B/\Delta \log \tau)$ in low spatial resolution data? Unresolved opposite polarity patches in the penumbra could have significant consequence to the estimation of $(\Delta B/\Delta \log \tau)$, especially, if the population of opposite polarity patches in the photosphere changes with height.

In next section we analyze the distribution of opposite polarity patches at different

$\log \tau$ surfaces both in the MHD simulations and the SOT/SP observations. There we also try to understand the relation between opposite polarity patches and the presence of negative ($\Delta B/\Delta \log \tau$).

4.5 Opposite polarity patches in penumbrae

The positions of patches with polarity opposite to that in the umbra at three $\log \tau$ levels (0.0, -0.9 and -2.5) in the MHD simulations are shown in Fig. 4.27. At $\log \tau=0$ the opposite polarity patches appears at almost all radial distances in the penumbra, however, the number of patches increases towards the outer penumbra. At $\log \tau=-0.9$ and $\log \tau=-2.5$ the opposite polarity patches are mainly restricted to the middle to outer penumbra and to the outer penumbra, respectively. The positions of the opposite polarity patches in the SOT/SP data show a consistency with the MHD simulations (see Fig. 4.28). The radial distribution of opposite polarity flux $B_z(opp)$ as a fraction of the net flux $|B_z|$ is plotted in Fig. 4.29. In the SOT/SP observations, opposite polarity flux appears even in the inner penumbra at $\log \tau=0$, and reaches a fraction of up to $\sim 55\%$ of the total flux at the outer boundary of the penumbra. The MHD simulations show $\sim 47\%$ flux with opposite polarity at the outer boundary of the penumbra. At $\log \tau=-0.9$ the SOT/SP data have only $\sim 15\%$ flux with opposite polarity at the outer boundary of the penumbra, whereas it amounts to $\sim 30\%$ in the MHD simulations. Approximately $\sim 8\%$ of the flux has the opposite polarity in the outer penumbra at $\log \tau=-2.5$ in both the SOT/SP data and the MHD simulations. When the MHD simulations is degraded to $1''.0$ only a small fraction of the opposite polarity flux survives (see panel (c) of Fig. 4.29). In degraded spatial resolution a higher number of pixels with $(\Delta B/\Delta \log \tau) < 0$ is found in the penumbra compared to that in the native resolution of the MHD simulations (see panel (d) of Fig. 4.29). In the umbra not a single pixel is found with $(\Delta B/\Delta \log \tau) < 0$ in the degraded spatial resolution data but almost $\sim 30\%$ of the pixels have $(\Delta B/\Delta \log \tau) < 0$ in the native resolution. In summary, low spatial resolution hides opposite polarity patches in the penumbra. However, it causes many pixels with $(\Delta B/\Delta \log \tau) < 0$, hence, it also produces $(\Delta B/\Delta \log \tau) < 0$ in the azimuthal averages.

4.6 Discussion

We determined the vertical gradient of the magnetic field strength throughout sunspots. From the VTT/TIP-2 observations we found that B increases at the rate of approximately 1.3 G km^{-1} with geometrical depth above $\log \tau=0.0$ in the umbra. In the SOT/SP data we found that B increases with depth at an average rate of $\sim 1.7 \text{ G km}^{-1}$ in the umbra (after converting $\Delta \log \tau$ to Δz assuming hydrostatic equilibrium). Similar values have been found by Borrero and Ichimoto (2011) based on Hinode SOT/SP data and by Sánchez Cuberes et al. (2005) from VTT/TIP data. Mathew et al. (2003) report values around 4 G km^{-1} and Westendorp Plaza et al. (2001c) found 2.5 G km^{-1} . We found that B increases rapidly with depth in the lower atmosphere while the gradient becomes flatter in the upper atmosphere above $\log \tau=-0.9$ in the SOT/SP data.

The vertical gradient of the magnetic field strength in the penumbra, reported in the present work, displays large fluctuations, changing its sign even on small scales. In the

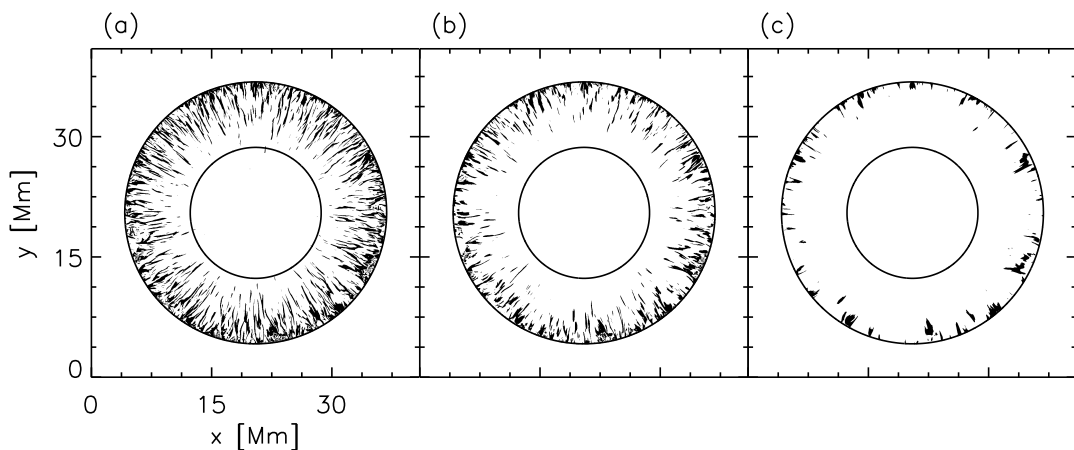


Figure 4.27: Maps of opposite polarity patches from the MHD simulations of a sunspot. *Black* areas show positions of opposite polarity. Panels (a), (b) and (c) correspond to $\log \tau=0$, $\log \tau=-0.9$ and $\log \tau=-2.5$, respectively. Circles in all panels represent the umbra-penumbra boundary and the outer boundary of the sunspot.

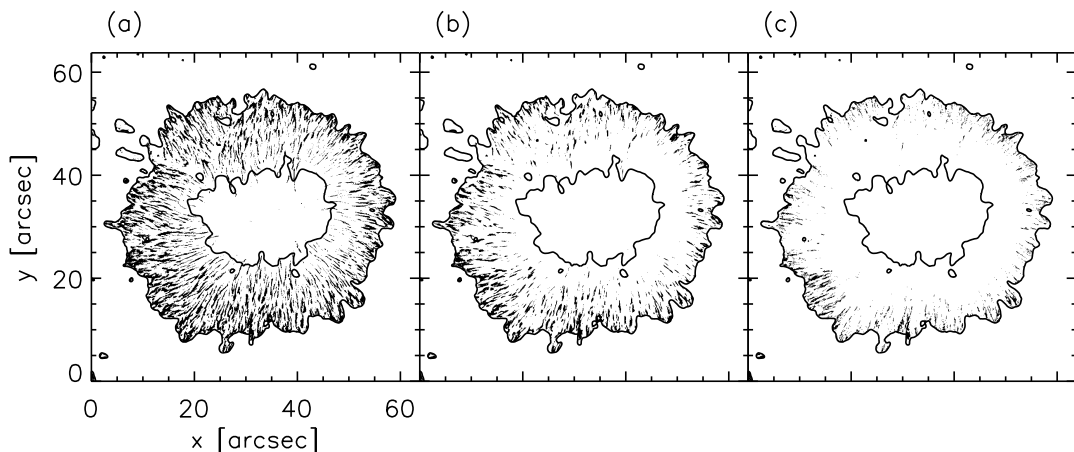


Figure 4.28: Same as Fig. 4.27 but it shows SOT/SP observations.

gradient maps of the penumbra derived from the SOT/SP observations, $(\Delta B/\Delta \log \tau)$ is always positive in spines. The gradient in the penumbral filaments has a more complex structure: in the lower layer of the inner half of filaments (i.e. the part of the filament closer to the umbra) has a positive $(\Delta B/\Delta \log \tau)$ which is surrounded by a negative $(\Delta B/\Delta \log \tau)$ at the sides. In the upper layer of the inner half part of the filaments it has only a negative $(\Delta B/\Delta \log \tau)$. The outer half of the filament has a positive $(\Delta B/\Delta \log \tau)$ both in the lower and upper layers. The positive $(\Delta B/\Delta \log \tau)$ in the tail can be explained by the fact that the horizontal field of the filament, which is returning to the surface is much stronger than the spine's field covering the filaments from the top (Tiwari et al. 2013a). The structure of the gradient in the body of filaments close to head can be explained by a penumbral model presented in Fig. 4.30. The penumbral filament is assumed to be a semi-circular structure containing nearly horizontal magnetic field. The filament is surrounded by a more vertical background magnetic field (spines) on the sides, which closes above the filament. The background field forms spines with B gradually decreas-

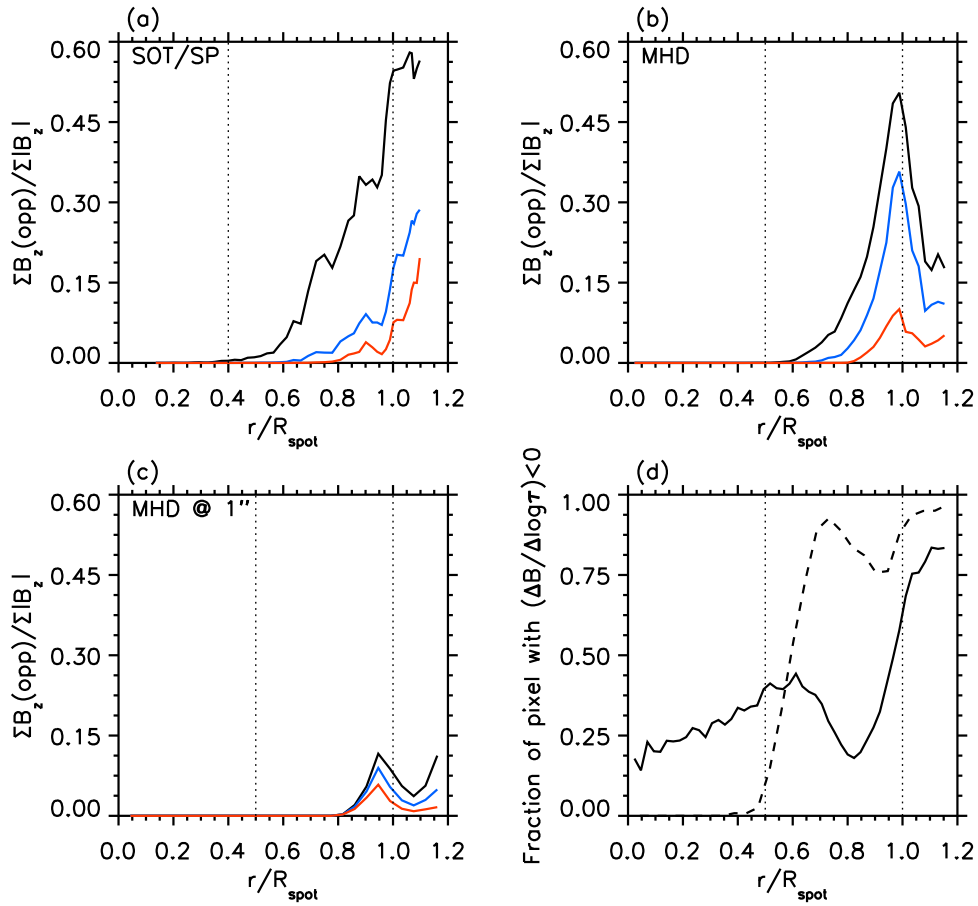


Figure 4.29: Panel (a) shows the radial distribution of opposite polarity flux $B_z(opp)$ as a fraction of the net flux $|B_z|$ from the SOT/SP observations. Panel (b) displays the radial distribution of opposite polarity flux for the MHD simulations. Panel (c) corresponds to opposite flux from inversions of synthesized Stokes profiles from the MHD simulations which was degraded by Gaussian of $1''.0$ width. *Black, blue and red* curves correspond to $\log \tau=0.0$, $\log \tau=-0.9$ and $\log \tau=-2.5$, respectively. *Solid and dashed* curves in panel (d) display the numbers of pixels where $(\Delta B/\Delta \log \tau)_{0.0,-2.3} < 0$ at native and degraded spatial resolution in MHD simulations. *Dotted* vertical lines in all the panels indicate the umbra-penumbra boundary and the outer boundary of the sunspot.

ing with height. This model assumes that the semicircular filament has its maximum magnetic field strength at its center, which gradually decreases towards the boundary between the spines and the filament. The $\log \tau=0.0$ level samples the whole width of the filament (shown by region B+A+B in Fig. 4.30), whereas $\log \tau=-0.9$ level samples only the central part of the filament's width (region A). Finally, the $\log \tau=-2.5$ level sees field only from the spines. In region A the field strength decreases between $\log \tau=0.0$ and $\log \tau=-0.9$, hence, $(\Delta B/\Delta \log \tau)_{0.0,-0.9} > 0$. In region B $(\Delta B/\Delta \log \tau)_{0.0,-0.9} < 0$ because the $\log \tau=0.0$ level probes only parts of the filament, whereas the $\log \tau=-0.9$ level samples the field from the spines which has a stronger field than the filament. $(\Delta B/\Delta \log \tau)_{-0.9,-2.5} < 0$ in region A because the $\log \tau=-0.9$ level is still within the filament's body whereas the $\log \tau=-2.5$ level is above the filament where the stronger field from the spines closes. In

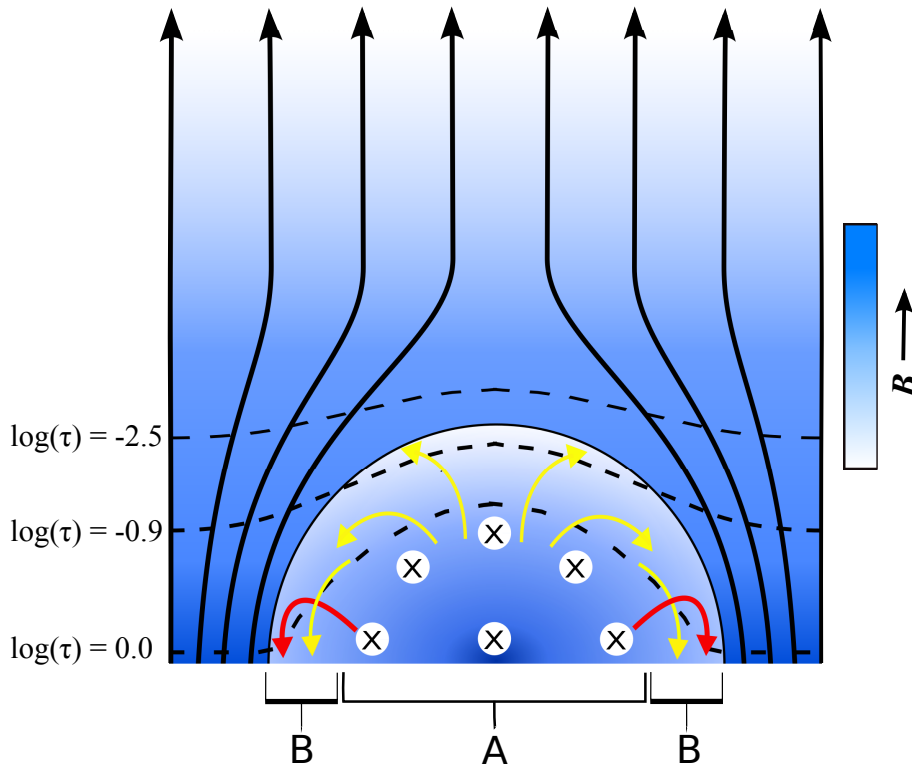


Figure 4.30: Schematic view of the vertical structure of the magnetic field in penumbral filaments. Depicted is a plane perpendicular to filament. The filament is represented by the semi-circular area. *Crosses* in circular *white* areas indicate the direction of the magnetic field in the penumbral filament, which is perpendicular to the plane. Arrows in *yellow* indicate the overturning convection within the filament and *red* arrows depict the field reversal at the edges of the filaments which is caused by the convective flow through advection of the filament's field. The background magnetic field (spines) is shown by nearly vertical *black* arrows. *Dashed* lines show different $\log \tau$ levels. *Lighter* and *darker* shades of *blue* correspond to weaker and stronger B , respectively.

summary, the expanding and closing magnetic field from the spines above the filament causes the negative $(\Delta B / \Delta \log \tau) < 0$ in the inner part of penumbral filaments.

In the MHD simulations $(\Delta B / \Delta \log \tau) < 0$ in the inner part of filaments in both layers. $(\Delta B / \Delta \log \tau)_{0.0, -0.9} > 0$ in the tail of filaments, whereas $(\Delta B / \Delta \log \tau)_{-0.9, -2.5} < 0$ there. The gradient maps show that there are differences in the magnetic field structure of the penumbral filaments in the MHD simulations and the observations.

After producing azimuthal averages, our results turn out to be rather different from results published previously (Westendorp Plaza et al. 2001c, Mathew et al. 2003, Sánchez Cuberes et al. 2005, Balthasar and Gömöry 2008, Borrero and Ichimoto 2011). In the VTT/TIP-2 data, where we assume that B varies linearly with $\log \tau$, we found that B decreases with depth from the umbra-penumbra boundary to $r \approx 0.75R_{\text{spot}}$. Between $r \approx 0.75R_{\text{spot}}$ and $r = R_{\text{spot}}$ B increases with depth. The SOT/SP observations exhibit a similar profile of $(\Delta B / \Delta \log \tau)$ in the lower layers. In the upper atmosphere B increases on average with depth at all radial distances in the penumbra. $(\Delta B / \Delta \log \tau)_{0.0, -0.9}$ estimated from the MHD simulations shows good qualitative similarities with the SOT/SP data in

the lower layers. The average radial profiles of $(\Delta B/\Delta \log \tau)$, found in the present study with VTT/TIP-2 and SOT/SP observations disagree with earlier works. [Westendorp Plaza et al. \(2001c\)](#) and [Borrero and Ichimoto \(2011\)](#) found that B increases with depth in the inner half radius of the sunspot. In the outer half radius the field decreases with depth. On the other hand [Mathew et al. \(2003\)](#) and [Sánchez Cuberes et al. \(2005\)](#) found that B increases with depth everywhere within the sunspot's visible boundary.

The expansion of the sunspot's magnetic field caused by the stratified gas pressure, $(\partial P/\partial d) > 0$, should always produce a positive $(\Delta B/\Delta \log \tau)$ in global scale. This is in contradiction with the radial profiles of $(\Delta B/\Delta \log \tau)_{0.0,-0.9}$ found in the observations and the MHD simulations where $(\Delta B/\Delta \log \tau)_{0.0,-0.9} < 0$ in the inner penumbra. Highly corrugated optical surfaces can cause the observed negative gradient in the azimuthal averages. One factor which has to be considered here is that the $\log \tau$ surfaces sample the atmosphere at different geometrical depth in different parts of the penumbra. In the penumbral filaments the $\log \tau$ surfaces are elevated compared to the spines (see Fig 4.30). In the spines the magnetic field strength changes gradually compared to the filament where an abrupt change in the atmosphere (from filament to spines) between two $\log \tau$ surfaces leads to a higher difference in the field strength. The scenario described above leads to a negative $(\Delta B/\Delta \log \tau)$ with higher magnitude in the filaments compared to a positive $(\Delta B/\Delta \log \tau)$ in the spines. The negative $(\Delta B/\Delta \log \tau)_{0.0,-0.9}$ is only seen at the head of the filaments and the more filament heads are present higher is the probability that the azimuthal averages will lead to negative $(\Delta B/\Delta \log \tau)_{0.0,-0.9}$. This is the case rather in the inner penumbra, compared to the middle and outer penumbra.

The statement that the highly corrugated $\log \tau$ surfaces causes the negative gradients in the azimuthal averages is supported by the MHD simulations where a negative $(\Delta B/\Delta d)$ is not found when it is estimated between fixed geometrical heights. Negative values of gradient appeared in the MHD simulations only when $(\Delta B/\Delta \log \tau)$ is examined.

An underestimation of B in deeper layers could also contribute to the observed negative $(\Delta B/\Delta \log \tau)$ in the inner penumbra. Underestimation of B can be caused by a cancellation of polarized signal stemming from unresolved opposite polarity areas. The presence of opposite polarity patches in sunspot penumbrae has been observed by [Ruiz Cobo and Asensio Ramos \(2013\)](#), [Franz and Schlichenmaier \(2013\)](#), [Scharmer et al. \(2012\)](#), [Tiwari et al. \(2013a\)](#) and [van Noort et al. \(2013\)](#). [Ruiz Cobo and Asensio Ramos \(2013\)](#) and [Franz and Schlichenmaier \(2013\)](#) have found the opposite polarity patches in the middle and outer penumbra in SOT/SP observations while [Scharmer et al. \(2012\)](#) found thinner and elongated lanes of opposite polarity everywhere in the penumbra in higher resolution SST/CRISP observations. Recent 3D MHD simulations of a sunspot by [Rempel \(2012\)](#); cf. [Rempel et al. \(2009a\)](#) show the presence of the opposite polarity patches in the penumbra. Our analysis of opposite polarity patches in the SOT/SP observations and the MHD simulations indicates that flux associated with opposite polarity patches increases from the inner to the outer penumbra (see also Fig. 13 of [Rempel 2012](#)). Both the MHD simulations and the SOT/SP observations indicate the presence of opposite polarity patches even in the higher atmosphere, i.e. up to $\log \tau = -2.3$. The distribution of opposite polarity patches in the penumbra observed with SOT/SP is qualitatively consistent with that of the MHD simulations (see Fig. 4.28 and Fig. 4.29), although there is a quantitative difference in the flux associated with opposite polarity patches in the SOT/SP observations and the MHD simulations. In the upper layers opposite polarity patches are restricted to

the middle and outer penumbra both in the SOT/SP observations and the MHD simulations. These opposite polarity patches are of two kinds: narrower and elongated lanes of opposite polarity at the edges of inner part of penumbral filaments (see Fig. 4.30) at the locations of downflow lanes which are the lateral components of overturning convection (Scharmer et al. 2012, Tiwari et al. 2013a). Patches found at the tail of the penumbral filaments are bigger in size (Franz and Schlichenmaier 2013, Ruiz Cobo and Asensio Ramos 2013, Scharmer et al. 2012, Tiwari et al. 2013a) and are associated with downflows at the tails.

Our experiment, estimating $(\Delta B/\Delta \log \tau)_{0.0,-2.3}$ from the degraded spatial resolution (1.0) MHD simulations shows that at this resolution opposite polarity patches disappear almost completely. At the same time a significant increase in the number of pixels with negative $(\Delta B/\Delta \log \tau)_{0.0,-2.3}$ occurs in the penumbra. This behavior reverse in the umbra where in the native resolution $\sim 30\%$ of the pixels have negative $(\Delta B/\Delta \log \tau)_{0.0,-2.3}$ which disappear completely in the degraded resolution data. As discussed above we have found more flux with opposite polarity in the lower layers compared to upper layers, thus lower spatial resolution causes more cancellation in the polarized signal from deeper layers and produces negative $(\Delta B/\Delta \log \tau)_{0.0,-2.3}$.

As far as the SOT/SP observations are concerned, a significant amount of flux is associated with opposite polarity patches. But it is still possible that narrow elongated opposite polarity lanes at the edges of the penumbral filaments are not completely resolved. In this case it is possible that some fraction of negative gradient originates from unresolved opposite polarity patches. However, the radial distribution of opposite polarity patches and number of pixels with $(\Delta B/\Delta \log \tau)_{0.0,-2.3} < 0$ are rather different. This suggests that the main cause of the observed negative $(\Delta B/\Delta \log \tau)_{0.0,-2.3}$ in the azimuthal averages are the highly corrugated iso- τ surfaces.

The presence of a magnetic canopy outside the visible boundary of the sunspot (Solanki et al. 1992, Lites et al. 1993, Solanki et al. 1994, Adams et al. 1994, Skumanich et al. 1994, Keppens and Martinez Pillet 1996, Rueedi et al. 1998, Solanki et al. 1999), with the canopy base rising with distance from the sunspot, can be concluded from the SOT/SP observations. This is also consistent with the results from MHD simulations. The vertical gradient of B turns out to be a useful quantity for identifying or detecting magnetic canopies.

An important result of this study is that on a large scale the magnetic canopy only exists at and outside the visible boundary of the sunspot ($r/R_{\text{spot}} > 0.9$). We do not see a canopy structure in the middle penumbra caused by the expansion of field from the umbra or the inner penumbra as reported by Westendorp Plaza et al. (2001c) and Borrero and Ichimoto (2011). Instead, we found local canopies in the penumbra i.e., patches where the magnetic field strength decreases with optical depth caused by the stronger field in the spines closing above the filaments (see Fig. 4.30). The corrugation effect of the τ surfaces leads to $(\Delta B/\Delta \log \tau) < 0$ in the inner penumbra in the lower atmosphere in the azimuthal average. In addition to the corrugation of the τ surfaces, the effect of the unresolved, deep-lying opposite polarity patches can also lead to negative $(\Delta B/\Delta \log \tau)$ patches in the penumbra.

5 3D Structure of a Sunspot: From the Photosphere to the Upper Chromosphere

In the previous chapter we presented the vertical gradient of the magnetic field strength of sunspots in the photosphere. In the present chapter we investigate the sunspot's magnetic field in the upper chromosphere and compare it to the photospheric properties. We obtained the magnetic field vector of sunspots through state-of-the-art inversion of the upper chromospheric He I triplet at 10830 Å. For comparison with the photosphere we used the magnetic field vector retrieved in the previous chapter by inversions of Si I 10827.1 Å and Ca I 10833.4 Å lines. We found that the umbral magnetic field strength in the upper chromosphere is lower by a factor 1.4-1.6 compared to the photosphere. The magnetic field strength of the umbra decreases from the photosphere towards upper chromosphere by an average rate of 0.5-1.0 G km⁻¹. The difference in the magnetic field strength between both atmospheric layers steadily decreases from the sunspot center to the outer boundary of the sunspot. The magnetic field vector is more inclined, i.e. more horizontal in the photosphere compared to the upper chromosphere.

5.1 Introduction

Whereas the photospheric structure of the sunspot's magnetic field has been studied very extensively in last few decades through the Zeeman diagnostics, the knowledge of its chromospheric properties is relatively poor.

The He I triplet at 10830 Å provides a promising avenue to study the upper chromospheric magnetic field (see overview by [Lagg et al. 2007](#)), because generally small optical depth reached in He I triplet ([Penn and Kuhn 1995](#), [Rüedi et al. 1995](#)) makes it a simpler tool to diagnose the magnetic field, compare to most other chromospheric spectral lines. Many studies of the magnetic field vector in the upper chromospheric layer have been done using the He I triplet (e.g., [Rüedi et al. 1996](#), [Trujillo Bueno et al. 2005](#), [Solanki et al. 2003, 2006](#), [Lagg et al. 2004](#), [Merenda et al. 2011](#), [Xu et al. 2010, 2012](#)). The He I triplet is produced by transitions between the $1s2s\ ^3S_1$ and the $1s2p\ ^3P_{0,1,2}$ energy levels. EUV irradiance from the corona ionizes neutral helium atoms in the upper chromosphere, which then populate the lower level of the transition by recombination ([Avrett et al. 1994](#), [Andretta and Jones 1997](#), [Centeno et al. 2008](#)).

[Trujillo Bueno et al. \(2002\)](#) have shown that polarized light coming from the He I triplet is influenced by both the Zeeman effect and the Hanle effect. At solar disk center

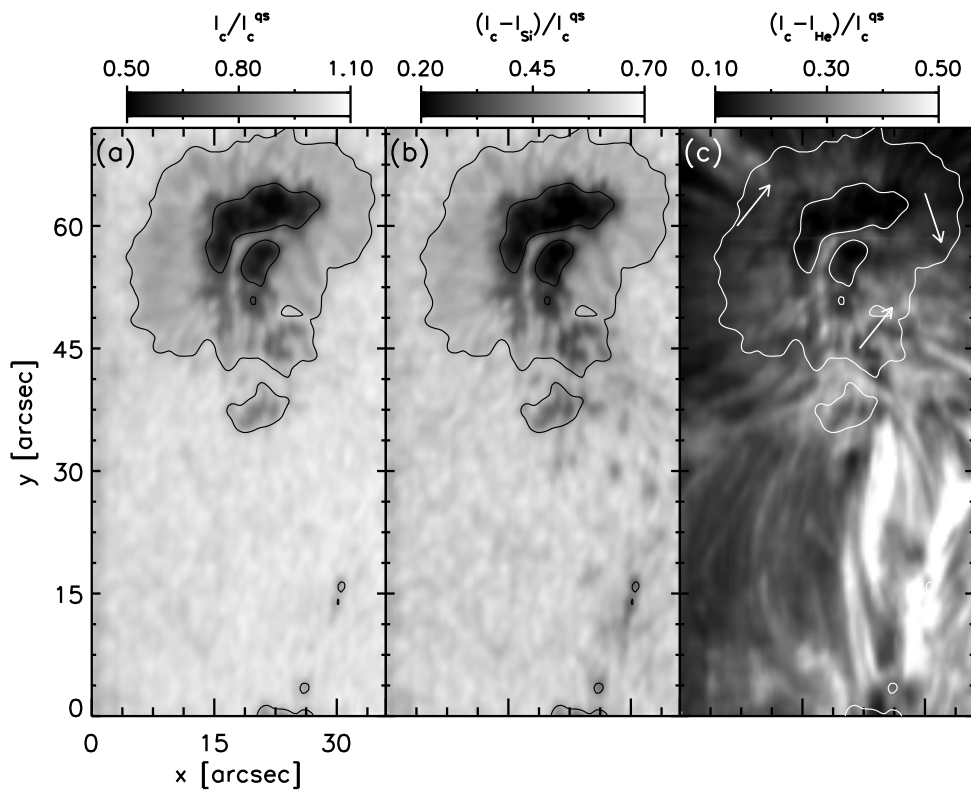


Figure 5.1: Panel (a) shows the observed field-of-view (FOV) on 14 November, 2010 as observed in the continuum. Panels (b) and (c) depict depression of the line core of the Si I 10827 Å line and the He I b/c, respectively. Observations are recorded with VTT/TIP-2. Inner and outer contours in all panels indicate the umbra-penumbra boundary and the outer boundary of the sunspot, respectively.

the Hanle effect in the forward scattering can produce linearly polarized light in the He I triplet only in the presence of inclined magnetic field with respect to the solar radius vector. In the presence of strong magnetic fields, as in sunspots, linear polarization is dominated by the transverse Zeeman effect.

Rüedi et al. (1995) studied the upper chromospheric magnetic field of a sunspot using the He I triplet and compared it with its photospheric counterpart. The vertical gradient of the magnetic field strength in the umbra found by Rüedi et al. (1995) is around 0.35-0.60 G km⁻¹ (with positive values denoting increasing field strength with geometrical depth). This value is similar to that found by Abdussamatov (1971a) by comparing magnetograms derived from the H α line with those derived from the Fe I 6302.5 Å line. Values of the vertical magnetic field gradient found by Henze et al. (1982) and Hagyard et al. (1983) fall in the same range. They derived it from the C IV 1548 Å emission line in the transition region and the photospheric Fe I 5250 Å absorption line. Rüedi et al. (1995) reported a value of the vertical gradient of the magnetic field in penumbra of around 0.1-0.3 G km⁻¹. A canopy like structure in the longitudinal magnetic field at the upper chromosphere around the sunspot was also observed by Rüedi et al. (1995).

Here we present state-of-the-art inversions of the full Stokes vectors of the He I triplet at 10830 Å, the Si I 10827.1 Å and the Ca I 10833.4 Å lines. The latter two give us maps

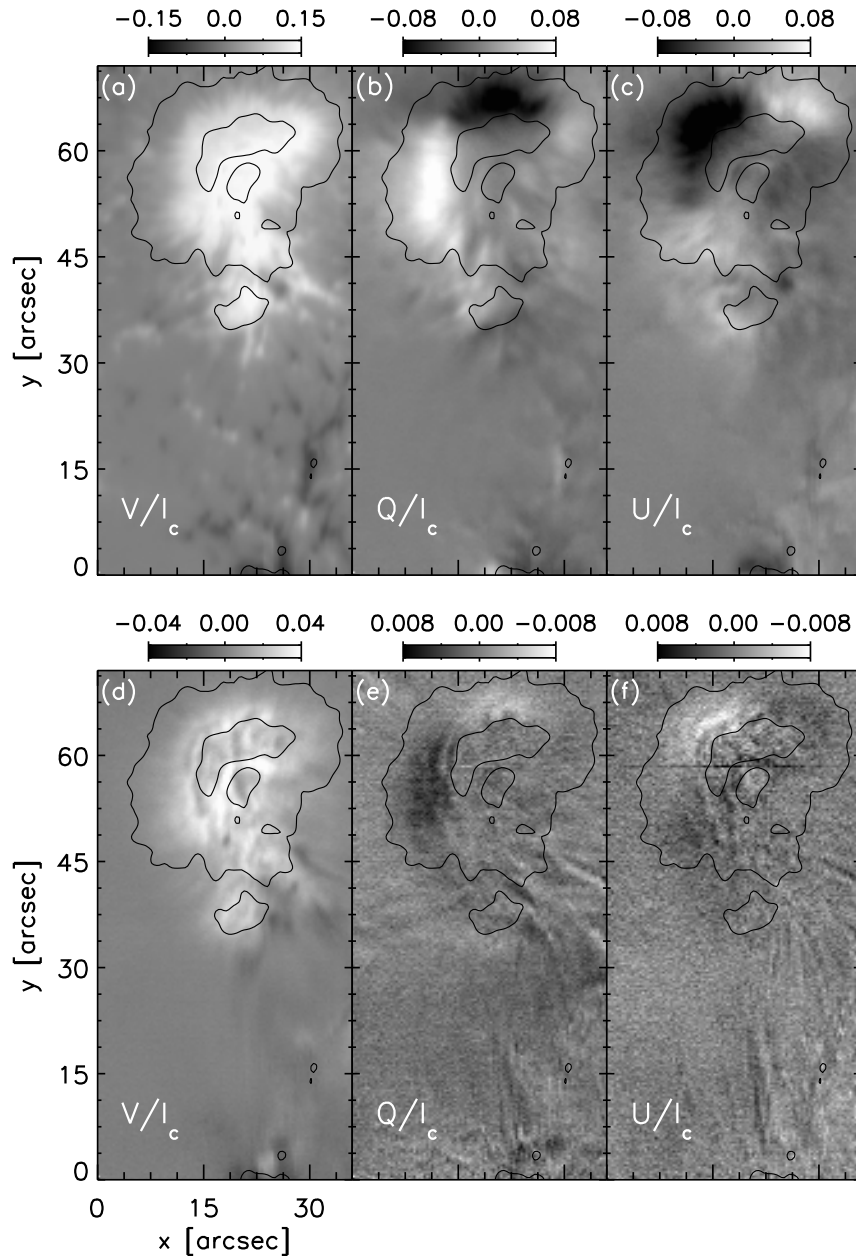


Figure 5.2: Stokes maps of Si I 10827 Å and He I 6678 Å from the observations recorded on 14 November, 2010. Panels (a), (b) and (c) correspond to Stokes V/I_c , Q/I_c and U/I_c in the red wing of Si I, respectively. Panels (d), (e) and (f) corresponds to Stokes V/I_c , Q/I_c and U/I_c in the red wing of He I, respectively. Inner and outer contours in all panels indicate the umbra-penumbral boundary and the outer boundary of the sunspot, respectively.

of the magnetic vector in the photosphere. These maps are analyzed to discuss the differences between the photospheric and the upper chromospheric magnetic field structure of the sunspot.

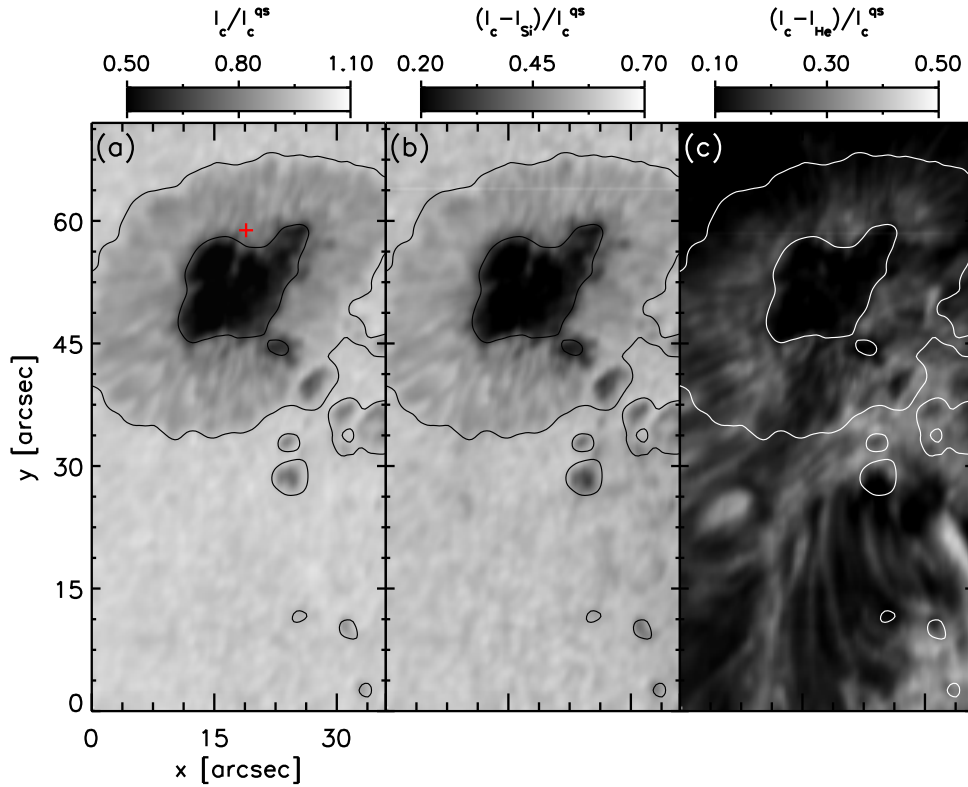


Figure 5.3: Same as Fig. 5.1, but showing the observed FOV on 16 November, 2010.

Table 5.1: Line parameters of He I triplet at 10830 Å.

Line	wavelength [Å]	transition	g_{eff}	relative strength
He Ia	10829.09	$1s2s\ ^3S_1 - 1s2p\ ^3P_0$	2.0	0.09
He Ib	10830.25	$1s2s\ ^3S_1 - 1s2p\ ^3P_1$	1.75	0.30
He Ic	10830.34	$1s2s\ ^3S_1 - 1s2p\ ^3P_2$	0.875	0.60

5.2 VTT/TIP-2 Observations

We used the data set already presented in the previous chapter. The full Stokes vector of the photospheric Si I 10827.1 Å and Ca I 10833.4 Å lines and upper chromospheric He I triplet at 10830 Å was recorded of a sunspot and its close surrounding using the TIP-2 (Collados et al. 2007) mounted on the VTT. The sunspot was recorded on 14 November, 2010 (12°N, 10°W, $\mu=0.96$) and 16 November, 2010 (14°N, 32°W, $\mu=0.84$). Atomic parameters of the He I triplet are provided in Table 5.1 (see table 4.1 for line parameters of the Si I and the Ca I). From now on we refer to the blue component of the triplet as He Ia and to the red components of the triplet as He Ib and He Ic.

Fig. 5.1 shows maps of the observed continuum intensity at 10832.6 Å, depression of the Si I line core, $(I_c - I_{\text{Si}})/I_c^{\text{qs}}$ and depression of the line core of the He Ib/c, $(I_c - I_{\text{He}})/I_c^{\text{qs}}$. Here I_c and I_c^{qs} represent continuum intensity, averaged continuum intensity in the quiet Sun, respectively. Intensity of the Si I line core and the He Ib/c line core represented by

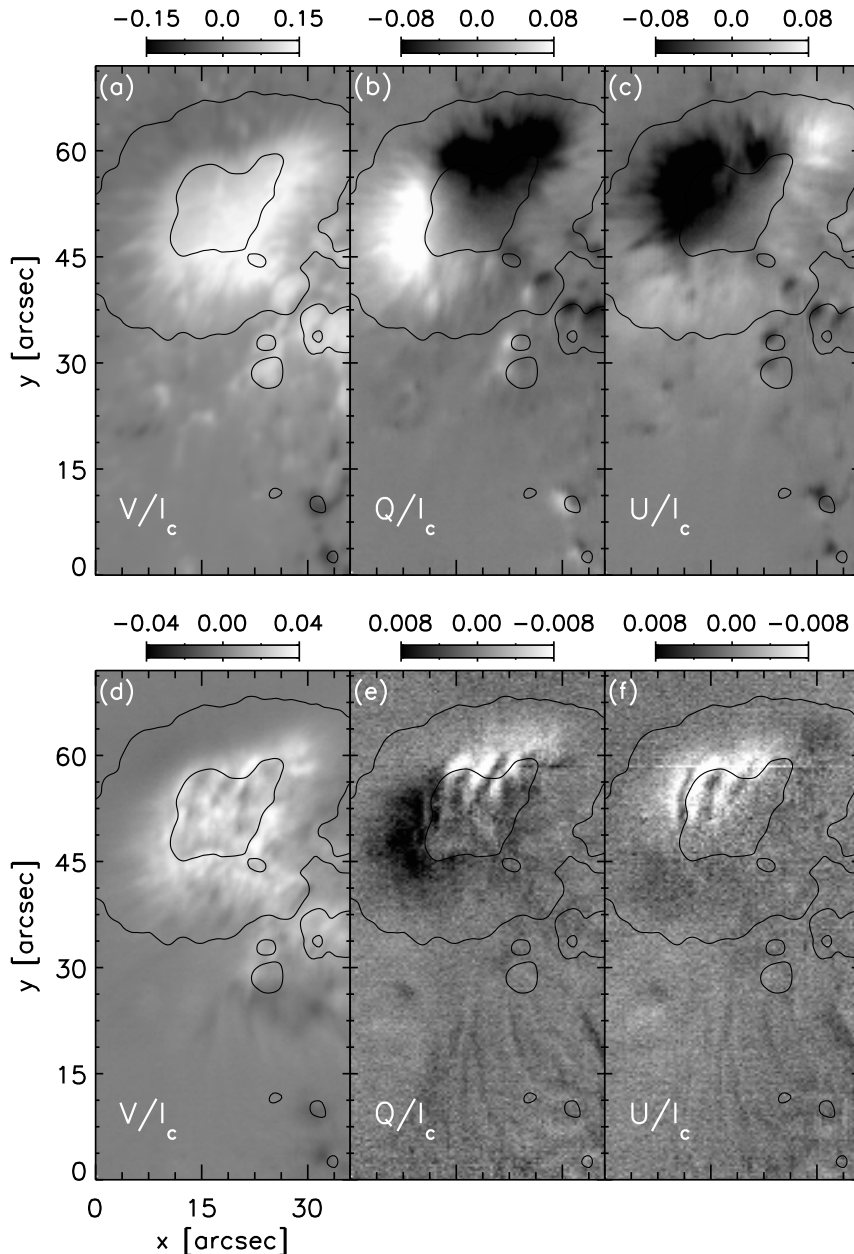


Figure 5.4: Same as Fig. 5.2, but showing Stokes maps observed on 16 November, 2010.

I_{Si} and I_{He} , respectively. An arc filament can be seen in the He Ib/c line core depression map. Stokes V/I_c , Q/I_c and U/I_c maps of the Si I line and the red component of the He I triplet are displayed in Fig. 5.2. All Stokes maps shown here are at $\lambda - \lambda_0 = 160 \text{ m\AA}$ for both lines (where λ_0 is the line core wavelength averaged over FOV). In contrast to Stokes V/I_c of the He Ib/c and the Si I data, Stokes Q/I_c and U/I_c maps in He Ib/c show signals at the location of the arc filament in the map of line core depression of the He Ib/c . These signals are due to LOS velocity and not due to the magnetic field (see Figs. 5.7 and 5.8).

Maps of the continuum intensity at 10832.6 \AA , depression of the Si I line core and the line core depression of the He Ib/c , observed on 16 November, 2010 are displayed in Fig. 5.3. Corresponding Stokes maps are shown in Fig. 5.4. The sunspot was observed

in a growing phase certainly on 14 November, 2010, as can be seen from the fact that its projected area grew from 450 Mm^2 on 14 November, 2010 to 1054 Mm^2 on 16 November, 2010, as increase of 234%. If we correct for foreshortening then it grew by 281% in two days. The magnetic field vector in the photosphere is inferred from SPINOR inversions of the Si I and the Ca I lines. The details of the inversions are mentioned in the Chapter 4.

5.2.1 HeLIx⁺ inversions of the He I 10830 Å triplet

Very small optical depth is reached at the upper chromosphere in the He I triplet (no contribution from the photosphere), so we assume that atmospheric parameter do not vary in the height range where the He I triplet forms. Hence we inverted all three components of the He I triplet with the HeLIx⁺ inversion code assuming a Milne-Eddington atmosphere. For Details about the HeLIx⁺ and the Milne-Eddington atmosphere, see Chapter 2, [Lagg et al. \(2004\)](#) and [Sasso et al. \(2006\)](#). The HeLIx⁺ code includes a consideration of the incomplete Paschen-Back effect regimes.

The blue component of the He I triplet is blended by the red wing of the Si I line. In order to consider the effect of these blends in the inversions we inverted the He I triplet and the Si I line simultaneously. Our model atmosphere consists of eight free parameters to fit the observed Stokes profiles of the He I triplet. Free parameters in the inversions are the magnetic field strength, B , the inclination of the magnetic field vector, γ , the azimuth angle of the magnetic field vector, ϕ , the LOS velocity, v_{los} , the Doppler width, $\Delta\lambda_{\text{D}}$, the damping constant, a , the gradient of the source function, S_1 , and the opacity ratio between line-center and continuum, η_0 . To fit the Si I line, the model atmosphere consists of the same free parameters as the He I triplet along with two additional free parameters, the filling factor, α of global straylight and v_{los} for straylight components are used. For detailed information on global straylight, see Section 4.2.2.1 of Chapter 4.

To take into account the blends from the Si I line into the He I triplet in the inversions, we took a multi-step approach. We first inverted the Stokes profiles from the Si I line. Then, in a second run, we fitted the Stokes profiles from the He I triplet and we fixed the free parameters for the Si I line to the values retrieved from the first run. At last we fitted both the Si I line and the He I triplet simultaneously, but we allowed the parameters to vary only within $\pm 5\%$ of the values fitted in the previous runs. The H₂O telluric line at 10832 Å which can blend with strongly redshifted He I triplet is fitted with a Voigt function.

Observed Stokes profiles at one penumbral pixel along with the best fits are depicted in Fig. 5.5.

Scattered plots between component of magnetic vector retrieved from HeLIx⁺ inversions of Si I and those from SPINOR inversions of the Si I and Ca I lines are presented in Fig. 5.6. In SPINOR inversions we obtained B and its linear gradient with respect to $\log \tau$, constant γ and ϕ with respect to height. For comparison average of B between $\log \tau=0.0$ (the lowermost node) and $\log \tau=-2.3$ (the uppermost node) is used from SPINOR inversions. As expected, retrieved values of γ and ϕ from both the inversion schemes agree very well. There is a difference in the values of B which may be due to the fact that in the atmosphere obtained from SPINOR inversions, B varies linearly with respect to $\log \tau$, whereas it is a constant in HeLIx⁺ inversions.

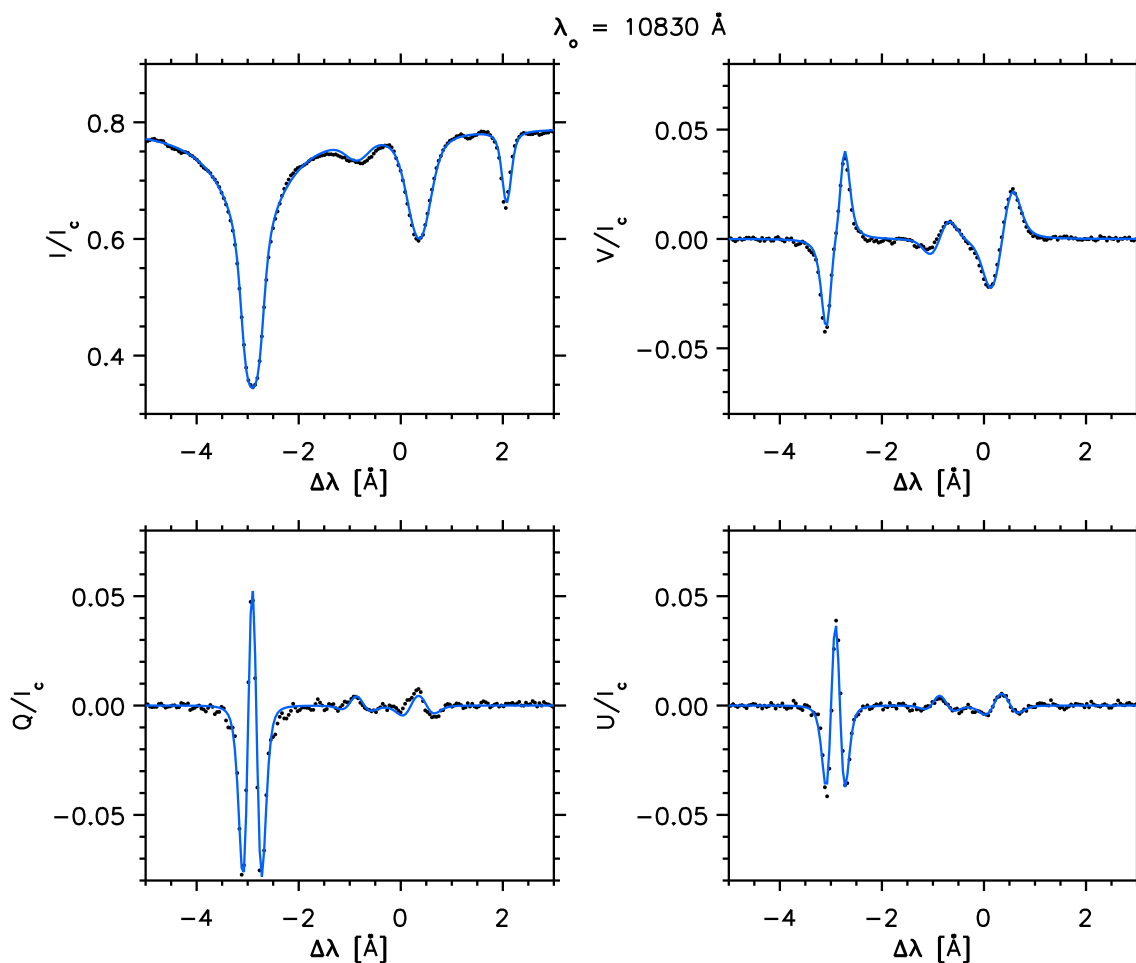


Figure 5.5: Best fit HeLiX⁺ inversions of example Stokes profiles in the penumbra. Their spatial location is marked by a red plus sign in Fig. 5.3(a). Black dots represent observed data points and solid blue curves represent best fits.

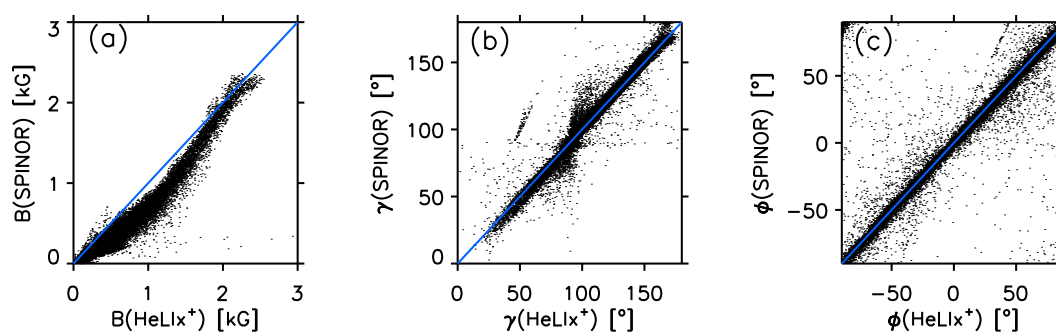


Figure 5.6: Scattered plots between the magnetic vector obtained from HeLiX⁺ inversions and those from SPINOR inversions. Panels (a), (b) and (c) correspond to B , γ and ϕ , respectively. Values of B used here from SPINOR inversions are averaged between $\log \tau=0$ and $\log \tau=-2.3$.

5.3 Analysis and results

5.3.1 Parameter maps

Maps of the magnetic field vector and the LOS velocity retrieved from the observations recorded on 14 November, 2010 are displayed in Fig. 5.7. Maps on the *left* in each panel correspond to the parameters obtained in the photosphere through SPINOR inversions of the Si I 10827.1 Å and Ca I 10833.4 Å lines. In SPINOR inversions we obtained B and its linear gradient with respect to $\log \tau$, but for comparison of the photospheric magnetic field properties with the upper chromosphere we use average values of B between $\log \tau=0.0$ and $\log \tau=-2.3$. The atmospheric parameters obtained in the upper chromosphere through He Ix⁺ inversions of the He I triplet are displayed in the *right* side of panels.

The magnetic field vector and LOS velocity maps obtained from the data observed on 16 November, 2010 are displayed in Fig. 5.8.

The 180° ambiguity in the azimuth direction was resolved by applying the “acute angle” method (Sakurai et al. 1985, Cuperman et al. 1992). The magnetic field vectors presented here are projected to disk center coordinates using the transformation matrix by Wilkinson et al. (1989). The inclination angle with respect to solar surface normal and ambiguity resolved azimuth angle are denoted by γ' and ϕ' , respectively.

Overall, the magnetic field strength within the sunspot’s visible boundary in the upper chromosphere is weaker than in the photosphere. This is particularly striking in the umbra, as can be found in the maps of B from both days. The light-bridge observed on 14 November, 2010 shows weaker B compared to the umbra in its photospheric layer, in the upper chromosphere no signature of the light-bridge is present in the B map. The values of B in the upper chromosphere at the location of the light-bridge are comparable to the umbral magnetic field strength.

The inclination of the magnetic field vector in the upper chromospheric heights looks qualitatively similar to the one in the photosphere. In the photosphere, outside the boundary, but close to the sunspot, we see few small patches where γ' has values less than 90°, i.e. at those locations the magnetic field has the opposite polarity to that of the umbra. These opposite polarity patches are not visible in the upper chromosphere, suggesting that they do not reach the height of the formation of He I triplet, being covered by the sunspot’s canopy. Maps of γ' from both days show more fine structure in the photosphere as compared to the upper chromosphere. In the sunspot the magnetic field’s azimuth in the upper chromosphere is generally similar to that in the photosphere, one exception is the light-bridge, which shows the signature of the field from the umbra on both sides expanding over it in the photosphere, but no signature at all in the upper chromosphere. Outside the sunspot, maps of the magnetic field vector in the upper chromosphere are much noisier than the photosphere, because the Stokes Q and U signals are much weaker in the He I triplet compared to the Si I line, so that the former are easily affected by noise.

LOS velocity maps are shown in Fig. 5.7(d) and Fig. 5.8(d). In the photosphere these refer to $\log \tau=0.0$. In the photosphere disk-center side of the penumbra shows negative velocities (blueshift) and limb side of penumbra shows positive velocities (redshift) on both days, although the magnitude of velocities is considerably strong on the 16 November, 2010, when the sunspot is closer to the limb ($\mu=0.84$). This is consistent with the signature of the Evershad effect.

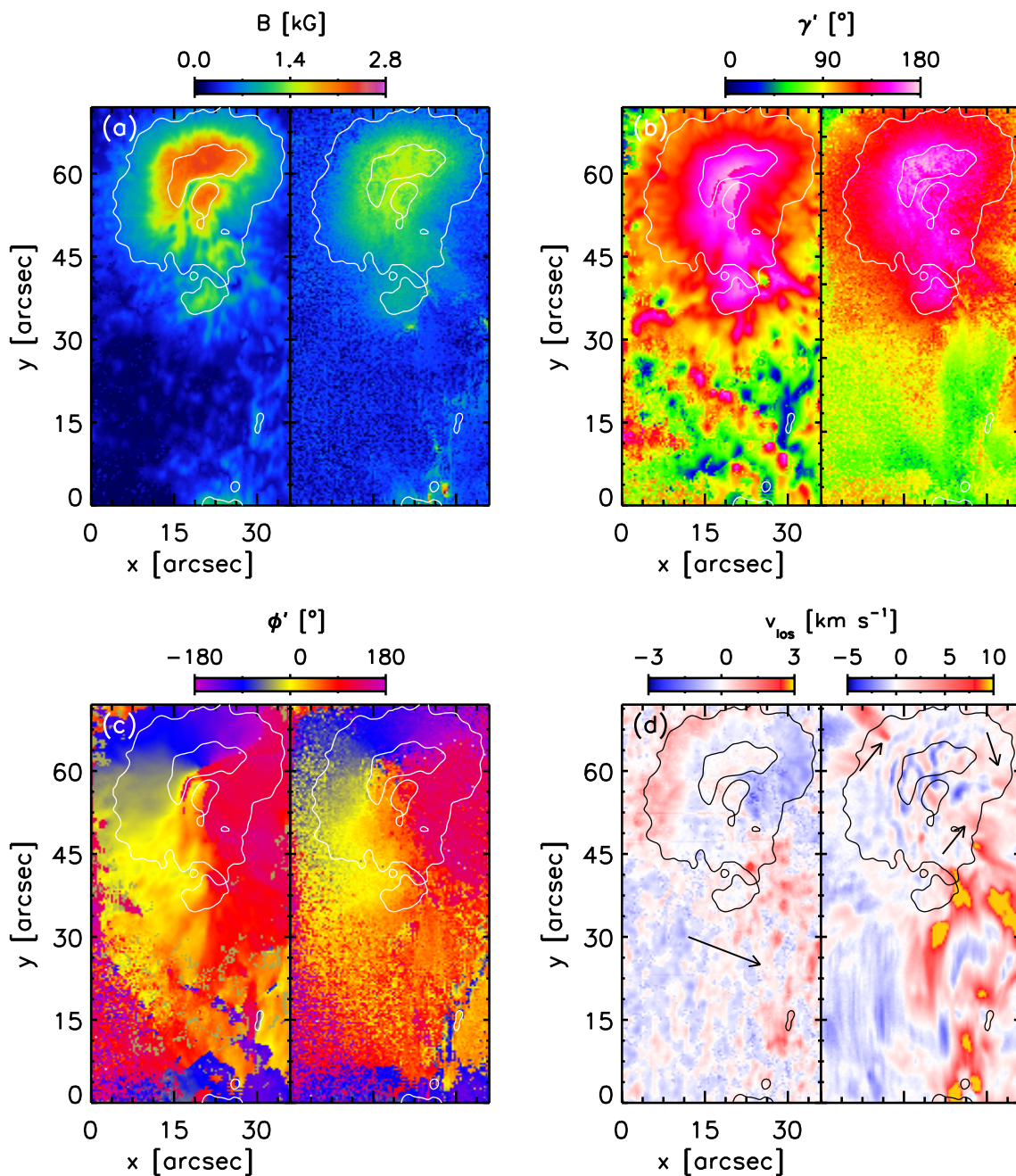


Figure 5.7: Magnetic field vector and line-of-sight velocity maps obtained in the photosphere and upper chromosphere from the observations recorded on 14 November, 2010. (a) Magnetic field strength B , (b) inclination angle, γ' , of the magnetic field vector with respect to the solar surface normal, (c) azimuth direction, ϕ' , of the magnetic field vector and (d) line-of-sight velocity. *Left* and *right* maps in all panels represent atmospheric parameters obtained in the photosphere and the upper chromosphere, respectively. An arrow in map at *left* of panel (d) indicates disk center direction and three arrows in map at *right* points three downflow intrusions in the penumbra.

LOS velocities derived in the upper chromosphere show radial inflows on 16 November, 2010, consistent with the inverse Evershed effect. On the 14 November, 2010 the sit-

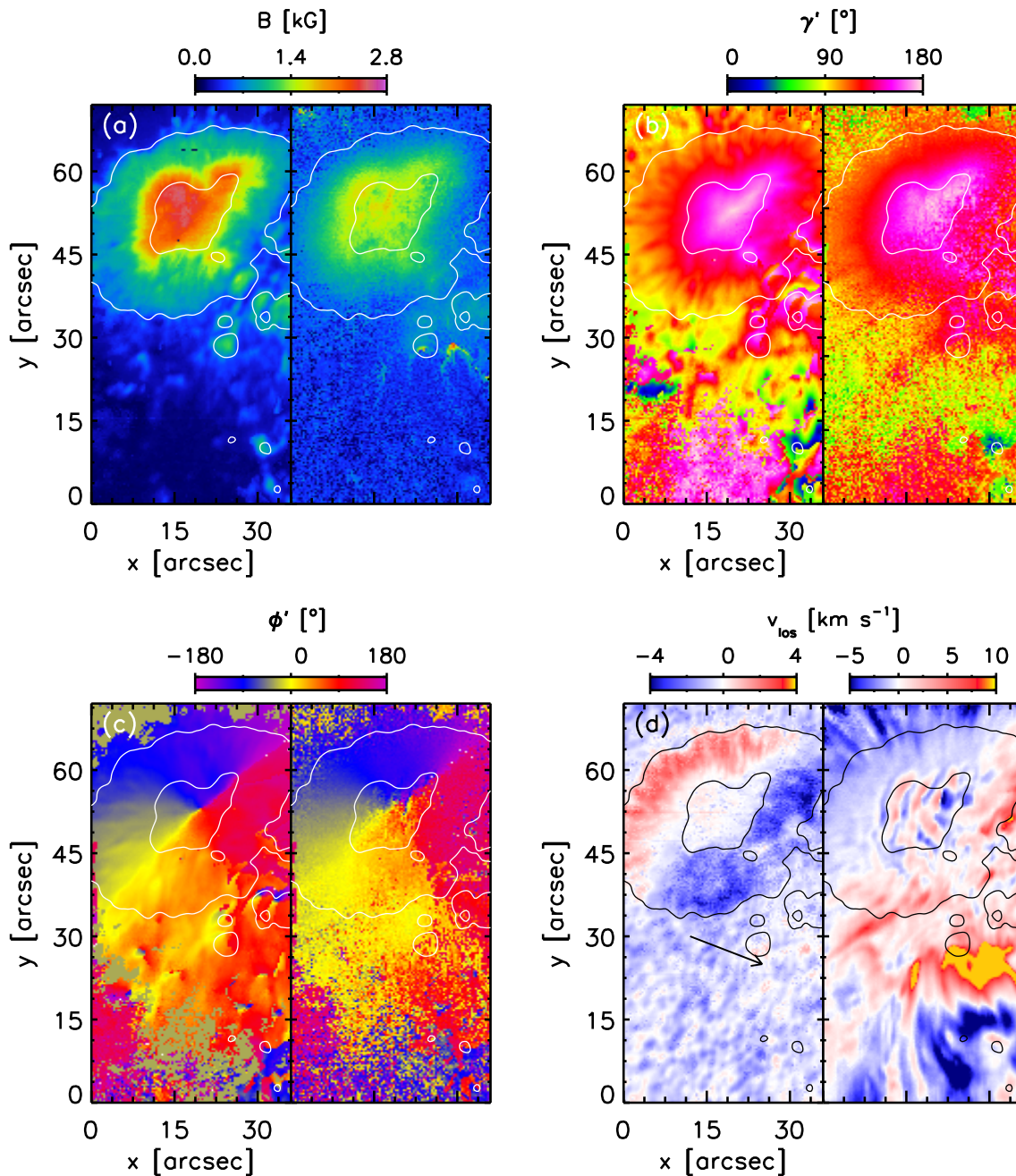


Figure 5.8: Same as Fig. 5.7, but for the observations recorded on 16 November, 2010.

uation is less clear cut, with no clear sign of the inverse Evershed effect in the He I triplet. Besides a wave pattern (see below) and three intrusions of denser (brighter in Fig. 5.1(c)) downflowing gas are identified (see small arrows in Fig. 5.1(c) and Fig. 5.7(d)). These may be associated with sunspot plumes (Fludra et al. 1997, Maltby et al. 1998, 1999, Brynildsen et al. 1998, 1999, 2001, Fludra 2001, Brosius and White 2004, Brosius 2005). The maps of v_{los} derived from the He I triplet show wave-like structures in the sunspot umbra and in the inner penumbra. This wave structure is elongated in direction of the y-axis (in direction of the slit of the spectrograph). This pattern is produced by running penumbral waves and umbral flashes (Zirin and Stein 1972, Christopoulou et al. 2000,

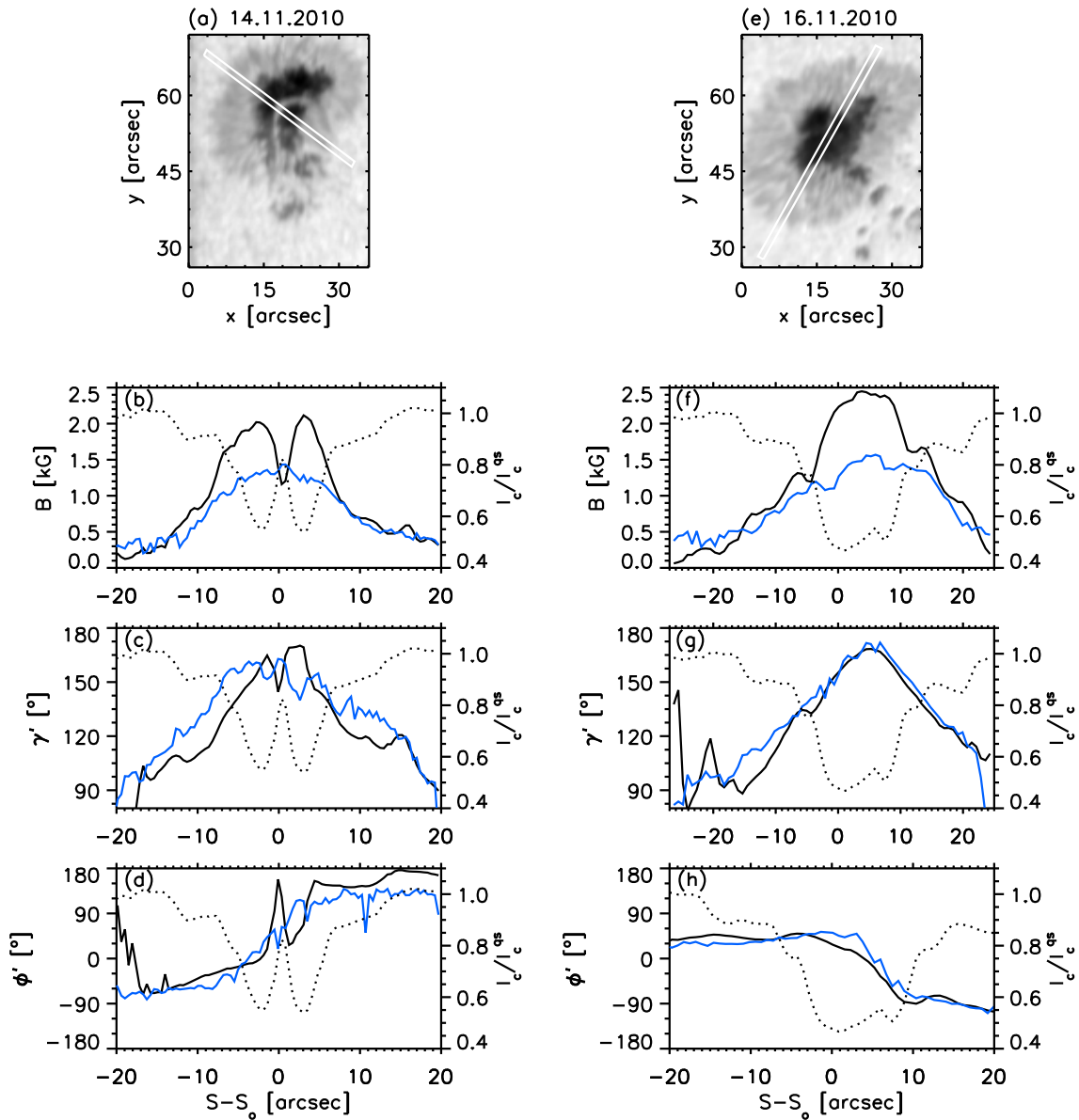


Figure 5.9: Cross sections through the observed sunspots: Panels (b)/(f), (c)/(g) and (d)/(h) depict profiles of B , γ' and ϕ' , respectively, along artificial slits represented by the *white* lines in panels (a)/(e). Panels (a), (b), (c) and (d) refers to observations recorded on 14 November, 2010 and (e), (f), (g) and (h) to 16 November, 2010. *Black* and *blue* curves in panels (b), (c), (d), (f) (g) and (h) correspond to the photosphere and upper chromosphere, respectively, while *dotted* curves represent continuum intensity.

Georgakilas et al. 2000, Christopoulou et al. 2001, Bogdan and Judge 2006, Centeno et al. 2006, Tziotziou et al. 2006, 2007, Bloomfield et al. 2007, Felipe et al. 2010). The effect of running penumbral waves and umbral flashes are also visible in the Stokes maps (see Fig. 5.2 and Fig. 5.4).

We expect a small offset between the parameter maps obtained in the photosphere and upper chromosphere, because of the viewing geometry (the sunspot was observed away from disk center on both days). If we assume a height difference of 1000 km between both observed layers of the atmosphere, which is a conservative estimate, then the chro-

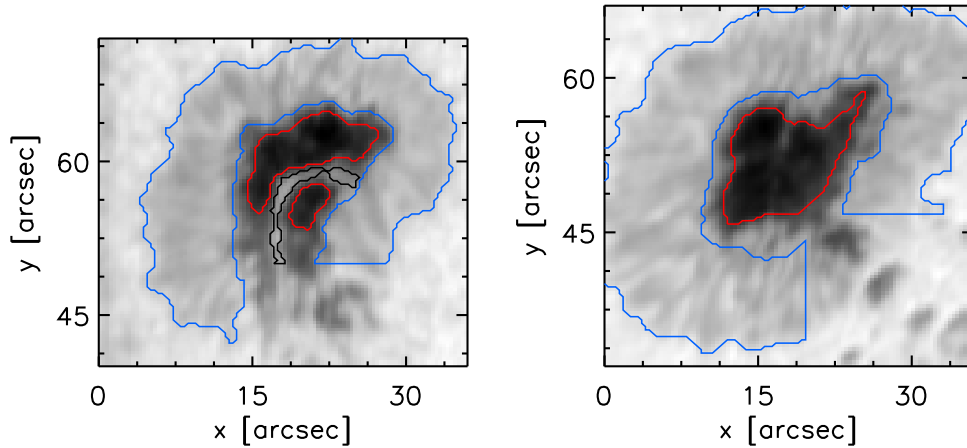


Figure 5.10: Division of different sunspot areas: *Red* and *blue* contours in both panels encircle umbral and penumbral areas which are used to compare the magnetic field vector retrieved at the photosphere and upper chromosphere. The area within the *black* contour in the *left* panel represents the light-bridge. The *left* and *right* panels correspond to the observations recorded on 14 and 16 November, 2010, respectively.

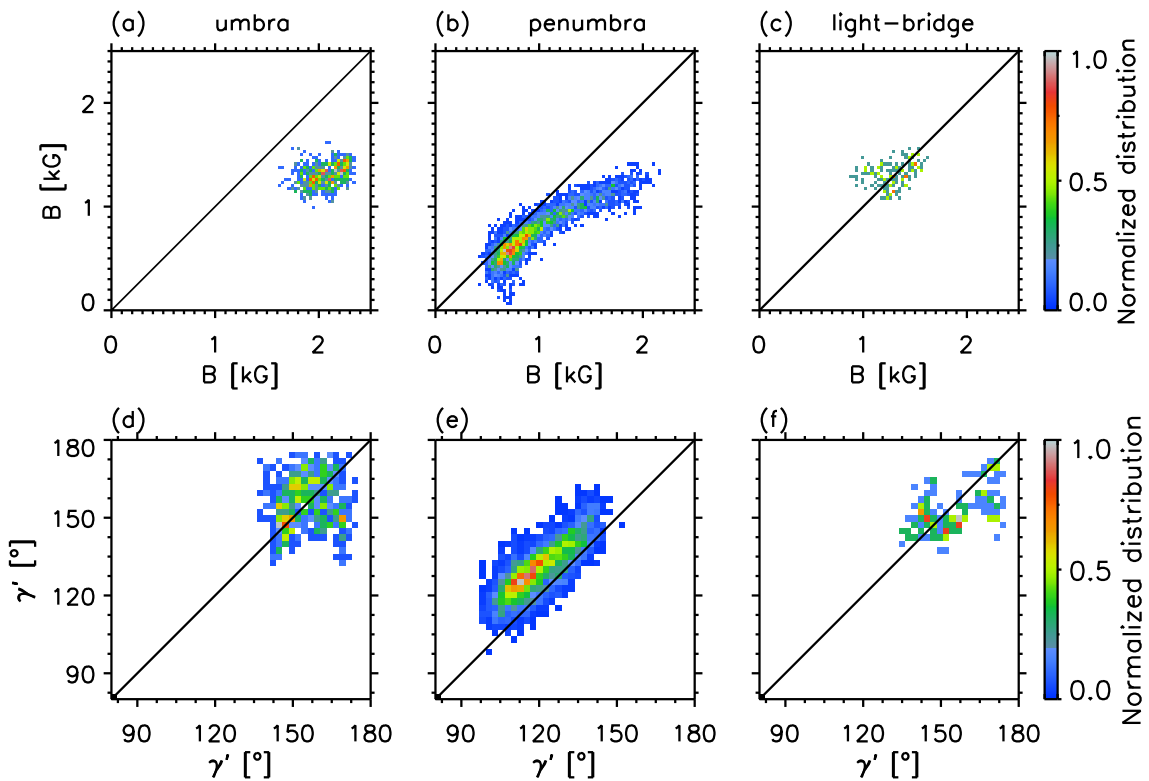


Figure 5.11: Scatter plots of the magnetic field components obtained in the upper chromosphere versus those obtained in the photosphere from the observations recorded on 14 November, 2010. Panels (a), (b) and (c) show scatter plots of B from the umbral, penumbral and light-bridge pixels, respectively. γ' values of data points from same spatial positions are displayed in panels (d), (e) and (f), respectively. Which pixels are classified into the umbral, penumbral and light-bridge pixels is shown in the *left* panel of Fig. 5.10.

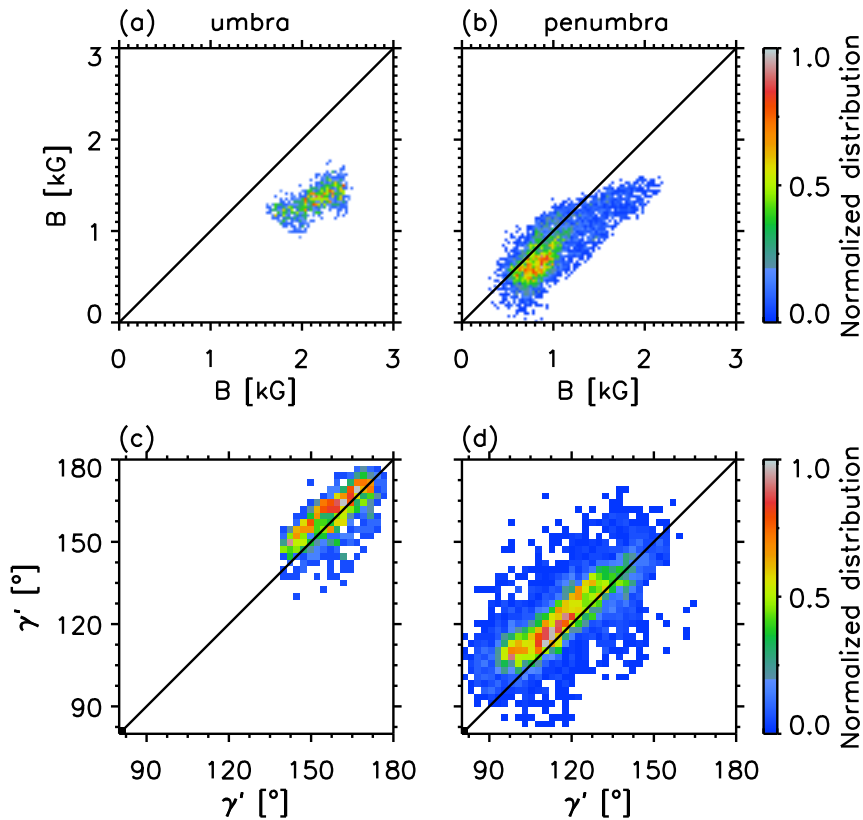


Figure 5.12: Same as Fig. 5.11 but for the observations recorded on 16 November, 2010 and restricted to umbral and penumbral pixels.

ospheric parameter maps are offset by ~ 275 km and ~ 575 km towards the limb on 14 and 16 November, 2010, respectively. The analysis described in the following sections was done after correcting for these offsets.

5.3.2 Radial cuts through the sunspots

For a more detailed and quantitative insight into the magnetic field properties of the sunspot and the connection between its photospheric layer and upper chromospheric layer, B , γ' and ϕ' are plotted along an artificial slit laid across the sunspot (see Fig. 5.9). Slits shown in panels (a) and (e) are $3.0''$ wide and B , γ' and ϕ' are averaged perpendicular to the slit direction. On 14 November, 2010 the profile of B along the slit in the photosphere shows a dip at the location of the light-bridge with a minimum value of B of ~ 1.2 kG which is ~ 1.0 kG weaker than the surrounding umbra. In the upper chromosphere at the location of the light-bridge B is ~ 1.4 kG. This value is comparable with, may be even slightly higher than the value in the surrounding umbra and is higher than in the photosphere. The similar B in light-bridge and umbra in chromosphere was clearly noticed [Ruedi et al. \(1995\)](#), but this present results is based on many more data points and hence is much more robust. The difference between the photospheric and the upper chromospheric magnetic field strength becomes rather small in the penumbra. Just outside of the sunspot's visible boundary, the values of B are higher by up to ~ 300 G in the upper chromosphere as compared to the photosphere.

Profiles of γ' along the slit on 14 November, 2010 indicate that in general the magnetic

field is more horizontal in the photosphere inside the sunspot compared to the upper chromosphere. This is particularly marked in the penumbra and more so on the 14 November, 2010. At the center of the light-bridge the magnetic field in the photosphere becomes more horizontal in agreement with results in the literature. In the chromosphere the field in the center of the light-bridge is as vertical as anywhere along the cut and more vertical than in the umbra directly at the light-bridge's edge. It is also more vertical in the upper chromosphere compared to the photosphere. The umbra close to the light-bridge shows the opposite trend. On 16 November, 2010, the photospheric and the upper chromospheric profile of γ' are quantitatively more similar.

On 14 November, 2010 profiles of ϕ' in the photosphere along the slit shows a spike at the location of the light-bridge suggesting that the magnetic field line fanning out at the the location of the light-bridge. Variation in ϕ' in the upper chromosphere is rather smooth.

The small difference between the light-bridge and its immediate surroundings may be due to a difference in the formation height of the He I 10830 Å over the light-bridge compared to the umbra. The sudden difference in the gradient of B between umbra, on the one hand and the penumbra and light-bridge on the other, also suggest a difference in formation height.

5.3.3 Scatter plots

Scatter plots of the magnetic field components in the upper chromosphere versus those of the photosphere are shown in Fig. 5.11 and Fig. 5.12 for 14 and 16 November, 2010, respectively. We plot for the umbral, penumbral and light-bridge points separately. The areas in the sunspot used for the scatter plots for these different regions are indicated in Fig. 5.10 by *red*, *blue* and *black* contours. The Blue contours exclude strongly distorted parts of the penumbra. Also, the boundary region between the umbra and the penumbra is excluded to make sure that the pixels under consideration are either from the umbra or from the penumbra and to avoid transition parts in the analysis.

All the pixels in the umbra indicate the B in the upper chromosphere is a factor of 1.4-1.6 the photosphere on both days of the observations. The inclination angle of the magnetic field vector shows slightly higher values (i.e. less inclined) in the upper chromosphere compared to the photosphere. The lower the penumbral field strength, B , the smaller the difference between the photosphere and the upper chromosphere.

The scatter plots of γ' from the observations on both days, indicate that the upper chromospheric magnetic field is more vertical compared to the photospheric magnetic field by roughly 5-20°, since signal to noise ratio is lower in the He I triplet, specially for Q and U and low signal to noise ratio lead inversion codes to return more horizontal \mathbf{B} (Borrero and Kobel 2012, Jafarzadeh 2013), this results is not an artifact of the noise. the values of B and γ' in the light-bridge observed on 14 November, 2010 are comparable in the photosphere and in the upper chromosphere.

5.3.4 Azimuthal averages

To derive the average radial dependence of the components of the magnetic field vector we take azimuthal averages along iso-thermal contours. Figs. 5.13(a) and 5.14(a) show these

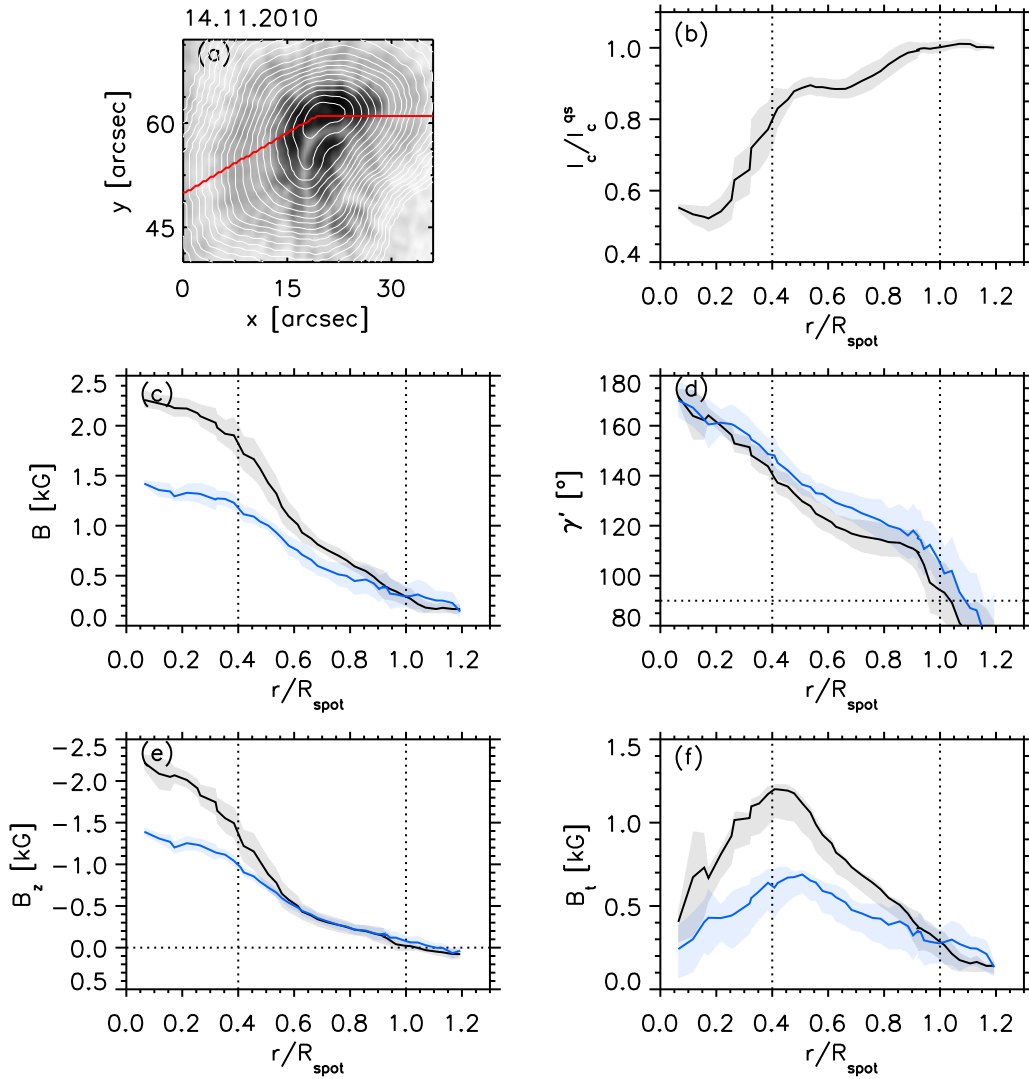


Figure 5.13: Averaged radial distribution of magnetic field properties in the observed sunspot: Panel (a) represents the continuum intensity map with contours used to calculate azimuthal averages for 14 November, 2010. The area below the *red* line has been neglected. Panel (b) shows the relative continuum intensity (normalized to the quiet-Sun) of the sunspot as a function of the normalized radial distance, r/R_{spot} . Panels (c), (d) (e) and (f) depict the radial dependency of B , γ' , the vertical component of the magnetic field, B_z , and the transverse component of the magnetic field, B_t , respectively. *Black* and *blue* curves correspond to the magnetic field vector derived in the photosphere and in the upper chromosphere, respectively. Dotted vertical lines in panels (b)-(f) indicate the umbra-penumbra boundary and the outer boundary of the sunspot.

contour-lines. Areas below the *red* line are excluded in the computation of azimuthal averages because of their complex photospheric structure. The remainder of the panels depicts the azimuthal averages of I_c and various magnetic parameters and corresponding standard deviations as a function of normalized radial distance, r/R_{spot} , from the sunspot center for 14 and 16, November 2010.

On 14 November, 2010, B at the darkest part of the umbra has an average value of

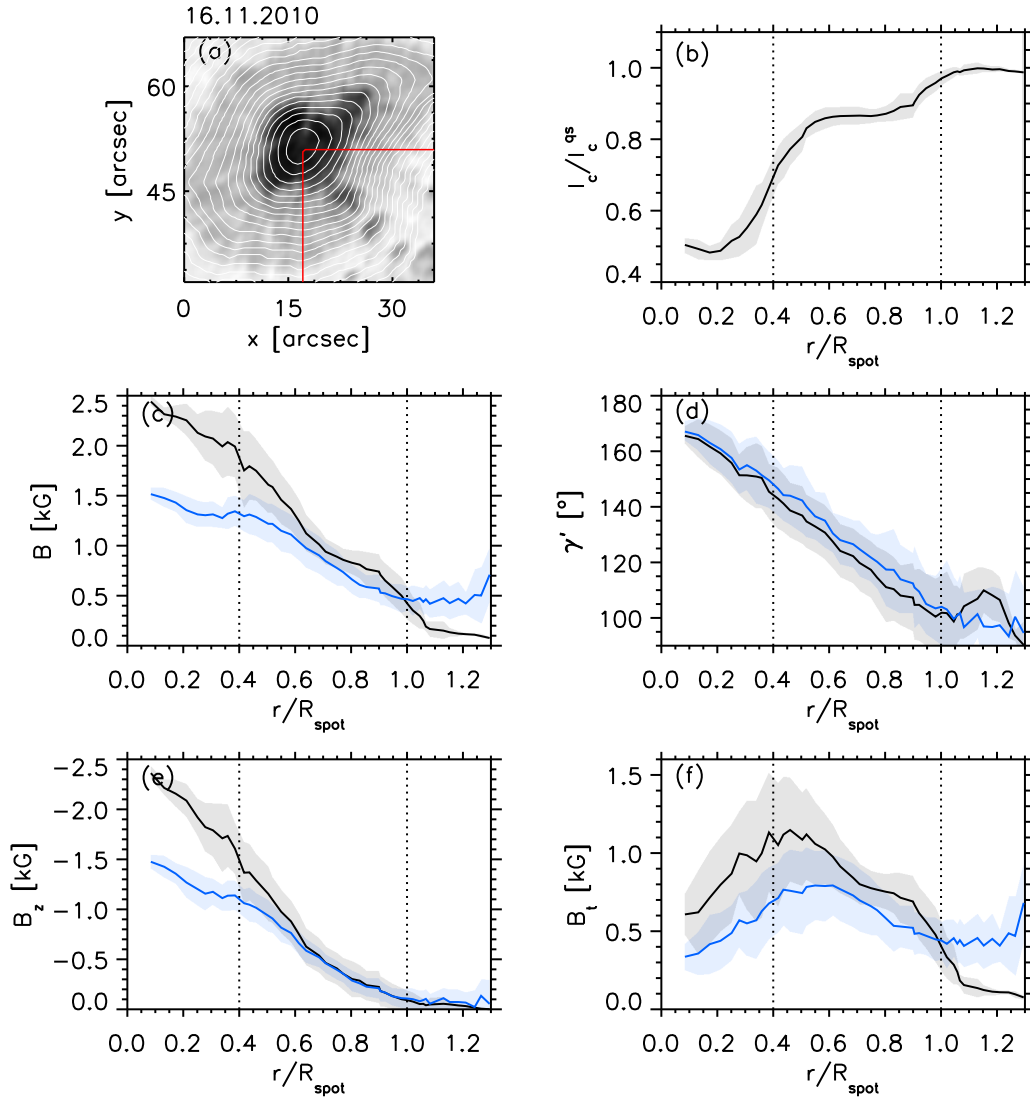


Figure 5.14: Same as Fig. 5.13, but for the observations recorded on 16 November, 2010.

~ 2.3 kG in the photosphere, decreasing to ~ 1.8 kG at the umbra-penumbra boundary. In the upper chromosphere it amounts to ~ 1.3 kG at the sunspot center and it remains almost constant to the umbra-penumbra boundary. The center of the sunspot on 16 November, 2010 has a value of B around ~ 2.5 kG and of ~ 1.9 kG at the umbra-penumbra boundary in the photosphere. In the upper chromosphere B is nearly constant at a value ~ 1.4 kG from the sunspot center to the umbra-penumbra boundary. The difference in the values of B between the photosphere and upper chromosphere, decreases from the umbra-penumbra boundary towards the outer boundary of the sunspot. This is valid for both days. Outside the sunspot's boundary, the radial profile of B on 14 and 16 November, 2010 indicates higher values in the upper chromosphere compared to the photosphere.

Azimuthally averaged radial profiles of γ' from both days suggest that the magnetic field in the upper chromosphere is more vertical compared to the magnetic field in the photosphere both in the umbra and the penumbra. The magnetic field in the upper chromosphere is on average 10 - 20° less inclined compared to the photosphere on 14 November, 2010. On 16 November, 2010 it is only 5 - 10° less inclined in the upper chromosphere.

The vertical component of the magnetic field, B_z , shows a negligible difference between the upper chromosphere and the photosphere for $r \geq 0.6R_{\text{spot}}$ on both days. The maximum of the transverse component of the magnetic field, B_t , in the photosphere is found at the $r \approx 0.4R_{\text{spot}}$ and in the upper chromosphere it is at $r \approx 0.60R_{\text{spot}}$.

5.3.5 Vertical gradient of B

We estimated the vertical gradient of the magnetic field $\Delta B/\Delta d$ (here d denotes the geometrical depth, i. e. d increases into the Sun) between the photosphere and upper chromosphere by assuming that the He I triplet forms approximately 1000 km above the formation height of Si I 10827.1 Å in the sunspots. This difference is inferred from a study of Centeno et al. (2006) who retrieved this height difference between the photosphere and formation height of the He I triplet in the sunspot umbra by analyzing phase spectra of LOS velocities inferred from the Si I 10827.1 Å and the He I triplet. We are aware that the formation height of the He I triplet could be significantly different for the umbra and the penumbra.

We learned in the previous chapter that due to the highly corrugated iso- τ surfaces of sunspot penumbrae we see the decreasing magnetic field strength with optical depth in the azimuthal averages. So, it is important to know how it affects the estimation of $\Delta B/\Delta d$ between the photosphere and the upper chromosphere. This is why we also estimate $\Delta B/\Delta d$ between $\log \tau=0.0$ and the upper chromosphere and between $\log \tau=-2.3$ and the upper chromosphere. First we estimated difference of geometrical depth, d_{diff} between $\log \tau=0.0$ and $\log \tau=-2.3$ for each pixel, assuming hydrostatic equilibrium. And then geometrical depth difference between $\log \tau=0.0$ and the upper chromosphere and between $\log \tau=-2.3$ and the upper chromosphere are assumed to be $1000+(d_{\text{diff}}/2)$ km and $1000-(d_{\text{diff}}/2)$ km, respectively.

The radial dependence of $\Delta B/\Delta d$, estimated between the photosphere and upper chromosphere, is displayed in Fig. 5.15 for both days. *Solid* curves represent $\Delta B/\Delta d$ between the average photosphere and the upper chromosphere. $\Delta B/\Delta d$ from $\log \tau=0.0$ as well as $\log \tau=-2.3$ to the upper chromosphere is presented by *dot-dashed* and *dashed* curves, respectively. In the center of the umbra $\Delta B/\Delta d$ is similar, irrespective of the photospheric layer used in estimation of the gradient. B decreases in the darkest part of umbra on average by 0.8-0.9 G km⁻¹ between the photosphere and the upper chromosphere. From the center of the sunspot towards its outer boundary, the values of $\Delta B/\Delta d$ decrease, i.e., B increases with geometrical depth with a slower rate in the penumbra compared to the umbra. The way $\Delta B/\Delta d$ drops with r/R_{spot} depends significantly on the layer at which the photospheric field is taken. The higher this is the more closely linear $\Delta B/\Delta d$ becomes.

5.3.6 Magnetic field twist

To learn about the twist of the sunspot's magnetic field we calculated the difference between azimuth angle of the magnetic field in the photosphere and that of a potential field, $\phi'_{\text{Ph}} - \phi'_{\text{Pot}}$, where ϕ'_{Ph} and ϕ'_{Pot} denotes the azimuth angle in the photosphere and the azimuth angle of a potential field derived from the photospheric magnetic field, respectively. We also calculated the twist of the upper chromospheric magnetic vector, $\phi'_{\text{Ch}} - \phi'_{\text{Pot}}$, where ϕ'_{Ch} denotes azimuth angle in the upper chromosphere and the potential field is calculated

Table 5.2: Statistics of twist and differential twist on 14, November 2010.

$\Delta\phi'$	Area under consideration	Mean [°]	FWHM [°]
$\phi'_{\text{Ph}} - \phi'_{\text{Pot}}$	Right	-16	40
	Left	5	20
	All	-6	30
$\phi'_{\text{Ch}} - \phi'_{\text{Pot}}$	Right	-16	50
	Left	4	40
	All	-7	40
$\phi'_{\text{Ch}} - \phi'_{\text{Ph}}$	Right	0	30
	Left	-1	40
	All	-1	30

Table 5.3: Statistics of twist and differential twist on 16, November 2010.

$\Delta\phi'$	Area under consideration	Mean [°]	FWHM [°]
$\phi'_{\text{Ph}} - \phi'_{\text{Pot}}$	Right	-24	30
	Left	1	30
	All	-13	50
$\phi'_{\text{Ch}} - \phi'_{\text{Pot}}$	Right	-25	60
	Left	4	40
	All	-12	50
$\phi'_{\text{Ch}} - \phi'_{\text{Ph}}$	Right	-1	20
	Left	3	20
	All	1	20

from the chromospheric magnetic field. The potential field is calculated with the Fourier method (Alissandrakis 1981, Gary 1989). Finally, we determined the differential twist between the photosphere and the upper chromosphere, i.e. difference of the azimuth angle between the upper chromosphere and the photosphere, $\phi'_{\text{Ch}} - \phi'_{\text{Ph}}$. All twist maps are displayed in Fig. 5.16 for both days of observations. Positive values denote anti-clockwise twist. The sunspot obviously exhibits twist in both directions, but clockwise twist (*green* and *blue* in Fig. 5.16) being more common in both atmospheric layers on both days. The pattern suggest by Fig. 5.16(a),(b),(d),(e) is of the field of the sunspot diverging slightly away from the negative y-axis on the 14 November 2010 and away from roughly the direction of the disk center on the 16 November 2010. Figs. 5.7(a) and 5.8(a) reveal the presence of same polarity magnetic flux just outside the sunspot's border on these days Fig. 5.16 indicates that the sunspot's field opens up to move around this external field. The maps of $\phi'_{\text{Ch}} - \phi'_{\text{Ph}}$ show differential twist in both directions in some areas but $\phi'_{\text{Ch}} - \phi'_{\text{Ph}}$ is small in most parts of the penumbra. $\phi'_{\text{Ch}} - \phi'_{\text{Ph}}$ maps also show that differential twist is higher in the outer penumbra compared to the inner penumbra.

For a more quantitative insight we plotted histograms of all the twist maps. Histograms shown in Fig. 5.17 are plotted separately for the right and the left half part of

the sunspot as well as for the complete sunspot. Separation of the left part from the right part is shown by a line in Fig. 5.16. On average the right part has clockwise twist and the left part has anti-clockwise twist in both atmospheric heights on both days. For quantitative information see Tables 5.2 and 5.3. On 14 November, 2010, the average twist of the photospheric and the upper chromospheric azimuth angle was -6° and -7° , respectively. The average twist is -13° in the photosphere and -12° in the upper chromosphere on 16 November 2010. Histograms of the twist maps indicate that the distribution of the upper chromospheric twist is wider than that of the photosphere. On average, the differential twist between the photosphere and the chromosphere is very small.

The radial dependence of the differential twist, $\phi'_{\text{Ch}} - \phi'_{\text{Ph}}$ for both days is presented in Fig. 5.18. Azimuthal averages are only calculated for areas shown above the *red* lines in Figure 5.13(a) and Figure 5.14(a) for 14 and 16 November, 2010, respectively. On 14 November, 2010 the differential twist increases from 0° to $\sim 21^\circ$ between the umbra-penumbra boundary and the outer boundary of the sunspot. On 16 November, 2010 the differential twist average $\sim 4^\circ$ out to $r = R_{\text{spot}}$.

5.4 Discussion and conclusion

5.4.1 Magnetic field strength

We have measured and compared the magnetic field vector of a sunspot in its photospheric and upper chromospheric layers. In the umbra we found the a value of B around 2.5/2.8 kG in the photosphere and 1.6/1.8 kG in the upper chromosphere from the observations recorded on 14/16 November, 2010. On average the upper chromospheric umbral magnetic field strength is reduced by a factor 1.4-1.6 compared to the photosphere. These difference between the upper chromospheric and the photospheric magnetic field strength are comparable with the results of Rüedi et al. (1995), who used the same spectral lines. A striking feature of the upper chromospheric magnetic field is that it is almost constant from the sunspot's center to the umbra-penumbra boundary; it decreases by less than a factor of 1.1. For the comparison at the umbra-penumbra boundary the photospheric magnetic field is reduced by factor 1.2-1.4 compared to the center of the sunspot, which is consistent with values found earlier (Solanki et al. 1992, Balthasar and Schmidt 1993, Skumanich et al. 1994, Keppens and Martinez Pillet 1996, Westendorp Plaza et al. 2001c, Mathew et al. 2003, Borrero and Ichimoto 2011).¹

The the magnetic field strength in the penumbra drop by an average factor of 1.2 between the photosphere and the chromosphere and this factor decreases steadily from the umbra-penumbra boundary (1.4) to the outer boundary of the sunspot (1.0). We see a magnetic canopy structure outside the visible boundary of the sunspot, where the upper chromospheric field is higher by up to ~ 300 G compared to the field at the photopshere. These magnetic canopy results from expansion of the sunspot's magnetic field with height, thus the magnetic field continue beyond the the visible boundary of sunspots as seen in continuum images. The magnetic canopy has been observed by Jones and Giovanelli (1982) comparing magnetogram obtained in the photosphere using the Fe I 8688 Å line

¹We inferred this number from published figures, or those provided by authors, for those papers where this number was not explicitly stated.

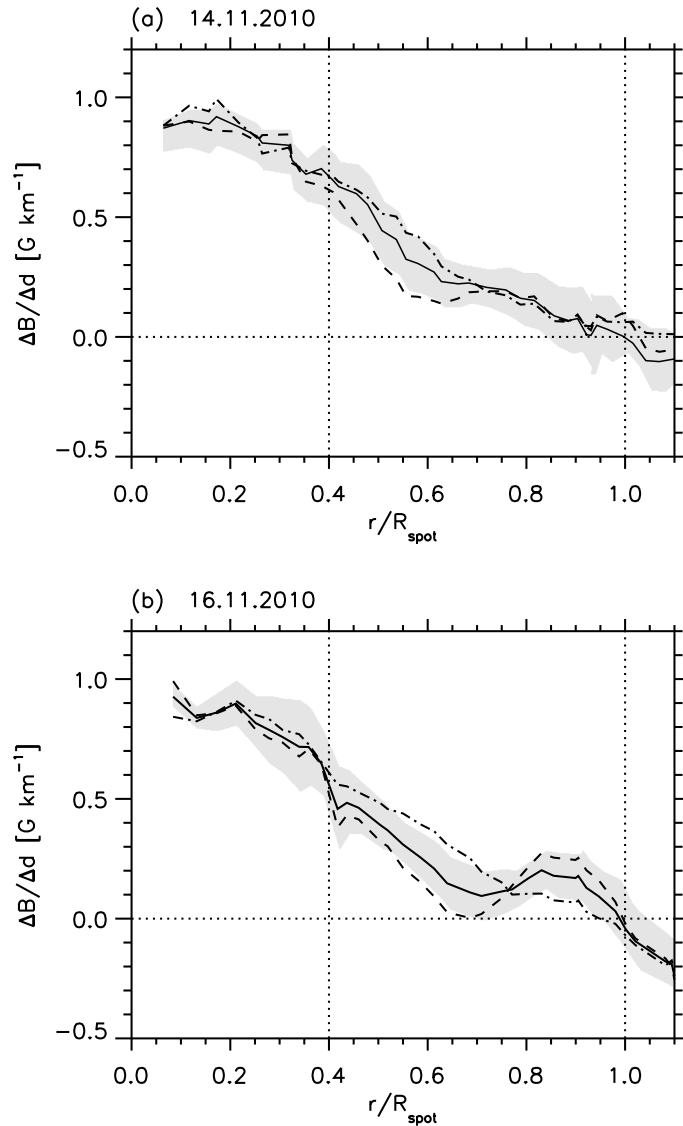


Figure 5.15: Vertical gradient of B , $\Delta B/\Delta d$, between the photosphere and upper chromosphere as a function of r/R_{spot} . *Solid* curves represent $\Delta B/\Delta d$ estimated with the average value of B in the photosphere. *Dashed* and *dot-dashed* curves show $\Delta B/\Delta d$ from $\log \tau=0.0$ and $\log \tau=-2.3$, respectively. *Upper* and *lower* panels correspond to 14 and 16 November, 2010, respectively.

and that of obtained from the chromospheric Ca II 8542 Å line. Magnetic canopy in the photosphere have been regularly detected using different spectral lines as a diagnostic (Solanki et al. 1992, Lites et al. 1993, Solanki et al. 1994, Adams et al. 1994, Skumanich et al. 1994, Keppens and Martinez Pillet 1996, Rueedi et al. 1998, Solanki et al. 1999). The general structure of the field is consistent with magnetic flux concentration expanding with height.

The light-bridge exhibits a lower magnetic field strength compared to the surrounding umbra at its photospheric layer. This is a well known property of light-bridges (Rimmele 1997, Berger and Berdyugina 2003, Jurčák et al. 2006, Rimmele 2008). Signatures of the light-bridge do not exist in the upper chromosphere, thus at these height, at the location of light-bridge the magnetic field has a similar strength as the surrounding umbra. These

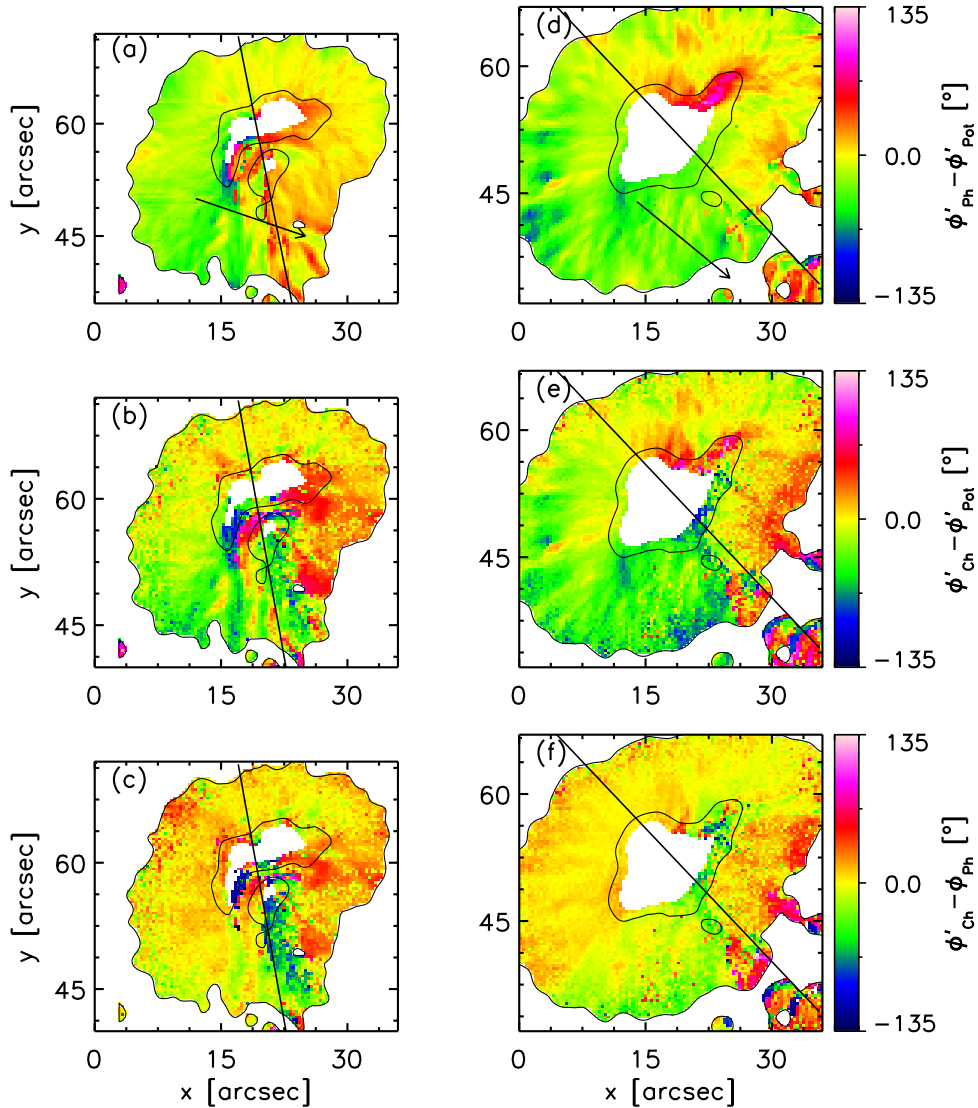


Figure 5.16: Maps of the twist and differential twist angles of the sunspot's magnetic field. Panels (a) and (d): The twist of the photospheric field defined as the difference between the azimuth angle of the photosphere ϕ'_{Ph} and that of a potential field ϕ'_{Pot} , $\phi'_{\text{Ph}} - \phi'_{\text{Pot}}$. Panels (b) and (e): Twist of the field at chromospheric layers, $\phi'_{\text{Ch}} - \phi'_{\text{Pot}}$, where ϕ'_{Ch} is the azimuth angle of the measured chromospheric field. Panels (b) and (e): Differential twist, i.e. the difference between the azimuth angle of the upper chromosphere and that of the photosphere, $\phi'_{\text{Ch}} - \phi'_{\text{Ph}}$. Panels in *left* and *right* columns correspond to the observations recorded 14 November, 2010 and 16 November, 2010, respectively. *Arrows* in the panels (a) and (d) mark the direction to disk center.

results are consistent with the findings of Rüedi et al. (1995). In the brightest part of the light-bridge the upper chromospheric magnetic field is higher in strength by ~ 200 G compared to the photosphere. This and other results of our work are consistent indicate a cusp-like shape of the magnetic field lines above the light-bridge forming a canopy as proposed by Jurčák et al. (2006). In the deep photosphere magneto-convection causes nearly field free gaps. In the upper atmosphere field from surrounding umbra expands

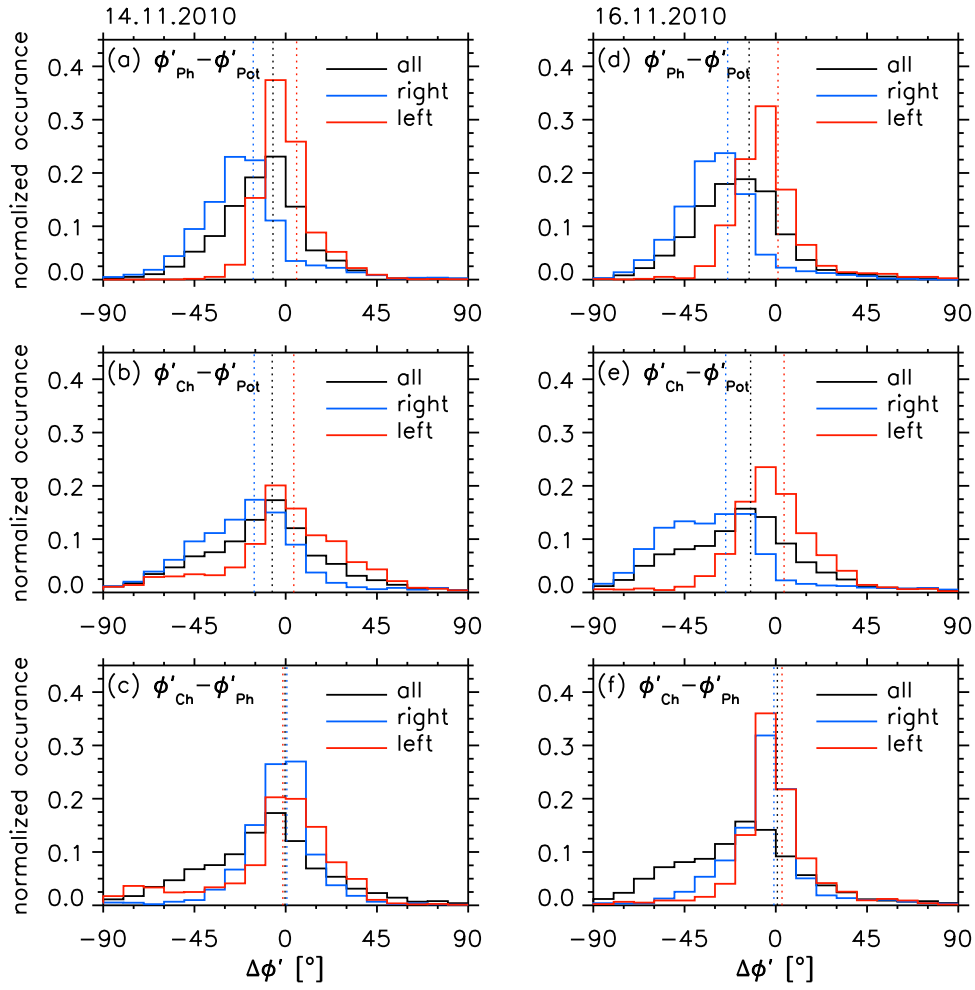


Figure 5.17: Histograms of twist and differential twist of the sunspot’s magnetic field. Panels (a) and (d): $\phi'_{Ph} - \phi'_{Pot}$. Panels (b) and (e): $\phi'_{Ch} - \phi'_{Pot}$. Panels (c) and (f): $\phi'_{Ch} - \phi'_{Ph}$. *Blue, red and black* histograms derived from pixels in *right, left and all* parts of the sunspot, respectively (*right and left* part is separated by a *line* in Fig. 5.16). *Dotted* vertical lines represent the average twist. Panels in *left* and *right* columns correspond to the observations recorded on 14 November, 2010 and 16 November, 2010, respectively.

and fills the field free gaps above the light-bridge.

5.4.2 Vertical gradient of B

We found that the darkest part of the sunspot, magnetic field strength decreases from the photosphere towards the upper chromosphere by the rate of $0.5\text{-}1.0\text{ G km}^{-1}$. These values are higher than values found by Ruedi et al. (1995). The reason for this discrepancy is mainly the assumption about the formation height of the He I triplet. Whereas Ruedi et al. (1995) assume that in sunspots He I triplet forms 1500-2000 km above the photosphere, we considered height difference of 1000 km. In the penumbra the magnetic field strength decreases more slowly, with values between $0\text{-}0.85\text{ G km}^{-1}$. In the outer penumbra and outside the visible boundary of the sunspot the gradient has negative values, indicating the

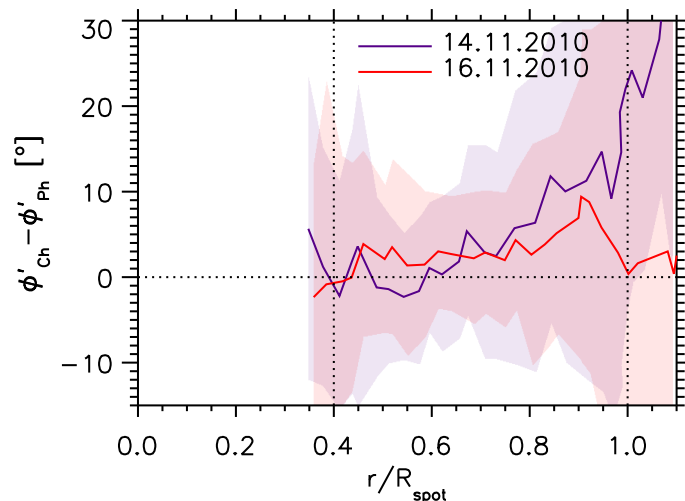


Figure 5.18: Radial dependence of $\phi'_{Ch} - \phi'_{Ph}$ as a function of r/R_{spot} . *Blue* and *red* curves correspond to $\phi'_{Ch} - \phi'_{Ph}$ as obtained from the observations recorded on 14 November, 2010 and 16 November, 2010, respectively.

presence of a magnetic canopy. Here the vertical gradient in the penumbra may be underestimated because of the underestimation of the magnetic field strength in the photosphere due to unresolved opposite polarities.

5.4.3 Inclination

We found that the magnetic field in the penumbra is less inclined in the upper chromosphere compared to the photosphere by $10\text{-}20^\circ/5\text{-}10^\circ$ on 14/16 November, 2010. More vertical magnetic field in penumbrae at higher photospheric layers compared to the deep photosphere has reported by few authors (Westendorp Plaza et al. 2001c, Sánchez Cuberes et al. 2005, Borrero and Ichimoto 2011). Westendorp Plaza et al. (2001c) and Borrero and Ichimoto (2011) explain the more vertical field in the upper photosphere by the existence of a magnetic canopy, which they observed in outer half of the sunspot. SOT/SP observations with recently developed spatially coupled inversions (van Noort 2012) also show that, in azimuthal averages, everywhere in the sunspot the magnetic field becomes more vertical with heights (Tiwari et al. 2013b). The more inclined magnetic field in lower photospheric layer can be explained by penumbral fine structure. Borrero et al. (2008) and Tiwari et al. (2013a) have shown that the more vertical field of spines expands and cover the more horizontal magnetic field lines (intra-spines) or filaments (in general accordance with the geometry proposed by Solanki and Montavon (1993)) i.e., in upper photosphere and in chromosphere we see mostly field from spines whereas in deeper layer we see both spines and intra-spine. Therefore, the inclination in the azimuthal averages appears more horizontal in deeper photosphere, resulting from smearing of horizontal and vertical field lines. This could also be the case in the umbra due to presence of umbral dots.

5.4.4 Twist of sunspot's magnetic field

We found that both, the upper chromospheric and the photospheric magnetic field of the sunspot, was clockwise twisted with respect to the potential field by an average angle of 6° and 7° , respectively on 14 November, 2010. On 16 November, 2010 the twist increases to 13° and 12° in the photosphere and upper chromosphere, respectively. The sunspot has twist in both direction but clockwise twist dominates. Sunspots with both senses of twist at the same time have been observed earlier (Tiwari et al. 2009, Socas-Navarro 2005). A clockwise twist corresponds to negative magnetic helicity (Tiwari et al. 2009). The observed sunspot therefore follows the helicity hemispheric rule (Hale 1925, 1927, Richardson 1941, Hagino and Sakurai 2004, Nandy 2006, Bernasconi et al. 2005, Pevtsov et al. 2008). According to the helicity hemispheric rule sunspots in the northern and southern hemispheres exhibit negative and positive helicity, respectively.

6 Summary and Outlook

Magnetic and velocity fields of sunspots have been studied on both fine and global spatial scales in the preceding chapters of the thesis.

The first part (Chapter 3, which largely follows the paper published by [Joshi et al. 2011](#)) of the thesis presents the observations of cooler downflows in the body of a penumbra, providing first direct indication of the presence of the overturning convection in penumbrae. The analyzed data comprise the deep photospheric C I 5380 Å line obtained with SST/CRISP. These observations support the convection as a heat transport mechanism in penumbrae as proposed in the gappy penumbra model ([Scharmer and Spruit 2006](#)) and in the convective roll model ([Zakharov et al. 2008](#)). These results are supported by [Scharmer et al. \(2011\)](#), who also analyzed the C I 5380 Å line observed with SST/CRISP. Evidences in support of the presence of the overturning convection in penumbrae have been growing: narrow lanes of downflows at the edges of penumbral filaments that harbour hot upflows have been observed in the Fe I 6301.5 Å and Fe I 6302.5 Å spectral lines by [Scharmer and Henriques \(2012\)](#) (using SST/CRISP observations) and [Tiwari et al. \(2013a\)](#) (using Hinode SOT/SP observations).

Results from [Tiwari et al. \(2013a\)](#) have shown that these downflows appear at the edges of penumbral filaments and the filaments carry a substantial amount of horizontal magnetic field (~ 1 kG) which modifies the assumption of the field free gap model of the penumbra proposed by [Scharmer and Spruit \(2006\)](#). The study of penumbral filaments using spectro-polarimetric observation of the Fe I 15648.5 Å line, which forms in the deep photosphere and has the highest magnetic sensitivity (effective Landé factor $g_{\text{eff}}=3$), can be a next step in establishing and confirming the convective nature of the penumbral filaments as well as to investigate the magnetic structure of penumbral filaments in the deep photosphere. Big telescopes of the new generation like the GREGOR (1.5 m primary aperture, [Schmidt et al. 2012](#)) and the New Solar Telescope (NST, 1.6 m primary aperture, [Cao et al. 2010](#)) will be able to provide observations with a spatial resolution around $0''.25$, at 15648.5 Å (close to spatial resolution of SOT/SP at 6301.5 Å). The spatial distribution of the net circular polarization observed in the Fe I 15648.5 Å line is found to be completely different compared to that in the Fe I 6301.5 Å and Fe I 6302.5 Å lines ([Schlichenmaier and Collados 2002](#)). Counting on this fact, studying penumbrae in the Fe I 15648.5 Å line would be interesting.

Another important study to carry out in future is about the twisting motions of penumbral filaments. Twisting motions of penumbral filaments ([Ichimoto et al. 2007b](#)) are thought to be an indirect evidence of convection in penumbral filaments ([Ichimoto et al. 2007b](#), [Spruit et al. 2010](#), [Bharti et al. 2010](#)). Recently, however, [Bharti et al. \(2012\)](#) suggested that this apparent twisting motion of filaments could be due to the transverse (kink) oscillation of penumbral filaments. These oscillations are excited near the heads of the fila-

ments and travel towards their tails. To confirm and establish the relation between twisting motions and transverse oscillations of penumbral filaments Doppler measurements with high spatial and temporal resolution are required.

Chapter 4 presents a study of vertical gradients of the magnetic field strength of a sunspot observed with SOT/SP. The stratified atmosphere of the sunspot is obtained with spatially coupled inversion (SPINOR) of the Fe I 6301.5 Å and Fe I 6302.5 Å lines. We found patches where the magnetic field strength decreases with optical depth in the penumbra and these patches are arranged in a ring-like structure in the inner penumbra. These patches coincides with the inner parts (i.e. towards the umbra) of bright penumbral filaments. We conclude that these local canopy-like structures are due to expanding strong magnetic fields from the spines which cover the weaker and more horizontal field of the filaments from the top. The magnetic field in the umbra increases with geometrical depth at an average rate of $\sim 1.7 \text{ G km}^{-1}$. The magnetic field retrieved from the VTT/TIP-2 observations (the Si I 10827.1 Å and the Ca I 10833.4 Å lines) shows a gradient of around 1.3 G km^{-1} . These results agree with values found earlier in the literature. The most striking result found in this study is that radial profiles of the magnetic field gradient, obtained from azimuthal averages, shows that the magnetic field strength decreases with optical depth in the inner penumbra. This result is found independently in both VTT/TIP-2 and SOT/SP observations. A comparison of the observational results with MHD simulations suggests that the observation of the decreasing magnetic field strength with optical depth is an effect of the strongly corrugated iso- τ surfaces. In addition to the corrugated iso- τ surfaces, unresolved deep-lying opposite polarity patches can also contribute to the observed decreasing magnetic field strength with optical depth. This is due to a cancellation of polarized signals. This latter statement that unresolved opposite polarities cause the observed decrease of magnetic field strength with depth remains unproven due to the small spatial scales and the limited spatial resolution of the available observations. This statement could be tested by higher spatial resolution observations from SST, GREGOR and NST.

The 3D structure of a sunspot (observed with VTT/TIP-2) obtained through state-of-the-art inversion techniques is presented in Chapter 5. We compared the magnetic field structure in the photosphere retrieved from the Si I 10827.1 Å and the Ca I 10833.4 Å with that in the upper chromosphere retrieved from the He I triplet at 10830.0 Å. The magnetic field in the upper chromosphere is found to be lower than that of the photosphere by a factor of 1.4-1.6. The most striking result is that the magnetic field in the upper chromosphere is less inclined, i.e. less horizontal, compared to that in the photosphere. We interpret that is due to spatial averaging (low spatial resolution, $1''0$) over fluted magnetic structures of the penumbra (spines and inter-spines). The photosphere shows more inclined magnetic field, whereas the inclination of the field in the upper chromosphere does not fluctuate on small scales. In Chapter 5 we also analyzed the magnetic field properties of a light-bridge. The magnetic field strength of the light-bridge is found to be weaker compared to the surrounding umbra at the photospheric level. In the upper chromosphere light-bridge is not visible in the map of magnetic field strength. The field strength in the upper chromosphere above the light-bridge is found to be similar or higher than that in the light-bridge at the photospheric layer. The observed inclination angle, azimuth direction and strength of the magnetic field suggest that the umbral field expands and covers the light-bridge at the upper chromospheric level.

High spatial resolution observations of the upper chromospheric magnetic field of sunspots have not been possible so far. Spectro-polarimetric observations of sunspots in the He I 10830 Å triplet with TIP-2 at the GREGOR will be a next big step in understanding the chromospheric magnetic field. The study presented in Chapter 5 can be revisited with higher spatial resolution observations of sunspots and pores.

Another outlook of the thesis is to study penumbrae formation. A few recent studies suggest the pre-existing canopy field in the chromosphere as a precursor of penumbra formation in the photosphere (Shimizu et al. 2012, Lim et al. 2013, Romano et al. 2013). Lim et al. (2013) have suggested that a penumbra forms when the emerging field in the photosphere is constrained to emerge further to higher layers by the pre-existing chromospheric canopy field. So far, the vector magnetic field has not been observed simultaneously in the photosphere and in the chromosphere during formation of a penumbra. Simultaneous Spectro-polarimetric observations in the photospheric Si I 10827.1 Å line and the upper chromospheric He I triplet at 10830 Å of an emerging flux region can substantially improve our understanding of the physical processes behind penumbrae formation.

Bibliography

- Abdussamatov, H. I., 1971a, On the Magnetic Fields and Motions in Sunspots at Different Atmospheric Levels, *Solar Phys.*, 16, 384
- Abdussamatov, H. I., 1971b, Observations of the Two-Level Structure of Sunspot Magnetic Fields (presented by N. S. Soboleva), in *Solar Magnetic Fields*, (Ed.) R. Howard, vol. 43 of IAU Symposium, p. 231
- Abdussamatov, K. I., 1976, On fine structure of the magnetic field and brightness in the penumbrae of sunspots, *Solar Phys.*, 48, 117
- Adams, M., Solanki, S. K., Hagyard, M. J., Moore, R. L., 1994, A Search for Sunspot Canopies Using a Vector Magnetograph, in *Cool Stars, Stellar Systems, and the Sun*, (Ed.) J.-P. Caillault, vol. 64 of *Astronomical Society of the Pacific Conference Series*, p. 342
- Adjabshirzadeh, A., Koutchmy, S., 1983, Photometric analysis of sunspot umbral dots. III Spectrophotometry and preliminary model of a 2-component umbra, *A&A*, 122, 1
- Alissandrakis, C. E., 1981, On the computation of constant alpha force-free magnetic field, *A&A*, 100, 197
- Alissandrakis, C. E., Dialetis, D., Mein, P., Schmieder, B., Simon, G., 1988, The Ever-shed flow in the solar photosphere, chromosphere and chromosphere-corona transition region, *A&A*, 201, 339
- Andretta, V., Jones, H. P., 1997, On the Role of the Solar Corona and Transition Region in the Excitation of the Spectrum of Neutral Helium, *ApJ*, 489, 375
- Anstee, S. D., O'Mara, B. J., 1995, Width cross-sections for collisional broadening of s-p and p-s transitions by atomic hydrogen, *MNRAS*, 276, 859
- Asai, A., Ishii, T. T., Kurokawa, H., 2001, Plasma Ejections from a Light Bridge in a Sunspot Umbra, *ApJ*, 555, L65
- Auer, L. H., Heasley, J. N., 1978, The origin of broad-band circular polarization in sunspots, *A&A*, 64, 67
- Avrett, E. H., Fontenla, J. M., Loeser, R., 1994, Formation of the Solar 10830 Angstrom Line, in *Infrared Solar Physics*, (Eds.) D. M. Rabin, J. T. Jefferies, C. Lindsey, vol. 154 of IAU Symposium, p. 35

- Balthasar, H., 1984, Asymmetries and wavelengths of solar spectral lines and the solar rotation determined from Fourier-transform spectra, *Solar Phys.*, 93, 219
- Balthasar, H., Gömöry, P., 2008, The three-dimensional structure of sunspots. I. The height dependence of the magnetic field, *A&A*, 488, 1085
- Balthasar, H., Schmidt, W., 1993, Polarimetry and spectroscopy of a simple sunspot. 2: On the height and temperature dependence of the magnetic field, *A&A*, 279, 243
- Balthasar, H., Schmidt, W., 1994, Polarimetry and spectroscopy of a simple sunspot. IV. Umbral structures observed in FeI 1027nm, *A&A*, 290, 649
- Bard, S., Carlsson, M., 2008, Constructing Computationally Tractable Models of Si I for the 1082.7 nm Transition, *ApJ*, 682, 1376
- Barklem, P. S., O'Mara, B. J., 1997, The broadening of p-d and d-p transitions by collisions with neutral hydrogen atoms, *MNRAS*, 290, 102
- Barklem, P. S., O'Mara, B. J., Ross, J. E., 1998, The broadening of d-f and f-d transitions by collisions with neutral hydrogen atoms, *MNRAS*, 296, 1057
- Beck, C., 2011, An uncombed inversion of multiwavelength observations reproducing the net circular polarization in a sunspot's penumbra, *A&A*, 525, A133
- Beckers, J. M., Schröter, E. H., 1969, The Intensity, Velocity and Magnetic Structure of a Sunspot Region. IV: Properties of a Unipolar Sunspot, *Solar Phys.*, 10, 384
- Bellot Rubio, L. R., Balthasar, H., Collados, M., Schlichenmaier, R., 2003, Field-aligned Evershed flows in the photosphere of a sunspot penumbra, *A&A*, 403, L47
- Bellot Rubio, L. R., Balthasar, H., Collados, M., 2004, Two magnetic components in sunspot penumbrae, *A&A*, 427, 319
- Bellot Rubio, L. R., Langhans, K., Schlichenmaier, R., 2005, Multi-line spectroscopy of dark-cored penumbral filaments, *A&A*, 443, L7
- Bellot Rubio, L. R., Schlichenmaier, R., Tritschler, A., 2006, Two-dimensional spectroscopy of a sunspot. III. Thermal and kinematic structure of the penumbra at 0.5 arcsec resolution, *A&A*, 453, 1117
- Bellot Rubio, L. R., Schlichenmaier, R., Langhans, K., 2010, Searching for Overturning Convection in Penumbral Filaments: Slit Spectroscopy at Ofarcs2 Resolution, *ApJ*, 725, 11
- Berger, T. E., Berdyugina, S. V., 2003, The Observation of Sunspot Light-Bridge Structure and Dynamics, *ApJ*, 589, L117
- Bernasconi, P. N., Rust, D. M., Hakim, D., 2005, Advanced Automated Solar Filament Detection And Characterization Code: Description, Performance, And Results, *Solar Phys.*, 228, 97

- Bharti, L., Joshi, C., Jaaffrey, S. N. A., 2007, Observations of Dark Lanes in Umbral Fine Structure from the Hinode Solar Optical Telescope: Evidence for Magnetoconvection, *ApJ*, 669, L57
- Bharti, L., Solanki, S. K., Hirzberger, J., 2010, Evidence for Convection in Sunspot Penumbrae, *ApJ*, 722, L194
- Bharti, L., Schüssler, M., Rempel, M., 2011, Continuum brightness of solar magnetic elements, *ApJ* (submitted)
- Bharti, L., Cameron, R. H., Rempel, M., Hirzberger, J., Solanki, S. K., 2012, Waves as the Source of Apparent Twisting Motions in Sunspot Penumbrae, *ApJ*, 752, 128
- Biermann, L., 1941, Der gegenwärtige Stand der Theorie konvektiver Sonnenmodelle, *Vierteljahresschrift der Astronomischen Gesellschaft*, 76, 194
- Bloomfield, D. S., Lagg, A., Solanki, S. K., 2007, The Nature of Running Penumbrae Waves Revealed, *ApJ*, 671, 1005
- Bogdan, T. J., Judge, P. G., 2006, Observational aspects of sunspot oscillations, *Royal Society of London Philosophical Transactions Series A*, 364, 313
- Bonet, J. A., Sobotka, M., Vazquez, M., 1995, Photometry of sunspot pores from partial eclipse observations., *A&A*, 296, 241
- Börner, P., Kneer, F., 1992, High resolution observations of the Evershed flow, *A&A*, 259, 307
- Borrero, J. M., 2007, The structure of sunspot penumbrae. IV. MHS equilibrium for penumbral flux tubes and the origin of dark core penumbral filaments and penumbral grains, *A&A*, 471, 967
- Borrero, J. M., Ichimoto, K., 2011, Magnetic Structure of Sunspots, *Living Reviews in Solar Physics*, 8, 4
- Borrero, J. M., Kobel, P., 2012, Inferring the magnetic field vector in the quiet Sun. II. Interpreting results from the inversion of Stokes profiles, *A&A*, 547, A89
- Borrero, J. M., Solanki, S. K., 2010, Convective Motions and Net Circular Polarization in Sunspot Penumbrae, *ApJ*, 709, 349
- Borrero, J. M., Solanki, S. K., Bellot Rubio, L. R., Lagg, A., Mathew, S. K., 2004, On the fine structure of sunspot penumbrae. I. A quantitative comparison of two semiempirical models with implications for the Evershed effect, *A&A*, 422, 1093
- Borrero, J. M., Lagg, A., Solanki, S. K., Collados, M., 2005, On the fine structure of sunspot penumbrae. II. The nature of the Evershed flow, *A&A*, 436, 333
- Borrero, J. M., Solanki, S. K., Lagg, A., Socas-Navarro, H., Lites, B., 2006, On the fine structure of sunspot penumbrae. III. The vertical extension of penumbral filaments, *A&A*, 450, 383

- Borrero, J. M., Lites, B. W., Solanki, S. K., 2008, Evidence of magnetic field wrapping around penumbral filaments, *A&A*, 481, L13
- Brants, J. J., Zwaan, C., 1982, The structure of sunspots. IV - Magnetic field strengths in small sunspots and pores, *Solar Phys.*, 80, 251
- Bray, R. J., Loughhead, R. E., 1959, High Resolution Observations of the Granular Structure of Sunspot Umbrae, *Australian Journal of Physics*, 12, 320
- Bray, R. J., Loughhead, R. E., 1964, Sunspots, *The International Astrophysics Series*, London: Chapman Hall
- Brekke, K., Maltby, P., 1963, The Evershed effect at the outer edge of sunspot penumbras, *Annales d'Astrophysique*, 26, 383
- Brosius, J. W., 2005, Mass Flows in a Disappearing Sunspot Plume, *ApJ*, 622, 1216
- Brosius, J. W., White, S. M., 2004, Close Association of an Extreme-Ultraviolet Sunspot Plume with Depressions in the Sunspot Radio Emission, *ApJ*, 601, 546
- Brynildsen, N., Maltby, P., Brekke, P., Fredvik, T., Haugan, S. V. H., Kjeldseth-Moe, O., Wikstol, O., 1998, Flows in Sunspot Plumes Detected with Solar and Heliospheric Observatory, *ApJ*, 502, L85
- Brynildsen, N., Maltby, P., Brekke, P., Haugan, S. V. H., Kjeldseth-Moe, O., 1999, SOHO Observations of the Structure and Dynamics of Sunspot Region Atmospheres, *Solar Phys.*, 186, 141
- Brynildsen, N., Maltby, P., Fredvik, T., Kjeldseth-Moe, O., Wilhelm, K., 2001, Sunspot Plumes and Flow Channels, *Solar Phys.*, 198, 89
- Buente, M., Steiner, O., Pizzo, V. J., 1993, On the interchange instability of solar magnetic flux tubes. I - The influence of magnetic tension and internal gas pressure, *A&A*, 268, 299
- Buurman, J., 1973, The Spectrum of a Large Umbra I, *A&A*, 29, 329
- Cao, W., Gorceix, N., Coulter, R., Ahn, K., Rimmele, T. R., Goode, P. R., 2010, Scientific instrumentation for the 1.6 m New Solar Telescope in Big Bear, *Astronomische Nachrichten*, 331, 636
- Carlsson, M., 1986, A computer program for solving multi-level non-LTE radiative transfer problems in moving or static atmospheres., *Uppsala Astronomical Observatory Reports*, 33
- Centeno, R., Collados, M., Trujillo Bueno, J., 2006, Spectropolarimetric Investigation of the Propagation of Magnetoacoustic Waves and Shock Formation in Sunspot Atmospheres, *ApJ*, 640, 1153
- Centeno, R., Trujillo Bueno, J., Uitenbroek, H., Collados, M., 2008, The Influence of Coronal EUV Irradiance on the Emission in the He I 10830 Å and D₃ Multiplets, *ApJ*, 677, 742

- Chapman, G. A., 1979, New models of solar faculae, *ApJ*, 232, 923
- Charbonneau, P., 1995, Genetic Algorithms in Astronomy and Astrophysics, *ApJS*, 101, 309
- Charbonneau, P., 2005, Dynamo Models of the Solar Cycle, *Living Reviews in Solar Physics*, 2, 2
- Chevalier, S., 1914a, Étude photographique de la photosphère solaire, *Annales de l'Observatoire astronomique de Zô-sè (Chine)*, Tome VIII, Pages C1 - C24, 8, C1
- Chevalier, S., 1914b, Granulation de la photosphère solaire, *Annales de l'Observatoire astronomique de Zô-sè (Chine)*, Tome VIII, Plates I - XIV, 8, 1P
- Chevalier, S., 1916, Étude photographique des taches solaire, *Annales de l'Observatoire astronomique de Zô-sè (Chine)*, Tome IX, Page B1 - B16, 9, B1
- Choudhuri, A. R., 1992, The cluster model of sunspots, in *NATO ASIC Proc. 375: Sunspots. Theory and Observations*, (Eds.) J. H. Thomas, N. O. Weiss, p. 243
- Christopoulou, E. B., Georgakilas, A. A., Koutchmy, S., 2000, Oscillations and running waves observed in sunspots, *A&A*, 354, 305
- Christopoulou, E. B., Georgakilas, A. A., Koutchmy, S., 2001, Oscillations and running waves observed in sunspots. III. Multilayer study, *A&A*, 375, 617
- Collados, M., Martinez Pillet, V., Ruiz Cobo, B., del Toro Iniesta, J. C., Vazquez, M., 1994, Observed differences between large and small sunspots, *A&A*, 291, 622
- Collados, M., Lagg, A., Díaz Garcí A, J. J., Hernández Suárez, E., López López, R., Páez Mañá, E., Solanki, S. K., 2007, Tenerife Infrared Polarimeter II, in *The Physics of Chromospheric Plasmas*, (Eds.) P. Heinzel, I. Dorotovič, R. J. Rutten, vol. 368 of *Astronomical Society of the Pacific Conference Series*, p. 611
- Cowling, T. G., 1957, *Magnetohydrodynamics*, Interscience, New York
- Cuperman, S., Li, J., Semel, M., 1992, Magnetic shear-based removal of the 180-degree ambiguity in the observed transverse photospheric magnetic field - Feasibility and limitations, *A&A*, 265, 296
- Danielson, R. E., 1961a, The Structure of Sunspot Penumbrae. I. Observations., *ApJ*, 134, 275
- Danielson, R. E., 1961b, The Structure of Sunspot Penumbrae. II. Theoretical., *ApJ*, 134, 289
- Danielson, R. E., 1964, The Structure of Sunspot Umbras. I. Observations., *ApJ*, 139, 45
- Danilovic, S., Gandorfer, A., Lagg, A., Schüssler, M., Solanki, S. K., Vögler, A., Katsukawa, Y., Tsuneta, S., 2008, The intensity contrast of solar granulation: comparing Hinode SP results with MHD simulations, *A&A*, 484, L17

- de La Cruz Rodríguez, J., Kiselman, D., Carlsson, M., 2011, Solar velocity references from 3D HD photospheric models, *A&A*, 528, A113
- de Wijn, A. G., Stenflo, J. O., Solanki, S. K., Tsuneta, S., 2009, Small-Scale Solar Magnetic Fields, *Space Sci. Rev.*, 144, 275–315, [0812.4465](#)
- Degenhardt, D., 1991, Stationary siphon flows in thin magnetic flux tubes. II - Radiative heat exchange with the surroundings, *A&A*, 248, 637
- Degenhardt, D., Wiehr, E., 1991, Spatial variation of the magnetic field inclination in a sunspot penumbra, *A&A*, 252, 821
- Deinzer, W., 1965, On the Magneto-Hydrostatic Theory of Sunspots., *ApJ*, 141, 548
- del Toro Iniesta, J. C., 2003, Introduction to Spectropolarimetry
- del Toro Iniesta, J. C., Bellot Rubio, L. R., Collados, M., 2001, Cold, Supersonic Evershed Downflows in a Sunspot, *ApJ*, 549, L139
- Denker, C., 1998, Speckle Masking Imaging of Sunspots and Pores, *Solar Phys.*, 180, 81
- Denker, C., de Boer, C. R., Volkmer, R., Kneer, F., 1995, Speckle masking imaging of the moustache phenomenon., *A&A*, 296, 567
- Dere, K. P., Schmieder, B., Alissandrakis, C. E., 1990, Flow patterns in a sunspot region observed in the photosphere, chromosphere and transition region, *A&A*, 233, 207
- Dialetis, D., Mein, P., Alissandrakis, C. E., 1985, The Evershed flow as a steady-state homogeneous phenomenon, *A&A*, 147, 93
- Felipe, T., Khomenko, E., Collados, M., Beck, C., 2010, Multi-layer Study of Wave Propagation in Sunspots, *ApJ*, 722, 131
- Fludra, A., 2001, Transition region oscillations above sunspots, *A&A*, 368, 639
- Fludra, A., Brekke, P., Harrison, R. A., Mason, H. E., Pike, C. D., Thompson, W. T., Young, P. R., 1997, Active Regions Observed in Extreme Ultraviolet Light by the Coronal Diagnostic Spectrometer on SOHO, *Solar Phys.*, 175, 487
- Franz, M., Schlichenmaier, R., 2009, The velocity field of sunspot penumbrae. I. A global view, *A&A*, 508, 1453
- Franz, M., Schlichenmaier, R., 2013, The velocity field of sunspot penumbrae. II. Return flow and magnetic fields of opposite polarity, *A&A*, 550, A97
- Frutiger, C., Solanki, S. K., Fligge, M., Bruls, J. H. M. J., 1999, Inversion of Stokes profiles, in *Polarization*, (Eds.) K. N. Nagendra, J. O. Stenflo, vol. 243 of *Astrophysics and Space Science Library*, p. 281
- Frutiger, C., Solanki, S. K., Fligge, M., Bruls, J. H. M. J., 2000, Properties of the solar granulation obtained from the inversion of low spatial resolution spectra, *A&A*, 358, 1109

- Gary, G. A., 1989, Linear force-free magnetic fields for solar extrapolation and interpretation, *ApJS*, 69, 323
- Georgakilas, A. A., Christopoulou, E. B., Koutchmy, S., 2000, Oscillations and running waves observed in sunspots. II. Photospheric waves, *A&A*, 363, 306
- Giordano, S., Berrilli, F., Del Moro, D., Penza, V., 2008, The photospheric structure of a solar pore with light bridge, *A&A*, 489, 747
- Gizon, L., Schunker, H., Baldner, C. S., Basu, S., Birch, A. C., Bogart, R. S., Braun, D. C., Cameron, R., Duvall, T. L., Hanasoge, S. M., Jackiewicz, J., Roth, M., Stahn, T., Thompson, M. J., Zharkov, S., 2009, Helioseismology of Sunspots: A Case Study of NOAA Region 9787, *Space Sci. Rev.*, 144, 249
- Grevesse, N., Sauval, A. J., 1998, Standard Solar Composition, *Space Sci. Rev.*, 85, 161
- Hagino, M., Sakurai, T., 2004, Latitude Variation of Helicity in Solar Active Regions, *PASJ*, 56, 831
- Hagyard, M. J., Teuber, D., West, E. A., Tandberg-Hanssen, E., Henze, J. W., Beckers, J. M., Bruner, M., Hyder, C. L., Woodgate, B. E., 1983, Vertical gradients of sunspot magnetic fields, *Solar Phys.*, 84, 13
- Hale, G. E., 1908a, SOLAR VORTICES (Contributions from the Mt. Wilson Solar Observatory, No. 26), *ApJ*, 28, 100
- Hale, G. E., 1908b, On the Probable Existence of a Magnetic Field in Sun-Spots, *ApJ*, 28, 315
- Hale, G. E., 1925, Nature of the Hydrogen Vortices Surrounding Sun-spots, *PASP*, 37, 268
- Hale, G. E., 1927, The Fields of Force in the Atmosphere of the Sun, *Nature*, 119, 708
- Hamedivafa, H., 2008, Application of an Improved Method of Image Segmentation and Some Considerations on Identification and Tracking of Umbral Dots, *Solar Phys.*, 250, 17
- Hartkorn, K., Rimmele, T., 2003, Velocity Measurements of Umbral Dots, in *Current Theoretical Models and Future High Resolution Solar Observations: Preparing for ATST*, (Eds.) A. A. Pevtsov, H. Uitenbroek, vol. 286 of *Astronomical Society of the Pacific Conference Series*, p. 281
- Harvey, J., Hall, D., 1971, Magnetic Fields Measured with the 10830 Å HeI Line, in *Solar Magnetic Fields*, (Ed.) R. Howard, vol. 43 of *IAU Symposium*, p. 279
- Harvey, J. W., Breckinridge, J. B., 1973, Solar Speckle Interferometry, *ApJ*, 182, L137
- Heinemann, T., Nordlund, Å., Scharmer, G. B., Spruit, H. C., 2007, MHD Simulations of Penumbra Fine Structure, *ApJ*, 669, 1390

- Henson, G. D., Kemp, J. C., 1984, Broad-band circular polarimetry of sunspots, 0.4-1.7 microns Spatial scans with a 3.4 arc SEC diameter aperture, *Solar Phys.*, 93, 289
- Henze, J. W., Tandberg-Hanssen, E., Hagyard, M. J., West, E. A., Woodgate, B. E., Shine, R. A., Beckers, J. M., Bruner, M., Hyder, C. L., West, E. A., 1982, Observations of the longitudinal magnetic field in the transition region and photosphere of a sunspot, *Solar Phys.*, 81, 231
- Hewagama, T., Deming, D., Jennings, D. E., Osherovich, V., Wiedemann, G., Zipoy, D., Mickey, D. L., Garcia, H., 1993, Solar magnetic field studies using the 12 micron emission lines. II - Stokes profiles and vector field samples in sunspots, *ApJS*, 86, 313
- Hirzberger, J., Kneer, F., 2001, 2D-spectroscopy of the Evershed flow in sunspots, *A&A*, 378, 1078
- Hirzberger, J., Bonet, J. A., Sobotka, M., Vázquez, M., Hanslmeier, A., 2002, Fine structure and dynamics in a light bridge inside a solar pore, *A&A*, 383, 275
- Hirzberger, J., Stangl, S., Gersin, K., Jurčák, J., Puschmann, K. G., Sobotka, M., 2005, The structure of a penumbral connection between solar pores, *A&A*, 442, 1079
- Hirzberger, J., Feller, A., Riethmüller, T. L., Schüssler, M., Borrero, J. M., Afram, N., Unruh, Y. C., Berdyugina, S. V., Gandorfer, A., Solanki, S. K., Barthol, P., Bonet, J. A., Martínez Pillet, V., Berkefeld, T., Knölker, M., Schmidt, W., Title, A. M., 2010, Quiet-sun Intensity Contrasts in the Near-ultraviolet as Measured from SUNRISE, *ApJ*, 723, L154
- Hofmann, J., Deubner, F.-L., Fleck, B., Schmidt, W., 1994, On the correlation of magnetic field strength and inclination with continuum brightness of a sunspot penumbra, *A&A*, 284, 269
- Holmes, J., 1961, A study of sunspot velocity fields using a magnetically undisturbed line, *MNRAS*, 122, 301
- Holmes, J., 1963, Micrometer and photometric observations of a sunspot velocity field, *MNRAS*, 126, 155
- Hoyle, F., 1949, *Some recent researches in solar physics*, Cambridge University Press
- Ichimoto, K., Shine, R. A., Lites, B., Kubo, M., Shimizu, T., Suematsu, Y., Tsuneta, S., Katsukawa, Y., Tarbell, T. D., Title, A. M., Nagata, S., Yokoyama, T., Shimojo, M., 2007a, Fine-Scale Structures of the Evershed Effect Observed by the Solar Optical Telescope aboard Hinode, *PASJ*, 59, 593
- Ichimoto, K., Suematsu, Y., Tsuneta, S., Katsukawa, Y., Shimizu, T., Shine, R. A., Tarbell, T. D., Title, A. M., Lites, B. W., Kubo, M., Nagata, S., 2007b, Twisting Motions of Sunspot Penumbral Filaments, *Science*, 318, 1597

- Ichimoto, K., Lites, B., Elmore, D., Suematsu, Y., Tsuneta, S., Katsukawa, Y., Shimizu, T., Shine, R., Tarbell, T., Title, A., Kiyohara, J., Shinoda, K., Card, G., Lecinski, A., Stenander, K., Nakagiri, M., Miyashita, M., Noguchi, M., Hoffmann, C., Cruz, T., 2008a, Polarization Calibration of the Solar Optical Telescope onboard Hinode, *Solar Phys.*, 249, 233
- Ichimoto, K., Tsuneta, S., Suematsu, Y., Katsukawa, Y., Shimizu, T., Lites, B. W., Kubo, M., Tarbell, T. D., Shine, R. A., Title, A. M., Nagata, S., 2008b, Net circular polarization of sunspots in high spatial resolution, *A&A*, 481, L9
- Illing, R. M. E., Landman, D. A., Mickey, D. L., 1974a, Observations of broad-band circular polarization in sunspots - Magnetic field correspondence, *A&A*, 37, 97
- Illing, R. M. E., Landman, D. A., Mickey, D. L., 1974b, Broad-band circular and linear polarization in sunspots Center-to-limb variation, *A&A*, 35, 327
- Jafarzadeh, S., 2013, Dynamics of magnetic bright points in the lower solar atmosphere, Ph.D. thesis, Göttingen University, ISBN 978-3-942171-75-5, uni-edition GmbH 2013
- Jahn, K., 1989, Current sheet as a diagnostic for the subphotospheric structure of a SPOT, *A&A*, 222, 264
- Jahn, K., 1992, Magnetohydrostatic equilibrium in sunspot models, in *NATO ASIC Proc. 375: Sunspots. Theory and Observations*, (Eds.) J. H. Thomas, N. O. Weiss, p. 139
- Jahn, K., Schmidt, H. U., 1994, Thick penumbra in a magnetostatic sunspot model., *A&A*, 290, 295
- Jones, H. P., Giovanelli, R. G., 1982, Magnetograph response to canopy-type fields, *Solar Phys.*, 79, 247
- Joshi, J., Pietarila, A., Hirzberger, J., Solanki, S. K., Aznar Cuadrado, R., Merenda, L., 2011, Convective Nature of Sunspot Penumbra Filaments: Discovery of Downflows in the Deep Photosphere, *ApJ*, 734, L18
- Jurčák, J., Bellot Rubio, L., Ichimoto, K., Katsukawa, Y., Lites, B., Nagata, S., Shimizu, T., Suematsu, Y., Tarbell, T. D., Title, A. M., Tsuneta, S., 2007, The Analysis of Penumbra Fine Structure Using an Advanced Inversion Technique, *PASJ*, 59, 601
- Jurčák, J., Sobotka, M., 2007, Observational Evidence for Rising Penumbra Flux Tubes?, *Solar Phys.*, 241, 223
- Jurčák, J., Martínez Pillet, V., Sobotka, M., 2006, The magnetic canopy above light bridges, *A&A*, 453, 1079
- Kalman, B., 1991, Vector magnetic field measurements and penumbra structure, *Solar Phys.*, 135, 299
- Katsukawa, Y., 2007, Observational Analysis of the Relation between Coronal Loop Heating and Photospheric Magnetic Fields, in *New Solar Physics with Solar-B Mission*, (Eds.) K. Shibata, S. Nagata, T. Sakurai, vol. 369 of *Astronomical Society of the Pacific Conference Series*, p. 287

- Katsukawa, Y., Yokoyama, T., Berger, T. E., Ichimoto, K., Kubo, M., Lites, B., Nagata, S., Shimizu, T., Shine, R. A., Suematsu, Y., Tarbell, T. D., Title, A. M., Tsuneta, S., 2007, Formation Process of a Light Bridge Revealed with the Hinode Solar Optical Telescope, *PASJ*, 59, 577
- Keller, C. U., Stenflo, J. O., von der Luhe, O., 1992, High Spatial Resolution Magnetograms of Solar Active Regions, *A&A*, 254, 355
- Keppens, R., Martínez Pillet, V., 1996, The magnetic structure of pores and sunspots derived from Advanced Stokes Polarimeter data., *A&A*, 316, 229
- Kneer, F., 1973, On Some Characteristics of Umbral Fine Structure, *Solar Phys.*, 28, 361
- Kopp, G., Rabin, D., 1992, A relation between magnetic field strength and temperature in sunspots, *Solar Phys.*, 141, 253
- Kosugi, T., Matsuzaki, K., Sakao, T., Shimizu, T., Sone, Y., Tachikawa, S., Hashimoto, T., Minesugi, K., Ohnishi, A., Yamada, T., Tsuneta, S., Hara, H., Ichimoto, K., Suematsu, Y., Shimojo, M., Watanabe, T., Shimada, S., Davis, J. M., Hill, L. D., Owens, J. K., Title, A. M., Culhane, J. L., Harra, L. K., Doschek, G. A., Golub, L., 2007, The Hinode (Solar-B) Mission: An Overview, *Solar Phys.*, 243, 3
- Kuckein, C., Martínez Pillet, V., Centeno, R., 2012a, An active region filament studied simultaneously in the chromosphere and photosphere. I. Magnetic structure, *A&A*, 539, A131
- Kuckein, C., Martínez Pillet, V., Centeno, R., 2012b, An active region filament studied simultaneously in the chromosphere and photosphere. II. Doppler velocities, *A&A*, 542, A112
- Küveler, G., Wiehr, E., 1985, Velocity and asymmetry mapping of sunspots, *A&A*, 142, 205
- Lagg, A., Woch, J., Krupp, N., Solanki, S. K., 2004, Retrieval of the full magnetic vector with the He I multiplet at 1083 nm. Maps of an emerging flux region, *A&A*, 414, 1109
- Lagg, A., Woch, J., Solanki, S. K., Krupp, N., 2007, Supersonic downflows in the vicinity of a growing pore. Evidence of unresolved magnetic fine structure at chromospheric heights, *A&A*, 462, 1147
- Lagg, A., Ishikawa, R., Merenda, L., Wiegmann, T., Tsuneta, S., Solanki, S. K., 2009, Internetwork Horizontal Magnetic Fields in the Quiet Sun Chromosphere: Results from a Joint Hinode/VTT Study, in *The Second Hinode Science Meeting: Beyond Discovery-Toward Understanding*, (Eds.) B. Lites, M. Cheung, T. Magara, J. Mariska, K. Reeves, vol. 415 of *Astronomical Society of the Pacific Conference Series*, p. 327
- Landi Degl'Innocenti, E., Landolfi, M. (Eds.), 2004, *Polarization in Spectral Lines*, vol. 307 of *Astrophysics and Space Science Library*

- Landolfi, M., Landi Degl'Innocenti, E., 1996, Net Circular Polarization in Magnetic Spectral Lines Produced by Velocity Gradients: Some Analytical Results, *Solar Phys.*, 164, 191
- Langhans, K., Scharmer, G. B., Kiselman, D., Löfdahl, M. G., Berger, T. E., 2005, Inclination of magnetic fields and flows in sunspot penumbrae, *A&A*, 436, 1087
- Langhans, K., Scharmer, G. B., Kiselman, D., Löfdahl, M. G., 2007, Observations of dark-cored filaments in sunspot penumbrae, *A&A*, 464, 763
- Leka, K. D., 1997, The Vector Magnetic Fields and Thermodynamics of Sunspot Light Bridges: The Case for Field-free Disruptions in Sunspots, *ApJ*, 484, 900
- Lim, E.-K., Yurchyshyn, V., Goode, P., Cho, K.-S., 2013, Observation of a Non-radial Penumbra in a Flux Emerging Region under Chromospheric Canopy Fields, *ApJ*, 769, L18
- Lites, B. W., Bida, T. A., Scharmer, G. B., 1989, The Magnetic Field Strength of Umbral Dots, in *Bulletin of the American Astronomical Society*, vol. 21 of *Bulletin of the American Astronomical Society*, p. 854
- Lites, B. W., Skumanich, A., Scharmer, G. B., 1990, High-resolution spectra of solar magnetic features. I - Analysis of penumbral fine structure, *ApJ*, 355, 329
- Lites, B. W., Bida, T. A., Johannesson, A., Scharmer, G. B., 1991, High-resolution spectra of solar magnetic features. II - Magnetic fields of umbral brightenings, *ApJ*, 373, 683
- Lites, B. W., Elmore, D. F., Seagraves, P., Skumanich, A. P., 1993, Stokes Profile Analysis and Vector Magnetic Fields. VI. Fine Scale Structure of a Sunspot, *ApJ*, 418, 928
- Lites, B. W., Scharmer, G. B., Berger, T. E., Title, A. M., 2004, Three-Dimensional Structure of the Active Region Photosphere as Revealed by High Angular Resolution, *Solar Phys.*, 221, 65
- Liu, S., 2012, A Coronal Jet Ejection from a Sunspot Light Bridge, *PASA*, 29, 193
- Livingston, W., Wallace, L., 1991, An atlas of the solar spectrum in the infrared from 1850 to 9000 cm⁻¹ (1.1 to 5.4 micrometer)
- Löfdahl, M. G., 2002, Multi-frame blind deconvolution with linear equality constraints, in *Image Reconstruction from Incomplete Data II*, (Ed.) P. J. Bones, M. A. Fiddy, & R. P. Millane, vol. 4792 of *Proc. SPIE*, p. 146
- Loughhead, R. E., Bray, R. J., 1960, The Lifetime and Cell Size of the Granulation in Sunspot Umbrae, *Australian Journal of Physics*, 13, 139
- Louis, R. E., Bayanna, A. R., Mathew, S. K., Venkatakrishnan, P., 2008, Dynamics of Sunspot Light Bridges as Revealed by High-Resolution Images from Hinode, *Solar Phys.*, 252, 43

- Makita, M., Ohki, Y., 1986, The broad-band polarization of sunspots observed from 8 February 1981 to 30 August 1982, *Annals of the Tokyo Astronomical Observatory*, 21, 1
- Maltby, P., 1964, On the velocity field in sunspots, *Astrophysica Norvegica*, 8, 205
- Maltby, P., Brynildsen, N., Brekke, P., Haugan, S. V. H., Kjeldseth-Moe, O., Wikstol, O., Rimmele, T., 1998, Extreme-Ultraviolet Sunspot Plumes Observed with SOHO, *ApJ*, 496, L117
- Maltby, P., Brynildsen, N., Fredvik, T., Kjeldseth-Moe, O., Wilhelm, K., 1999, On the sunspot transition region, *Solar Phys.*, 190, 437
- Martínez Pillet, V., 2000, Spectral signature of uncombed penumbral magnetic fields, *A&A*, 361, 734
- Martínez Pillet, V., 2000, Spectral signature of uncombed penumbral magnetic fields, *A&A*, 361, 734
- Martínez Pillet, V., 2001, Spectral signature of uncombed penumbral magnetic fields. Reply, *A&A*, 369, 644
- Martinez Pillet, V., Vazquez, M., 1993, The continuum intensity-magnetic field relation in sunspot umbrae, *A&A*, 270, 494
- Martínez Pillet, V., Del Toro Iniesta, J. C., Álvarez-Herrero, A., Domingo, V., Bonet, J. A., González Fernández, L., López Jiménez, A., Pastor, C., Gasent Blesa, J. L., Mellado, P., Piqueras, J., Aparicio, B., Balaguer, M., Ballesteros, E., Belenguer, T., Bellot Rubio, L. R., Berkefeld, T., Collados, M., Deutsch, W., Feller, A., Girela, F., Grauf, B., Heredero, R. L., Herranz, M., Jerónimo, J. M., Laguna, H., Meller, R., Menéndez, M., Morales, R., Orozco Suárez, D., Ramos, G., Reina, M., Ramos, J. L., Rodríguez, P., Sánchez, A., Uribe-Patarroyo, N., Barthol, P., Gandorfer, A., Knoelker, M., Schmidt, W., Solanki, S. K., Vargas Domínguez, S., 2011, The Imaging Magnetograph eXperiment (IMaX) for the Sunrise Balloon-Borne Solar Observatory, *Solar Phys.*, 268, 57
- Mathew, S. K., Lagg, A., Solanki, S. K., Collados, M., Borrero, J. M., Berdyugina, S., Krupp, N., Woch, J., Frutiger, C., 2003, Three dimensional structure of a regular sunspot from the inversion of IR Stokes profiles, *A&A*, 410, 695
- Mathew, S. K., Solanki, S. K., Lagg, A., Collados, M., Borrero, J. M., Berdyugina, S., 2004, Thermal-magnetic relation in a sunspot and a map of its Wilson depression, *A&A*, 422, 693
- Mathew, S. K., Zakharov, V., Solanki, S. K., 2009, Stray light correction and contrast analysis of Hinode broad-band images, *A&A*, 501, L19
- Mattig, W., Mehlretter, J. P., 1968, Fine Structure of Brightness, Velocity and Magnetic Field in the Penumbra, in *Structure and Development of Solar Active Regions*, (Ed.) K. O. Kiepenheuer, vol. 35 of IAU Symposium, p. 187

- McPherson, M. R., Lin, H., Kuhn, J. R., 1992, Infrared array measurements of sunspot magnetic fields, *Solar Phys.*, 139, 255
- Merenda, L., Lagg, A., Solanki, S. K., 2011, The height of chromospheric loops in an emerging flux region, *A&A*, 532, A63
- Meyer, F., Schmidt, H. U., 1968a, Magnetisch ausgerichtete Strömungen zwischen Sonnenflecken., *Zeitschrift Angewandte Mathematik und Mechanik*, 48, 218
- Meyer, F., Schmidt, H. U., 1968b, A Model for the Evershed Flow in Sunspots, *Mitteilungen der Astronomischen Gesellschaft Hamburg*, 25, 194
- Meyer, F., Schmidt, H. U., Weiss, N. O., 1977, The stability of sunspots, *MNRAS*, 179, 741
- Moradi, H., Baldner, C., Birch, A. C., Braun, D. C., Cameron, R. H., Duvall, T. L., Gizon, L., Haber, D., Hanasoge, S. M., Hindman, B. W., Jackiewicz, J., Khomenko, E., Komm, R., Rajaguru, P., Rempel, M., Roth, M., Schlichenmaier, R., Schunker, H., Spruit, H. C., Strassmeier, K. G., Thompson, M. J., Zharkov, S., 2010, Modeling the Subsurface Structure of Sunspots, *Solar Phys.*, 267, 1
- Müller, D. A. N., Schlichenmaier, R., Steiner, O., Stix, M., 2002, Spectral signature of magnetic flux tubes in sunspot penumbrae, *A&A*, 393, 305
- Müller, D. A. N., Schlichenmaier, R., Fritz, G., Beck, C., 2006, The multi-component field topology of sunspot penumbrae. A diagnostic tool for spectropolarimetric measurements, *A&A*, 460, 925
- Muller, R., 1973, Étude photométrique des structures fines de la pénombre d'une tache solaire, *Solar Phys.*, 32, 409
- Muller, R., 1976, Characteristics of the Displacement of the Penumbral Bright Grains of Sunspots, *Solar Phys.*, 48, 101
- Nandy, D., 2006, Magnetic helicity and flux tube dynamics in the solar convection zone: Comparisons between observation and theory, *Journal of Geophysical Research (Space Physics)*, 111, A12S01
- Orozco Suarez, D., Lagg, A., Solanki, S. K., 2005, Photospheric and Chromospheric Magnetic Structure of a Sunspot, in *Chromospheric and Coronal Magnetic Fields*, (Eds.) D. E. Innes, A. Lagg, S. A. Solanki, vol. 596 of ESA Special Publication
- Ortiz, A., Bellot Rubio, L. R., Rouppe van der Voort, L., 2010, Downflows in Sunspot Umbral Dots, *ApJ*, 713, 1282
- Pahlke, K.-D., Wiehr, E., 1990, Magnetic field, relative Doppler shift and temperature for an inhomogeneous model of sunspot umbrae, *A&A*, 228, 246
- Parker, E. N., 1975, The Nature of the Sunspot Phenomenon. IV: The Intrinsic Instability of the Magnetic Configuration, *Solar Phys.*, 40, 291

- Parker, E. N., 1978, Hydraulic concentration of magnetic fields in the solar photosphere. VI - Adiabatic cooling and concentration in downdrafts, *ApJ*, 221, 368
- Parker, E. N., 1979a, Sunspots and the physics of magnetic flux tubes. I - The general nature of the sunspot. II - Aerodynamic drag, *ApJ*, 230, 905
- Parker, E. N., 1979b, Sunspots and the physics of magnetic flux tubes. II. Aerodynamic drag., *ApJ*, 230, 914
- Parker, E. N., 1979c, Sunspots and the physics of magnetic flux tubes. IX - Umbral dots and longitudinal overstability, *ApJ*, 234, 333
- Penn, M. J., Kuhn, J. R., 1995, Imaging spectropolarimetry of the He I 1083 nanometer line in a flaring solar active region, *ApJ*, 441, L51
- Pevtsov, A. A., Canfield, R. C., Sakurai, T., Hagino, M., 2008, On the Solar Cycle Variation of the Hemispheric Helicity Rule, *ApJ*, 677, 719
- Piddington, J. H., 1975, Solar magnetic fields and convection. I - Active regions and sunspots, *Ap&SS*, 34, 347
- Press, W. H., Flannery, B. P., Teukolsky, S. A., 1986, Numerical recipes. The art of scientific computing
- Rachkovsky, D. N., 1962, Magnetic rotation effects in spectral lines, *Izvestiya Ordena Trudovogo Krasnogo Znameni Krymskoj Astrofizicheskoj Observatorii*, 28, 259
- Rachkovsky, D. N., 1967, The reduction for anomalous dispersion in the theory of absorption line formation in a magnetic field, *Izvestiya Ordena Trudovogo Krasnogo Znameni Krymskoj Astrofizicheskoj Observatorii*, 37, 56
- Rempel, M., 2011, Penumbra Fine Structure and Driving Mechanisms of Large-scale Flows in Simulated Sunspots, *ApJ*, 729, 5
- Rempel, M., 2012, Numerical Sunspot Models: Robustness of Photospheric Velocity and Magnetic Field Structure, *ApJ*, 750, 62
- Rempel, M., Schlichenmaier, R., 2011, Sunspot Modeling: From Simplified Models to Radiative MHD Simulations, *Living Reviews in Solar Physics*, 8, 3
- Rempel, M., Schüssler, M., Cameron, R. H., Knölker, M., 2009a, Penumbra Structure and Outflows in Simulated Sunspots, *Science*, 325, 171
- Rempel, M., Schüssler, M., Knölker, M., 2009b, Radiative Magnetohydrodynamic Simulation of Sunspot Structure, *ApJ*, 691, 640
- Rezaei, R., Schlichenmaier, R., Beck, C., Bellot Rubio, L. R., 2006, The flow field in the sunspot canopy, *A&A*, 454, 975
- Richardson, R. S., 1941, The Nature of Solar Hydrogen Vortices, *ApJ*, 93, 24

- Riethmüller, T. L., 2013, Investigations of small-scale magnetic features on the solar surface, Ph.D. thesis, Braunschweig University, ISBN 978-3-942171-73-1, uni-edition GmbH 2013
- Riethmüller, T. L., Solanki, S. K., Lagg, A., 2008, Stratification of Sunspot Umbral Dots from Inversion of Stokes Profiles Recorded by Hinode, *ApJ*, 678, L157
- Riethmüller, T. L., Solanki, S. K., van Noort, M., Tiwari, S. K., 2013, Vertical flows and mass flux balance of sunspot umbral dots, *A&A*, 554, A53
- Rimmele, T., 2008, On the Relation between Umbral Dots, Dark-cored Filaments, and Light Bridges, *ApJ*, 672, 684
- Rimmele, T., Marino, J., 2006, The Evershed Flow: Flow Geometry and Its Temporal Evolution, *ApJ*, 646, 593
- Rimmele, T. R., 1994, On the temporal behaviour of the Evershed effect., *A&A*, 290, 972
- Rimmele, T. R., 1995a, Evidence for thin elevated evershed channels., *A&A*, 298, 260
- Rimmele, T. R., 1995b, Sun center observations of the Evershed effect, *ApJ*, 445, 511
- Rimmele, T. R., 1997, Evidence for Magnetoconvection in a Sunspot Light Bridge, *ApJ*, 490, 458
- Ringnes, T. S., Jensen, E., 1960, On the relation between magnetic fields and areas of sunspots in the interval 1917-56, *Astrophysica Norvegica*, 7, 99
- Romano, P., Frasca, D., Guglielmino, S. L., Ermolli, I., Tritschler, A., Reardon, K. P., Zuccarello, F., 2013, Velocity and Magnetic Field Distribution in a Forming Penumbra, *ApJ*, 771, L3
- Roupe van der Voort, L., Bellot Rubio, L. R., Ortiz, A., 2010, Upflows in the Central Dark Lane of Sunspot Light Bridges, *ApJ*, 718, L78
- Roupe van der Voort, L. H. M., 2002, Penumbral structure and kinematics from high-spatial-resolution observations of Ca II K, *A&A*, 389, 1020
- Roupe van der Voort, L. H. M., Löfdahl, M. G., Kiselman, D., Scharmer, G. B., 2004, Penumbral structure at 0.1 arcsec resolution. I. General appearance and power spectra, *A&A*, 414, 717
- Rüedi, I., Solanki, S. K., Livingston, W. C., 1995, Infrared lines as probes of solar magnetic features. X. He I 10830A as a diagnostic of chromospheric magnetic fields., *A&A*, 293, 252
- Rüedi, I., Keller, C. U., Solanki, S. K., 1996, Measurement of the full Stokes vector of He I 10830 Å, *Solar Phys.*, 164, 265
- Rüedi, I., Solanki, S. K., Keller, C. U., Frutiger, C., 1998, Infrared lines as probes of solar magnetic features. XIV. Ti I and the cool components of sunspots, *A&A*, 338, 1089

- Ruiz Cobo, B., Asensio Ramos, A., 2013, Returning magnetic flux in sunspot penumbrae, *A&A*, 549, L4
- Rutten, R. J., Hammerschlag, R. H., Bettonvil, F. M., 1997, The Dutch Open Telescope, in *SCORE'96 : Solar Convection and Oscillations and their Relationship*, (Eds.) F. P. Pijpers, J. Christensen-Dalsgaard, C. S. Rosenthal, vol. 225 of *Astrophysics and Space Science Library*, p. 289
- Sakurai, T., Makita, M., Shibasaki, K., 1985, Observation of magnetic field vector in solar active regions., *Max Planck Institut fur Astrophysik Report*, 212, 312
- Sanchez Almeida, J., 1998, Optically Thin Irregularities in the Penumbrae of Sunspots, *ApJ*, 497, 967
- Sanchez Almeida, J., Lites, B. W., 1992, Observation and interpretation of the asymmetric Stokes Q, U, and V line profiles in sunspots, *ApJ*, 398, 359
- Sánchez Almeida, J., Márquez, I., Bonet, J. A., Domínguez Cerdeña, I., 2007, The Evershed Effect Observed with 0.2'' Angular Resolution, *ApJ*, 658, 1357
- Sánchez Cuberes, M., Puschmann, K. G., Wiehr, E., 2005, Spectropolarimetry of a sunspot at disk centre, *A&A*, 440, 345
- Sasso, C., Lagg, A., Solanki, S. K., 2006, Milne-Eddington inversions of the He 10830 Å Stokes profiles: influence of the Paschen-Back effect, *A&A*, 456, 367
- Scharmer, G., Blomberg, H., 1999, Optimized Shack-Hartmann Wavefront Sensing for Adaptive Optics and Post Processing, in *High Resolution Solar Physics: Theory, Observations, and Techniques*, (Eds.) T. R. Rimmele, K. S. Balasubramaniam, R. R. Radick, vol. 183 of *Astronomical Society of the Pacific Conference Series*, p. 239
- Scharmer, G. B., 2009, Recent Evidence for Convection in Sunspot Penumbrae, *Space Science Reviews*, 144, 229
- Scharmer, G. B., Henriques, V. M. J., 2012, SST/CRISP observations of convective flows in a sunspot penumbra, *A&A*, 540, A19
- Scharmer, G. B., Spruit, H. C., 2006, Magnetostatic penumbra models with field-free gaps, *A&A*, 460, 605
- Scharmer, G. B., Gudiksen, B. V., Kiselman, D., Löfdahl, M. G., Rouppe van der Voort, L. H. M., 2002, Dark cores in sunspot penumbral filaments, *Nature*, 420, 151
- Scharmer, G. B., Bjelksjo, K., Korhonen, T. K., Lindberg, B., Petterson, B., 2003, The 1-meter Swedish solar telescope, in *Innovative Telescopes and Instrumentation for Solar Astrophysics*, (Eds.) S. L. Keil, S. V. Avakyan, vol. 4853 of *Society of Photo-Optical Instrumentation Engineers (SPIE) Conference Series*, p. 341
- Scharmer, G. B., Narayan, G., Hillberg, T., de la Cruz Rodriguez, J., Löfdahl, M. G., Kiselman, D., Sütterlin, P., van Noort, M., Lagg, A., 2008a, CRISP Spectropolarimetric Imaging of Penumbral Fine Structure, *ApJ*, 689, L69

- Scharmer, G. B., Nordlund, Å., Heinemann, T., 2008b, Convection and the Origin of Evershed Flows in Sunspot Penumbrae, *ApJ*, 677, L149
- Scharmer, G. B., Henriques, V. M. J., Kiselman, D., de la Cruz Rodríguez, J., 2011, Detection of Convective Downflows in a Sunspot Penumbra, *Science*, 333, 316
- Scharmer, G. B., de la Cruz Rodríguez, J., Sütterlin, P., Henriques, V. M. J., 2012, Opposite polarity field with convective downflow and its relation to magnetic spines in a sunspot penumbra, *ArXiv e-prints*
- Schlichenmaier, R., 2002, Penumbra fine structure: Theoretical understanding, *Astronomische Nachrichten*, 323, 303
- Schlichenmaier, R., 2003, The Sunspot Penumbra: New Developments (Invited review), in *Current Theoretical Models and Future High Resolution Solar Observations: Preparing for ATST*, (Eds.) A. A. Pevtsov, H. Uitenbroek, vol. 286 of *Astronomical Society of the Pacific Conference Series*, p. 211
- Schlichenmaier, R., Collados, M., 2002, Spectropolarimetry in a sunspot penumbra. Spatial dependence of Stokes asymmetries in Fe I 1564.8 nm, *A&A*, 381, 668
- Schlichenmaier, R., Franz, M., 2013, Stray-light correction in 2D spectroscopy, *A&A*, 555, A84
- Schlichenmaier, R., Schmidt, W., 2000, Flow geometry in a sunspot penumbra, *A&A*, 358, 1122
- Schlichenmaier, R., Solanki, S. K., 2003, On the heat transport in a sunspot penumbra, *A&A*, 411, 257
- Schlichenmaier, R., Jahn, K., Schmidt, H. U., 1998a, Magnetic flux tubes evolving in sunspots. A model for the penumbral fine structure and the Evershed flow, *A&A*, 337, 897
- Schlichenmaier, R., Jahn, K., Schmidt, H. U., 1998b, A Dynamical Model for the Penumbral Fine Structure and the Evershed Effect in Sunspots, *ApJ*, 493, L121+
- Schlichenmaier, R., Bellot Rubio, L. R., Tritschler, A., 2004, Two-dimensional spectroscopy of a sunspot. II. Penumbral line asymmetries, *A&A*, 415, 731
- Schlichenmaier, R., Bellot Rubio, L. R., Tritschler, A., 2005, On the relation between penumbral intensity and flow filaments, *Astronomische Nachrichten*, 326, 301
- Schmidt, W., Hofmann, A., Balthasar, H., Tarbell, T. D., Frank, Z. A., 1992, Polarimetry and spectroscopy of a simple sunspot. I - On the magnetic field of a sunspot penumbra, *A&A*, 264, L27
- Schmidt, W., Knoelker, M., Westendorp Plaza, C., 1994, Limb observations of the He I 1083.0 NM line, *A&A*, 287, 229–232

- Schmidt, W., von der Lühe, O., Volkmer, R., Denker, C., Solanki, S. K., Balthasar, H., Bello Gonzalez, N., Berkefeld, T., Collados, M., Fischer, A., Halbgewachs, C., Heidecke, F., Hofmann, A., Kneer, F., Lagg, A., Nicklas, H., Popow, E., Puschmann, K. G., Schmidt, D., Sigwarth, M., Sobotka, M., Soltau, D., Staude, J., Strassmeier, K. G., Waldmann, T. A., 2012, The 1.5 meter solar telescope GREGOR, *Astronomische Nachrichten*, 333, 796
- Schnerr, R. S., de la Cruz Rodriguez, J., van Noort, M., 2010, Stokes imaging polarimetry using image restoration at the Swedish 1-m Solar Telescope II: A calibration strategy for Fabry-Perot based instruments, *A&A* (submitted)
- Schröter, E. H., 1965, Der Evershed-Effekt in einem inaktiven symmetrischen Einzelfleck. Mit 9 Textabbildungen, *ZAp*, 62, 228
- Schüssler, M., 1984, The interchange instability of small flux tubes, *A&A*, 140, 453
- Schüssler, M., Vögler, A., 2006, Magnetoconvection in a Sunspot Umbra, *ApJ*, 641, L73
- Servajean, R., 1961, Contribution à l'étude de la cinématique de la matière dans les taches et la granulation solaire, *Annales d'Astrophysique*, 24, 1
- Shchukina, N., Sukhorukov, A., Trujillo Bueno, J., 2012, Non-LTE Determination of the Silicon Abundance Using a Three-dimensional Hydrodynamical Model of the Solar Photosphere, *ApJ*, 755, 176
- Sheeley, Jr., N. R., 1972, Observations of the Horizontal Velocity Field Surrounding Sunspots, *Solar Phys.*, 25, 98
- Shi, J. R., Gehren, T., Butler, K., Mashonkina, L. I., Zhao, G., 2008, Statistical equilibrium of silicon in the solar atmosphere, *A&A*, 486, 303
- Shimizu, T., 2011, Long-term Evolution of Magnetic and Dynamical Properties in A Sunspot Light Bridge, *ApJ*, 738, 83
- Shimizu, T., Nagata, S., Tsuneta, S., Tarbell, T., Edwards, C., Shine, R., Hoffmann, C., Thomas, E., Sour, S., Rehse, R., Ito, O., Kashiwagi, Y., Tabata, M., Kodeki, K., Nagase, M., Matsuzaki, K., Kobayashi, K., Ichimoto, K., Suematsu, Y., 2008, Image Stabilization System for Hinode (Solar-B) Solar Optical Telescope, *Solar Phys.*, 249, 221
- Shimizu, T., Ichimoto, K., Suematsu, Y., 2012, Precursor of Sunspot Penumbral Formation Discovered with Hinode Solar Optical Telescope Observations, *ApJ*, 747, L18
- Shine, R. A., Title, A. M., Tarbell, T. D., Topka, K. P., 1987, White light sunspot observations from the Solar Optical Universal Polarimeter on Spacelab-2, *Science*, 238, 1264
- Shine, R. A., Title, A. M., Tarbell, T. D., Smith, K., Frank, Z. A., Scharmer, G., 1994, High-resolution observations of the Evershed effect in sunspots, *ApJ*, 430, 413

- Skumanich, A., Lites, B. W., Martínez Pillet, V., 1994, Vector spectropolarimetry with the Advanced Stokes Polarimeter (ASP) for quantitative solar magnetometry, in *Solar Surface Magnetism*, (Eds.) R. J. Rutten, C. J. Schrijver, p. 99
- Sobotka, M., Hanslmeier, A., 2005, Photometry of umbral dots, *A&A*, 442, 323
- Sobotka, M., Puschmann, K. G., 2009, Morphology and evolution of umbral dots and their substructures, *A&A*, 504, 575
- Sobotka, M., Sütterlin, P., 2001, Fine structure in sunspots. IV. Penumbral grains in speckle reconstructed images, *A&A*, 380, 714
- Sobotka, M., Bonet, J. A., Vazquez, M., 1993, A High-Resolution Study of Inhomogeneities in Sunspot Umbrae, *ApJ*, 415, 832
- Sobotka, M., Bonet, J. A., Vazquez, M., Hanslmeier, A., 1995, On the Dynamics of Bright Features in Sunspot Umbrae, *ApJ*, 447, L133
- Sobotka, M., Brandt, P. N., Simon, G. W., 1997a, Fine structure in sunspots. I. Sizes and lifetimes of umbral dots, *A&A*, 328, 682
- Sobotka, M., Brandt, P. N., Simon, G. W., 1997b, Fine structure in sunspots. II. Intensity variations and proper motions of umbral dots, *A&A*, 328, 689
- Sobotka, M., Brandt, P. N., Simon, G. W., 1999, Fine structure in sunspots. III. Penumbral grains, *A&A*, 348, 621
- Socas-Navarro, H., 2005, The Three-dimensional Structure of a Sunspot Magnetic Field, *ApJ*, 631, L167
- Socas-Navarro, H., Martínez Pillet, V., Sobotka, M., Vázquez, M., 2004, The Thermal and Magnetic Structure of Umbral Dots from the Inversion of High-Resolution Full Stokes Observations, *ApJ*, 614, 448
- Socas-Navarro, H., Trujillo Bueno, J., Landi Degl'Innocenti, E., 2005, Polynomial Approximants for the Calculation of Polarization Profiles in the He I 10830 Å Multiplet, *ApJS*, 160, 312
- Solanki, S. K., 1987, The Photospheric Layers of Solar Magnetic Flux Tubes, Ph.D. thesis, PhD thesis No. 8309, ETH, Zürich, (1987)
- Solanki, S. K., 1993, Smallscale Solar Magnetic Fields - an Overview, *Space Sci. Rev.*, 63, 1–188
- Solanki, S. K., 1997, Empirical Modelling and Thermal Structure of Sunspots, in *1st Advances in Solar Physics Euroconference. Advances in Physics of Sunspots*, (Eds.) B. Schmieder, J. C. del Toro Iniesta, M. Vazquez, vol. 118 of *Astronomical Society of the Pacific Conference Series*, p. 178
- Solanki, S. K., 2003, Sunspots: An overview, *A&A Rev.*, 11, 153

- Solanki, S. K., Brigljevic, V., 1992, Continuum brightness of solar magnetic elements, *A&A*, 262, L29
- Solanki, S. K., Montavon, C. A. P., 1993, Uncombed fields as the source of the broad-band circular polarization of sunspots, *A&A*, 275, 283
- Solanki, S. K., Schmidt, H. U., 1993, Are sunspot penumbrae deep or shallow?, *A&A*, 267, 287
- Solanki, S. K., Ruedi, I., Livingston, W., 1992, Infrared lines as probes of solar magnetic features. V - The magnetic structure of a simple sunspot and its canopy, *A&A*, 263, 339
- Solanki, S. K., Walther, U., Livingston, W., 1993, Infrared lines as probes of solar magnetic features. VI. The thermal-magnetic relation and Wilson depression of a simple sunspot, *A&A*, 277, 639
- Solanki, S. K., Montavon, C. A. P., Livingston, W., 1994, Infrared lines as probes of solar magnetic features. 7: On the nature of the Evershed effect in sunspots, *A&A*, 283, 221
- Solanki, S. K., Finsterle, W., Rüedi, I., Livingston, W., 1999, Expansion of solar magnetic flux tubes large and small, *A&A*, 347, L27
- Solanki, S. K., Lagg, A., Woch, J., Krupp, N., Collados, M., 2003, Three-dimensional magnetic field topology in a region of solar coronal heating, *Nature*, 425, 692–695
- Solanki, S. K., Lagg, A., Aznar Cuadrado, R., Orozco Suárez, D., Collados, M., Wiegmann, T., Woch, J., Sasso, C., Krupp, N., 2006, Measuring the Magnetic Vector with the He I 10830 Å Line: A Rich New World, in *Astronomical Society of the Pacific Conference Series*, (Eds.) R. Casini, B. W. Lites, vol. 358 of *Astronomical Society of the Pacific Conference Series*, p. 431
- Spruit, H. C., 1979, Convective collapse of flux tubes, *Solar Phys.*, 61, 363
- Spruit, H. C., 1981, A cluster model for sunspots, in *The Physics of Sunspots*, (Eds.) L. E. Cram, J. H. Thomas, p. 98
- Spruit, H. C., Scharmer, G. B., 2006, Fine structure, magnetic field and heating of sunspot penumbrae, *A&A*, 447, 343
- Spruit, H. C., Scharmer, G. B., Löfdahl, M. G., 2010, Striation and convection in penumbral filaments, *A&A*, 521, A72
- St. John, C. E., 1913, Radial Motion in Sun-Spots, *ApJ*, 37, 322
- Stachnik, R. V., Nisenson, P., Noyes, R. W., 1983, Speckle image reconstruction of solar features, *ApJ*, 271, L37
- Stanchfield, I. D. C. H., Thomas, J. H., Lites, B. W., 1997, The Vector Magnetic Field, Evershed Flow, and Intensity in a Sunspot, *ApJ*, 477, 485
- Stellmacher, G., Wiehr, E., 1981, Line profiles and magnetic field in penumbral fine structures, *A&A*, 103, 211

- Stuereburg, S., Holweger, H., 1990, Statistical equilibrium and photospheric abundance of carbon in the sun and in VEGA, *A&A*, 237, 125
- Suematsu, Y., Tsuneta, S., Ichimoto, K., Shimizu, T., Otsubo, M., Katsukawa, Y., Nakagiri, M., Noguchi, M., Tamura, T., Kato, Y., Hara, H., Kubo, M., Mikami, I., Saito, H., Matsushita, T., Kawaguchi, N., Nakaoji, T., Nagae, K., Shimada, S., Takeyama, N., Yamamuro, T., 2008, The Solar Optical Telescope of Solar-B (Hinode): The Optical Telescope Assembly, *Solar Phys.*, 249, 197
- Sütterlin, P., 2001, The size of penumbral fine structure, *A&A*, 374, L21
- Thiessen, G., 1950, The structure of the sunspot-umbra, *The Observatory*, 70, 234
- Thomas, J. H., 1988, Siphon flows in isolated magnetic flux tubes, *ApJ*, 333, 407
- Thomas, J. H., Montesinos, B., 1990, Siphon flows in isolated magnetic flux tubes. III - The equilibrium path of the flux-tube arch, *ApJ*, 359, 550
- Thomas, J. H., Montesinos, B., 1991, Siphon flows in isolated magnetic flux tubes. IV - Critical flows with standing tube shocks, *ApJ*, 375, 404
- Thomas, J. H., Weiss, N. O., 1992, *Sunspots: Theory and Observations*, Kluwer, Dordrecht
- Title, A. M., Frank, Z. A., Shine, R. A., Tarbell, T. D., Topka, K. P., Scharmer, G., Schmidt, W., 1992, High resolution observations of the magnetic and velocity field of simple sunspots, in *NATO ASIC Proc. 375: Sunspots. Theory and Observations*, (Eds.) J. H. Thomas, N. O. Weiss, p. 195
- Title, A. M., Frank, Z. A., Shine, R. A., Tarbell, T. D., Topka, K. P., Scharmer, G., Schmidt, W., 1993, On the magnetic and velocity field geometry of simple sunspots, *ApJ*, 403, 780
- Tiwari, S. K., Venkatakrishnan, P., Sankarasubramanian, K., 2009, Global Twist of Sunspot Magnetic Fields Obtained from High-Resolution Vector Magnetograms, *ApJ*, 702, L133
- Tiwari, S. K., van Noort, M., Lagg, A., Solanki, S. K., 2013a, Structure of sunspot penumbral filaments: a remarkable uniformity of properties, *A&A*, 557, A25
- Tiwari, S. K., van Noort, M., Solanki, S. K., Lagg, A., 2013b, Depth-dependent global properties of a sunspot observed from Hinode (SOT/SP), p. in preparation
- Toenjes, K., Woehl, H., 1982, Motions and lifetimes of the penumbral bright grains in sunspots, *Solar Phys.*, 75, 63
- Tritschler, A., Schmidt, W., 1997, Some properties of sunspot umbral dots., *A&A*, 321, 643
- Tritschler, A., Schlichenmaier, R., Bellot Rubio, L. R., KAOS Team, Berkefeld, T., Schelenz, T., 2004, Two-dimensional spectroscopy of a sunspot. I. Properties of the penumbral fine structure, *A&A*, 415, 717

- Tritschler, A., Müller, D. A. N., Schlichenmaier, R., Hagenaar, H. J., 2007, Fine Structure of the Net Circular Polarization in a Sunspot Penumbra, *ApJ*, 671, L85
- Trujillo Bueno, J., Landi Degl'Innocenti, E., Collados, M., Merenda, L., Manso Sainz, R., 2002, Selective absorption processes as the origin of puzzling spectral line polarization from the Sun, *Nature*, 415, 403
- Trujillo Bueno, J., Merenda, L., Centeno, R., Collados, M., Landi Degl'Innocenti, E., 2005, The Hanle and Zeeman Effects in Solar Spicules: A Novel Diagnostic Window on Chromospheric Magnetism, *ApJ*, 619, L191
- Tsuneta, S., Ichimoto, K., Katsukawa, Y., Nagata, S., Otsubo, M., Shimizu, T., Suematsu, Y., Nakagiri, M., Noguchi, M., Tarbell, T., Title, A., Shine, R., Rosenberg, W., Hoffmann, C., Jurcevich, B., Kushner, G., Levay, M., Lites, B., Elmore, D., Matsushita, T., Kawaguchi, N., Saito, H., Mikami, I., Hill, L. D., Owens, J. K., 2008, The Solar Optical Telescope for the Hinode Mission: An Overview, *Solar Phys.*, 249, 167
- Tziotziou, K., Tsiropoula, G., Mein, N., Mein, P., 2006, Observational characteristics and association of umbral oscillations and running penumbral waves, *A&A*, 456, 689
- Tziotziou, K., Tsiropoula, G., Mein, N., Mein, P., 2007, Dual-line spectral and phase analysis of sunspot oscillations, *A&A*, 463, 1153
- Unno, W., 1956, Line Formation of a Normal Zeeman Triplet, *PASJ*, 8, 108
- van Noort, M., 2012, Spatially coupled inversion of spectro-polarimetric image data. I. Method and first results, *A&A*, 548, A5
- van Noort, M., Rouppe van der Voort, L., Löfdahl, M. G., 2005, Solar Image Restoration By Use Of Multi-frame Blind De-convolution With Multiple Objects And Phase Diversity, *Solar Phys.*, 228, 191
- van Noort, M., Lagg, A., Tiwari, S. K., Solanki, S. K., 2013, Peripheral downflows in sunspot penumbrae, *A&A*, 557, A24
- Wallace, L., Hinkle, K., Livingston, W. C., 1993, An atlas of the photospheric spectrum from 8900 to 13600 cm^{-1} (7350 to 11230 [angstroms])
- Wang, H., Zirin, H., 1992, Flows around sunspots and pores, *Solar Phys.*, 140, 41
- Wedemeyer-Böhm, S., Rouppe van der Voort, L., 2009, On the continuum intensity distribution of the solar photosphere, *A&A*, 503, 225
- Westendorp Plaza, C., del Toro Iniesta, J. C., Ruiz Cobo, B., Martínez Pillet, V., Lites, B. W., Skumanich, A., 1997, Evidence for a downward mass flux in the penumbral region of a sunspot, *Nature*, 389, 47
- Westendorp Plaza, C., del Toro Iniesta, J. C., Ruiz Cobo, B., Martínez Pillet, V., 2001a, Optical Tomography of a Sunspot. III. Velocity Stratification and the Evershed Effect, *ApJ*, 547, 1148

- Westendorp Plaza, C., del Toro Iniesta, J. C., Ruiz Cobo, B., Martínez Pillet, V., Lites, B. W., Skumanich, A., 2001b, Optical Tomography of a Sunspot. II. Vector Magnetic Field and Temperature Stratification, *ApJ*, 547, 1130
- Westendorp Plaza, C., del Toro Iniesta, J. C., Ruiz Cobo, B., Martínez Pillet, V., Lites, B. W., Skumanich, A., 2001c, Optical Tomography of a Sunspot. II. Vector Magnetic Field and Temperature Stratification, *ApJ*, 547, 1130
- Wiehr, E., 1994, The height variation of sunspot umbral dots, *A&A*, 287, L1
- Wiehr, E., 1996, The spatial structure of the Evershed effect., *A&A*, 309, L4
- Wiehr, E., 2000, Magnetic field strength and inclination in the penumbral fine-structure, *Solar Phys.*, 197, 227
- Wiehr, E., Degenhardt, D., 1992, Spatial structure of the Evershed effect, *A&A*, 259, 313
- Wiehr, E., Degenhardt, D., 1993, Magnetic field strengths in umbral dots, *A&A*, 278, 584
- Wiehr, E., Stellmacher, G., 1989, Velocity and magnetic field fluctuations in penumbral fine-structures, *A&A*, 225, 528
- Wiehr, E., Knoelker, M., Grosser, H., Stellmacher, G., 1986, The sharp decrease of Evershed effect and magnetic field at the outer sunspot border, *A&A*, 155, 402
- Wilkinson, L. K., Emslie, G. A., Gary, G. A., 1989, The effects of viewing angle on the inference of magnetic shear in preflare active regions, *Solar Phys.*, 119, 77
- Xu, Z., Lagg, A., Solanki, S. K., 2010, Magnetic structures of an emerging flux region in the solar photosphere and chromosphere, *A&A*, 520, A77
- Xu, Z., Lagg, A., Solanki, S., Liu, Y., 2012, Magnetic Fields of an Active Region Filament from Full Stokes Analysis of Si I 1082.7 nm and He I 1083.0 nm, *ApJ*, 749, 138
- Zakharov, V., Hirzberger, J., Riethmüller, T. L., Solanki, S. K., Kobel, P., 2008, Evidence of convective rolls in a sunspot penumbra, *A&A*, 488, L17
- Zirin, H., Stein, A., 1972, Observations of Running Penumbral Waves, *ApJ*, 178, L85
- Zwaan, C., Brants, J. J., Cram, L. E., 1985, High-resolution spectroscopy of active regions. I - Observing procedures, *Solar Phys.*, 95, 3

Publications and Presentations

Publications

- **Joshi, J.**, Pietarila, A., Hirzberger, J., Solanki, S. K., Aznar Cuadrado, R., Merenda, L., Convective Nature of Sunspot Penumbra Filaments: Discovery of Downflows in the Deep Photosphere, *Astrophysical Journal Letters*, 734, L18 (2011).

Presentations

- **Joshi, J.**, Lagg, A., Hirzberger, J., Solanki, S. K., 3D Structure of a Sunspot: From Photosphere to Upper Chromosphere (Oral), *The Solar System within Geo- and Astrophysics (Rocks 'n' Stars)*, Veranstaltungszentrum am Wilhelmsplatz, Göttingen, Germany, 8-11, October (2012)
- **Joshi, J.**, Lagg, A., Hirzberger, J., Solanki, S. K., Kim, H., 3D Structure of a Sunspot: From Photosphere to Upper Chromosphere (Poster), *Hinode-6 meeting*, St Andrews, Scotland, UK, 14-17, August (2012)
- **Joshi, J.**, Danilovic, S., Hirzberger, J., Rubio da Costa, F., Solanki, S. K., Spectroscopy of a Sunspot Penumbra in the Deep Photospheric C I 5380 Å Spectral Line (Poster), *Hinode-5 meeting*, Cambridge, Massachusetts, USA, 10-15, October (2011)

Acknowledgements

First of all, I would like to express my heartfelt gratitude to my supervisor Prof. Dr. Sami K. Solanki, for his support and guidance throughout my PhD. I thank him for reading and improving my manuscripts and thesis as well as for teaching me the way of scientific writing. I am also very much grateful to my supervisor Dr. Johann Hirzberger for his support and guidance from the very beginning of my arrival in Lindau. I would like to thank Dr. Andreas Lagg and Dr. Johann Hirzberger, for being available at all times to discuss my problems and ideas and for answering my questions. My thesis has largely benefited from the in-depth knowledge of Sami, Johann and Andreas in the field. I am also thankful to Dr. Michiel van Noort for many interesting discussions. A big thanks to Prof. Dr. Karl-Heinz Glaßmeier for agreeing to be in my thesis advisory committee and for his encouragement.

I want to thank Dr. Alex Feller, Dr. Sanjiv Tiwari, Dr. Sanja Danilovic, Dr. Nagaraju Krishnappa and all other SLAMers for their advise and discussions. A special thanks to my office-mates David and Shahin for the good company and for interesting discussions on many things. Observing campaigns at Lapalma are wonderful memories. Thank you Johann, Shahin, Regina, Sanja, Fatima, Gautam and Björn for your company during observing campaigns.

Thank you very much Navdeep for being a supportive and wonderful friend from the very beginning of our time together in Lindau. A big thanks also go to all my Indian friends in Lindau for so many get-together and dinners. How can I forget my coffee time buddies in institute? Thank you Bharti ji, Nagaraju, Gautam, Guni, Girjesh, Jisesh (boss) and Meetu. Megha, Maria and David, I have very fond memories of working with you in the GalileoMobile project.

Last but not the least I owe tremendous gratitude to my family. Without their encouragement and support this thesis would not have been possible.

Curriculum Vitae

Personal details

Name	Jayant Joshi
Date of birth	05 May 1983
Place of birth	Damri-Dungarpur, India
Nationality	Indian

Educational details

07.2001-07.2004	B.Sc. (Physics, Mathematics and Statistics) Mohanlal Sukhadia University, Udaipur, India
07.2004-07.2006	M.Sc. (Physics) Mohanlal Sukhadia University, Udaipur, India
02.2010-2013	PhD student Max-Planck-Institut für Sonnensystemforschung, Katlenburg-Lindau, Germany Technische Universität Carolo-Wilhelmina zu Braunschweig, Germany

Professional details

07.2006-06.2008	Project Associate Udaipur Solar Observatory, Udaipur, India
06.2008-10.2009	Junior Research Fellow Space Applications Center, Indian Space Research Organization, Ahmedabad, India
09.2009-12.2009	Scientist-B Indian Institute of Astrophysics, Bengaluru, India